Irreversible aggregation of patchy colloidal particles : a computer simulation study

Achutha Prabhu

Agrégation irréversible par patchs de particules colloïdales. Une étude par simulation numérique

THÈSE

Présentée le 10 Decembre 2012

pour l'obtention du

Doctorat de l'Université du Maine - Le Mans

(Spécialité : Chimie et Physico-chimie des polymères)

par

Achutha PRABHU

Composition du jury:

Mme. Emanuela DEL GADO : ETH Zürich	Rapporteur
M. Albert JOHNER : Institut Charles Sadron, Strasbourg	Rapporteur
Mme. Marie Hélène MOREL : INRA - SupAgro, Montpellier	Examinatrice
M. Rémi BUSSELEZ : IMMM, Le Mans	Examinateur
M. Dominique DURAND : IMMM, Le Mans	Examinateur
M. Denis RENARD : INRA, Nantes	Co-directeur de thèse
M. Jean-Christophe GIMEL : IMMM, Le Mans	Directeur de thèse

Agrégation irréversible par patchs de particules colloïdales. Un étude par simulation numérique

Résumé :

La grande variabilité inhérente aux structures auto-assemblées est souvent due à la nature très anisotrope des interactions entre les particules qui les constituent. Cette anisotropie peut dans certains cas être représentée par un nombre limité de patchs à la surface de particules sphériques.

Cette thèse présente une nouvelle technique de simulation numérique pour étudier l'agrégation irréversible par patchs de particules colloïdales. Elle constitue une variation de la « dynamique d'amas browniens ». Elle prend en compte l'existence de ces patchs, mais aussi le mouvement brownien de rotation des particules. Pour représenter les patchs, nous utilisons le modèle de Kern-Frenkel avec des patchs univalents diamétralement opposés. Ils sont le moteur de l'agrégation irréversible entre les particules. La taille de ces patchs peut varier et une interaction isotrope de type puits-carré peut éventuellement être ajoutée pour prendre en compte la qualité thermodynamique du solvant.

Pour valider le modèle, le nouvel algorithme a été testé sur des chaînes isolées de polymères. Nous retrouvons bien les comportements statiques et dynamiques attendus pour des chaînes isolées en bon solvant. Cela a permis d'explorer plus finement la structure des chaines et de calculer les diverses longueurs de persistance définies dans la littérature. Nous avons ainsi pu donner une description phénoménologique de la transition entre le comportement idéal et celui auto-évitant d'une chaîne semi-flexible en bon solvant. Cependant cet algorithme n'est pas assez robuste pour aborder l'étude dynamique des longues chaînes.

Le phénomène d'agrégation étudié peut être assimilé à une polymérisation par étape. En fonction de la qualité du solvant et de la taille des patchs, différentes structures complexes peuvent être obtenues avec des évolutions temporelles complexes. Nous nous sommes attachés à comprendre la cinétique de ces processus dans le cadre d'une approche de type Smoluchowski (étude des collisions entre les particules). Pour ce faire, nous nous sommes focalisés sur l'étude de la simple réaction de formation des dimères en conditions diluées. Même aux très fortes dilutions, nous montrons que les collisions corrélées jouent un rôle central dans la cinétique de la réaction pour des particules anisotropes. L'approche de Smoluchowski n'est donc plus satisfaisante dans ce cas. Nous proposons quelques nouvelles pistes pour comprendre l'influence de cette anisotropie de surface sur la cinétique d'agrégation des particules.

Irreversible aggregation of patchy colloidal particles.
A computer simulation study

Abstract:

The versatility of self assembling structures is mostly due to the presence of anisotropic or patchy interactions. This thesis presents a new simulation method to study irreversible patchy aggregation of colloidal particles. The simulation method is a variation of the Brownian Cluster Dynamics method taking into account anisotropic interactions (patches) and rotational motions. The basic particle is a modified Kern-Frenkel model with two oppositely located univalent patches, through which irreversible aggregation takes place. The size of the patch may vary and an isotropic interaction may be superimposed around the particle to mimic the solvent quality.

To confirm the validity of this method, the new algorithm was tested on single polymer chains, the simplest object that can be built using this model. Various predicted static and dynamic properties of the polymer chains were perfectly recovered with this method and a deeper insight about the static properties of a self avoiding chain has been made. A detailed study of the different persistence length definitions in the literature was carried out and we were able to give a phenomenological description for the cross over from the ideal behavior to the swollen one. However, we were limited by the chain length and its local flexibility regarding dynamics.

In the case of aggregation studies, which correspond to step growth polymerization reactions with various solvent qualities, different aggregate structures were obtained. The kinetic studies of these reactions lead to a detailed analysis of the simple dimerization reaction. Even in the limit of extremely dilute solutions, we found that correlated collisions play an important role on the rate of the reaction and the Smoluchowski approach fails. We propose some new directions for a better understanding of anisotropy effects on kinetics.

Acknowledgements

List of symbols

α_0 Probability of forming an isotropic bond

α_1 Probability of forming a patchy bond

β_0 Probability of breaking an existing isotropic bond

β_1 Probability of breaking an existing patchy bond

χ Relative surface coverage by all patches

δ Bond angle in a polymer chain

γ_i Angle between bond vector and patch vector

γ_i Angle between the spin vector and bond vector for monomer i

$\mathbf{R}_e$ End to end vector

$\mathbf{r}_{ij}$ Bond vector connecting monomers i and j

ν Flory's exponent

ω Patch cone angle

ϕ Volume fraction

τ_R Rouse time

$\theta(s)$ Angle between bond vectors separated by s segments

ε_0 The relative well width for the isotropic square well potential

ε_1 The relative well width for the patchy square well potential

B_2 Reduced second virial coefficient

B_2^* Second virial coefficient

B_{att} Attractive part of reduced second virial coefficient

$C(t)$ Normalized time correlation function of end to end vector

C_0 Number density of particles at $t = 0$

C_i Number density of clusters having an aggregation number i

C_t Number density of clusters at time t

d Diameter of the particle

d_f Fractal dimension

D_i^T Translational diffusion coefficient of a cluster with aggregation number i

D_i^R Rotational diffusion coefficient of a cluster with aggregation number i

k_B Boltzmann constant

K_p Rate constant for patchy bond formation for correlated couples

K_u Rate constant for uncorrelation reaction

$K_{i,j}$ Rate constant for aggregation of clusters of aggregation numbers i and j

L Length of a polymer chain

l_1 Persistence length of a polymer chain

L_box Edge length of the simulation box

l_b Average bond length

l_K Kuhn length

m Number of monomers in a polymer chain

m_n Number average aggregation number

m_w Weight average aggregation number

n Simulation time

n_w Fraction of couples in interaction range

p Extent of reaction

P_0 Isotropic bond probability

P_1 Patchy bond probability

R_g Radius of gyration

$R_{col,i}$ Capture radius of a cluster with aggregation number i

s_R Rotational Brownian step length

s_T Translational Brownian step length

T Absolute temperature

t Time

t_0 Time required for a free monomer to diffuse a distance of d^2

t_{c}^{l} Average time spent in interaction range $l = 0$ for ideal and $l = 1$ for real cases

u_0 Isotropic well depth

u_1 Patchy well depth

V_{b} The interaction volume

Contents

Introduction

The significance of soft matter comes from the fact that a major part of the living being is made of living soft matter, mainly colloidal systems. The study of colloidal systems are covered by many active research areas of science because their wide range of occurrence and properties. A colloid is a microscopic dispersion of one substance in another one. The colloidal system can be solid, liquid or gaseous. The dispersed phase (or internal phase) generally consists of particles of size in the range nm to μm and the particles in dispersion medium (or continuous phase) have typically atomistic size range. Some typical examples of colloidal systems are blood, milk, gels, mist, smoke, stained glass, etc. Due to the size difference, the structural relaxation times also differ and for the dispersed phase, the typical relaxation time comes in the order of seconds. Since the size scales in the colloidal systems are in the range of the wavelength of light, light scattering techniques are widely used to study their structure and dynamics. Even though colloidal systems are very complex in nature, they could be described using simple effective potentials and we can integrate out the fast relaxation of the dispersion medium and other additives, which are comparatively small to the dispersed particles [1]. The result of this approximation directly enables the colloidal particles to be considered as 'superatoms', alternatives for atomistic and molecular systems. Such superatoms, having their own characteristic size and time scales could be used to study the various phenomena such as caging effect, disordered states, metastable fluids, etc.

The main feature we can see in colloidal systems is the large surface area of the dispersed phase. Hence, dispersed particles are largely affected by the surface chemistry in the colloid. Manipulation of the surface chemistry is thus very critical in fine tuning the inter particle interaction defining the system. This could be achieved using several methods like the use of additives, grafting polymer chains on to the particle surface, etc. The vast freedom of tunability of colloidal particles could be extended to directional interactions as present in atomistic systems, apart from the spherical isotropic interactions. These particles with highly directional or strongly anisotropic interactions or patches are called as patchy particles [2]. The fact that non spherical particles are intrinsically anisotropic does not make them patchy since all those interacting particles are similar. The presence of anisotropic interactions act as the driving force for the self assembly of colloidal particles. Patches are very important tools for engineering the self assembly to obtain a target structure. In practice, using various methods like physical and chemical depositions,

lithography, etc., large amounts of mono disperse patchy particles were obtained. A recent article [3] gives an overall comparison of various methods, the yield, and the prospective use of various kinds of well engineered patchy particles. The self assembly of particles or the bottom up approach is quite useful in the experimental field to overcome the size and processing limitation and offers a better control for obtaining less defective final structures.

Using the vast degree of tunability of these colloidal superatoms with the ideas from supra-molecular chemistry opens doors to a better understanding of aggregation, self assembly and their interplay in the molecular level. The vast tunability could be directly connected to the 'intrinsically patchy' protein systems, where phenomena are commonly explained using the lock and key mechanism. Glotzer and Solomon [4] put forward an effort to classify the tunability by considering the key parameters describing the anisotropy of the basic building block - 'patch dimensions' (see Figure 1.1). Using this concept, the complexity of the anisotropic nature could be resolved to basic patch dimensions for facility. In this approach, the complexity of a patchy particle model increases with the increase in orthogonal anisotropy dimensions. The authors propose that use of unique anisotropic dimensions could lead to commonality in different systems which differ by shape or by dimension of the particle, but still may differ by the phase behavior. Also, a detailed study may lead to some commonalities in different systems, but it is quite out of question when seen through the practical point of view. In this strategy, reverse engineering a complex structure to find the building block seems more relevant and designing rules could be made out.

Theoretical studies of colloidal systems with specific interactions started in the 1980s to study strongly associating fluids, long before the patchy particles were experimentally synthesized in comparatively large and mono disperse scale. These primitive systems were mainly focused around hard-core systems with specific attractive sites and with these models, it was possible to compare the features of the liquid and solid(crystalline) state [5]. It is also a key point on the introduction of a new model that it is tested against these simpler system before extending to more realistic situations. Using event-driven molecular dynamics for a classical hard-core model [6], the authors were able to investigate deeper in to the dynamics of molecular diffusion [7] and further understand the interplay between packing driven arrest and bond-driven arrest in network forming fluids [8]. Recent theoretical studies go in two directions - one using spherical particles (hard or soft) with various kinds of surface decorations for patchiness, which varies in shape and size [9, 10, 11, 12, 13, 7, 14, 15] and other with anisotropic particles with patchy interactions [16, 17, 18, 19, 20, 21]. Since there are still areas to be explored in colloidal patchy particle science, there is still room for many simple systems.

Whatever be the model, the final structure of aggregates always depends on the nature of the system. See figure 1.2 for a comparison of different structures obtained from the present study. In general, for irreversible interactions, we get fractal
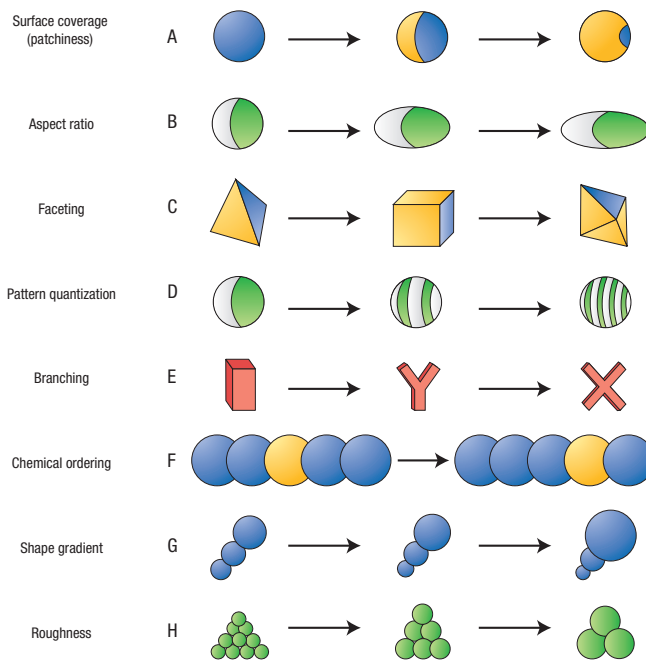
Figure 1.1: Some of the different anisotropy dimensions and their homologs used to describe the patchiness by Glotzer and Solomon [4].

structures, for reversible ones we get dense clusters and in the case of a mixture of reversible and irreversible interaction (two opposite patches, which are irreversible), the structures vary from single chain-like to bundles of chains to network-like structures. For patchy particle systems, the analysis of the final structure also present difficulties, because of its complex nature.

Protein aggregation is a phenomenon where a protein loses its native conformation leading to aggregation. Protein aggregation is important area of research because many of the human disorders like Alzheimers, Parkinsons disease etc. are induced by protein aggregation. The three main kinds of the observed aggregates are: fibrils, amorphous aggregates and soluble oligomers [22]. Protein aggregation is a complex phenomena and various mechanisms have been proposed. It has been proposed that proteins could be modeled using patchy particles. In the present context, comparing with the figure 1.2, we see that many aggregate structures observed in the protein aggregation could be achieved using patchy particles.

In this thesis, we introduce a spherical patchy particle model inspired from Kern and Frenkel [9] and Giacometti [15], and use a modified version of Brownian Cluster Dynamics simulation [23] to study the irreversible aggregation through patches. The areas we would like to explore from the point of view of short range attractive
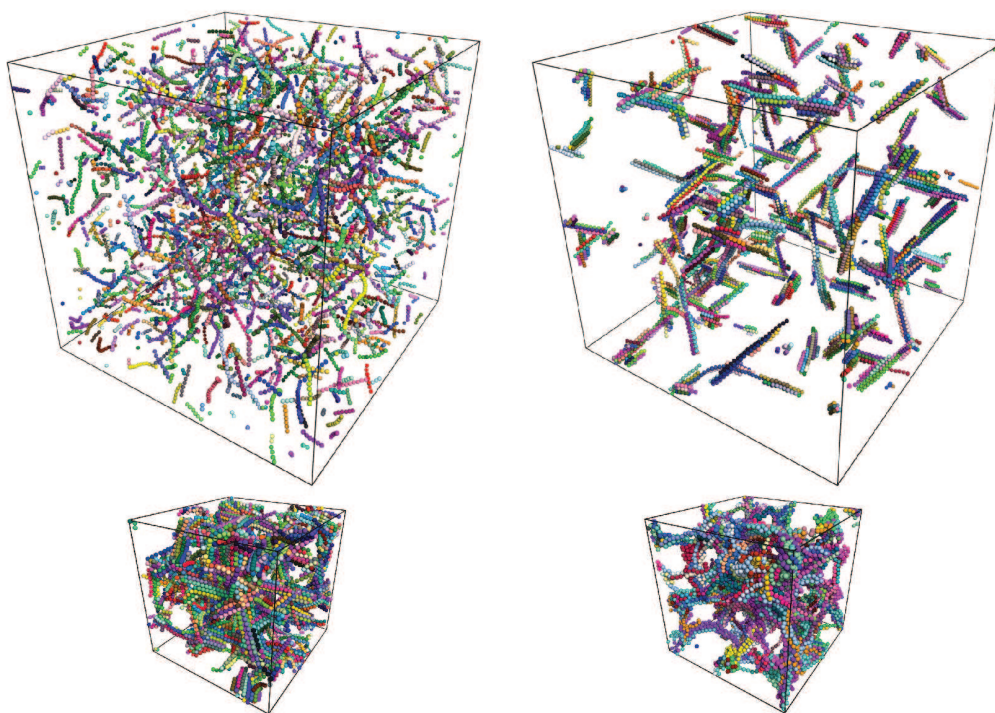
Figure 1.2: Some of the different aggregate structures obtained using our model.

potential are:

1. Irreversible aggregation through patches

2. The kinetics of the patchy aggregation

3. Possibility of extension of the system to model polymeric protein binding and aggregation

Outline of the thesis

In *Chapter 2*, a brief literature survey is presented in which the basic theories and the developments related to this work are discussed.

In *Chapter 3*, we introduce our patchy model and simulation technique.

In *Chapter 4*, to verify the validity of our model, we explore static and dynamic properties of single polymer chains - the simplest structure obtained from our model.

In *Chapter 5*, we present our efforts to understand the patchy aggregation reaction, by studying the simple case of dimerization.

Chapter 6 concludes the thesis and present future directions to be explored.

Self assembly of particles through short range potentials

Colloidal particles under the influence of attractive forces form aggregates, which grow with time. The basic parameters used to explain the aggregation process and its kinetics include the interaction parameters such as strength, direction and range, and concentration of the particles. By varying these parameters, different regions in the phase diagram of the system could be studied. Figure 2.1 shows the representative phase diagram for hard sphere colloidal systems. In the case of long range interactions, there exists a triple point where all the three phases coexist. For the short range interactions, the gas and crystal phases coexist and we also find a metastable liquid-liquid phase separation [24]. Various works can be found in the literature devoted to study of aggregation process and aggregate characterization such as [25], [26] etc.
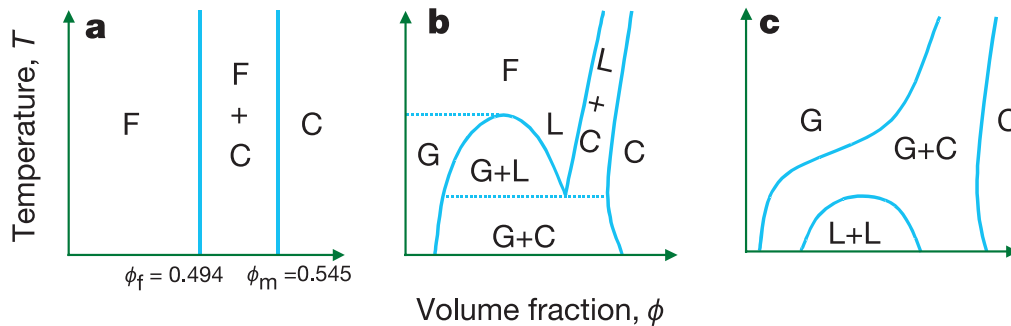
Figure 2.1: Schematic phase diagrams of (a) hard spheres, (b) hard spheres with long range interactions and (c) hard spheres with short range interactions. In the figures, C represents crystal, F fluid, G gas and L liquid respectively, and ϕ_f and ϕ_m represent the freezing and melting transitions respectively. Image taken from [24].

The microscopic state of a colloidal system could be explained using a Hamiltonian in terms of the position and momenta of the constituent particles. The kinetic energy of the system can be calculated from the momenta, but a well behaved potential energy term is needed to construct and evaluate an equation of

motion, which evolves in time and provides with the properties of the system. This potential energy term plays a role on the form of equilibrium distribution function of the particles in the system. The importance of the distribution function and its moments is its measurability from scattering experiments. For the simplest case of hard sphere systems, the important features of the potential are the hard core repulsion when hard spheres come too close and the short range attraction. It is these abrupt changes in the potential that results in the short range order in a given phase. For colloidal particles, the interaction range is small compared to the size of the particle and hence the number of interacting particles becomes limited. This makes the system easier to study. In this thesis, we will focus on the aggregation of hard sphere particles interacting through short range potentials.

2.1 Short range isotropic interaction

Spontaneous formation of ordered structures from randomly distributed entities such as atoms, molecules, colloidal particles etc., termed as self assembly is one of the basic areas of current research. The term isotropic means that the interaction potential is spherically symmetric around the basic entity under consideration, which is usually spherical for facility. For an aggregation process, there are two cases based on the nature of the interaction - whether it is reversible or irreversible. For reversible case, the system always tends to attain a maximum stable state (thermal equilibrium) through restructuration. This minimizes the free energy and hence they are termed thermodynamically driven systems. For the irreversible case, the aggregate structures formed are not equilibrated at any time. Since there is limited possibility of reorganization after the aggregation, the system is termed as kinetically driven.

2.1.1 Reversible aggregation

This case occurs when the thermal energy is of the order of the intensity of the potential, leading to fragmentation or bond breaking of already formed clusters. Reversibility plays an important role on the structure of the aggregates since the particles rearrange to attain a minimal free energy configuration.

In simulation, the usually employed pair potentials include square well, Lennard Jones, Baxter and Yukawa models. Figure 2.2 describes square well potential for hard spheres. The particle diameter is d and the well width (ε_0) is expressed in terms of the diameter of the particle. The potential energy of this system is given as

$$u(r_{ij}) = \begin{cases} \infty & , r_{ij} < d \\ u_0 & , d \leq r_{ij} \leq d \cdot (1 + \varepsilon_0) \\ 0 & , r_{ij} > d \cdot (1 + \varepsilon_0) \end{cases} \qquad (2.1)$$

where, r_{ij} is the distance between the interacting particles i and j and $u_0 < 0$ is the potential energy in the well. For a simple closed system having a N_0 particles

in a volume V at a temperature T acting through pairwise additive potential, the equation of state can be written as a power series in terms of the number density $C_0 = N_0/V$ as

$$\frac{P}{C_0 \cdot k_\mathrm{B} \cdot T} = 1 + \sum_{i=2}^{\infty} B_i^*(T) \cdot C_0^{i-1} = 1 + \sum_{i=2}^{\infty} B_i(T) \cdot \phi^{i-1} \tag{2.2}$$

$\phi = C_0 \cdot v_0$ is the volume fraction of the particles, v_0 is the volume of one particle and k_B the Boltzmann constant. The temperature dependent parameters $B_i^*(T)$ are the so called the virial coefficients and $B_i(T) = B_i^*(T)/v_0^{i-1}$, the dimensionless reduced virial coefficients.
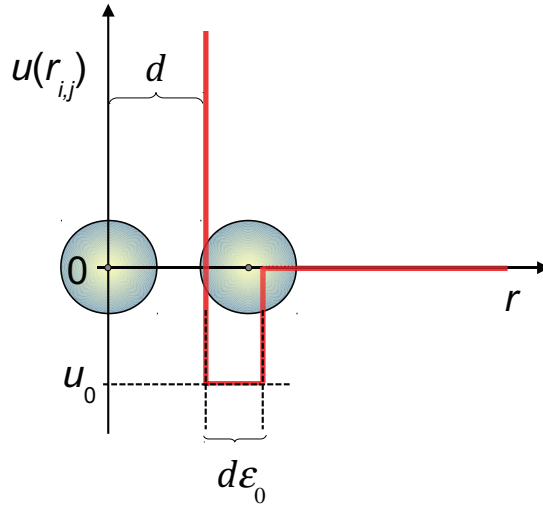
Figure 2.2: Potential energy diagram for a square well system.

Different systems can have different shapes for the potential energy curves but their phase diagrams have some similarities. Van der Waals pointed out the similarity in thermodynamic properties of simple gases, when expressed in terms of the reduced variables compared to their critical point. Later, Noro and Frenkel [27] extended this law of corresponding states as: short range attractive potentials (up to $\varepsilon_0 = 0.1$) are characterized by the same thermodynamic properties if compared at the same reduced density and second virial coefficient (B_2). The thermodynamic state does not depend on the shape of the potential energy curve. This means that a combination of different u_0 and ε_0 can give the same thermodynamic equilibrium state, when B_2 is kept constant. This concept helps the close comparison of the different works in the literature. Babu et al. [28] reported that this law holds up to $\varepsilon_0 = 0.1$ in the case of square well fluids.

The B_2^* parameter is given as

$$B_2^*(T) = -2 \cdot \pi \cdot \int_0^\infty r^2 \cdot \left[\exp \left(\frac{-u(r)}{k_\mathrm{B} \cdot T} - 1 \right) \right] \cdot \mathrm{d}r \tag{2.3}$$

For a spherical hard core square well system, B_2 is the sum of the excluded volume repulsion and the square well attraction.

$$B_2 = B_{rep} - B_{att} \tag{2.4}$$

The repulsive part has been calculated to be $B_{rep}=4$ and B_{att} can be expressed in terms of ε_0 and a function of the interaction potential u_0[29].

$$B_{att} = 4 \cdot \left[\exp \left(\frac{-u_0}{k_{\mathrm{B}} \cdot T} \right) - 1 \right] \cdot [(1 + \varepsilon_0)^3 - 1] \tag{2.5}$$

The equilibrium states of a reversibly aggregating system depends on the volume fraction (ϕ) , interaction energy and the interaction range. We take the particular case of hard spheres interacting through an isotropic square well potential. See figure 2.3 for the state diagram, the shape of which could be directly compared to that in figure 2.1(c).
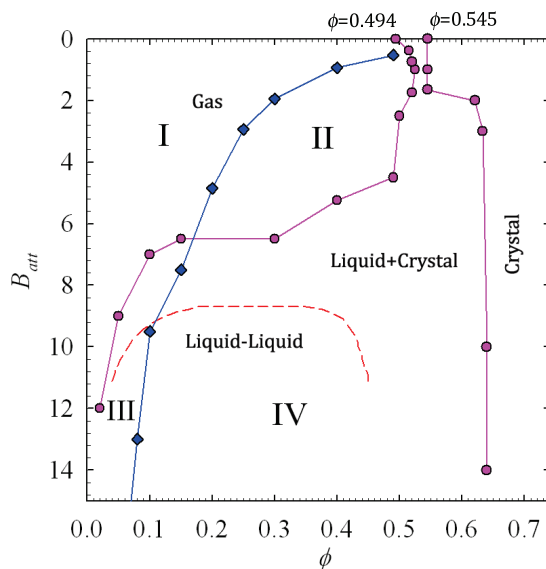
Figure 2.3: State diagram of hard sphere square well system with $\varepsilon_0=0.1$ and varying well depths. B_{att} is the attractive part of B_2. The circles represent liquid-crystal phase transition, diamonds indicate the percolation point and the broken lines represent the metastable liquid-liquid phase separation. Image adapted from [30]

Reversible aggregation leads to formation of transient clusters or a phase separated system or a percolating network depending on B_{att} and ϕ. Four different regions can be identified in the phase diagram on the basis of coexistence lines and the percolation line, below which spanning clusters are formed. At low concentration, for weak attraction finite clusters are formed (region I) and strong attraction leads to phase separation (region III). As the concentration increases, the small clusters formed start to grow and interpenetrate leading to percolation (region II)

where the percolating clusters are transient. Stronger attraction leads to temporary gels, which ages and finally phase separates (region IV).

In the absence of any attractive potential, the hard core repulsion causes the system to crystallize at higher volume fraction due to the increased configurational entropy (see figure 2.1 a). At low potentials, the liquid state is stabilized by the weak interactions and the coexistence gap is narrowed. As the interaction strengthens, the lower volume fractions get unstabilized and a transition to denser crystalline phase occurs at higher volume fractions. For a broad range of volume fractions from 0.05 to 0.4, the coexistence curve is situated around B_{att}=7. Crystallization occurs in two ways - nucleation and growth type and spinodal decomposition type[24]. At higher B_{att} liquid droplets are formed, which undergoes restructuration to form a crystalline seed, which then grows in time. In the region between the coexistence curve and the liquid-liquid curve, it is difficult to observe crystallization in a reasonable time unless some seeding is done. The liquid-liquid curve is metastable in the case of short range interaction and hence the system always crystallizes. For strong attraction and higher ϕ, a percolating network may form. As time passes, particles get detached from the dangling ends and get added to the network thickening the strands and finally the gel is destroyed resulting in phase separation. In the beginning this process is very similar to spinodal decomposition. In both cases, finally, a single crystal should form. In practice, it takes quite a long time in the case of strong interactions and hence is not generally observed.

There are many ways to slow down or prevent crystallization in the coexistence region. One method is to make the bonds rigid [31], which tremendously slows down the reorganization inside clusters. Another method is to introduce polydispersity in the system [32, 33]. Depending on the type and amount of polydispersity introduced, crystallization could be slowed down or completely suppressed [34]. Suppressing crystallization makes it possible to observe another region liquid-liquid curve in the phase diagram, where liquids of different densities coexist.

If neither liquid-liquid phase separation nor crystallization occurs at higher concentrate, we get virtually dynamically arrested homogeneous systems containing disordered liquid phase. Colloidal glass comes under this region [35]. One way to achieve this is to restrict the number of sticky contacts between particles [35]. This could be done using two methods: by limiting the valency, where the number of sticky contacts per particle is limited irrespective of the position of the participating particles (if more particles are in the interaction range, only a fixed number of randomly selected contacts are considered sticky and the rest is excluded from the internal energy calculation); or by using directional interactions, also termed as patches (see section 2.2). This makes the coexistence line shift towards the lower concentration and frees up a homogeneous region with strong interaction and high ϕ. It is in this region where studies have been going on for attractive glass [36].

2.1.2 Irreversible aggregation

The kinetic approach for irreversible aggregation was introduced by von Smoluchowski [37, 38]. The reaction mechanism of irreversible aggregation could be simply represented as an addition reaction between clusters A_i and A_j of aggregation numbers i and j respectively. The mechanism could be simply written as

$$A_i + A_j \xrightarrow{K_{i,j}} A_{i+j} \tag{2.6}$$

where, $K_{i,j}$ is the rate of the aggregation for clusters made of i and j particles respectively. Here, there are two limiting conditions based the probability that two particles stick together on collision (α_0). When $\alpha_0=1$, every collision leads to bond formation and when $\alpha_0 \ll 1$, a large number of collisions are required before a bond is formed. When $\alpha_0 = 1$, the reaction is controlled only by the diffusion of particles and hence is termed as diffusion limited cluster aggregation (DLCA) and when $\alpha_0 \ll 1$, it is known as reaction limited cluster aggregation (RLCA).

Following the chemical equation 2.6, the temporal evolution of a distribution of cluster sizes could be calculated [37, 39, 40]. The total change in the clusters with $m = i + j$ particles can be written as

$$\frac{dC_m}{dt} = \frac{1}{2} \cdot \sum_{i+j=m} K_{i,j} \cdot C_i \cdot C_j - C_m \cdot \sum_{i=1}^{\infty} K_{m,i} \cdot C_i \tag{2.7}$$

where C_i is the number density of clusters made up of i individual particles. The second term in this equation stands for the loss of the m-mer due to further aggregation with any i-mer.

In the DLCA case, the analytical derivation of $K_{i,j}$ was carried out by von Smoluchowski [37, 38] for very low concentrations. Here, the distance between particles/clusters is much bigger than their size and they show free Brownian motion between collisions. The dilute condition limits the reaction to binary collisions. All these conditions together constitute the flocculation regime. Under flocculation conditions and assuming that clusters should be within a certain radius of influence called collision radius ($R_{col,i}$) to interact, we have

$$K_{i,j} = 2 \cdot \pi \cdot (R_{col,i} + R_{col,j}) \cdot (D_i^{\mathrm{T}} + D_j^{\mathrm{T}}) \tag{2.8}$$

where, D_i^{T} is the translational diffusion coefficient for a cluster with aggregation number i. Here, the sum term with collision radius is used to calculate the average collision radius of different interacting particles. The sum term with diffusion coefficients accounts for the relative motion of interacting clusters. In the case of a hard sphere square well potential, $R_{col,1} = d \cdot (1+\varepsilon_0)$. D_i^{T} is related to the hydrodynamic radius R_{h_i} by the Stokes-Einstein equation

$$D_i^{\mathrm{T}} = \frac{k_{\mathrm{B}} \cdot T}{6 \cdot \pi \cdot \eta \cdot R_{h_i}} \tag{2.9}$$

where, η is the viscosity of the solvent medium. Assuming that $R_{h_i} \sim R_{col_i}$, which is reasonable, we have

$$D_i^{\mathrm{T}} \cdot R_{col,i} = D_1^{\mathrm{T}} \cdot R_{col,1} \quad , i = 1, 2, 3... \tag{2.10}$$

We make another assumption that $R_{col,i} = R_{col,j}$, (all interacting species have identical dimensions) which is not very realistic. This gives

$$K_{i,j} = K_{1,1} = 8 \cdot \pi \cdot D_1^{\mathrm{T}} \cdot R_{col,1} \tag{2.11}$$

Using this relation, equation 2.6 can be solved analytically to get number density of m-mer at any time t for an initial particle density C_0 as [40]

$$C_m = C_0 \cdot \frac{\left(\dfrac{K_{1,1}}{2} \cdot C_0 \cdot t\right)^{m-1}}{\left(1 + \dfrac{K_{1,1}}{2} \cdot C_0 \cdot t\right)^{m+1}} \tag{2.12}$$

From this equation, the kth moment of distribution could be calculated as

$$M_k \equiv \sum_{m=1}^{\infty} m^k \cdot C_m \tag{2.13}$$

From here, the number average aggregation number($m_n = \frac{M_1}{M_0}$) and the weight average aggregation number ($m_w = \frac{M_2}{M_1}$) could be obtained.

$$m_w \approx 1 + K(1, 1) \cdot C_0 \cdot t \tag{2.14}$$

$$m_n \approx 1 + \frac{K(1, 1)}{2} \cdot C_0 \cdot t \tag{2.15}$$

The polydispersity index is given as $PDI = m_w/m_n$. In the flocculation regime, after an initial aggregation period, PDI becomes stable and $PDI = 2$. A detailed study on the binary reaction will be presented in chapter 5.

However, with these set of equations it is not possible to explain successfully the RLCA process. So, new kernels were introduced, which take care the probability of bond formation or in other words, the correlated collision leading to a bond formation [41].

Irreversible aggregation leads to formation of self similar structures. The radius of gyration of cluster R_{g} is related to the aggregation number m through the fractal dimension d_{f} by the following equation [25, 26].

$$m \propto R_{\mathrm{g}}^{d_{\mathrm{f}}} \tag{2.16}$$

For the flocculation regime in DLCA, d_{f} has been found to be around 1.8 and for RLCA this value comes around 2.1 [26]. This means that RLCA clusters are

denser than DLCA ones. This is directly understood, since particles can explore the interior of the cluster in RLCA, leading to densification of the cluster. In the case of DLCA, a variation with "slippery bonds" has been proposed, where bound particles can move freely within the interaction range without breaking the bonds [42, 43]. Aggregates formed in this way are denser than aggregates formed by the classical "rigid bond" type, where particles link on contact and do not rearrange after. Even though both of these models ends up having similar fractal dimension, the local structures and hence the prefactors in equation 2.16 differ. The average coordination number varies, which is 2 for the rigid DLCA and is found to vary for the slippery DLCA depending on ϕ (this depends also on the interaction range for the slippery case) [31]. Also, we can see a slowing down of the aggregation process due to the restructuration in the case of smaller ϕ. Restructuration continues until a maximum number of bonds are formed without breaking any existing bonds. Restructuration time varies depending on the cluster size. For dilute cases, clusters undergo complete restructuration before their next collision, leading to a slowing down of the kinetics. For high volume fraction cases, the kinetics is enhanced due to the flexibility [42].

2.2   Directional interactions

Searching for key forces behind the versatility of materials in nature leads to directional interactions. Directional interactions result in the organization of basic building blocks in to more sophisticated ordered arrangements, which is termed as self assembly. Self assembly is of great importance in biological sciences and various studies are still in progress to understand the process through biomimetic approaches [44]. Also, the self assembly of viruses has been of great interest [45]. These studies of selective binding and assembly are quite helpful in the process of drug discovery and in medicine. The classical self assembly examples are formation of micelles, aggregation of block co-polymers in solution, etc., which are guided by different interactions present in the system. Now, supra-molecular chemists are trying to come up with exotic molecular structures with specific interaction sites as the building blocks to get a desired self assembled structure for new advanced functional materials.

The process of self assembly is not restricted to molecular level. When appropriate conditions are met, systems with various sizes ranging to nano and micro scales are shown to follow self assembly [46]. This opens up a better insight in to the process, since this can be easily studied using microscopic techniques available now, whereas monitoring the molecular level is still under development. Another possibility is versatility in shape that could be produced using novel methods, which is difficult to achieve using synthetic atomistic methods. So is the case for tuneability of the interactions and the interaction sites on the basic building block. As the size becomes large compared to molecular scale, the choice of selection of the material, interactions and its parameters also increases, simplifying bonding restrictions

at the molecular scale. For atomic scales, the interactions are usually medium to long ranged (at their length scale) and the highly symmetric low energy structures (global minima) are formed in abundance. For colloids, short range interactions come in to play and the yield of an expected structure becomes entropy limited and hence the amount of highly symmetric compact structures formed becomes lesser [47, 48]. At microscopic colloidal level, the motion of the particles is described as Brownian (see equation 2.9). Even though studying colloidal aggregation helps understanding the mechanism, it is limited by the fact that the larger the size, higher is the time the particle takes to diffuse and hence increased defect in resulting structures. Also, introduction of patches results in a change of the aggregation kinetics from the well studied isotropic case. Hence in the case of targeted assembly, the expected structure should be thermodynamically stable and at the same time kinetically accessible [49].

In practice, there are two ways to study the association of patchy particles. Experimentally, patchy particles are fabricated using the various methods available and their aggregation behavior in solution is studied. Figure 2.4 shows some of the various physical and chemical methods available for fabrication of patchy particles of which template assisted methods are used mainly for creating one patch and offers a better yield [3]. Each method has its own advantages in terms of easiness of preparation and scalability, while the separation and the transfer to the media of interest cause some issues. Another main issue is in terms of the size and accurate positioning of the patch. Another method is simulation and modeling studies. In both of these methods, the basic principle for creation of the particle is decorating the surface of a colloidal particle so that a difference in the interaction is achieved in some regions of the surface. In the modeling approach, besides the directional interaction due to the shape of the basic particle, patchiness could be introduced in the following methods

I Building small clusters of particles to constitute the basic shape and assigning different interaction potentials to some of the chosen spheres at specific locations on the surface of the particle. Being able to make different basic shapes as the advantage, the increased number of the particles in the system causes computational slowing down. This method has been used in [2].

II Positioning small spherical square well patchy regions on the surface of the basic particle. The size, number and position of the patch could be varied. This method is quite popular and was also used to model small chemical entities like water and also to study the formation of colloidal gels. [50, 51, 52, 53]

III The sticky patchy sphere with a conical square well potential on the surface of the sphere, with the cones originating from the center of the particle. Here the patch number, size, potential type and range could be varied.[54, 55, 9]

IV Considering the continuous potential in nature, patch directors are specified
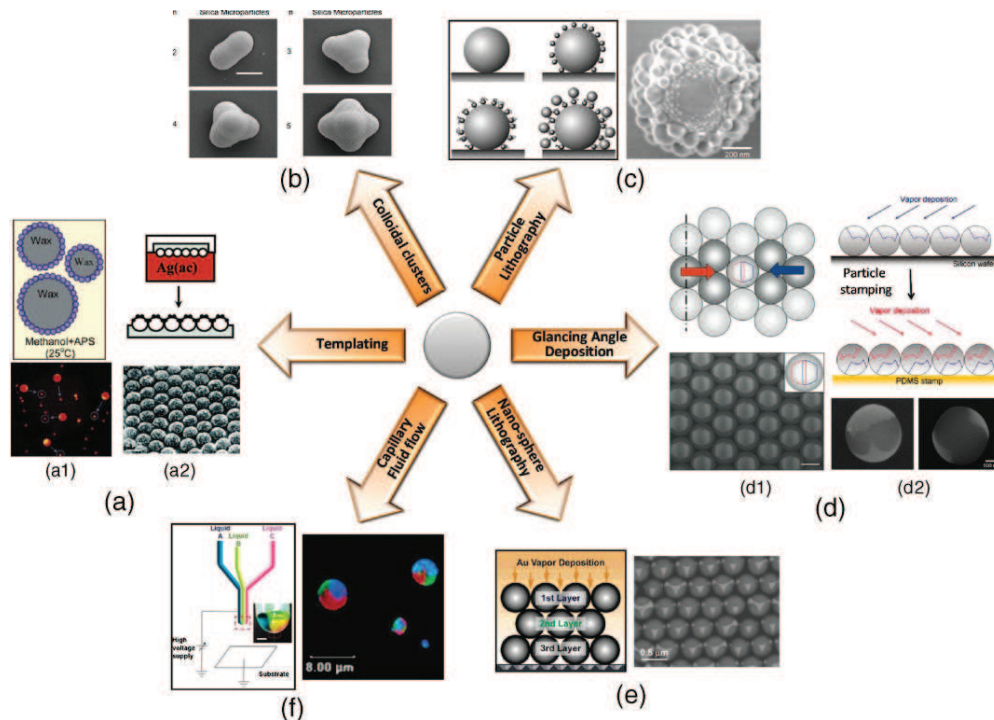
Figure 2.4: Different routes to fabricate patchy particles. a) Templating - a1) Schematic of emulsion technique and epifluorescent microscope image of single patch particles obtained from the emulsion technique and a2) Schematic of electroless deposition technique and SEM image of 2.4mm polystyrene particles with silver coating. b) Colloidal assembly - colloidal clusters with n=2-5 prepared from emulsion of a mixture of silica particles with 800 and 12nm diameters. c) Particle lithography - schematic of particle lithography technique and resulting 1mm amine-functionalized silica particle with a single patch obtained after sequential coating with 10nm polystyrene particles and 84nm sulfate polystyrene spheres. d) Glancing-angle deposition - d1) Schematic of sequential vapor deposition process performed on same hemisphere and SEM image of resulting polystyrene patchy particle with overlapping patches; and d2) Schematic of combined PDMS stamping and sequential GLAD technique and SEM images of two-pole polystyrene patchy particles with 25 and 11 percent patches. e) Nanosphere lithography - schematic of nanosphere lithography technique and resulting 520nm silica particles with gold patches in the second layer of the colloidal crystal (scale bar: 0.5mm). f) Capillary fluid flow - schematic of capillary fluid flow technique and confocal laser scanning microscopy image of triphasic particles obtained (scale bar: 8 mm). Image and caption taken from [3].

for the basic particle and the potential is modified such that it changes with the alignment of the patch directors.[56]

This could be pictorially represented, as in figure 2.5. It is shown that positioning patches at appropriate positions and at appropriate conditions leads to predictable assemblies like rods, sheets, polyhedra etc. [2]. Fine tuning of the interaction could be achieved by varying the selectivity of the interaction, which is quite essential in the case of protein modeling. Selectivity results in structures, which may seem identical from a macroscopic point of view, but may differ in their internal structure, symmetry and energy. This can be easily represented for the case of a two patch particle, see figure 2.6. For different kinds of interaction, the overall external appearance is the same for dimers and tetramers, but in terms of symmetry they are different and also the internal energy may differ.
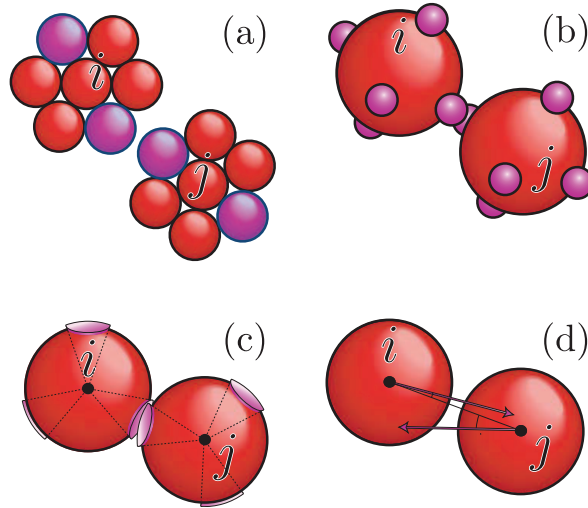
Figure 2.5: Methods used to model spherical patchy particles. Basic colloidal spheres are colored red and the attractive patches are represented in purple. (a) Clusters of spheres with some spheres at specific positions acting as patches. (b) Spheres decorated with spherical square well patchy sites. (c) Spheres with a conical patchy interaction volume, where the cone originates at the center of the particle. (d) Alignment dependent patches, where the interaction potential varies with respect to the patch directions, indicated by the purple vectors. Image taken from [57].

2.2.1 Reversible aggregation

While modeling aggregation, for simplicity, it was always taken care: 1. not make any double bonds between particles, 2. avoid multiple bonding through patches and 3. avoid cyclization.

This has direct outcomes in thermodynamical calculation of the system properties. Under these limits, Wertheim [59, 60, 61] used perturbation theory to obtain
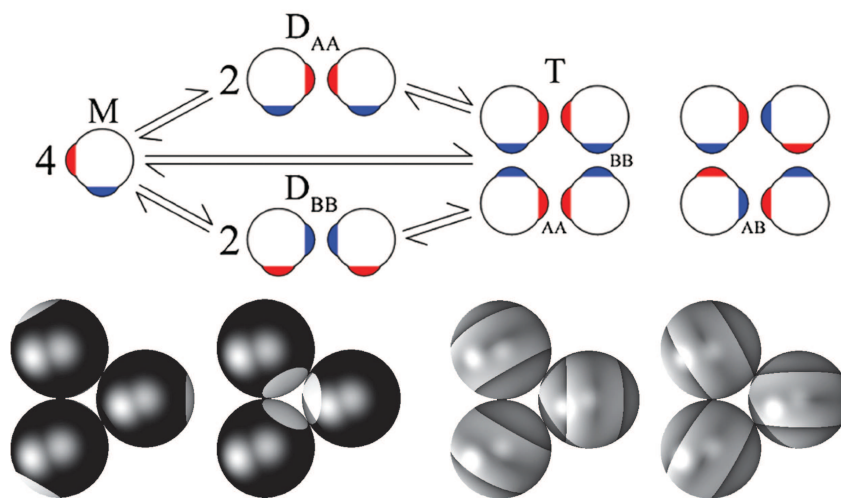
Figure 2.6: Effect of selectivity: Top image shows how the selectivity of the patchy interaction changes the resulting structure and symmetry and bottom image shows various bonding possibilities for a one patch and two patch systems. Images taken from [58] and [12] respectively.

the free energy of the system using the bonding probability, which is seen as the ratio of the number of bonds present in the system to the total number of bonds that is possible [11]. Using this theory for a two oppositely placed patch system, the number density of a chain having m monomers was calculated to be

$$C_m = C_0 \cdot X^2 \cdot (1 - X)^{m-1} \tag{2.17}$$

where C_0 is the initial particle number density and X is the fraction of sites that are not bonded, which could be calculated as $X = 1/(1 + 2 \cdot C_0 \cdot X \cdot \Delta)$. Here Δ is a term having dimensions equivalent to the B_{att}^* (the attractive part of B_2^*, which has a dimension of volume) and accounts to all possibilities of a single patch-patch interaction. Under low ϕ conditions, it could be approximated as $\Delta = V_b \cdot [\exp(-u_1/(k_b \cdot T)) - 1]$, where V_b is the interaction volume and u_1 is the intensity of the patchy interaction. The bond probability is simply given as $1 - X$. Using this method, we have the simple relation $m_n = 1/X$. Combining Wertheim approach with Flory-Stockmayer theory, a generalized model for patchy particles to find the cluster size distribution and the extent of reaction has been carried out by Tavares et al. [62].

The bond probability at the liquid-gas critical point is shown to have more importance as it could be used for extending the law of corresponding states to patchy systems under Wertheim conditions [63]. For the Kern-Frenkel model without any valence limitations, B_{att} is given by [9]

$$B_{att} = \chi^2 \cdot [(1 + \varepsilon_1)^3 - 1] \cdot [\exp(-u_1/(k_B \cdot T)) - 1] \tag{2.18}$$

where, χ is the fractional surface coverage of the patch. Here B_{att} is influenced by the surface coverage of the patch and the interaction range in opposing ways to have a constant B_{att}. Hence, it becomes difficult to scale the critical points only on the basis of B_{att}. The authors argue that the bonding pattern plays an important role, which is statistically identical for each patchy class at corresponding conditions. They conclude that for a system with given number of monovalent patches, it is the bond probability and not the B_{att} that is constant at critical conditions [63].
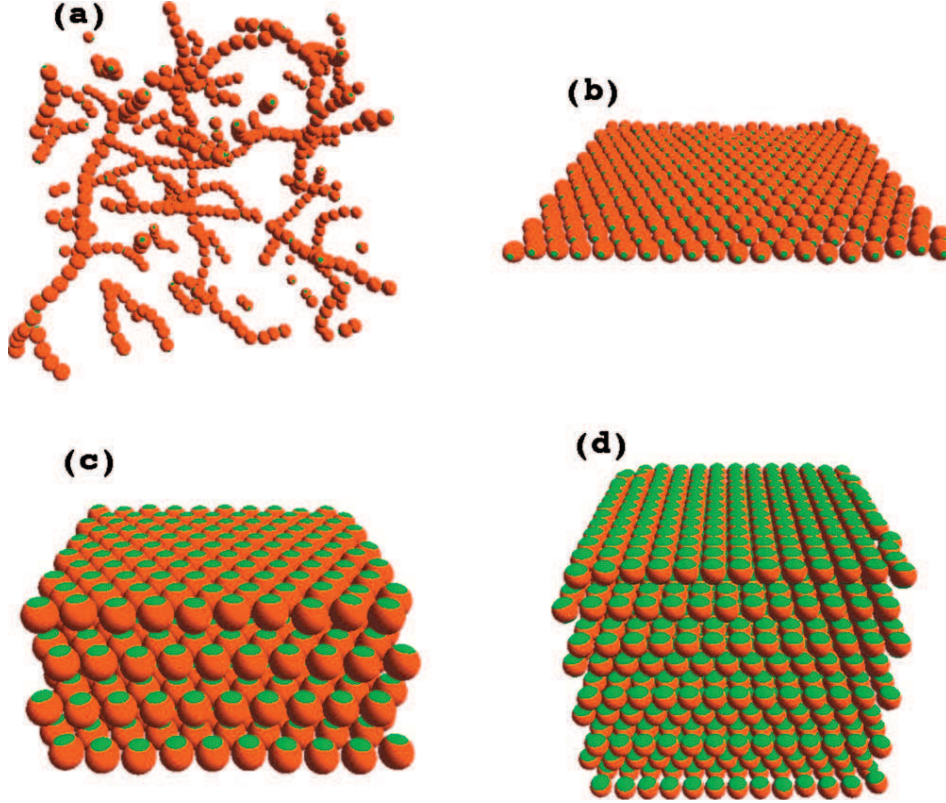
Figure 2.7: Effect of valency in a two patch Kern-Frenkel system at low temperatures: Maximum valency is tuned by changing the coverage of the patch. (a) Maximum valency=1. Polydisperse chains are formed. (b) Valency=2. Planar structures are formed. (c) Valency=3 and (d) valency=4 give stacked planes with different particle arrangements. Image taken from [15].

For patchy systems, the density of the aggregate depends on the number of patches, the size of the patch and the valency [15, 64]. With decreasing number of patches, the liquid-gas critical point shifts towards lower ϕ and higher B_{att}, similar to the behavior observed for the restricted valency model in the case of isotropic interaction [35]. Thus with smaller number of patches and coverage, it becomes possible to reach liquid states, where the density becomes vanishingly small. These are termed as empty liquids, and recently it has been shown to exist by experimental methods [51, 21]. So is the case for the patch coverage in the case

of Kern-Frenkel models - the critical points shifts towards slightly lower density and temperature. Systems with tetrahedrally placed patches were studied for their similarity to produce diamond like crystals and the interaction range was found to be not a limiting factor for the nucleation of a crystal [19]. For higher coverage of patch, it was found that liquid phase is stabilized by higher valence [15]. For the two patch case, by setting a maximum valency per patches and by varying the coverage, it was shown to aggregate (see figure 2.7) from interconnected planes (maximum valency 4 and 3) to simple planes interacting though excluded volume interactions (valency 2) to polydisperse chains (valency 1). Apart from coverage, the relative placement of patches were found to have lesser effects than the number of patches, but the effect is still visible on the critical values [65]. These structural differences in the assemblies could be clearly seen in the phase diagram. See figure 2.8 for an example phase diagram of Kern-Frenkel type particles with four tetrahedrally placed monovalent patches.
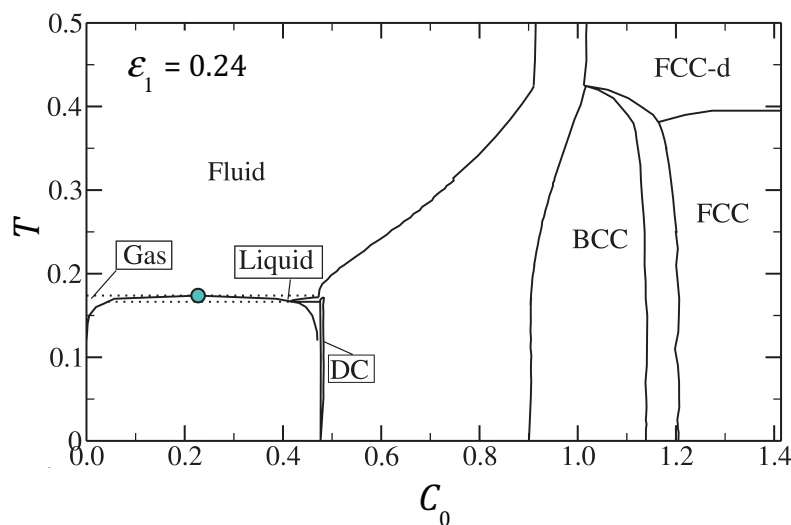
Figure 2.8: Phase diagram of spherical particles with tetrahedrally placed monovalent patches in as a function of number density C_0 and temperature T in terms of $k_B \cdot T$ for a relative interaction range $\varepsilon_1 = 0.24$. The blue circle is the critical point, the gas-liquid coexistence line is shown with dashed lines. DC represents diamond cubic, FCC : face centered cubic, FCC-d : disordered FCC and BCC : body centered cubic. Image taken from [19].

2.2.2 Irreversible aggregation

Irreversible aggregation can be simply seen as polymerization reactions, where the number of patches corresponds to the functionality of the monomer. Since the aggregation is not one by one addition of monomers, step growth polymerization theory is applicable. The theory of linear step growth polymerization is mainly based on the works of Carothers [66, 67] and Flory [68]. Their theory was based on the principle of equal reactivity ie. the reactivity of the end groups does not

depend on the chain length. Also, they did not differentiate between the kinetically controlled and thermodynamically controlled polymerization reactions and loop formation was neglected [69]. The formation of loops/cycles has been studied later by many groups experimentally and by simulation [69, 70, 71, 72].

For simplicity, we will discuss only the linear polymerization, which corresponds to aggregation of a monovalent patchy particle having two patches. Here the term monovalent is used to denote the valency of the patch and the total bonds that could be formed by a particle (functionality) is the product of the valency of the patch and the number of patches. The easiest way to visualize the mechanism of a step-growth polymerization is a group of people reaching out to hold their hands to form a human chain, where the two hands of each person stands for the functionality. There is also the possibility to have more than two functionalities, which lead to branched polymers. In step growth polymerization, chains build up slowly and there is only one reaction mechanism behind the polymerization. The chemical reaction for step growth polymerization is similar to the cluster aggregation process and the general scheme of step growth homo polymerization for a bifunctional system could be written as

$$\text{XAX} + \text{XAX} - (\text{XAX})_n - \text{XAX} \longrightarrow \text{XAX} - (\text{XAX})_{n+1} - \text{XAX} \qquad (2.19)$$

where X is the functional group. In the case of polymerization, the number of unreacted functional groups in a chain remains the same at all times. This is based on the assumption that a functionality reacts only once and no loops are formed in the course of the reaction.

Under these conditions, the extent of the reaction or the fractional conversion at any given time is given by

$$p = \frac{\sum (m-1) \cdot C_m}{C_0} = 1 - \frac{C_t}{C_0} \qquad (2.20)$$

where C_m is the number density of polymer chains made of m monomers, C_0 the initial number density of chains and C_t is the number density of chains at the given time t.

To calculate the distribution of chain lengths, the conditions of equi-reactivity is imposed, meaning all the functionality are equally reactive, irrespective of the size of the chain to which it belongs to. The chain length distribution can be calculated as follows:

1. A chain of length m has $(m-1)$ fully reacted monomers and two unreacted chain ends, which is equivalent to a single unreacted monomer.

2. The probability that a randomly selected monomer is fully reacted is p. In the chain, the probability of finding $(m-1)$ reacted monomers is then $p^{(m-1)}$.

$m{=}1$

Unreacted functionality

$m{=}4$

$m{=}9$

Reacted functionality
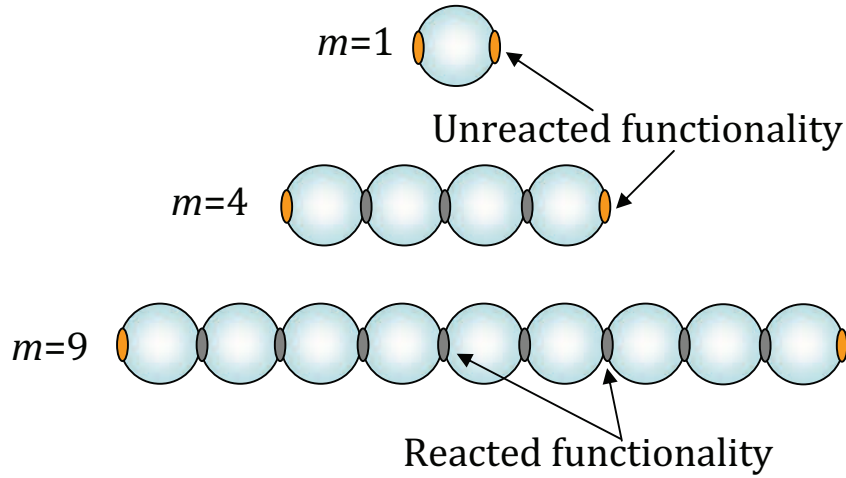
Figure 2.9: Schematic representation of polymer chains with different lengths start-ing from a bifunctional monomer, $m{=}1$. For each m, there is $m-1$ bonds and one unreacted functionality at each chain end. According to equireactivity principle, all the unreacted chain ends are equally reactive.

3. The probability of finding an unreacted species is given by $(1-p)$. Note that there is no term associated with m, meaning that all the chains are equally reactive.

Combining these, we get the probability of finding an m-mer as

$$f_m = p^{(m-1)} \cdot (1-p) \tag{2.21}$$

and the number density of m-mers in the system at a given time can be calculated as

$$C_m = C_t \cdot p^{(m-1)} \cdot (1-p) \tag{2.22}$$

which in turn by substitution of $C_t = C_0 \cdot (1-p)$ from equation 2.20 gives

$$C_m = C_0 \cdot p^{(m-1)} \cdot (1-p)^2 \tag{2.23}$$

We have already seen the expression for number average aggregation number, which could be recovered as

$$m_n = \frac{\sum\limits_{m=1}^{\infty} m \cdot C_m}{\sum\limits_{m=1}^{\infty} C_m} = \frac{\sum_{m=1}^{\infty} m \cdot C_0 \cdot p^{(m-1)}(1-p)^2}{C_t} = \frac{1}{1-p} \tag{2.24}$$

using the relation $\sum\limits_{m=1}^{\infty} m \cdot p^{m-1} = 1/(1-p)^2$.   Similarly, using the relation $\sum\limits_{m=1}^{\infty} m^2 \cdot p^{(m-1)} = (1+p)/(1-p)^3$, the second moment, the weight average aggre-

gation number can be calculated to be

$$m_w = \frac{\sum\limits_{m=1}^{\infty} m^2 \cdot C_m}{\sum\limits_{m=1}^{\infty} m \cdot C_m} = \frac{\sum\limits_{i=1}^{\infty} m^2 \cdot p^{(m-1)}}{\sum\limits_{i=1}^{\infty} m \cdot p^{(m-1)}} = \frac{(1+p)}{(1-p)} \tag{2.25}$$

The polydispersity index, PDI, is given by

$$PDI = \frac{m_w}{m_n} = 1 + p \tag{2.26}$$

and we see that initially when $p = 0$, $PDI = 1$ and as the polymerization proceeds, the value slowly increases to the maximum possible value of 2.

The kinetics for the polymerization reaction can be derived considering that no catalyst is participating in the reaction or the catalyst is external. It means that the concentration of catalyst is constant at all times. Assuming equi-reactivity of the C_t species, the rate of polymerization can be written as

$$-\frac{\mathrm{d}C_t}{\mathrm{d}t} = k_\mathrm{p} \cdot N_c^2 \tag{2.27}$$

where k_p is the rate constant. Rearranging followed by integration and substituting the initial condition that at $t=0$, $C_t=C_0$ gives

$$\frac{C_0}{C_t} - 1 = k_\mathrm{p} \cdot N_0 \cdot t \tag{2.28}$$

Recalling the equation 2.20 we get

$$\frac{1}{1-p} = m_n = 1 + k_\mathrm{p} \cdot C_0 \cdot t \tag{2.29}$$

This solution could be directly compared with the solution for Smoluchowski's equation and it could be showed that the kinetic solution is equivalent to the probabilistic approach [73] while there are no diffusion effects.

2.2.2.1 Diffusion effects

The principle of equal reactivity is based on the idea that only the reactive chain end needs to diffuse and collide with other reactive sites and does not require the motion of the entire chain [68]. It is also estimated that in the case of typical polymerization, only one in the 10^{13} leads to the reaction [68]. This is valid for the fully flexible polymers where to some extends the diffusion of chain ends can be compared to that of freely moving monomers. In cases where the chains are far apart (in case of very dilute systems) and for highly entangled systems (concentrated systems), this approach starts to fail. In the first case, the chain ends become isolated by the distance and in the second case by the caging of unreactive polymeric parts. Also,

as the reaction proceeds the number of chain ends becomes lower and hence the system experiences a limitation due to diffusion.

For rigid rod-like polymers, the segmental diffusion theory becomes invalid, hence the effects will be more pronounced. The diffusion effects in step-growth polymerization has been studied both experimentally and theoretically [74, 75, 76, 77, 78, 79, 80] because of the commercial importance of such polymers due to their high mechanical properties. Kline et al. [81] studied the enzyme catalyzed esterification reaction under solvent free conditions and noted that the PDI is initially increasing to reach maximum value and then decreases. This behavior was attributed to the diffusion limitations, which limit the formation of longer chains. A similar evolution was noted by Guzman et al. [80] and the subsequent increase in the PDI was explained as due to the concentration effects, which outweigh diffusion limitations. This occurs when the chain length distribution becomes narrow and the concentration of the average length becomes maximized.

Using Smoluchowski approach, the effective rate constant of the system can be seen as the sum of a diffusional part and an intrinsic bond probability part, which could be expressed as [80]

$$\frac{1}{k_p} = \frac{1}{k_{int}} + \frac{1}{K_{i,j}} \tag{2.30}$$

where k_{int} is the intrinsic term and $K_{i,j}$ is the diffusivity term. As in the Smoluchowski approach for cluster aggregation, the diffusional part is composed of a diffusivity term and a trapping radius of the reacting chains (see equation 2.8). For an ideal polymer chain of length m, the trapping radius is equal to the radius of gyration and for an ideal chain $R_{col,i} \propto \sqrt{m}$ [82]. The diffusivity varies with the chain length and depends on the system conditions whether the chains are entangled or not. For dilute conditions (Rouse dynamics), it is calculated that $D_m^T \propto 1/m$ and for concentrated conditions (entangled system), the chains move by reptation and $D_m^T \propto 1/m^2$ [82]. In the absence of diffusion limitations, PDI increases linearly with conversion as seen before. In the case of diffusion limitations, PDI goes through a maximum and reaches a final value somewhere around 1.27 to 1.3. For higher rigidity of the chain and branching, PDI is expected to go below 1.27 [80].

2.2.2.2 Cyclization

Cyclization is the main side reaction of step-growth polymerization. Stepto et al. [83, 72, 84] and Gordon et al. [85] studied the effect of cyclization and concluded that it can compete with chain growth irrespective of the conversion and concentration. Mathematical analysis of irreversible systems were carried out by Ercolani et al. [86]. For single chains and for polymerizing systems, various simulations [70, 71, 87] and analytical studies [88] can be found in the literature. Generally, as the dilution increases, the more the chances to form cyclic structures. This can be explained - when the chains become far apart, chain ends explores the volume around chains

which they belong to until they react to form a loop [69]. The size of the cycles depends on the flexibility and the concentration and cyclization always compete with chain growth and theoretically, the 100% conversion should give cycles.

The main consequence of cyclization is seen in the chain length distribution. Here the classical equations becomes no longer valid and the competition between cyclization and chain growth varies with concentration. In this scenario, the modified conversion (p') for the chain growth can be written as

$$p' = 1 - \frac{1-p}{1-w_c} \tag{2.31}$$

where, w_c is the total weight fraction of the cycles. The ratio of cyclization to linear polymerization can be expressed as [89]

$$\frac{\text{cyclization}}{\text{linear polymerization}} = \frac{k_c \cdot C_t}{k_p \cdot C_t^2} = \frac{k_c}{k_p \cdot c_t} \tag{2.32}$$

where k_c is the rate constant for cyclization. Here k_p does not change under the equal reactivity assumptions, but k_c decreases with increasing chain length.

2.3 Combined isotropic and directional interactions

Conceptual modeling of globular proteins using patchy particles was introduced by Sear [90]. He used hard sphere systems with repulsive cores and a fixed number of patches so that the pair potential becomes the sum of the repulsive part and the attractive patchy part. Addition of a weak isotropic attraction with the patchy system results in more resemblance to actual protein systems [91, 56] and polymerization reactions. See figure 2.10 for representative potential energy curves of a patchy square well system. Here, the isotropic attraction makes appear the liquid-liquid coexistence curve for the two patch case and helps form bundles of chains. These two interactions could be independently varied to observe the various parts of the complex phase diagram, where different crystalline phases are observed. A Kern-Frenkel type system was shown to have a crossover from the isotropic fluid to patchy fluid as the patchy potential increases under single bond per patch conditions [92]. For this model, the expression for B_{att} could be written as [92]

$$\begin{aligned}
B_{att} = 4 \cdot [(1+\varepsilon_0)^3 - 1] \cdot \bigg[&\chi^2 \cdot \left(\exp\left(-\frac{u_0}{k_B \cdot T} - \frac{u_1}{k_B \cdot T} \right) - 1 \right) \\
&+ (1-\chi^2) \cdot \left(\exp\left(-\frac{u_0}{k_B \cdot T} \right) - 1 \right) \\
&- \left((1+\varepsilon_0)^3 - (1+\varepsilon_1)^3 \right) \cdot \left(\exp\left(-\frac{u_0}{k_B \cdot T} \right) - 1 \right) \bigg]
\end{aligned} \tag{2.33}$$

where, ε_1 is the relative well width and u_1 is the well depth in the patchy region when no isotropic interaction is present. This expression accounts for all the possible

configuration of the particles. Note that the potential in the patchy region is the sum of isotropic and anisotropic contributions. When the behavior changes to more patchy, the general assumptions for phase separation becomes no longer valid and the critical parameters becomes a function of the number of patches, their coverage and potential [65, 92] and hence no law of corresponding states has been found for these kinds of systems.
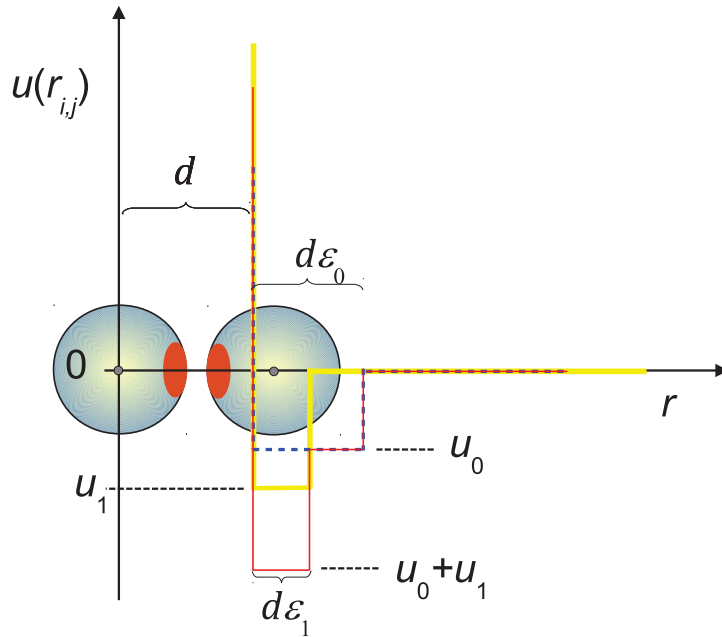
Figure 2.10: Potential of a square well Kern-Frenkel pair. The dashed blue curve represents the isotropic interaction with a relative well width ε_0. The yellow curve represents the patchy interaction with a relative well width ε_1. The thin red curve is the sum of both interactions.

For the irreversible aggregation through patches, no explicit studies have been found in the literature. Here, the effect of isotropic interaction could be interpreted as the influence of solvent quality on irreversible step growth polymerization. In this thesis, we will focus on the aggregation of a square well two patch system with a secondary isotropic interaction with both interactions having the same interaction range.

Model and simulation details

Computer simulations are used as alternative methods to solve problems, where analytical approach becomes difficult. At present, computer simulations have become a well established tool, which brings together the study of microscopic and macroscopic systems. This quick growth and interest in numerical simulations are because of its ability to study complex systems and better insight to the details, otherwise difficult by analytical or experimental methods. Various computational simulation methods exist, each with its own advantages and drawbacks. In this section, we will talk about major approaches used to study cluster aggregation and discuss in detail our method. More general details about different simulation methods could be found in books like [93, 94, 95, 96].

Cluster aggregation could be studied in two ways, depending on the nature of interaction in the system. When the interaction range is short, we can have well defined transient clusters made up of strongly interacting particles. For long range interactions, the presence of numerous possible interactions make it difficult to define a cluster and it becomes easier to study the concentration fluctuations of particles (also called particle point of view). Both of these approaches are equivalent and it is the observer, who decides whether to call two strongly interacting particles performing correlated motion as a single transient cluster. In the cluster point of view, particles move together as a transient cluster. In the particle point of view, they move individually, but in a highly correlated manner. Theoretical studies mainly use the particle point of view. Statistical mechanics is one of such methods, which gives good results and predicts the relation with thermodynamic quantities. Even though these studies give the properties of a system at a given state, we do not get any information on the path or trajectory followed to reach there. At this point, simulation studies can provide better insight.

Molecular Dynamics (MD) is one of the techniques using the particle concept, which solves equations of motion to get the trajectory. MD assumes the system to be ergodic i.e. time average is equal to ensemble average. The time scale in MD can be directly compared with experiments. But, the presence of a large number of solvent molecules in the system makes it difficult to reach the equilibrium conditions for strongly interacting systems (phase separating systems).

To mimic the particle's Brownian motion resulting from collision with solvent molecules, a random fluctuating force and a friction term were introduced, leading

to Brownian Dynamics (BD). If hydrodynamic interactions are considered with BD, the method is called Dissipative Particle Dynamics (DPD). BD method is generally used to study systems reaching equilibrium very quickly. The absence of solvent molecules permit simulations to reach longer times. BD is generally used to explain diffusion limited process with negligible inertial effect.

For stronger interactions, the time needed for thermal equilibrium becomes out of the accessible range for MD approaches. In this case, Monte Carlo (MC) simulations can be used. MC methods with Metropolis algorithm could be used to study binary phase transitions. Here a system of configurations are generated with some probability distributions and the parameter of interest is obtained from statistical estimates. Systems are allowed to jump from one state to another with Boltzmann weights. This technique naturally converges towards thermal equilibrium. Since time is calculated in MC steps, we do not obtain the dynamics nor kinetics.

In all these methods discussed above, we notice that they become limited in a way that we only have either the thermodynamic equilibrium state at large times (without obtaining dynamics) or the dynamics for short times. A compromise between these limitations becomes possible by using our home developed simulation method named Brownian Cluster Dynamics.

3.1 Brownian cluster Dynamics

Brownian cluster dynamics (BCD) is a simulation technique, developed in Polymers Colloids and Interfaces laboratoty in the University of Le Mans. BCD is inspired from the work of Meakin [97] and Kolb [98]. It does not try to solve the equations of motion and is entirely based on a probabilistic approach. BCD is based on the transient cluster point of view and could give information on the kinetics and dynamics over a longer time scale. Initially, it was used on lattice [99, 100], but now modified to be used on off-lattice conditions [101, 102, 103]. The off-lattice BCD algorithm uses hard spheres (with diamter d) with an isotropic SW potential around them with a relative well width ε_0. The simulation usually starts with a given configuration of the particles (usually randomly distributed) and allowed to form aggregates. The time scale is defined as the time required for a particle to travel a distance of its own square diameter. The basic algorithm can be written as below

1. Initialize the positions of N_0 particles in a cubic box of edge L.

2. Form random clusters of particles in range using a probability value P_0 and perform required measurements for initial simulation time, $n = 0$. Consider we have N_c clusters formed in this step.

3. Perform small random displacements to the particles/clusters maintaining cluster integrity. Here we have three choices as given by [23]

(a) **BCD1** - Select N_0 times randomly a monomer and move it in a random direction by a distance s_T. s_T should be small enough to recover the Brownian behavior. This gives Rouse clusters, which are flexible.

(b) **BCD2** - Randomly select N_c times a cluster and move the entire cluster in a random direction retaining the bond integrity. The movement is done over a distance of $s_T/\sqrt{R}$, where R is the diameter of the cluster. This gives rigid Zimm clusters.

(c) **BCD3** - This is a combination of BCD1 and BCD2. First, BCD1 is carried out, which moves the center of mass of the cluster. Then BCD2 is carried out in the same direction as for the change of center of mass. This gives flexible Zimm clusters.

Note that in all of these movement steps, if an overlapping configuration occurs after the movement, the motion step is rejected and the last positions are retained.

4. Random cluster construction using a probability β_0 for breaking the existing bonds and α_0 for forming non existing bonds, such that $P_0 = \alpha_0/(\alpha_0 + \beta_0)$

5. Measure the quantities of interest and increment the simulation time by one $(n = n + 1)$

6. Return to step 3

The displacement step in BCD could be closely compared as an off-lattice version of the Bond Fluctuation Model (BFM) [104]. The off-lattice setting helps to effectively model the excluded volume interactions. Using this method, it was possible to obtain similar dynamics as that of the BD and similar predictions of phase diagram and static properties to that of the MC methods [23, 28, 30]. Choosing the values of α_0 and β_0 determines the reversible nature of the bond and it has been successfully able to simulate Diffusion Limited Cluster Aggregation (DLCA) [31]. Using BCD, we get information about the kinetics o aggregation as well as the structure of aggregates. BCD can handle up to 10^6 particles during several hours of physical time for micrometric colloidal particles in water at $20\,°C$. It must be noted that using BCD, we can study out of equilibrium systems. One of the drawbacks is that in BCD, we do not account for the hydrodynamic interactions. More technical details about this method will be provided later, where we will introduce modifications to this method.

3.1.1 Relation with thermodynamics

In the case of reversible bonds, this approach with bond breaking and forming probabilities prevent the direct calculation of the total energy of the system by just finding the distribution of particles. Two spheres in the interaction range can be either linked (with a probability P_0) or not (with probability $1 - P_0$). These two
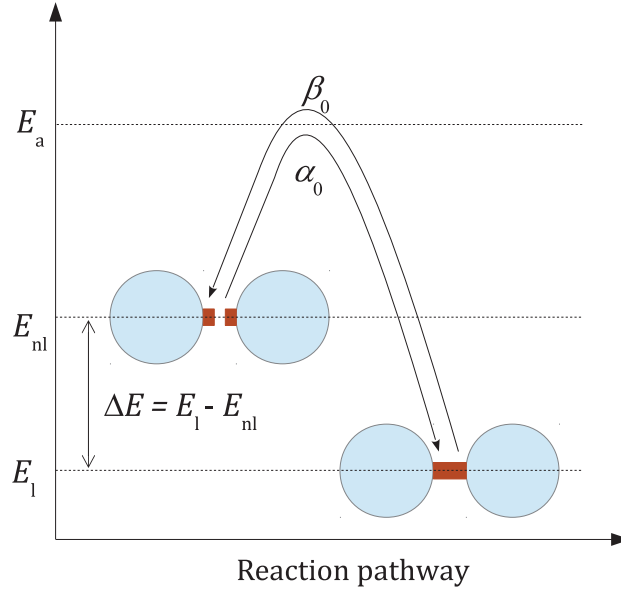
Figure 3.1: The energy profile of the transition between two states.

states can be considered to be of different energy. From this point of view, we can see α_0 and β_0 as the energy barriers to change from one state to another or in other words the activation energy for the bond formation. Consider the reaction of forming a link (see figure 3.1) with E_a being the activation energy for the forward reaction and E_{nl} and E_l being the energy of the non linked and linked state respectively. For the link to be formed, E_a should be overcome, from which we can write

$$\alpha_0 = \exp\left(\frac{-(E_a - E_{nl})}{k_B \cdot T}\right) \tag{3.1}$$

$$\beta_0 = \exp\left(\frac{-(E_a - E_l)}{k_B \cdot T}\right) \tag{3.2}$$

Consider a frozen system where only the bonds fluctuate between the particles in the range. If there are N_{range} contacts, out of which N_l are linked and N_{nl} are non linked, we have at simulation time n

$$N_{range}(n) = N_{nl}(n) + N_l(n) \tag{3.3}$$

When $N_{range} \gg 1$, we can write

$$N_l(n) = \alpha_0 \cdot N_{nl} \cdot (n-1) + (1 - \beta_0) \cdot N_l \cdot (n-1) \tag{3.4}$$

$$N_{nl}(n) = \beta_0 \cdot N_l \cdot (n-1) + (1 - \alpha_0) \cdot N_{nl} \cdot (n-1) \tag{3.5}$$

We call P_0 the probability of having a link between two particles in contact. P_0 is simply given by the ratio N_l/N_{range}. When the system is equilibrated and if α_0 and

β_0 are neither both zero or one ($0 < \alpha_0 + \beta_0 < 2$), we obtain

$$P_0 = \frac{\alpha_0}{\alpha_0 + \beta_0} = \frac{1}{1 + \beta_0/\alpha_0} \tag{3.6}$$

Comparing with equations 3.1 and 3.2, we get

$$P_0 = \frac{1}{1 + \exp\left(\dfrac{\Delta E}{k_{\mathrm{B}} \cdot T}\right)} \tag{3.7}$$

where $\Delta E = E_{\mathrm{l}} - E_{\mathrm{nl}}$.

In the framework of this probabilistic approach, $N_{\mathrm{range}} \cdot u_0$ can be seen as a reduction of the free energy when N_{range} contacts are made. The internal energy term is given by $N_{\mathrm{range}} \cdot P_0 \cdot \Delta E$. Also, we have a set of N_{l} randomly distributed links over the N_{range} contacts, which contributes to an increase in entropy. Using Boltzmann relation for the entropy (S), we have

$$\Delta S = k_{\mathrm{B}} \cdot \ln\left(\frac{N_{\mathrm{range}}!}{N_{\mathrm{l}}! \cdot (N_{\mathrm{range}} - N_{\mathrm{l}})!}\right) \tag{3.8}$$

$$\sim k_{\mathrm{B}} \cdot N_{\mathrm{range}} \cdot \left[P_0 \cdot \ln\left(\frac{1 - P_0}{P_0}\right) - \ln(1 - P_0)\right] \tag{3.9}$$

Using these relations, we have the total free energy as the sum of the enthalpic and entropic contributions, leading to:

$$N_{\mathrm{range}} \cdot u_0 = P_0 \cdot N_{\mathrm{range}} \cdot \Delta E - T \cdot \Delta S \tag{3.10}$$

Substituting for S with 3.9 and using the relation 3.7, we get a simple relation for P_0 in terms of u_0 as

$$\boxed{P_0 = 1 - \exp\left(\frac{u_0}{k_{\mathrm{B}} \cdot T}\right)} \tag{3.11}$$

Thus, by tuning P_0 we get the corresponding u_0.

3.2 The patchy particle model

Our model is inspired from the Kern-Frenkel [9] model, where we use two diametrically opposite square well patches, like in [15]. The base system in our model is a hard sphere with a square-well (SW) potential around it. The diameter of the hard sphere, d, is the unit of length in our system. The isotropic square well potential u_0 is experienced in the relative range ε_0. The patch is characterized by a "spin"/"patch" vector, $\mathbf{v}$ centered inside the sphere. As both patch are in opposite directions, only one patch vector is used. Each patch can be seen as the intersection of a cone with the vertex centered on the sphere center and its axis along the direction of $\mathbf{v}$. The semi-amplitude of the cone, ω measured in radians determines the area covered by the patch. This cone angle can vary as $0 \leq \omega \leq \pi$. In the

patchy region defined by this cone, we impose another square well potential u_1 with a relative well width ε_1. The interaction through the patchy region is possible only when two interacting particles are in the range defined by ε_1 and the line joining the centers of the two spheres passes through the patchy regions of both spheres. Thus the pair potential of two such interacting particles i and j could be written as a sum of the isotropic hard sphere square well potential $u_{\text{isotropic}}$ and another square well potential u_{patchy} with an angular dependence.

$$u_{ij} = u_{\text{isotropic}}(r_{ij}) + u_{\text{patchy}}(r_{ij}, \gamma_i, \gamma_j) \tag{3.12}$$

where r_{ij} is the distance between particles i and j; and γ_i and γ_j are angles defined in figure 3.2. The isotropic square well potential is defined as

$$u_{\text{isotropic}}(r_{ij}) = \begin{cases} \infty & r_{ij} < d \\ u_0 & d \leq r_{ij} \leq d \cdot (1 + \varepsilon_0) \\ 0 & r_{ij} > d \cdot (1 + \varepsilon_0) \end{cases} \tag{3.13}$$

and the orientation dependent patchy interaction can be represented mathematically as

$$u_{\text{patchy}}(r_{ij}, \gamma_i, \gamma_j) = \begin{cases} \infty & r_{ij} < d \\ u_1 & d \leq r_{ij} \leq d \cdot (1 + \varepsilon_1) \text{ and } \begin{cases} \gamma_i < \omega \\ \text{and} \\ \gamma_j < \omega \end{cases} \\ 0 & r_{ij} > d \cdot (1 + \varepsilon_1) \text{ or } \begin{cases} \gamma_i > \omega \\ \text{or} \\ \gamma_j > \omega \end{cases} \end{cases} \tag{3.14}$$

Using this potential, we can separate out and study the radial and orientational parts unambiguously. See Figure 3.2 for a schematic representation of the model and the parameters involved.

In our case the patch is monovalent, meaning that only one patch could be interacting with another patch at a given time. The fraction of the surface area covered by the two patches could be expressed as $\chi = (1 - \cos \omega)$ and the total patchy interaction volume is calculated to be $V_{\text{b}} = \pi/6 \cdot (1 - \cos \omega) \cdot ((1 + \varepsilon_1)^3 - 1) \cdot d^3$ (see appendix A for more details). Also, we mainly use $\varepsilon_0 = \varepsilon_1 = 0.1$.

We have two different potentials in our system and both of them are variable from reversible to irreversible. We have the same relations with thermodynamics, as explained in section 3.1.1 with P_0 and P_1 related to u_0 and u_1. Here, we just need to sum the contribution from patchy and isotropic bonds to calculate the full internal energy.
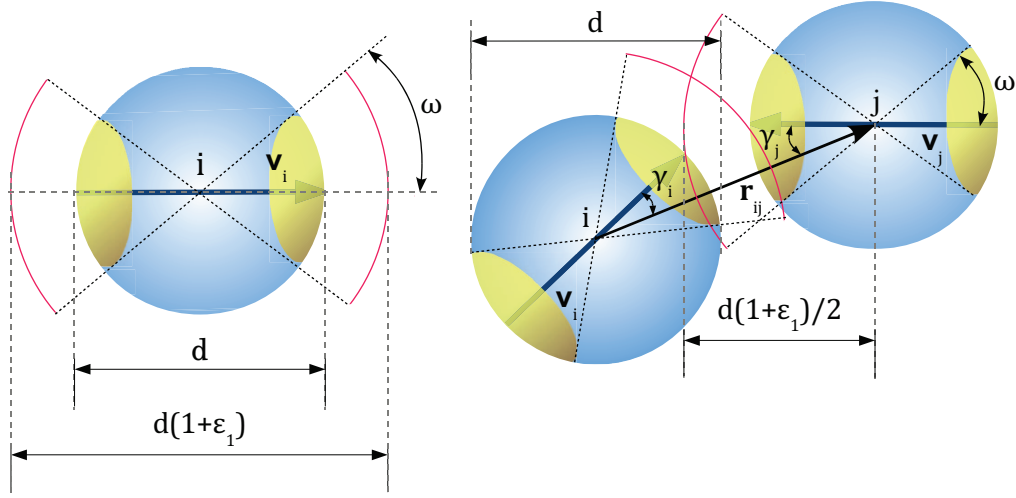
Figure 3.2: Schematic representation of our patchy model and parameters defining the interactions. The isotropic interaction range is not shown for clarity. The yellow colored region represents the patchy region and the red curves and the angle ω define the interaction volume for a patch. The figure on the right shows two spheres linked through patches. The vector connecting the centers of the spheres i and j is represented by $\mathbf{r}_{ij}$. This bond vector passes through the patchy region defined by the positive direction of patch for both spheres. The angles γ_i and γ_j are the smallest angles possible between $\mathbf{r}_{ij}$ and both spin axes.

3.3   BCD improvements : PBCD

We use a modified version of Brownian Cluster Dynamics (BCD) [23]. Our modifications to BCD include fine tuning of the algorithm to suit the patchiness in our model and hence we call it as Patchy BCD referred as PBCD. For the model, we need to express the bonding through patches and since the interaction is anisotropic, we need to introduce rotational motion of particles in our simulations. To account for the patchy bonding, two new bonding probabilities α_1 and β_1 are introduced for bond forming and bond breaking respectively. When bonded through patches, the random translational displacement is allowed only inside the patchy interaction volume and the random rotational motion should also keep the patchy bond integrity.

Rotational motion is modeled as a random walk of the tip of $\mathbf{v}$ on a virtual sphere with a radius v, with elementary step size s_{R}. To reduce the number of calculations, we generate a quasi-regular spherical mesh and save the coordinates of each vertex, which are indexed with their nearest neighbors identified. This spherical grid is obtained from regular icosahedron inscribed in the sphere with radius v. This icosahedron is having 12 vertices, 20 faces and 30 edges with an

edge length a. Using a given q, a non zero positive integer, we construct the grid as follows. We divide each edge by q and transform each triangular face to q^2 new triangular faces, each with an edge length of a/q. The obtained vertices are projected to the surface of the sphere. This gives $q - 1$ new vertices per edge and $(q-1) \cdot (q-2)/2$ vertices per face. Thus the total number of directions or the vertices obtained is given as $N_{\mathrm{dir}} = 10q^2 + 2$. See figure 3.3 for a visualization of a mesh with $q = 4$, giving $N_{\mathrm{dir}} = 162$. For sufficiently large q, the density distribution of the vertices could be taken as isotropic. Each vertex has five (the initial 12 vertices of icosahedron) or six neighboring vertices and knows what are the indices of those vertices and their coordinates. Refer programming details 3.5 for technical details regarding the representation of these vertices. The average distance between two neighboring vertices is called s_{R}, which is our small rotational displacement length on the surface of the virtual sphere. The value of s_{R} should be sufficiently small ($s_{\mathrm{R}} \ll \omega \cdot v$) to recover good statistics of a random walk inside the cone. While the initial generation of the system, spin vectors point to one of these vertices. When a spin of a monomer is entitled to a rotational motion, $\mathbf{v}$ jumps to one of its neighboring site. We call the rotational displacement vector $\mathbf{s}_{\mathrm{R}}$. Also for the translational motion, we choose randomly, one of these directions and do a small translational displacement s_T to the center of of mass of the selected sphere in that direction. The value of s_T should be sufficiently small ($s_{\mathrm{T}} \ll d \cdot \varepsilon_0$). We call this translational displacement vector $\mathbf{s}_{\mathrm{T}}$. The meaning of 'sufficiently small' will be discussed later.
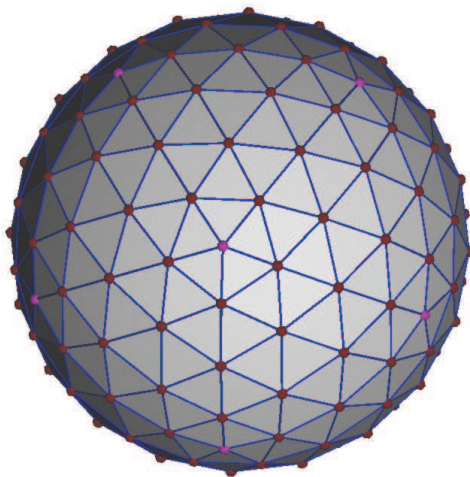

Figure 3.3: Schematic of the mesh with $q = 4$, giving $N_{\mathrm{dir}} = 162$. The pink vertices are the vertices of the inital icosahedron.

The algorithm for the simulation could be explained as follows and the technical details are given in section 3.5

1. Initialization: As in BCD, we start the simulation from a system of N_0 randomly distributed hard spheres with randomly oriented spins in a cubic box of size L_{box}, with periodic boundary conditions. This gives a volume fraction of the occupied space as $\phi = N_0 \cdot \pi/6 \cdot d^3/L_{\text{box}}^3$. The starting time of the simulation is $n = 0$.

2. Cluster construction: At $n = 0$, we scan the entire system and find particles that are in interaction range. We form bonds among these particles with a bonding probability P_0. P_0 is obtained from the bond forming probability α_0 and a breaking probability β_0 such that $P = \alpha_0/(\alpha_0 + \beta_0)$. At the same time, if the patchy bond condition is satisfied, we form bonds with a probability $P_1 = \alpha_1/(\alpha_1 + \beta_1)$. Collection of m such bound particles is termed as a cluster with size m, where an unbound particle is considered as a cluster of size 1. At any time, we consider that N_c such clusters exist.

3. Measurements for initial time: We do measurements such as the number of clusters, the number of particles in the bonding range, the number of particles that are bonded (isotropic bond and patchy bonds) etc. for $n = 0$.

4. Motion procedure: We randomly select $2 \cdot N_0$ times a particle and try to move it either by an elementary translation or rotation with equal probability for each. The motion steps should be sufficiently small such that the motion is Brownian. The motion is accepted only if bonding condition of the particle is retained after the motion is carried out and there is no overlap between particles.

5. Cluster construction: Here we rebuild the clusters. First we scan for the distance between particles and determine particles in the bonding range. If particles in question are already bonded, we break the bond with a probability β_0 and if not, we form bonds using a probability α_0. The same procedure applies to patches, with probabilities α_1 and β_1.

6. Measurements and time increment: We do the measurements such as the number of clusters, the number of particles in the bonding range, particles that are bonded (isotropic bond and patchy bonds) etc. The simulation time is incremented by 1 and the next simulation step is started from step 4.

The outline of this modified algorithm is given in figure 3.4. The technical details of the simulation are given in section 3.5

We have seen while the description of the simulation method that as q becomes larger, the average step size s_{R} should decrease. If we compare $s_{\text{R}}/|\mathbf{v}|$ as a function of q (see figure 3.5), we see that $s_{\text{R}} \propto \frac{1}{q}$.
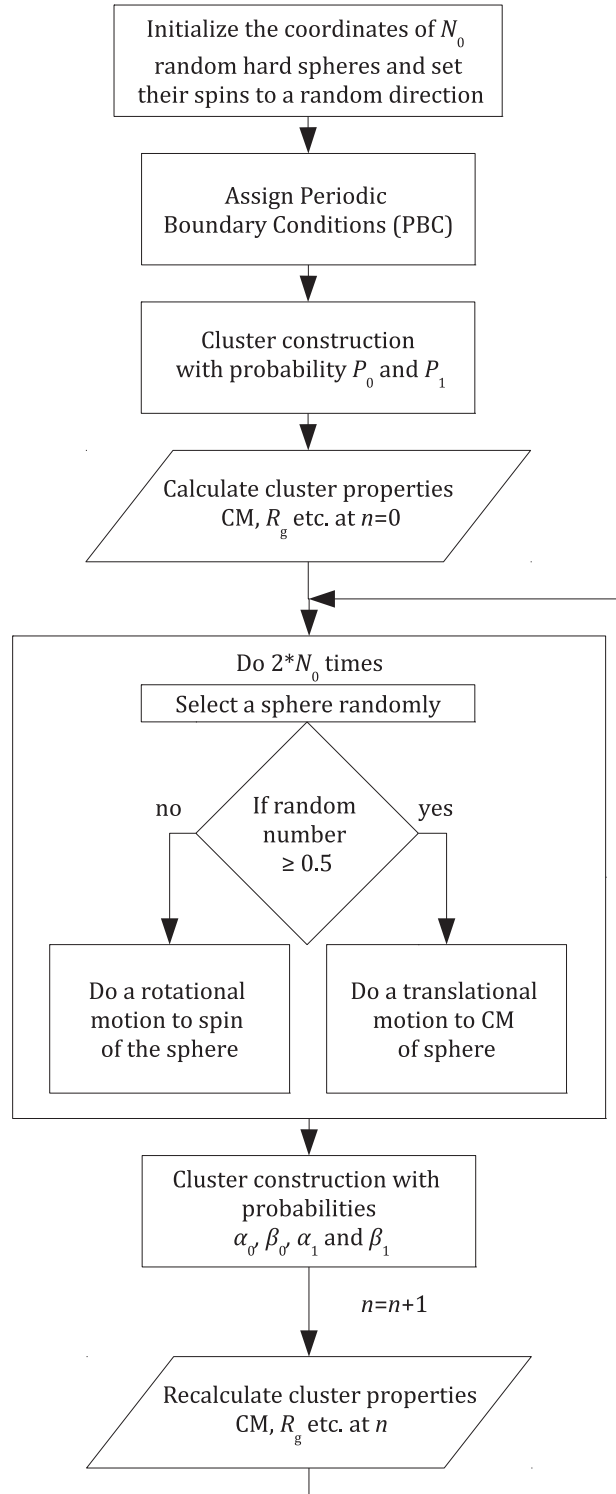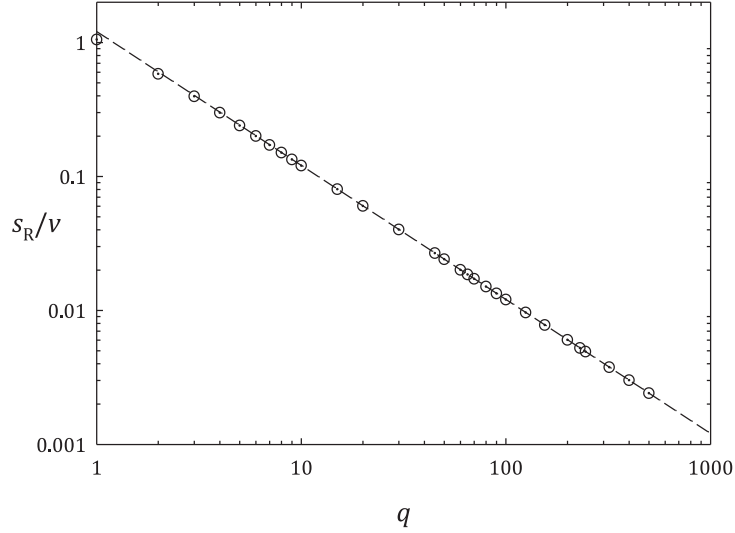
Figure 3.4: The algorithm of the modified BCD

Figure 3.5: Evolution of s_R/v as a function of q. The dashed line has a slope -1.

3.4 Basic units of length and time and their relations

Recalling the units defined so far, d is the diameter of the sphere, which is the unit of length in the system; m the aggregation number; n the number of simulation steps; s_T the small translational displacement vector and s_R the small rotational displacement vector for the tip of the spin on a virtual sphere of radius v. Using t as the physical time, we can deduce the relation between the basic units

From the Einstein's relations, for a freely diffusing particle ($m = 1$), we have the translational (D_1^T) and rotational (D_1^R) diffusion coefficients.

$$D_1^T = \frac{k_B \cdot T}{3 \cdot \pi \cdot \eta \cdot d} \tag{3.15}$$

$$D_1^R = \frac{k_B \cdot T}{\pi \cdot \eta \cdot d^3} \tag{3.16}$$

where η the solvent viscosity.

The average mean square displacement (MSD) of the particle is given by

$$\left\langle \mathbf{R}^2(t) \right\rangle = 6 \cdot D_1^T \cdot t = n \cdot s_T^2 \tag{3.17}$$

The average orientation decorrelation of the spin vector $\mathbf{v}$ is given by

$$\langle \mathbf{v}(t) \cdot \mathbf{v}(0) \rangle = \mathbf{v}^2 \cdot \exp\left(-2 \cdot D_1^R \cdot t\right) \tag{3.18}$$

$1/D_1^R$ can be seen as the relaxation time of the time correlation function of the orientation. Using the concept of the random walk on the surface of the virtual

sphere, the MSD of the tip is given by

$$\left\langle (\mathbf{v}(t) - \mathbf{v}(0))^2 \right\rangle = 2 \cdot \mathbf{v}^2 \cdot \left(1 - \exp\left(-2 \cdot D_1^{\mathrm{R}} \cdot t \right) \right) \tag{3.19}$$

At short times ($D_1^{\mathrm{R}} \cdot t \ll 1$ and for $s_{\mathrm{R}} \ll v$), we consider the tip of $\mathbf{v}$ to be doing a two dimensional random walk without feeling the curvature of the spherical surface, leading to

$$\left\langle (\mathbf{v}(t) - \mathbf{v}(0))^2 \right\rangle = 4 \cdot \mathbf{v}^2 \cdot D_1^{\mathrm{R}} \cdot t = n \cdot s_{\mathrm{R}}^2 \tag{3.20}$$

Now, introducing t_0, the time needed for a free sphere to diffuse a distance d^2, equation 3.17 gives the relation between the physical time t and the simulation time n.

$$\frac{\langle \mathbf{R}^2(t) \rangle}{d^2} = \frac{t}{t_0} = n \cdot \left(\frac{s_{\mathrm{T}}}{d} \right)^2 \tag{3.21}$$

Also, the definition of the time scale gives the relation

$$D_1^{\mathrm{T}} = \frac{d^2}{6 \cdot t_0} \tag{3.22}$$

and comparing equations 3.15 and 3.16 gives

$$D_1^{\mathrm{R}} = \frac{1}{2 \cdot t_0} \tag{3.23}$$

Substituting this value in relation 3.19 we get

$$\left\langle (\mathbf{v}(t) - \mathbf{v}(0))^2 \right\rangle = 2 \cdot \mathbf{v}^2 \cdot \left(1 - \exp\left(-\frac{t}{t_0} \right) \right) \tag{3.24}$$

Taking $v = d$ and combining equations 3.15, 3.16, 3.17 and 3.20 we get the relationship between the small Brownian step sizes as

$$2 \cdot \left(\frac{s_{\mathrm{T}}}{d} \right)^2 = \left(\frac{s_{\mathrm{R}}}{d} \right)^2 \tag{3.25}$$

From equation 3.21, we see that the simulation time needed to reach a given physical time is inversely proportional to the square of the Brownian step size. This again puts forward the question for the choice of the step length. Since we have added constraints of angles in this model, a bigger step size may not be a good choice because it may lead to a lot of rejection of motion to spheres linked through patches and will be discussed later in chapter 4.

3.5 Technical details of simulation

In this section, we will explain the technical details of the PBCD program. All the programs in this work were written in C language and compiled using the GNU compiler on a 64 bit Linux operating system. In our programs, we extensively use C structures and pointers. We use different C structures to store information

regarding clusters and monomers in the system. We also represent the space using another C structure. The construction of these structures will be roughly described in the following. More details could be had from [102] and [103]. All these structures are interlinked using pointers in such a way that if we choose a random monomer, we know its position in the space and also have its surrounding. In the same way, if we select a point in space, we know what is in its neighborhood. This means, we have a double representation of our system. Since memory is not a limiting factor nowadays, this method allows us to save some precious computational time.

3.5.1   Representation of space

For the simulation, we initialize a cubic box of size *Lbox* (with a given $L_{box} = Lbox/d$ an integer), which is divided in to $(L_{box})^3$ small cells. We construct an indexed array of these cells, where each cell can contain a maximum of 8 pointers, which point to monomers if their center of mass is present in the cell or else to a null pointer. We use 8 pointers because a unit cell may contain a maximum of 8 monomer centers if they are ordered in a face centered cubic manner, the maximum packing condition for hard spheres. In the program, it looks like:

```
1  struct cell
2  {
3      struct mono *ptm[8];
4  };
```

By identifying monomers to be belonging to the cell array makes it easier to find its neighbors, especially for short range interactions. Here, in order to find the neighbors we just need to scan the adjacent cells about the one where a monomer belongs instead of scanning for all the monomers in the system. For step sizes and interaction ranges smaller than the diameter of the particle, scanning within 2 adjacent cells in all the directions is sufficient. For easier programming of this scanning process, we keep our simulation box in a larger box of size $LL = L_{box} + 2 * GAP$, where GAP is kept 2 as noted above. The bigger box is also divided in to cells as before. This is represented in figure 3.6 for a two dimensional box, where the light blue box is the original box. The cells are not shown for clarity. With this trick, whatever is is the position of the monomer in the small box, its neighborhood is always defined and the same routine can be used whether it is close to an edge/face of the box or not.

When a monomer with coordinates (x0,y0,z0) is present in a cell in the original box, the first empty pointer in the cell is set to point towards the monomer. This is done each time the monomer position is updated. The index of the corresponding cell in the original box, *a*, could easily calculated

```
1  x=(unsigned long int)floor((double) x0);
2  y=(unsigned long int)floor((double) y0);
3  z=(unsigned long int)floor((double) z0);
```
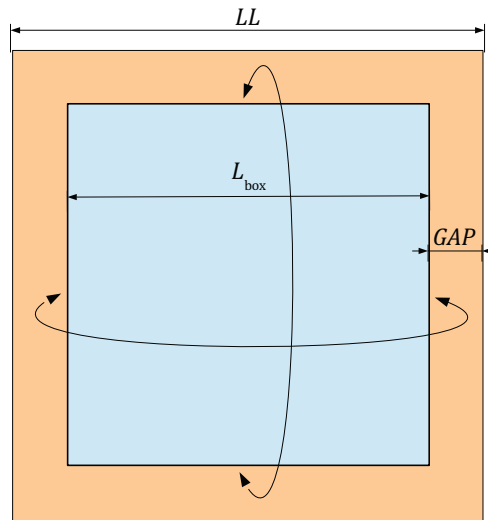
Figure 3.6: Schematic diagram of representation of space and periodic boundary creation using our method.

```
4  a = x + y * Lbox + z * Lbox * Lbox ;
```

This could be easily converted into the index for the bigger box in 3D using a defined calculated function

```
1  #define trans(a) (GAP*((1+LL+LL*LL)+2*(((a)/Lbox)+((a)/(
       Lbox*Lbox))*LL))+(a))
```

Please note that divisions are integer divisions. Once we find the index of the cell in the bigger box, we link both cell indices. We calculate the index of the cells in the original box, which should come in the region of GAP in the case of full periodic boundary conditions. Once we find the corresponding index for that position in the bigger box, we link their indices. This gives a thin slice around the box, which virtually creates periodic boundary condition by linking the corresponding cell indices. If we do the same kind of calculations in 2D, we get the results as in the image 3.6. Here the cells near to the edges of the original box are replicated in the light orange region of the bigger box in such a way that it corresponds periodic boundary condition.

We also initialize the spherical mesh, where the structure of a direction/vertex is

```
1  struct direction
2  {
3      double xd,yd,zd;     //direction
4      char n;          //number of neighbors
5      struct direction *neighbor[6];//pointer to neighbors
6  };
```

Each vertex has an x, y and z component of direction and the number of neighbors around it. It also has a pointer towards the neighboring vertex.

3.5.2 Representation of a cluster

A cluster is represented using a chained list of monomers. The C structure for a cluster is set to be

```
1  struct cluster
2  {
3      double Xmin ,Xmax ,Ymin ,Ymax ,Zmin ,Zmax ,Dl ;
4      unsigned long int mass ;
5      struct mono *pt_first ,*pt_last ;
6  };
```

A cluster knows its extent in all the three directions given as (ΔX=`Xmax-Xmin` etc.), where `Xmax` and `Xmin` represent the biggest and smallest value of the x coordinate in the cluster respectively, etc. and `Dl` gives the maximum value obtained from the three directions. These are calculated after each cluster construction step since the cluster structure is susceptible to change. From the header of the cluster (`pt_first`), the entire cluster could be reconstructed using the pointer `pt_next` in the monomer structure successively till `pt_last` is reached (when `pt_next` becomes NULL). We also keep track of the mass of the cluster or its aggregation number (`mass`).

We define three different cluster lists to differentiate the different kinds of interactions involved. The first kind are "regular clusters" (for which, the cluster integrity has to be kept during the motion procedure). They are made of monomers bound through patches and/or isotropic interaction. "P1 clusters" are made of particles in correct bonding conditions, but not necessarily linked. The third kind "PP cluster" are made of monomers linked only through patches.

3.5.3 Representation of a monomer

The C structure for the monomer contains all the information regarding the position, the spin orientation, the cluster it belongs to, neighbors in interacting range, neighbors to which it is bonded (patchy and isotropic bonds). The structure is given as

```
1  struct mono
2  {
3      double x ,y ,z ,dx ,dy ,dz ,dxP1 ,dyP1 ,dzP1 ,dxPP ,dyPP ,dzPP ;
4      float x0 ,y0 ,z0 ,xreal ,yreal ,zreal ;
5      char cellposition ,Nneighb ,Nconnect ,Npneighb ,Npconnect
            ;
6      struct direction *spin ,*spin0 ;
7      struct mono *pt_next ,*pt_nextP1 ,*pt_nextPP ;
```
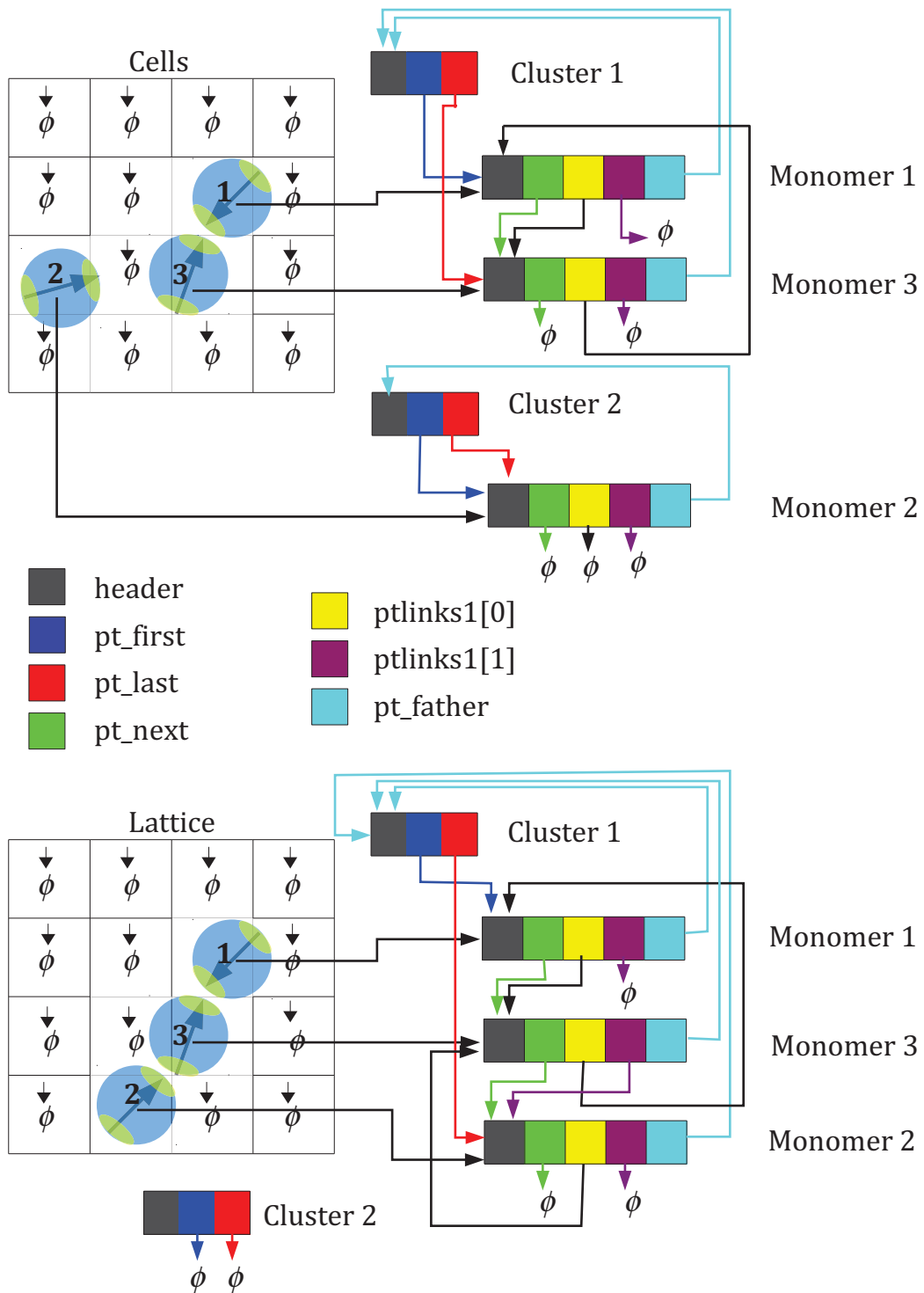
Figure 3.7: Schematic representation of cluster merging.

```
8          struct mono *ptlinks[40];
9          struct mono *ptlinks1[2];
10         struct cluster *pt_father,*pt_fatherP1,*pt_fatherPP;
11    };
```

The monomer knows its initial position (`x0,y0,z0`), the current position in the box (`x,y,z`) and the current position in the space (`xreal,yeral,zreal`) when no PBC is applied. Its squared displacement at a given time can be calculated as $(xreal-x0)^2+(yreal-y0)^2+(zreal-z0)^2$. It also knows the initial and current direction of the spin vector through the pointers (`spin0` and `spin1`). The structure also contains the index of the cell array to which it belongs (`cellposition`) and the number of monomers to which it is connected through isotropic interaction (`Nconnect`) and patchy interaction (`Npconnect`). Similarly, we have the number of non connected neighbors,(`Nneighb`). Each monomer has its own neighbor list pointing to all the connected monomers (`ptlinks[40]`) for isotropic interaction. Similarly we have `ptlinks1[2]` to identify the two patchy links, where `ptlinks1[0]` points to the monomer connected through the positive direction of the patch vector and `ptlinks1[1]` points to the monomer connected through negative direction of the patch. Note that we do not make any difference with any kind of patchy bonding (no selectivity) and this method is just to identify the bound monomers. The structure also has the pointers to the clusters which it belongs to. Each monomer knows the different cluster, which it belongs to (`pt_father, pt_fatherP1,...` for the regular clusters, P1 clusters,... etc.) and the next monomer in the corresponding cluster (`pt_next,...`). Also, the distance to the header monomer in the corresponding cluster is known (`dx,dy,dz,...`).

3.5.4 Cluster construction

For this step, we sweep trough the original box in ascending order of the cell index. For each cell having a monomer and for each monomer in the cell, we scan the neighboring cells (cells within a difference of GAP and by using the index of the bigger box) that are already visited and check for the presence of monomers. Clusters are constructed in a backward manner so that possible bonds are only tested once. If a monomer is found within the interaction range:

1. If it is already linked (isotropically) with the monomer in question, we try to break the link using a probability β_0. This is done by selecting a random number between 0 and 1. If the selected random number is less than β_0, we break the link by setting the corresponding pointers to NULL. The same is done if we choose the patch to be reversible, but with probability β_1.

2. If there is no link between the pair of monomers in question, we select a random number as before. If the random number is less than α_0, we create the link by setting the corresponding pointers in the cluster and monomer structures. Here, we can see a problem regarding the patchy bonds, which

are valency limited. When the patches are large enough that more than one monomer is within the bonding constraints, the first monomer found by the cell sweeping technique will be bound with probability α_1. Since this may cause a bias, we restrict the patch size such that only one particle can link through a patch.

This updating of cluster pointers on merging or on fragmentation is schematically shown in figure 3.7. Since we are merging two clusters, the cluster with the lower aggregation number is always selected to be emptied and appended with the bigger cluster. In the figure, since cluster 1 is bigger, we retain it and set cluster 2 to zero pointer and is thus unused. While merging the pt_next of monomer 3 is pointed to pt_father of the cluster 2 and the whole cluster structure of cluster 2 is updated and the distance to the new header is recalculated. At the same time, the pt_last of the cluster 1 is updated to be monomer 2.

Using this representation technique of interlinked structures and cell sweeping method, we can avoid many unnecessary time consuming calculations.

3.5.5 Input parameters

In this section, we specify the input parameters for our system

1. Initial configuration: For the initial configuration, we use a cubic box of edge L_{box} containing N_0 monomers. The positions of the monomers are randomly distributed and is given in a binary file in a specified format, from which the program can read it, given L_{box} and N_0.

2. After reading the positions, the spin has to be set. So, we provide the coordinates of N_{dir} vertices of the spherical mesh in another binary file in a specified format. This file also contains information about the neighboring vertices and s_{T} and s_{R}, which is set by the number of vertices present in the mesh. The step size is controlled by providing different files with different number of vertices.

3. Interaction parameters ε_0, ε_1, ω, α_0, α_1, β_0 and β_1 are chosen accordingly. We recall that we use $\varepsilon_0 = \varepsilon_1 = 0.1$ and the probability values should be in between or equal to 0 and 1. ω can take values from $0 < \omega \leq \pi$. For the irreverible aggregation through patches, we use $\alpha_1 = 1$ and $\beta_1 = 0$. This allows us to further simplify the cluster construction part because once bound, we no longer need to check neighboring monomers for patchy bonding conditions.

4. Seed for the random number generator.

We have also included a provision to restart a previous run from a given position of time, if provided the simulation time and snapshot of the system at that point (see below for explanation about snapshot).

3.5.6 Output

Consider a simulation starting from zero time. For the first 100 simulation steps, we store the results for each step. After, we start averaging the data over a logarithmic interval and print it in the middle of the interval (in log scale). In the output, we print all the measured parameters as a function of the physical time of the system. The averages of quantities of interest are printed out separately for properly bound clusters (bound through isotropic or anisotropic interactions) and also for unbound clusters, which are under bonding conditions. This gives us the description of all possible clusters within the system. For clusters, measured quantities include the total number of clusters, the average aggregation number (number average, weight average and z average), the average radius of gyration, whether the system has percolated or not and the fraction of monomers included in percolating clusters. For patchy clusters, the fraction of monomers in the loops is also collected. For each cluster type, we save the average distribution of the aggregation number. For each monomer, we collect the squared displacement from its initial position.

We also store snapshots of the system at regular intervals in a binary file. This contains all details of the system such as positions, spin orientation, complete cluster structure etc., such that it could be used as a starting point or to continue the simulation with the same cluster integrity. This is usually helpful in the case of unexpected interruptions of the program execution. This file is also used to visualize the system, where we read the monomer positions and transform them to be used with external visualization tools. Visualization tools used include a home-built program and "POV-Ray".

Modeling single polymer chains

Staudinger's macromolecular hypothesis that polymers are large molecules made up of covalently linked elementary units marks the starting point of the modern polymer science [105]. After him, the works of Flory, de Gennes, Doi, etc. laid the foundation of the basic theories in polymer physics. In this study, polymer is a focus because it is the simplest structure that could be made out from our basic building block with two patches. Also, since polymer science is a well studied area with a vast history of literature in theoretical predictions, simulations and experiments, it becomes a standard model for us to test our approach. All the detailed derivation of equations in this chapter could be found in standard polymer science text books such as [82, 68, 106, 107, 108].

For a polymer chain containing m linked monomers, the mean square end-to-end distance $\langle \mathbf{R}_e^2 \rangle$ scales as

$$\langle \mathbf{R}_e^2 \rangle \propto m^{2\nu} \qquad , m \gg 1 \tag{4.1}$$

where ν is the Flory exponent. Using the concept of fractality, we have $\langle \mathbf{R}_e^2 \rangle \propto m^{2/d_f}$ which in turn gives $\nu = 1/d_f$ showing polymer is a fractal object, where d_f is the fractal dimension. Ideal polymer chain, where there are no excluded volume interactions is simply represented by a *random walk* and is an analytically well studied polymer model. For an ideal chain, the Flory exponent $\nu = 0.5$ ($d_f = 2$). For a real polymer chain, the solvent quality plays a role on the value of ν and there are three different cases: in a theta solvent, attractive and repulsive parts of the monomer-monomer interaction cancels out (second virial coefficient becomes zero, $B_{att} = 4$) leading to ideal behavior with $\nu = 0.5$ ($d_f = 2$). In a bad solvent, when the monomer-monomer interaction is increased, the chain collapses leading to phase separation, giving $\nu = 0.33$ ($d_f = 3$). In athermal solvent or also called as a very good solvent, the interaction between monomers and solvent molecules is high compared to monomer-monomer interaction and pure hard core repulsion determines the configuration of the chain. This could be modeled as a *self avoiding walk* and in this case $\nu = 0.588$ ($d_f = 1.7$). These scalings are valid only when the contour length L is much greater than a characteristic length called persistence length, l_p which depends on the local flexibility of the chain and is the characteristic distance to be traveled along the backbone of a chain so that the bond vectors decorrelate significantly. Also, according to de Gennes [109], the scaling depends on relative length scales. The local flexibility of a polymer is attributed to the molecular structure and the composition of the monomeric units, whereas the

segmental flexibility arises from rotational conformation of bonds in the backbone and its restrictions. A chain is considered as rigid rod like, if $L \ll l_\mathrm{p}$ and flexible if $L \gg l_\mathrm{p}$. Many definitions exist for the persistence length in literature. In the case of ideal chains, these values turn out to be equivalent. But for real chains, some of the proposed quantities are found to diverge with m [110, 111]. In this chapter, we will explore some of the basic relations in polymer physics using our model.

4.1 Simulation details

In this section, we recall some of the relevant variables that were already defined in chapter 3 and give specific details on the polymer system. A polymer chain contains m monomers indexed from $i = 1$ to m irreversibly linked through patches ($\alpha_1 = 1$, $\beta_1 = 0$) or $u_1/(k_\mathrm{B} \cdot T) = -\infty$ and we set $B_{att} = 0$ ($u_0/(k_\mathrm{B} \cdot T) = 0$) such that there is no isotropic interaction within monomers in a chain. The interaction well width of a patch is fixed to be $\varepsilon_1 = 0.1$ and the patch angle ω, which determines the flexibility of the chain is chosen to our needs. The bond vector $\mathbf{r}_i$, ($1 \leq i \leq m - 1$) connects two consecutive monomers i and $i + 1$. The distance between connected monomers can vary freely between d and $d(1 + \varepsilon_1)$. All monomers in the chain, except two at chain ends are having two oppositely located patches. The first and the terminal monomer have only one patch. The chains are generated in space in an unbiased manner by random walk within the bonding parameters (center of mass of connected neighbors within distance d and $d(1 + \varepsilon_1)$ and bond vector passing through at least patch for each connected monomer). Excluded volume effects are taken into account for real chains. The unbiased method results in a huge generation time for real chains. This is due to the large amount of rejections coming from overlapping configurations. More details on the time taken for the generation will be given later.

For generation of a polymer chain, we begin with a monomer placed at origin with a randomly oriented patch vector. In the next step, we select a bond direction that lies inside the patch cone of this first monomer and place the next monomer randomly within the interaction volume and select randomly a spin vector for the second monomer such that the bond vector lies inside the patch. The patch vector $\mathbf{v}_i$ is set to point towards the next connected monomer in the chain. The distance to the center of mass of the next connected monomer is distributed assuming the uniform distribution within the volume of interaction (geometrically, the conic spherical shell) and the spin is distributed such that the tip of the spin vector is uniformly distributed on the surface covered by the patch. See appendix A for the distribution functions and procedure for selecting the position and spin of the connected monomer. This process is continued till the target length is achieved. While the chain is growing, if it is found that the position of a monomer is inaccessible due to excluded volume effects (for real chains), the chain is abandoned and the process started again from the beginning.

We use two different methods for assigning the spin vector. For the dynamic

property measurements, chains are generated using the coordinate mesh and spin vectors can only possess one of the predefined directions. For the static property measurements we avoid the coordinate mesh and the spin vector is allowed to occupy any coordinate within the cone. The mesh method becomes prone to finite size effects for very small values of ω and we become limited by the number of coordinate sets that lie inside the patch. This makes preferential selection of orientation of the spin vector and influences the static properties. See appendix A for a description of the method of selecting the position of the next connected monomer and the spin direction without the grid. Due to these reasons, the study of dynamics was limited to $\omega \geq 0.2$ rad. A large number of chains (10^5 for static property studies and 10^4 for dynamics studies) were taken into account to get better statistical averages for the measurements. All calculations were done on a single CPU for static property measurements and it should be noted that different programs has been used for the polymer property studies. Since all chains are transparent to each other (since we study individual chains) and we use good solvent conditions ($B_{att} = 0$), the cluster construction step is no longer needed and we also avoid the use of periodic boundary conditions to save calculation time. As an example, for the most stiff and longest ideal chain we have generated: $m = 30000$, $\omega = 0.1$ with 10^5 chains, it took around 15 days in a 3.4GHz processor. By setting the chains to be transparent to each other (single chain model), we can simulate a given system many times with different starting configurations and average the output for better results. This lead us to use parallel processing to obtain faster results for the dynamics, by simultaneously running different number of chains on different number of processors and averaging them. For example, in the case of $m = 10$, $\omega = 0.2$ we used around 8300 chains in total for the study. Using a $s_T/d = 0.0035$, we were able to reach $t/t_0 = 2000$ by distributing the simulation in to 64 cores of a parallel computing system equipped with 1.5GHz processors within 50 hours.

In this system of polymer chains, the bond length can fluctuate from d to $d(1 + \varepsilon_1)$ and the average bond length is defined as $\langle l_b \rangle = \sqrt{\langle \mathbf{r}_i^2 \rangle}$. The average contour length L is then $L = (m - 1) \cdot \langle l_b \rangle$. The angle between a patch and a bond (γ) can fluctuate within the range 0 to ω and its average cosine is $\langle \cos \gamma \rangle$. The bond angle δ fluctuates from 0 to 2ω and its average cosine is $\langle \cos \delta \rangle$. See figure 4.1 for a graphical representation of the parameters. G is the center of mass of the chain. $\mathbf{R}_e$ is the end to end vector and R_g^2 is the squared radius of gyration defined as the average squared distance of a monomer to G. $\langle \mathbf{R}^2(t) \rangle$ is the mean square displacement (MSD) of G. The relaxation of chain orientation is followed by monitoring the evolution of end to end vector decorrelation:

$$C(t) = \langle \mathbf{R}_e(t) \cdot \mathbf{R}_e(0) \rangle / \langle \mathbf{R}_e^2 \rangle \tag{4.2}$$

The angular brackets denote thermodynamic averages over all configurations and evolutions of the chain.

From simulation results, the average bond length $\langle l_b \rangle$ is found to be independent of m, ω and excluded volume effects, down to the third digit. In any case, the
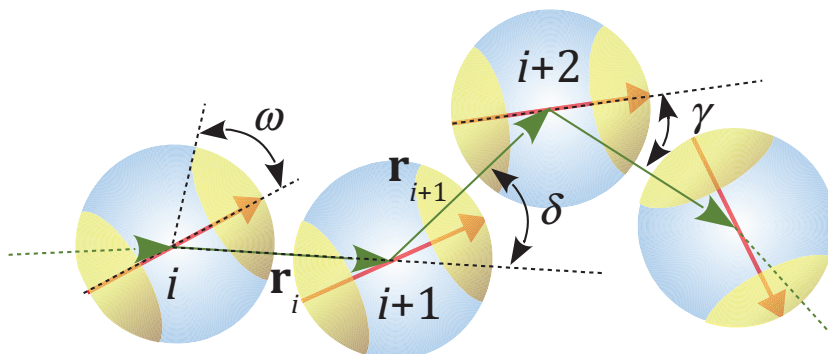
Figure 4.1: Schematic representation of a part of a polymer chain using the patchy square well spheres model to identify chain parameters. δ is the angle between two consecutive bonds $\mathbf{r}_i$ and $\mathbf{r}_{i+1}$ and γ is the angle between a bond vector and a spin vector.
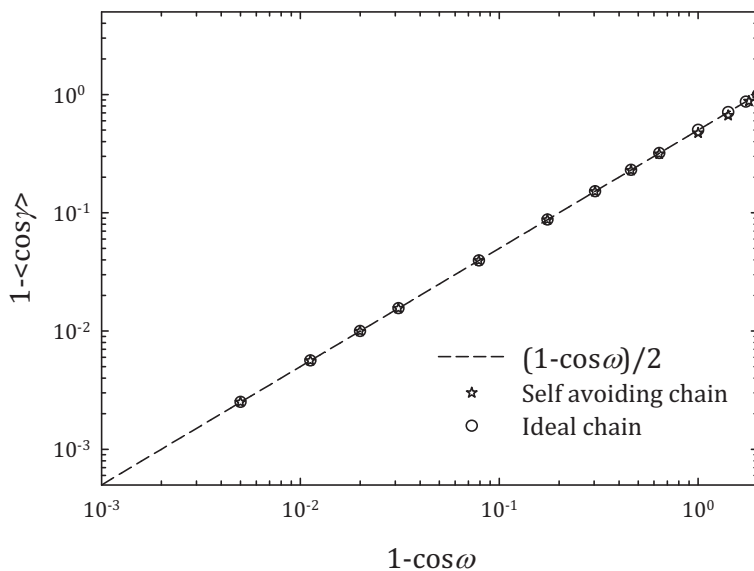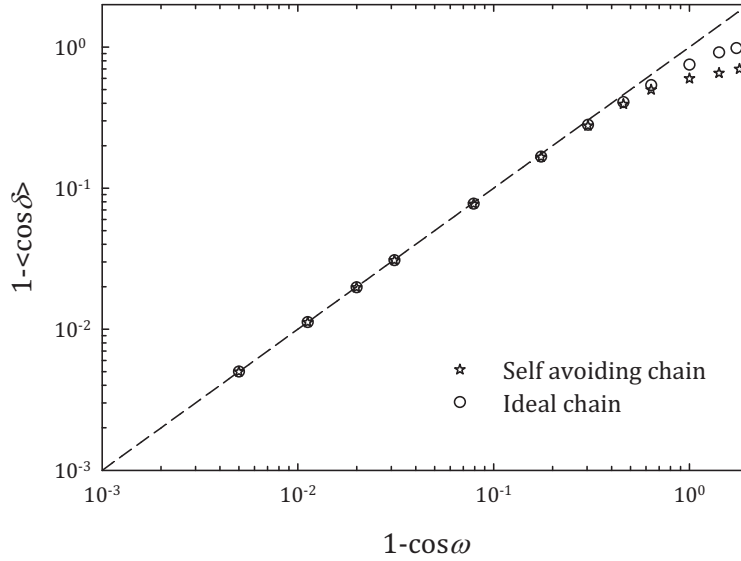

Figure 4.2: Variation of $(1 - \langle \cos \gamma \rangle)$ as a function of $(1 - \cos \omega)$. Circles indicate ideal chains and stars indicate self avoiding chains. Dashed line is the theoretical expression $\frac{1}{2}(1 - \cos \omega)$ (see appendix A).

Figure 4.3: Variation of $(1 - \langle\cos\delta\rangle)$ as a function of $(1 - \cos\omega)$. Circles indicate random chains and stars indicate self avoiding chains. Dashed line is the function $y = x$.

average value $\langle l_\mathrm{b}\rangle/d = 1.052$ is obtained. This value is expected, since we uniformly distribute the position of connected monomers within the interaction volume. From the calculations in appendix A, we have $l_\mathrm{b}/d = \sqrt{\frac{(1+\varepsilon_1)^3+1}{2}}$ which is independent of the patch size. Also from appendix A we have the relation between ω and γ as $(1 - \langle\cos\gamma\rangle) = \frac{1}{2}\cdot(1 - \cos\omega)$. Figure 4.2 shows that this relation is independent of the nature of the chain - whether it is ideal chain or self avoiding chain and is valid for all values of m and ω. The data from self avoiding chain show that averages are not significantly modified by excluded volume interactions and that distribution of the position of connected neighbor is still uniform in the interaction volume. In all figures, error bars are omitted if they are smaller than the size of the symbol.

The average bond angle δ depends on the value of ω, which determines the patch cone and hence the local flexibility of the polymer chain. Figure 4.3 shows the variation of $(1 - \langle\cos\delta\rangle)$ as a function of $(1 - \cos\omega)$. We see that

$$\boxed{\langle\cos\delta\rangle \approx \cos\omega \quad \text{as } \omega \to 0}$$

which is independent of excluded volume effects. The behavior starts to deviate for bigger ω and the extent of deviation depends on excluded volume effects. Also, no effect of m was seen in the case of δ. Thus we have an average bond length $\langle l_\mathrm{b}\rangle$ which is independent of m and ω, and an average bond angle δ which is independent of m and could be easily tuned by varying ω. Considering these average values, we see that the freely rotating chain model [68] may be a good candidate for a close comparison.

4.2 Static properties of single ideal chains

There are many theoretical polymer models in the literature. Freely jointed chain (FJC), freely rotating chain (FRC), Worm Like Chain (WLC) etc. are some of the well studied theoretical polymer models. In this section, we study the existing models in literature and try to compare our results in order to find the equivalent model.

The end to end distance ($|\mathbf{R}_\mathrm{e}|$) is a characteristic length of a polymer chain. It could be obtained by summing all bond vectors. For an ideal chain, the average end to end distance turns out to be zero and hence the mean square end to end distance is considered, which is given as

$$
\begin{aligned}
\langle \mathbf{R}_\mathrm{e}^2 \rangle &= \sum_{i}^{m-1}\sum_{j}^{m-1} \langle \mathbf{r}_i \cdot \mathbf{r}_j \rangle \\
&= (m-1) \cdot l_\mathrm{b}^2 + 2 \cdot \sum_{i<j} \langle \mathbf{r}_i \cdot \mathbf{r}_j \rangle \\
&= (m-1) \cdot l_\mathrm{b}^2 + 2 \cdot l_\mathrm{b}^2 \cdot \sum_{j=2}^{m-1}\sum_{i=1}^{j-1} \langle \cos\theta(s) \rangle
\end{aligned}
\tag{4.3}
$$

where $\theta(s)$ is the angle between segments i and j and $s = j - i$ where s can vary between $0 \leq s \leq m - 2$. Similarly, the mean squared radius of gyration or the average squared distance from a monomer to the center of mass of the chain could be calculated using Lagranges theorem [68], which gives

$$
\langle R_\mathrm{g}^2 \rangle = \frac{1}{m^2} \cdot \sum_{j=2}^{m}\sum_{i=1}^{j-1} \langle \mathbf{r}_{ij}^2 \rangle
\tag{4.4}
$$

where $\mathbf{r}_{ij}$ is the vector connecting monomer i to j and angular brackets denote the average over a large number of chains.

Freely Jointed Chain

For an ideal FJC, the bond length is fixed and no angle restrictions are made on the positioning of the connected monomers. This implies that the correlation between different bond vectors turns out to be zero in average. Hence we have $\langle \cos\theta(s) \rangle = 0$ for all $i \neq j$ and this leads to vanishing of the second term in equation 4.3 and hence

$$
\langle \mathbf{R}_\mathrm{e}^2 \rangle = (m-1) \cdot l_\mathrm{b}^2 = L \cdot l_\mathrm{b}
\tag{4.5}
$$

Calculating the radius of gyration using equation 4.4 and using same kind of relation above to calculate the distance between any monomer i and j in the chain $\langle \mathbf{r}_{ij}^2 \rangle = (j-i) \cdot l_\mathrm{b}^2$, we have

$$
\langle R_\mathrm{g}^2 \rangle = \frac{1}{m^2} \cdot \sum_{1 \leq i < j \leq m} (j-i) \cdot l_\mathrm{b}^2
\tag{4.6}
$$

on simplification, we get

$$\langle R_g^2 \rangle = \frac{1}{6} \cdot (m-1) \cdot l_b^2 \quad , m \gg 1 \tag{4.7}$$

Comparing above set of equations, we can show that $\langle \mathbf{R}_e^2 \rangle = 6\langle R_g^2 \rangle$ in the limit of $m \gg 1$ indicating that $\langle \mathbf{R}_e^2 \rangle$ and $\langle R_g^2 \rangle$ are proportional.

Freely Rotating Chain

FRC is a well studied ideal chain model, where each bond makes a fixed angle δ to its neighboring connected segments and has a constant bond length. These segments are entitled to free rotation and can occupy all torsion angles. Depending on the value of δ, the extent of spatial coverage by a chain can be modified. All calculations on this model are made such that $0 < \delta < \pi/2$. For the FRC case, the memory effect coming from the restriction to place the next connected monomer induces a correlation between the orientation of bond vectors. This results in a non zero value for the second term in the equation 4.3. The fixed bond angle δ causes a part of the orientation of bond vector to be propagated along the chain backbone. By taking successive projections of one bond on to another one, we can show that

$$\langle \cos \theta(s) \rangle = (\cos \delta)^s \tag{4.8}$$

Using this relation, we have

$$\langle \mathbf{R}_e^2 \rangle = l_b^2 \cdot \sum_i^{m-1} \sum_j^{m-1} (\cos \delta)^{|j-i|} \tag{4.9}$$

Further expansion followed by simplification gives

$$\frac{\langle \mathbf{R}_e^2 \rangle}{(m-1) \cdot l_b^2} = \frac{1 + \cos \delta}{1 - \cos \delta} - \frac{2 \cdot \cos \delta}{m - 1} \cdot \frac{1 - (\cos \delta)^{m-1}}{(1 - \cos \delta)^2} \tag{4.10}$$

Here we can have two asymptotic behaviors: when $m \gg 1$ keeping δ constant, the above equation reduces to

$$\frac{\langle \mathbf{R}_e^2 \rangle}{(m-1) \cdot l_b^2} = \frac{1 + \cos \delta}{1 - \cos \delta} \tag{4.11}$$

and when $\delta \to 0$ keeping m constant, the relation becomes

$$\frac{\langle \mathbf{R}_e^2 \rangle}{(m-1) \cdot l_b^2} = m - 1 \tag{4.12}$$

Using the same method as in FJC, from Flory [106], we have the average square radius of gyration as

$$\frac{6 \cdot \langle R_g^2 \rangle}{(m-1) \cdot l_b^2} = \frac{(m+1) \cdot (1 + \cos \delta)}{m \cdot (1 - \cos \delta)} - \frac{6 \cdot \cos \delta}{m \cdot (1 - \cos \delta)^2} \\ + \frac{12 \cdot (\cos \delta)^2}{m^2 \cdot (1 - \cos \delta)^3} - \frac{12 \cdot (\cos \delta)^3 \cdot (1 - (\cos \delta)^{m-1})}{(m-1) \cdot m^2 \cdot (1 - \cos \delta)^4} \tag{4.13}$$

For the $m \gg 1$ condition at constant δ, this simplifies to

$$\frac{6 \cdot \langle R_g^2 \rangle}{(m-1) \cdot l_b^2} = \frac{1 + \cos \delta}{1 - \cos \delta} \tag{4.14}$$

and for $\delta \to 0$ at constant m, we recover the radius of gyration of a thin beaded rod

$$\frac{6 \cdot \langle R_g^2 \rangle}{(m-1) \cdot l_b^2} = \frac{m+1}{2} \tag{4.15}$$

From the above set of equations, we have again $\langle \mathbf{R}_e^2 \rangle = 6 \cdot \langle R_g^2 \rangle$ for very long chains when $\pi/2 > \delta > 0$.

Persistence length

For the ideal semi flexible FRC model, a characteristic length termed as Kuhn length could be defined on comparison with FJC model. Kuhn length (l_K) is defined as the segment length of an equivalent FJC with the same $\langle \mathbf{R}_e^2 \rangle$ and L. For a very long chain, we have

$$\boxed{l_K = \frac{\langle \mathbf{R}_e^2 \rangle}{L}} \tag{4.16}$$

The complete expression for an ideal FRC could be obtained by multiplying the RHS of equation 4.10 by l_b. For very long chains, this expression reduces to

$$l_K \approx l_b \cdot \frac{1 + \cos \delta}{1 - \cos \delta} \quad , m >> 1 \tag{4.17}$$

This concept gives $l_K = l_b$ for a FJC.

For a freely rotating chain, another approach could be used to define the persistence length. We have seen that there is a correlation between bond segments present along the backbone of the chain. From equation 4.8, we see that the correlation decreases rapidly with the segment index, which is approximated to be an exponential decay. From the decorrelation behavior of the bond vector orientation along the chain, we can define a characteristic relaxation length at which the correlation decays. This gives from 4.8

$$\langle \cos \theta(s) \rangle = (\cos \delta)^s = \exp \left(-s \cdot \frac{l_b}{l_1} \right) \tag{4.18}$$

where, l_1 is the persistence length. This equation can be rearranged to obtain

$$l_1 = \frac{-l_b}{\ln(\cos \delta)} \tag{4.19}$$

Using relations $\cos \delta \cong 1 - \delta^2/2$ and $\ln(1-x) \cong -x$ for small δ and x, we make the approximation $\ln(\cos \delta) \cong -\frac{\delta^2}{2}$, which gives

$$\frac{l_1}{l_b} \approx \frac{2}{\delta^2} \quad , \delta \to 0 \tag{4.20}$$

Similarly, using the same relations in equation 4.16, and comparing with the equation above, we have

$$l_1 \approx \frac{l_\mathrm{K}}{2} \quad , m \gg 1 \text{ and } \delta \to 0 \tag{4.21}$$

Worm Like Chain

There exists a special case of freely jointed chain, called the Worm Like Chain (WLC) or the Kratky-Porod model, under the condition $l_1/l_\mathrm{b} \gg 1$. This means that discrete details of the chain become invisible and it appears to be made of a single continuous curve. In the WLC limit, basic relations we have seen so far could be rewritten using the relative size of the chain $X = L/l_1$:

$$\frac{\langle \mathbf{R}_\mathrm{e}^2 \rangle}{2 \cdot l_1^2} = X - 1 + \exp(-X) \tag{4.22}$$

which gives

$$\langle \mathbf{R}_\mathrm{e}^2 \rangle = L^2 \qquad\qquad\qquad , X \ll 1 \tag{4.23}$$
$$\langle \mathbf{R}_\mathrm{e}^2 \rangle = 2 \cdot L \cdot l_1 \qquad\qquad , X \gg 1 \tag{4.24}$$

Similarly,

$$\frac{\langle R_\mathrm{g}^2 \rangle}{2 \cdot l_1^2} = \frac{X}{6} - \frac{1}{2} + \frac{1}{X} - \frac{1}{X^2} \cdot (1 - \exp(-X)) \tag{4.25}$$

which gives

$$\langle R_\mathrm{g}^2 \rangle = \frac{L^2}{12} \qquad\qquad\qquad , X \ll 1 \tag{4.26}$$

$$\langle R_\mathrm{g}^2 \rangle = \frac{L \cdot l_1}{3} \qquad\qquad\qquad , X \gg 1 \tag{4.27}$$

We see that $\langle \mathbf{R}_\mathrm{e}^2 \rangle$ and $\langle R_\mathrm{g}^2 \rangle$ depend only on the relative quantity X. When $X \ll 1$, the chain behaves as rod-like, when $X \gg 1$ the chain is considered as a flexible chain and in between the chain is considered to be in the semiflexible regime. Similarly, the ratio $\langle \mathbf{R}_\mathrm{e}^2 \rangle/(6 \cdot \langle R_\mathrm{g}^2 \rangle)$, could be also expressed in terms of the relative chain length X. Comparing above set of equations we see that $\langle \mathbf{R}_\mathrm{e}^2 \rangle/(6 \cdot \langle R_\mathrm{g}^2 \rangle)$ varies from, 2 for $X \ll 1$ to 1 for $X \gg 1$.

The definition of l_1 gives $X = -(m-1) \cdot \ln(\cos \delta)$. This means that $\cos \delta$ determines the lowest accessible value of X, since $m = 3$ is the shortest chain possible to have a bond angle δ.

What is the patchy model equivalent to?

Figure 4.4 shows $\langle \mathbf{R}_\mathrm{e}^2 \rangle/(6 \cdot \langle R_\mathrm{g}^2 \rangle)$ obtained for ideal chains from our simulations for various m and ω, along with theoretical predictions from FRC model (equations 4.10 and 4.13). This plot was made using $\langle \cos \delta \rangle$ obtained from the simulation
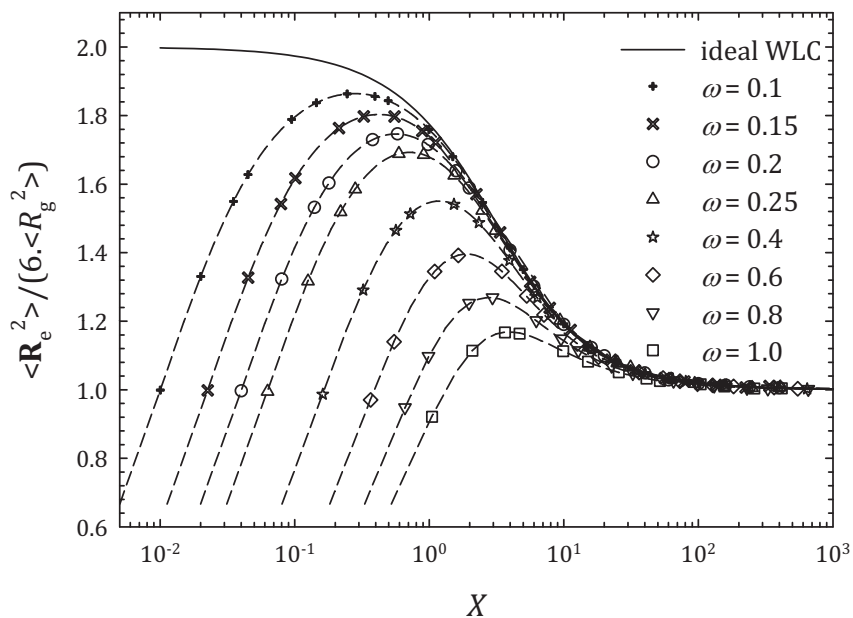
Figure 4.4: Evolution of $\langle \mathbf{R}_{\mathrm{e}}^2 \rangle / (6 \cdot \langle R_{\mathrm{g}}^2 \rangle)$ as a function of X for various ω in the case of ideal chains. The solid line is the theoretical WLC condition when $\omega \to 0$. The dashed lines are theoretical predictions for individual ω derived from equations 4.10 and 4.13.
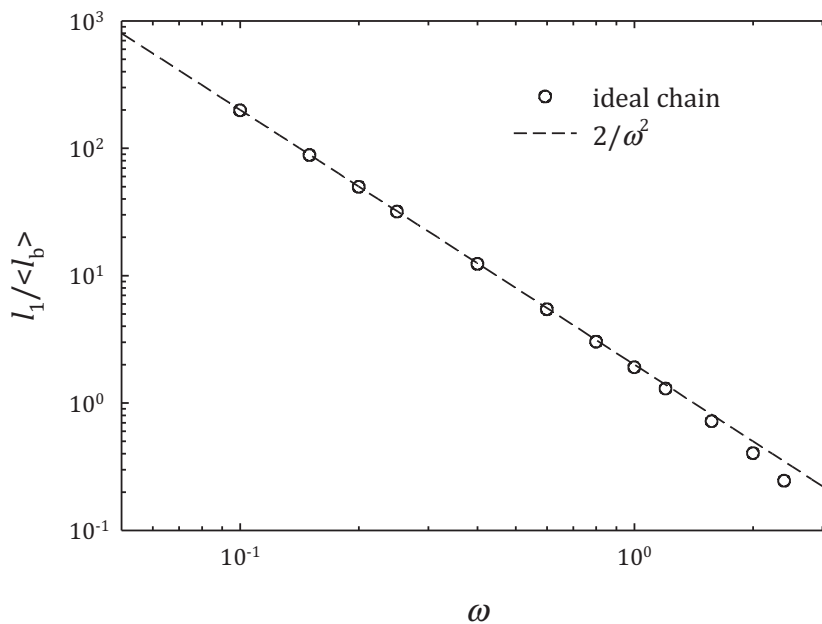

Figure 4.5: Variation of $l_1 / \langle l_{\mathrm{b}} \rangle$ as a function of ω. The dashed line is the function $2/\omega^2$.

instead of $\cos\delta$ of FRC. We see that theoretical curves superimpose perfectly with our results for all ω and m under the FRC framework, indicating that our model is equivalent to the FRC model.

In figure 4.5 we plot the variation of l_1/l_b obtained for ideal chains as a function of ω. In the same plot, we see that for small ω, the function $2/\omega^2$ gives a very good rapid approximation on l_1/l_b. (See equation 4.20 and figure 4.3).

Other definition for persistence length

Recently, Hsu et al. [112, 111] proposed another definition for persistence length. It does not assume any specific form for the bond correlation function and is given by

$$l_2 = l_b \cdot \sum_{s=0}^{m-2} \langle \cos\theta(s) \rangle \tag{4.28}$$

This expression calculates the area under bond correlation curve. For FJC, we have $l_2 = l_b$. For the FRC model, this expression becomes

$$l_2 = l_b \cdot \frac{1 - (\cos\delta)^{m-1}}{1 - \cos\delta} \tag{4.29}$$

and in the WLC limit,

$$\frac{l_2}{l_1} = 1 - \exp(-X) \tag{4.30}$$

In figure 4.6, we plot $l_2/l_1 = -\ln\langle\cos\delta\rangle \cdot \sum_{s=0}^{m-2}\langle\cos\theta(s)\rangle$ as a function of X for various ω and m along with the FRC predictions. Again, theoretical predictions are recovered using $\langle\cos\delta\rangle$ in the FRC framework. As X increases, l_2/l_1 gives a finite value independent of L for $L \gg l_1$. We see that l_2/l_1 is dependent on the local flexibility and is slightly higher than l_1. As ω becomes smaller the difference between l_2 and l_1 diminishes and in the WLC limit, they become similar.

Another commonly used persistence length is $l_p(k)$, with $1 \le k \le m-1$ [110]. It measures the local persistence length for any bond k along the chain

$$l_p(k) = \frac{\langle \mathbf{r}_k \cdot \mathbf{R}_e \rangle}{l_b} \tag{4.31}$$

For FJC, $l_p(k) = l_b$. For FRC, we have

$$l_p(k) = \frac{1}{l_b} \cdot \sum_{i=1}^{m-1} \langle \mathbf{r}_k \cdot \mathbf{r}_i \rangle = l_b \cdot \sum_{i=1}^{m-1} (\cos\delta)^{|k-i|} \tag{4.32}$$

On further simplification, we obtain

$$l_p(k) = l_b \cdot \frac{1 + \cos\delta - (\cos\delta)^k - (\cos\delta)^{m-k}}{1 - \cos\delta} \tag{4.33}$$
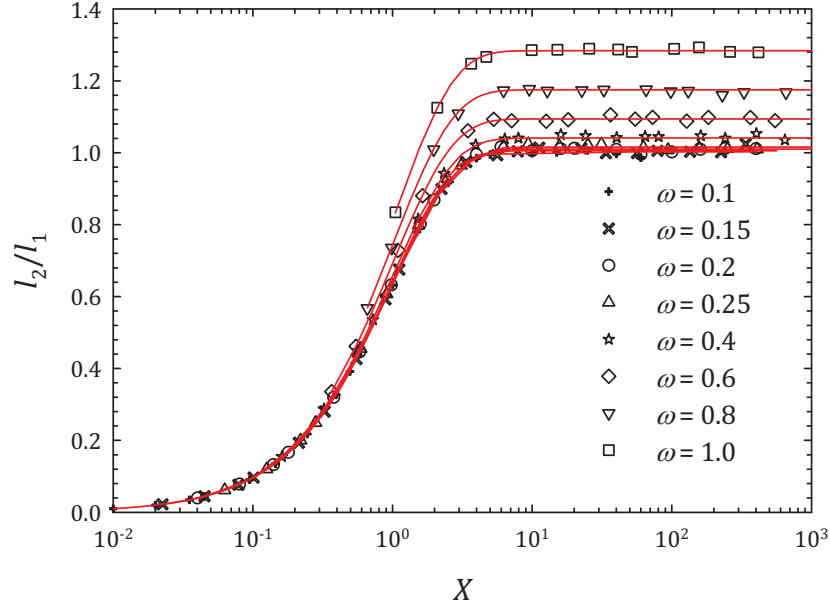
Figure 4.6: Evolution of l_2/l_1 as a function of X for various ω for ideal chains. The solid curves are obtained using the equations 4.29 and 4.19 for each ω plotted.

$l_p(k)$ is a bell shaped function, which is reduced near chain ends (at $k = 1$ and $k = m - 1$), and reaches a flat plateau l_{pmax}, independent of k in the middle of the chain ($k \sim m/2$) when the chain is long enough. From equation 4.33, for $m \gg 1$ we have

$$l_p(1) = l_p \cdot (m - 1) \approx l_b \cdot \frac{1}{1 - \cos \delta} \tag{4.34}$$

and

$$l_{pmax} \approx l_b \cdot \frac{1 + \cos \delta}{1 - \cos \delta} = l_K \quad \text{(see equation 4.17)} \tag{4.35}$$

Yamakawa [108] used $l_p(1)$ as a measure of persistence length.

From equation 4.34, we see that $l_p(1) \approx l_K/2$ as $\delta \to 0$ (see equation 4.20). Comparing above equations, we see for any $\omega < \pi/2$, the value of $l_p(k)$ is bounded and lies in between $l_K/2$ and l_K. Thus it becomes natural to study the reduced quantity $l_p(k)/l_K$. Using a reduced segment index $x = k/(m - 1)$, we have

$$\frac{l_p(k)}{l_K} = \frac{l_p(k) \cdot L}{\langle \mathbf{R}_e^2 \rangle} = \frac{1 + \cos \delta - \exp(-x \cdot X) - \exp((1 - \frac{m}{m-1}) \cdot X)}{1 + \cos \delta - \dfrac{2 \cdot \cos \delta \cdot (1 - \exp(-X))}{(m - 1) \cdot (1 - \cos \delta)}} \tag{4.36}$$

and in the WLC limit, we get

$$\frac{l_p(x)}{l_K} = \frac{X}{2} \frac{[2 - \exp(-x \cdot X) - \exp(-(1 - x) \cdot X)]}{[X - 1 + \exp(-X)]} \tag{4.37}$$
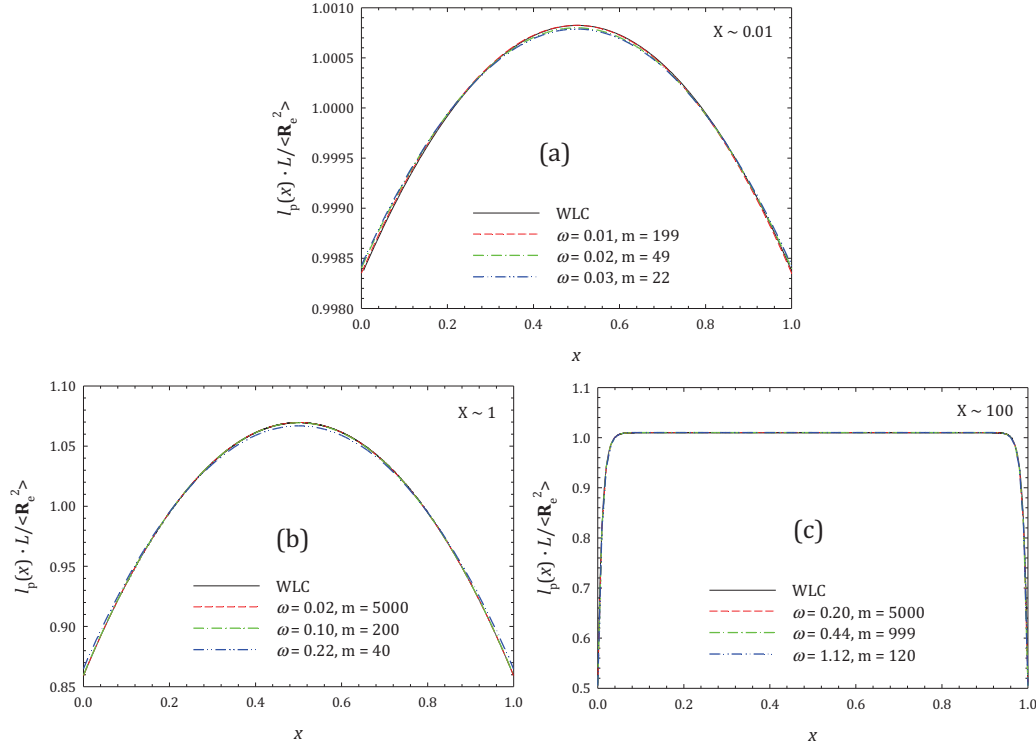
Figure 4.7: Comparison of equations 4.36 (colored curves) and 4.37 (solid black curve named WLC) for various m and ω as indicated in the figure and for (a) $X = 0.01$, (b) $X = 1$, and (c) $X = 100$. Note that Y axis scale is different for each plot.

In figure4.7, we compare equations 4.36 and 4.37 for different X. We see that for a given X, curves for different ω superimpose on each other and on the WLC curve. This suggests that the behavior of $l_\mathrm{p}(k)$ is independent of the nature of the chain, whether it is discrete or continuous, if the chain is sufficiently long. Figure 4.8 shows the reduced $l_\mathrm{p}(k)$ curves obtained from our simulations for different ω at a constant X and the theoretical prediction from equation 4.37. As expected, all curves superimpose on each other. ω plays no role except that it determines the lowest accessible value of X.

Now, to see the effect of X, we plot $l_\mathrm{p}(x)/l_\mathrm{K}$ from equation 4.37 for various X values in figure 4.9.We find that the shape of the curve is very dependent on X. For small values, the curve is almost flat in the entire region since for a rigid rod $l_\mathrm{p}(x)/l_\mathrm{K} \simeq 1$. As X is increased the curve starts to show a convex shape with reduced ends (see equation 4.34, which gives $l_\mathrm{p}(1)/l_\mathrm{K} \simeq 0.5$). The convexity reaches a maximum for a specific X and then starts to flatten again, while the values for the chain ends remain close to 0.5. Substituting $x = 0.5$ in equation 4.37 gives the maximum value of $l_\mathrm{pmax}/l_\mathrm{K}$ around $X = 4.42$ (see figure 4.10).
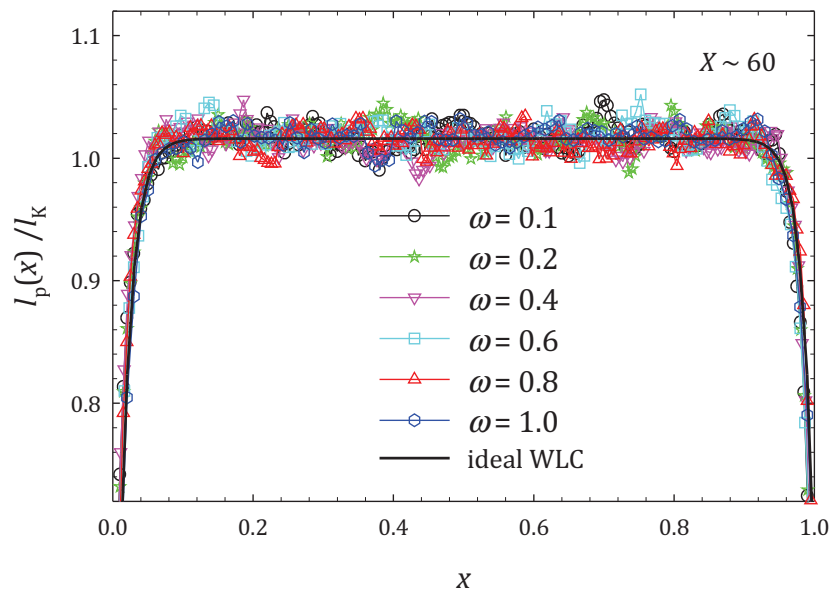
Figure 4.8:   Normalized $lp(x)$ for ideal chain with various local flexibility as indicated in the figure, with m corresponding to $X \approx 60$. The solid curve is from equation 4.37.
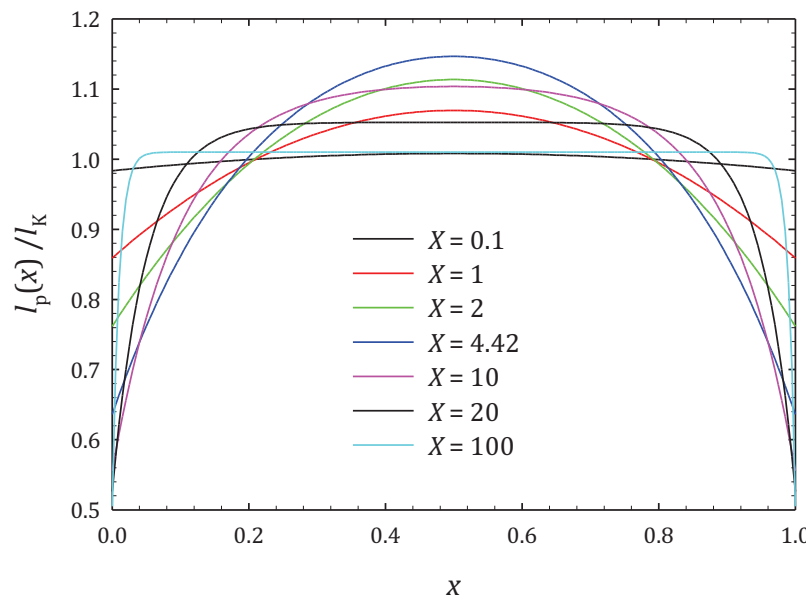

Figure 4.9: $l_p(k)/l_K$ as a function of the normalized segment index x for chains of different values of X as indicated in the figure given by the equation 4.37.
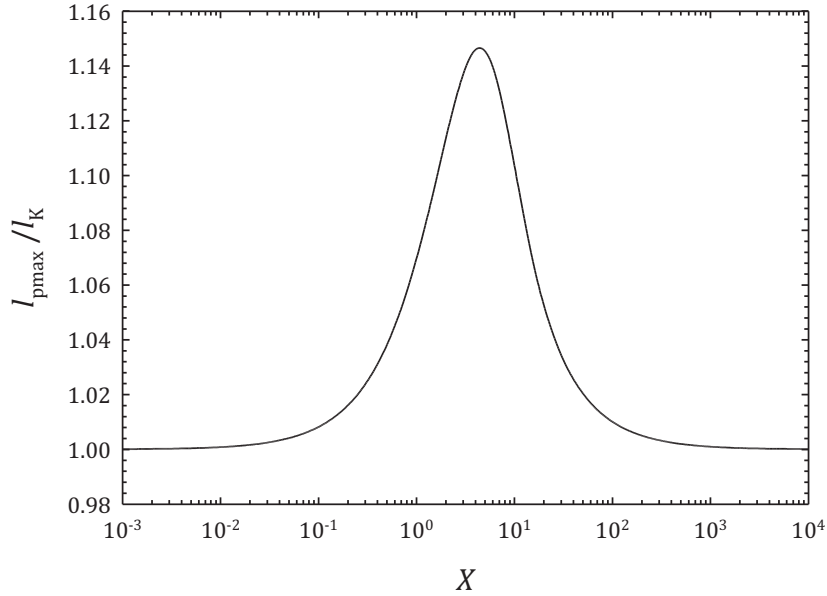
Figure 4.10:   Variation of $l_{\mathrm{pmax}}/l_{\mathrm{K}}$ as a function of X.

To conclude, we see that in the ideal case, our model is an equivalent of the FRC model and theoretical predictions could be recovered using $\langle \cos \delta \rangle$ instead of a fixed bond angle and $\langle l_{\mathrm{b}} \rangle$ instead of a fixed bond length. In the WLC limit ($L \gg l_1 \gg l_{\mathrm{b}}$), we obtain mutual relations between various persistence lengths

$$\boxed{l_1 = l_2 = l_{\mathrm{p}}(1) = \frac{l_{\mathrm{K}}}{2} = \frac{l_{\mathrm{pmax}}}{2} \simeq \frac{2\langle l_{\mathrm{b}} \rangle}{\omega^2}} \tag{4.38}$$

4.3   Deviation from ideality

For a real polymer chain in a good solvent, excluded volume interactions result in a swelling effect. It is seen as a self avoiding walk, which increases $\langle \mathbf{R}_{\mathrm{e}}^2 \rangle$ and its dependency on m giving the scaling $\langle \mathbf{R}_{\mathrm{e}}^2 \rangle \sim m^{2\nu}$, with $\nu = 0.588$. From equation4.3, we have

$$\langle \mathbf{R}_{\mathrm{e}}^2 \rangle = l_{\mathrm{b}}^2 \cdot \sum_{i}^{m-1} \sum_{j}^{m-1} \langle \cos \theta(s) \rangle \tag{4.39}$$

This implies that the stronger dependency on m is coming from increased bond correlation. This is due to the excluded volume effects, which restrict the chain conformations. The extended bond correlations along the chain will be discussed later. For small chain lengths ($L \ll l_{\mathrm{p}}$), the chain behaves as an ideal chain due to little excluded volume effects. As the chain length increases, excluded volume interactions build up, creating a chain expansion leading to the crossover to a swollen chain.

Noting that excluded volume effects lead to more open chains, we try to see the consequence on l_1 for various local flexibilities. In figure 4.11 we can see that values
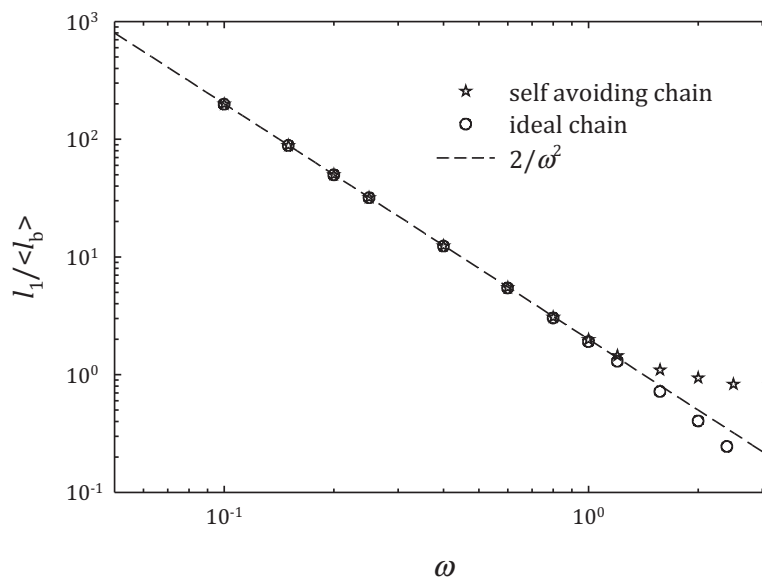
Figure 4.11: Behavior of $l_1/\langle l_b \rangle$ as a function of ω for ideal and self avoiding chains. The dashed line is the WLC condition $2/\omega^2$.

calculated from the obtained $\langle \cos \delta \rangle$ lie exactly on the theoretical curve, independent of excluded volume effects for smaller ω. For larger ω, values of l_1 diminishes after $\omega > \pi/2$ for ideal chains and reaches a constant value in for real chains. Also, we recall that we observe no dependence on m.

4.3.1   Influence on the bond correlation function

As said above, the direct consequence of the swelling is the long range bond correlations along the chain. For a flexible real polymer chain in good solvent, the bond correlation function must decrease as a power law of the segment index s when $s^* \ll s \ll m$ [110, 113, 111] as

$$\langle \cos \theta(s) \rangle \propto s^{2\nu - 2} \tag{4.40}$$

where, s^* depends on the persistence length. Similar results with an exponent of $-3/2$ have been found for chains in dense melts [114].

The direct consequence of this relation is the divergence of l_2 with m and this will be discussed in section 4.3.2.

We have seen that for ideal chains the bond correlation along the chain backbone follows an exponential decay (see equation 4.18). In general, a real chain does not feel excluded volume effects unless $L > l_1$ and hence we obtain similar initial behavior (exponential decay) for short semi flexible ideal and real chains. For chains with very small l_1, the initial exponential decay becomes hardly visible and the bond correlation function directly tends to follow the power law behavior. See figure 4.12 for the behavior of bond correlation function for real and ideal chains for various
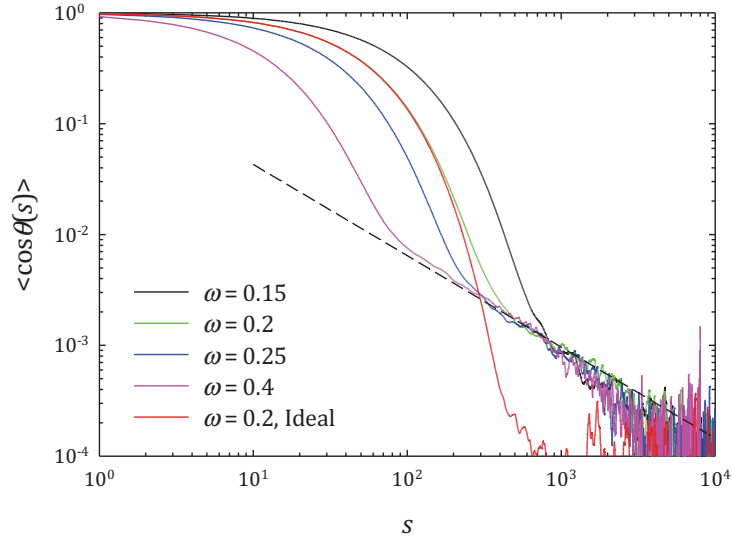
Figure 4.12: The decorrelation of bond vector as a function of the segment index for different ω. The dashed black line has a slope $s^{2\nu-2}$.

l_1 using our patchy model. Curves for $\omega = 0.2$ of the real and ideal case in the figure 4.12 show the independency of excluded volume effects on the initial decay behavior. According to Hsu et al. [111], the power law behavior is seen in the range $m/10 \ll s \ll m/2$ for fully flexible real chains.

For a bending rigidity driven polymer chain model [115], it was reported that a clear crossover from an exponential decay to the power law behavior could be seen. In that article, a cubic lattice was used and a bending probability at a lattice site, $q_b = \exp(-u/(k_B \cdot T))$ was set, where u is an energy term. At each growth step, the bending probability is tested with a random number. The chain grows straight until the random number is less than q_b. Each time the bending probability is overcome, the chain makes a $\pm 90°$ turn and the growth is continued. This gives the length of the straight segment as l_1. For a highly flexible self avoiding chain, $q_b = 1$ meaning that at each step of chain growth, a turn is made. As q_b is decreased, l_1 gets increased. Since no side chains are involved in this model, it is possible to reach large values of l_1/l_b.

After the persistence length has been overcome, the real chain begins to feel the presence of its neighbors and the decay becomes slower, following a power law. By a careful examination of the bond correlation function for semi flexible chains we can see that after a certain s, the function seems to follow another exponential decay due to the finite extent of the chain, which is not clearly seen in many cases due to the high fluctuations. This is shown in figure 4.13. So, to study the different behaviors and their limits, we try to fit the curve using an equation of the form

$$\langle \cos \theta(s) \rangle = A \cdot \exp\left(-\frac{s}{s_1}\right) + (1 - A) \cdot \left(1 + \frac{s}{s_1}\right)^{2\nu-2} \cdot \exp\left(-\frac{s}{s_2}\right) \qquad (4.41)$$

Here, the A parameter stands for the effect of local flexibility, which determines the extent of decorrelation of the first bond. The s_1 parameter is a measure of the persistence length, after which the power law appears. The s_2 parameter is to determine the length at which the power law again changes to an exponential decay due to the finite extent of the chain. Trial fits were made for different chains of various m and ω and it was seen that $s_1 \approx l_1/l_{\rm b}$ as expected (see figure 4.14) and is independent of m for a given l_1. Later $l_1/l_{\rm b}$ was used instead of s_1 to reduce the number of fitting parameters and improve the accuracy of the procedure.
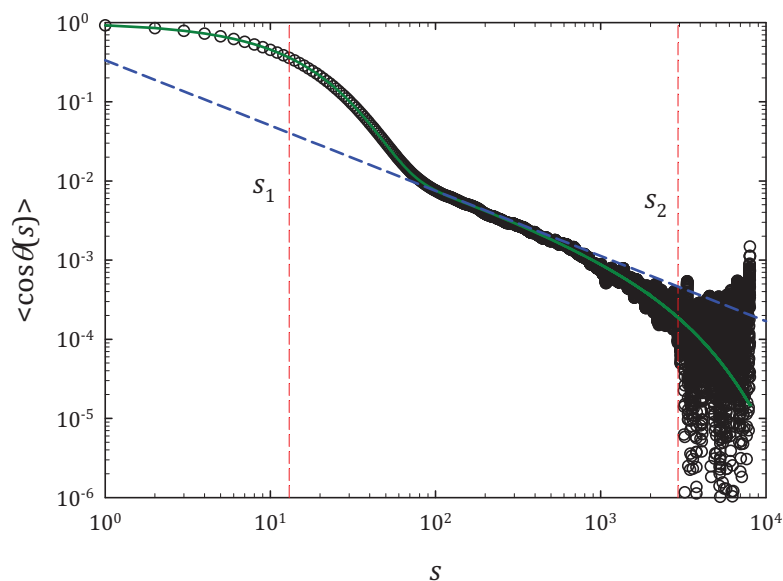
Figure 4.13: The decorrelation of the bond vector as a function of the bond distance for $\omega = 0.4$ and $m = 8000$. The solid green line is obtained by fitting this curve with the equation 4.41.The fit parameters are shown in the figure. Blue dashed line has a slope $2\nu - 2$.

The parameter A depends on ω and becomes independent of m for very large m (see figure 4.15). For very small ω, there is only very small amount of decorrelation in initial steps of s. Hence A is very close to 1. As l_1 decreases, the correlation of the bond direction is lost very fast resulting in lower values of A. The second term in the equation provides information about the length scale when the power law behavior begins to show up. If we take asymptotic values of A obtained for very large m and plot the prefactor of the power law in the second term of the equation,($(1 - A) \cdot s_1^{2\nu - 2}$ with $\nu = 0.588$) we see that this is a constant, independent of ω. This means that the prefactor of the power law behavior is the same for all local flexibilities (see figure 4.12). The factor s_2 showed a linear dependence on m in general, even though the values are highly spread in a log-log plot. From the plot 4.16, we see that s_2 is close to $m/5$.

Integrating the area under the bond correlation curve and comparing with the ideal chain case gives the excess in the bond correlation due to excluded volume
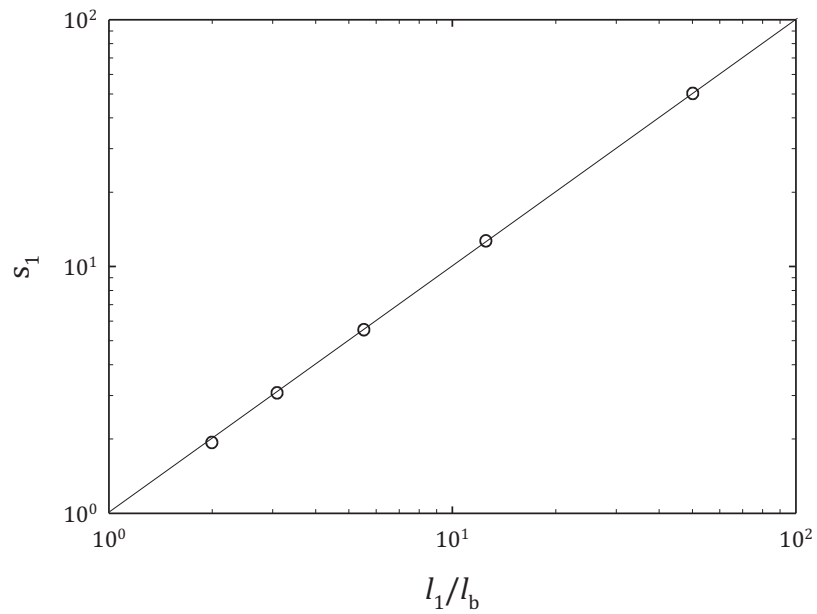
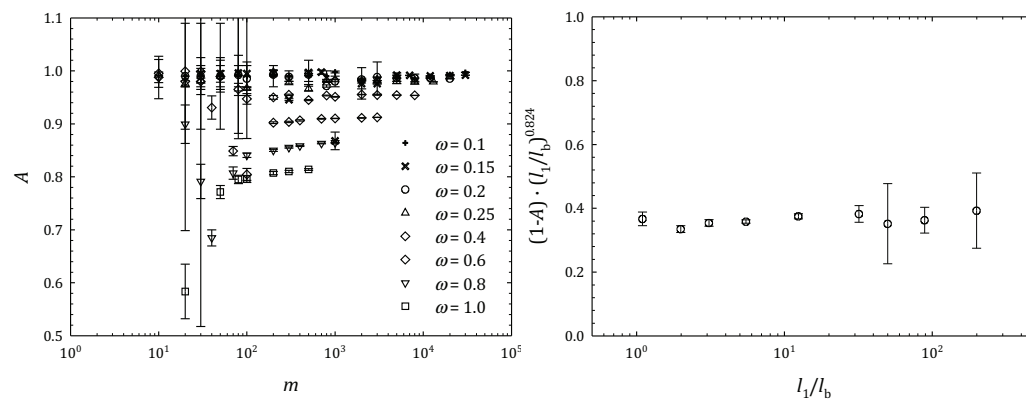Figure 4.14: Variation of s_1 as a function of persistence length. The line is the function $y = x$.

Figure 4.15: The fitting parameter A from the equation 4.41 as a function of m for various ω as indicated in the figure (left) and $(1 - A) \cdot (l_1/l_b)^{0.824}$ as a function of m (right).
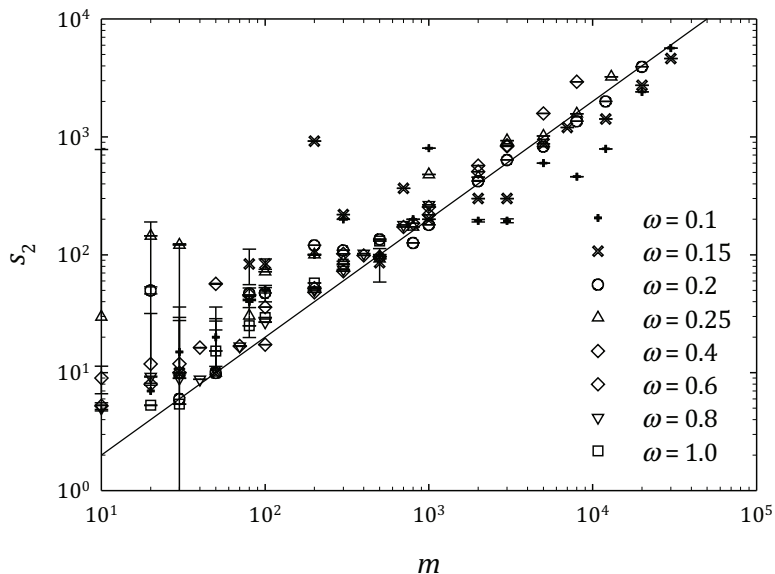
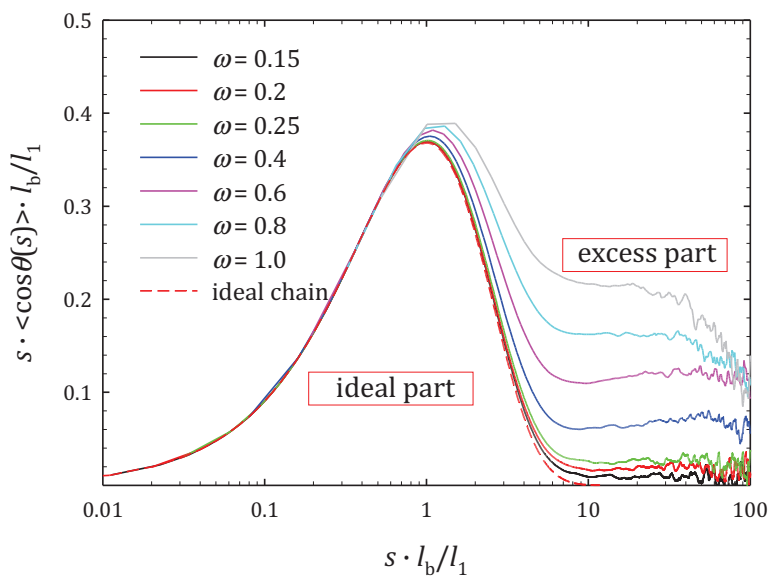Figure 4.16: Effect of m and ω on s_2. The solid line has a slope 1.

Figure 4.17: Rescaled bond correlation functions for real chains for various local flexibilities as indicated in the figure, compared with an exponential decay (ideal behavior). The normalized axes give the area under the curve for the ideal chain as 1. The plateau like part for different flexibility indicates the excess in bond correlation due to self avoiding nature of the chain.

interactions. See figure 4.17. Here we plot the rescaled bond correlation function of the longest chains we were able to obtain using our model. In the X axis, we have the segment index rescaled using l_1/l_b since all chains follow the exponential decay up to their respective l_1/l_b. In the Y axis, we have rescaled the bond correlation function such that the area under the curve for an ideal chain is unity. Any deviation from the ideal behavior shows the excess part of bond correlation function. The figure shows that as the chain becomes locally rigid, it follows the ideal chain behavior up to a higher s when compared with more locally flexible ones, where the deviation occurs very early.

4.3.2 Divergence in some persistence length definitions

We have already seen that l_1 is independent of m. The increased Flory exponent for real chains causes l_K to diverge with m, giving $l_K \propto m^{2\nu-1}$ for large m. Equation 4.40 indicates that l_2 also should diverge with m. This is the result of the excess in bond correlation function which increases the sum of $\langle \cos\theta(s) \rangle$ resulting in l_2 to get easily deviated at shorter chain lengths for more locally flexible chains. In figure 4.18, its ratio to the ideal chain case is plotted. Here we see that more rigid chains follow the ideal behavior even for a chain length much above the persistence length. For example $\omega = 0.15$, the ideal behavior is continued up to about 2 decades after the persistence length, before starting to show any deviation.
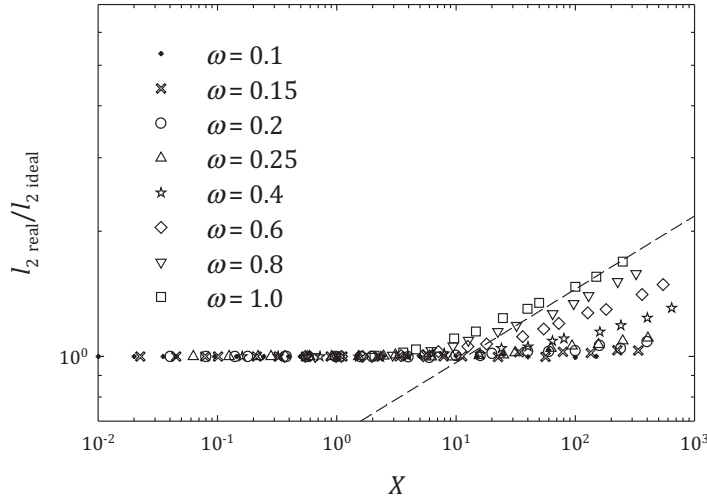

Figure 4.18: Variation of $l_{2\ \text{real}}/l_{2\ \text{ideal}}$ as a function of X for various values of ω as indicated in the figure. The dashed line has a slope of 2ν-2.

Due to the divergence of some persistence lengths, Hsu et al. [116, 111, 115] proposed another method to calculate the persistence length for real chains, given as

$$l_3 = \frac{\langle \mathbf{R}_e^2 \rangle}{2 \cdot l_b \cdot (m-1)^{2\nu}} \tag{4.42}$$

It is designed to be a non diverging quantity. In the case of ideal FRC, l_3 turns out

to be $l_{\mathrm{K}}/2$.

Figure 4.19 summarizes the scaling laws we have seen so far. Here, the behavior of curves could be explained as

1. When the chain is short, it shows a rod-like behavior ($\langle \mathbf{R}_{\mathrm{e}}^2 \rangle \propto m^2$) which gives the initial rise in the curve for l_3 till the respective l_1 has been reached.

2. After the rod-like regime, it follows an ideal behavior ($\langle \mathbf{R}_{\mathrm{e}}^2 \rangle \propto m$) and hence the decrease in l_3.

3. For very long chains and chains with short l_1, l_3 reaches a constant value, depending on the local flexibility.
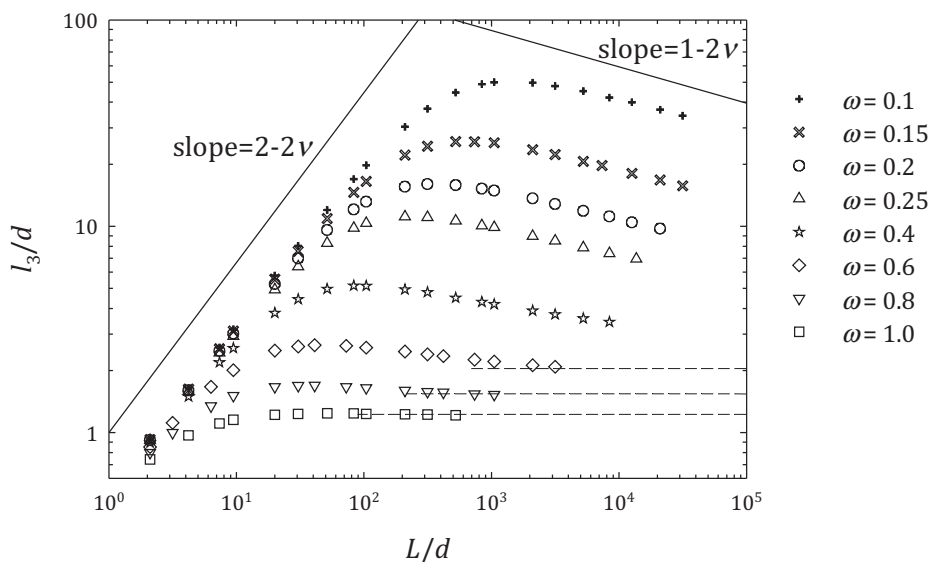

Figure 4.19: l_3/d plotted against chain length (L/d) for various flexibilities as indicated in the figure for a real chain. The solid lines have expected slopes for the rod-like and flexible ideal regime. Dashed lines are guides to the eye showing the expected plateau behavior.

We see that there is an intermediate regime, where sufficiently long locally rigid chains behave like ideal chains. We have similar results as in literature (see figure 4.20, obtained using the bending rigidity model on a cubic lattice, as explained in page 61) but with our chain generation method, we are not able to reach longer enough chains for lower ω and hence the final plateau behavior is not clearly visible. Also from this plot, we can see that the plateau behavior is observed after the ideal chain like behavior. This indicates the possibility of presence of another length scale bigger than l_1, where the semi flexible chains change from ideal to swollen.

Recently, Hsu et al. [111] have studied the structure of bottle brush polymers using on lattice Monte Carlo methods. Bottle brush polymers are composed of a
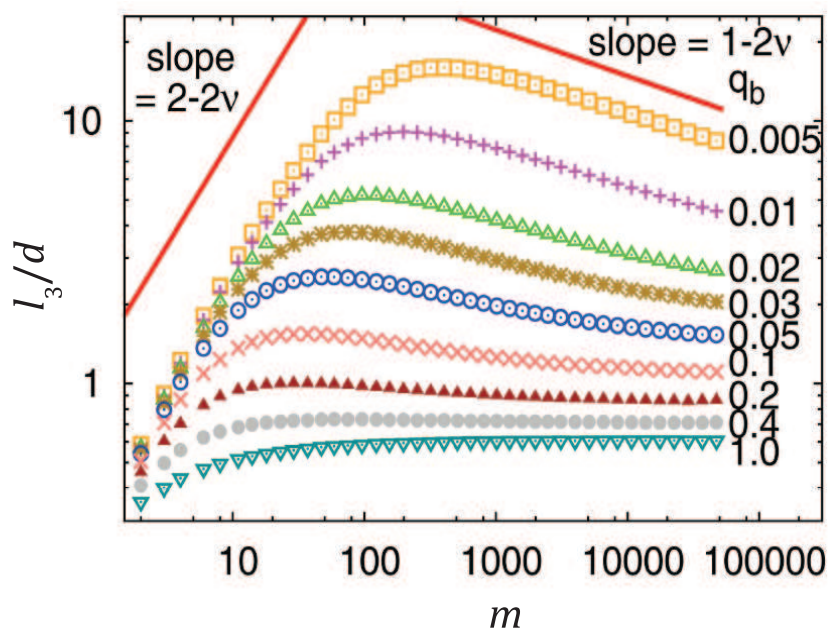
Figure 4.20: l_3/d plotted against chain length (m) for various bending probabilities (q_b) as indicated in the figure for a self avoiding walk on a cubic lattice. Image adapted from [115].
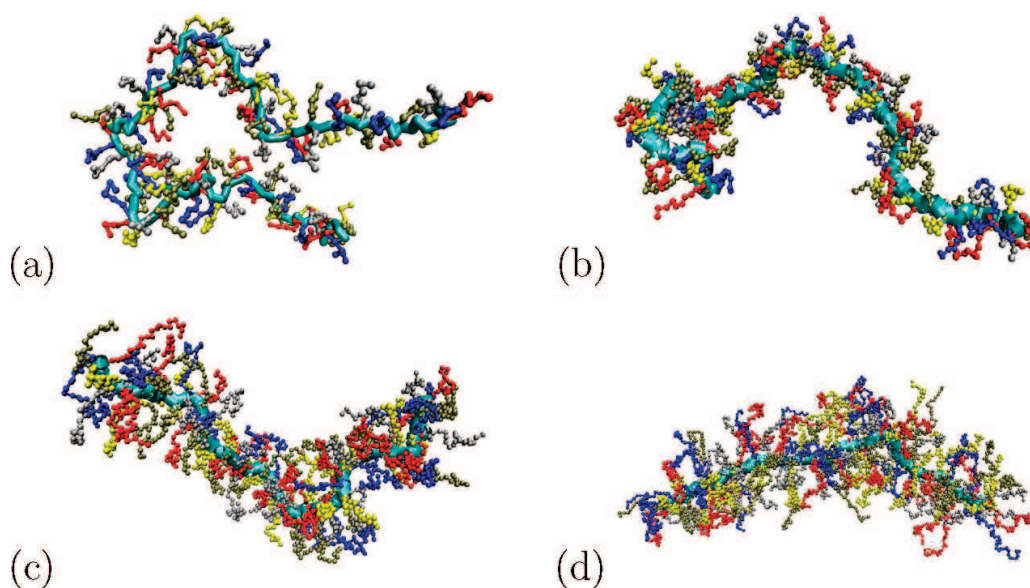

Figure 4.21: Bottle-brush polymers with backbone containing 131 monomers and with side chain lengths (a) N=6, (b) N = 12, (c) N = 24, and (d) N = 48, with a grafting density 1 per monomer. Image taken from [116]. Note how the thickness increases with increasing persistence length. See text for details.
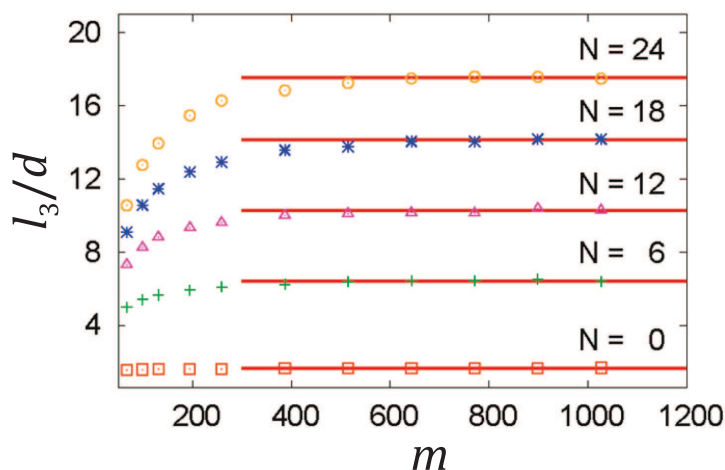
Figure 4.22: l_3/d for bottle-brush polymers plotted as a function of chain length for various grafted chain length (N). Image adapted from [111].

backbone, on to which a dense grafting of side chains is made. The backbone is very flexible and the rigidity of the chain is controlled by the length and grafting density of side chains (see figure 4.21). Changing the rigidity of the backbone also changes the diameter of the chain. Within the range of tested N, fig 4.22 shows (on a lin-lin plot) that l_3 does not follow the same behavior as observed in figures 4.19 and 4.20. As N increases, the chain does not show a range of m (in backbone units) where an ideal-like behavior is recovered (this will also the case for $Lp(k)$, and will be discussed later). We compile data from [115] and [111] regarding l_3 and R_c (diameter of the chain) for a graft density 1 per backbone unit in table 4.1

Length of side chains, N	l_3	R_c	l_3/R_c
6	6.43	11.62	0.55
12	10.30	17.76	0.58
18	14.15	22.94	0.62
24	17.55	27.48	0.64

Table 4.1: l_3 and R_c extracted from [115] and [111] for bottle brush polymers as a function of side chain length.

We see that as N increases both l_3 and R_c increase about the same factor (see the ratio l_3/R_c). This means the aspect ratio of the chain is conserved all along the process (see figure 4.21). On the contrary, in the WLC limit (where the ideal behavior of a real chain is observed on a certain range of m) this aspect ratio tends to be infinite and chains look thinner. Hence, from a rod-like behavior bottle brush polymers moves over to an excluded volume mediated behavior. In our case the monomer size is fixed, or the diameter of the chain remains constant. Hence, with the increase of persistence length, the ratio l_3/l_b diverges, giving a WLC behavior
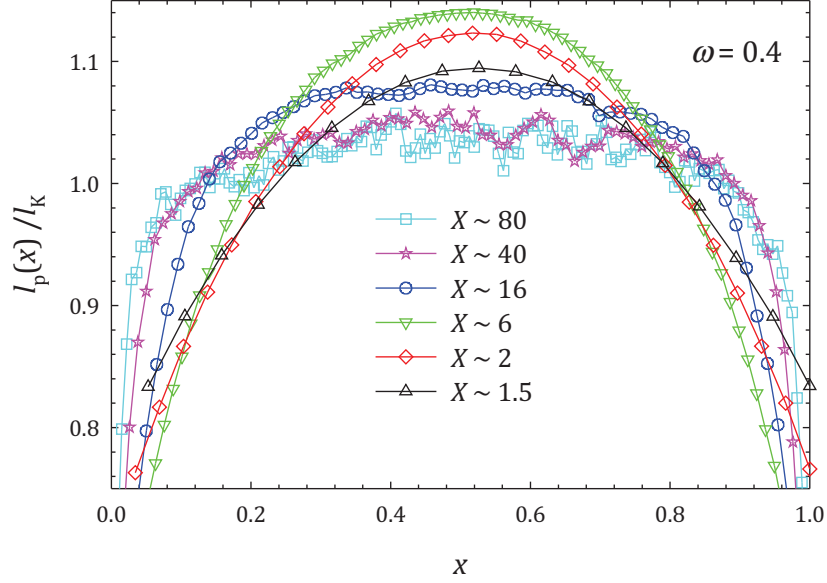
Figure 4.23: Normalized $lp(x)$ for real chains with various X as shown in figure at a constant local flexibility $\omega = 0.4$.

for large l_3.

We now study the behavior of $l_{\mathrm{p}}(k)$. Knowing $\sum_k l_{\mathrm{p}}(k) = \langle \mathbf{R}_{\mathrm{e}}^2 \rangle$, the local persistence length $l_{\mathrm{p}}(k)$ for k far from both ends (l_{pmax}) should behave as $l_{\mathrm{p}}(k)/l_{\mathrm{b}} \propto m^{2\nu-1}$ and it stays finite for the chain ends [110, 112, 111]. So, we have again another critical quantity that diverge with m

$$\boxed{l_{\mathrm{K}} \propto l_{\mathrm{pmax}} \propto l_2 \propto m^{2\nu-1}} \tag{4.43}$$

For ideal chains, we have seen that the shape of the normalized $l_{\mathrm{p}}(k)$ curve depends only on X with l_{pmax} reaching a maximum value around $X \approx 0.4$. A real chain with a given flexibility shows similar behavior on X (see figure 4.23). If we try to see the effect of ω on a given X, we find that the shape and l_{pmax} of curves are highly dependent on the local flexibility. See figure 4.24. From the figure, we see that even for moderate value of X ($X \approx 60$), more curved shapes can be observed for highly locally flexible chains. Thus it becomes possible that a given curve may be obtained from many combinations of X and ω, indicating a complex behavior for normalized $l_{\mathrm{p}}(k)$.

For a fully flexible three dimensional bead spring chain with excluded volume interaction, using renormalization group and ε_1-expansion, Schäfer and Elsner [110] proposed an expression for $l_{\mathrm{p}}(x)$, where $x = k/(m-1)$ as

$$\boxed{\frac{l_{\mathrm{p}}(x) \cdot L}{\langle \mathbf{R}_{\mathrm{e}}^2 \rangle} = \frac{l_{\mathrm{p}}(x)}{l_{\mathrm{K}}} \approx \frac{\Gamma(4\nu)}{\Gamma^2(2\nu)} \cdot (x \cdot (1-x))^{2\nu-1}} \tag{4.44}$$
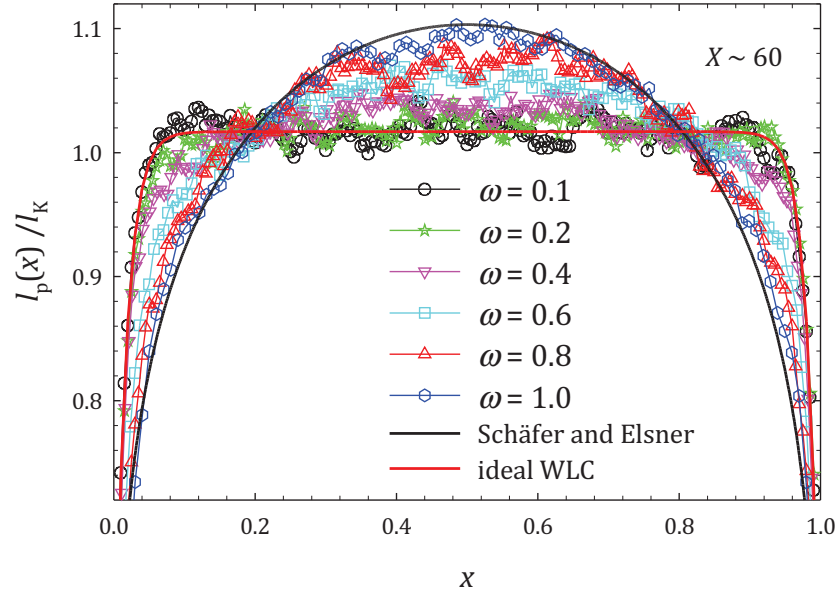
Figure 4.24:   Normalized $lp(x)$ for real chains with various local flexibility as indicated in the figure for a constant $X \approx 60$.

In figure 4.24, we see that the $X \approx 60$, $\omega = 1.0$ case correctly fits with this equation. This equation was also found to provide a very good approximation for all cases of self avoiding bottle brush model on a cubic lattice [116] which is contradictory to our case. This could be understood, because the backbone of the bottle brush is always highly locally flexible and tuning side chains does not significantly change the effective l_1/l_{b}. Thus for all cases, we get the same behavior for $l_{\mathrm{p}}(k)$ which follow Schäfer's predictions for fully flexible chains.

We use the equation suggested by Schäfer and Elsner with the exponent as a free parameter and try to fit curves obtained from our real chains. The rearranged equation used for the fit is given by

$$\frac{l_{\mathrm{p}}(x)}{l_{\mathrm{K}}} = \frac{\Gamma(2\alpha + 2)}{\Gamma^2(\alpha + 1)} \cdot (x \cdot (1 - x))^{\alpha} \tag{4.45}$$

where $\alpha = 2\nu - 1$ for fully flexible chains. When $x = 0.5$, we get

$$\frac{l_{\mathrm{pmax}}}{l_{\mathrm{K}}} = \frac{\Gamma(2\alpha + 2)}{\Gamma^2(\alpha + 1)} \cdot \left(\frac{1}{4}\right)^{\alpha} \tag{4.46}$$

In these equations, we know that the term $x \cdot (1 - x)$ is already a convex function, which means that α characterizes the shape and l_{pmax}. When $\alpha \to 0$, the reduced $l_{\mathrm{p}}(k)$ curve should be flat and as α increases, the curve becomes bell shaped. We fit only the middle portion of the curve obtained for $l_{\mathrm{p}}(k)/l_{\mathrm{k}}$ from $x = 0.25$ to 0.75 as described by [111]. This is done because the diminished chain ends affect the fitting procedure and give a lower α.
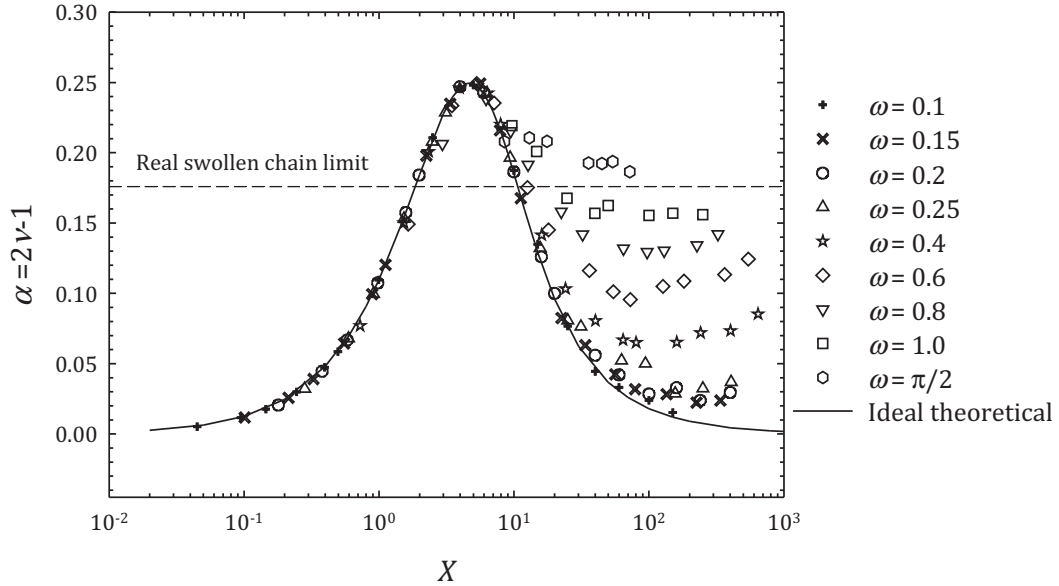
Figure 4.25: Variation of α as a function of X for various ω as shown in the figure for real chain case. The solid curve is obtained by fitting the ideal WLC theoretical $l_p(k)$ curves from equation 4.37.

We first tried to fit theoretical curves obtained for ideal FRC (equation 4.37) for various X and verify if the fitting procedure gives a maximum value of α around the same value of X which gives maximum l_{pmax}. Figure 4.25 shows the result of such fitting procedure. In the figure, the solid curve is the fit obtained for the ideal WLC condition (equation 4.37). The α value first increase from near zero, reaches a maximum around $X = 4.42$ and then decrease back to zero for larger X, which is in accord with the l_{pmax} measurements (see figure 4.26). To check the reliability of the fit, we injected these α values obtained for various X in equation 4.46 to recreate the $l_{\mathrm{pmax}}/l_{\mathrm{K}}$ curve (see figure 4.26). We see that the $l_{\mathrm{pmax}}/l_{\mathrm{K}}$ obtained from this method is very close to the one given by the theoretical prediction (equation 4.37 at $x = 0.5$), indicating the accuracy of the fitting procedure.

In the case of real chains, ideal chain behavior is observed for smaller X. As X becomes larger, the curve starts to deviate from the ideal behavior and the deviation is seen to be highly dependent on the local flexibility ω. We see that chains with lower local flexibility follow the ideal behavior over longer chain lengths after which α slowly starts to deviate. For chains which have an intermediate local flexibility, we see that the deviation starts early and the decreasing behavior is continued till a minima is reached, after which it appears to increase. Again using the prediction from Schäfer and Elsner, with $\nu = 0.588$, we should obtain $\alpha = 0.176$ for very long excluded volume dominated chains. From our data, we see α to be increasing again, but it is not clear whether it will reach this expected behavior as data for longer chains are not easily obtained in reasonable time. The effect of flexibility on the
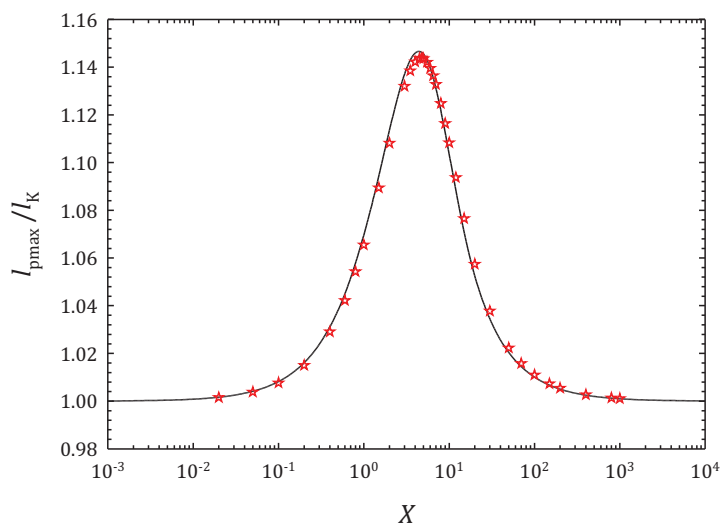
Figure 4.26:   Variation of l_{pmax}/l_K as a function of X. The solid curve is the theoretical expression for FRC (equation 4.37 at $x = 0.5$). The red filled stars come from equation 4.46 using previous α values obtained from fitting theoretical curve 4.37.

normalized $l_p(k)$ curves (figure 4.24) may be due to the fact that we are not in the long chain limit, where all chains should show similar $l_p(k)$ curves. This is observed as the increase in $l_p(k)$ for higher ω, which lies closer to the expression by Schäfer.

Recalling the figure 4.18, we see that the case of $\omega = 1.0$ is following a swollen behavior for longer chains. In the case of $l_p(k)$, the α value obtained is slightly less for the same chain, indicating that it is close to a swollen chain. This could be due to chains being not long enough. Moreover, shorter chains have low number of points on middle region of the $l_p(k)$ curve to be fitted and hence the fitting becomes prone to errors, which reflects in the value of α.

We have already seen that the diverging behavior of l_2 takes place at a chain length longer than l_1 and is dependent on ω. Similar behavior is also seen in the case of l_3, where it becomes independent of L. The $l_p(k)$ analysis also indicates that X may not be the correct scaling for a real chain to account for the excluded volume effects. We conclude the existence of a characteristic crossover length for the real chain other than l_1 after which it starts to show the swollen behavior as predicted by Flory.

4.3.3   The thermal blob

To visualize the swelling effect clearly, we use the ratio of the mean square end to end distance of the real chain to that of an ideal chain (figure 4.27). When the real and ideal chains behave as rod like or ideally, we have the ratio equals 1. As the chain length increases, the swelling effects starts to show up and for long chains,
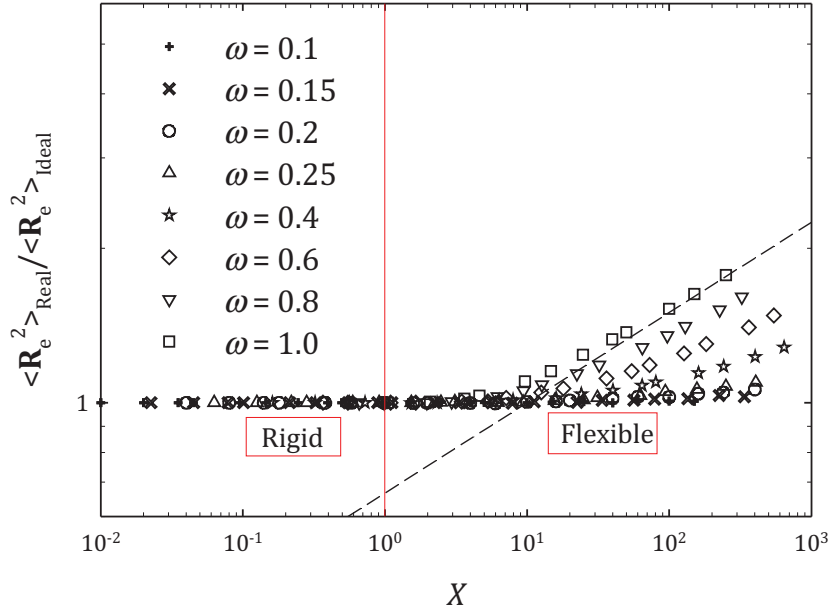
Figure 4.27: Ratio of the end to end distance of a real chain to that of an ideal chain as a function of X for various ω as indicated in the figure. The guiding line has a slope of $2\nu - 1 = 0.176$.

the ratio diverges as a function of the chain length, as predicted by Flory. Figure 4.27 clearly shows that l_1 is not a good scaling parameter since chains with different local flexibility deviate from the ideal behavior at different X.

Thus for a real polymer chain in a good solvent, another length scale is necessary to describe its conformation as the chain length is increased. We have seen that persistence length is not a relevant quantity to express the crossover from an ideal chain behavior to a swollen one, where excluded volume interactions starts to be of importance. The crossover is particularly noticeable in WLC limit, where the persistence length is much bigger than the size of the monomer. This could be understood as follows: Consider we are building a polymer chain with excluded volume interactions by progressive addition of monomers to one end of the chain. The probability of placing the ith monomer is very dependent on i and on the local flexibility ω. When ω is very small, the direction of the chain growth remains rather the same as in the beginning. When the persistence length is reached, the chain direction is significantly decorrelated (of the order of $1/e = 0.37$) and as $l_0.8 \gg l_{\text{b}}$, the monomer density around the growing end is still small and the chain is not greatly influenced by excluded volume interactions. Thus it becomes possible to obtain an ideal flexible regime. This is not the case if ω is large. Since the chain direction gets decorrelated vary fast, we rapidly start to find existing monomers in the neighborhood, reducing the space available to place the next one. Thus the excluded volume interactions become very important even at shorter length scales

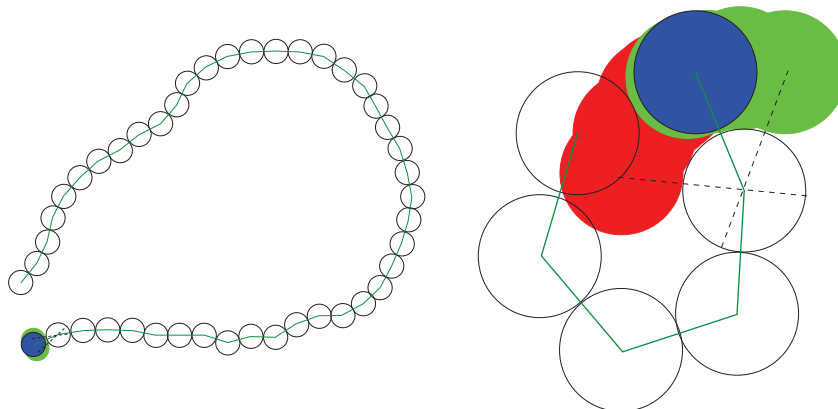(of the order of a few monomers). This is schematically shown in figure 4.28.

Figure 4.28: Schematic representation of the growth of a real chain. At left is a chain with higher persistence length than the one on the right. Both chains are almost at the same X. The black circles indicate the monomers placed so far and the blue filled circle is the monomer at the growing end. The red and green area together form the interaction volume. The green area shows the part accessible for placing the monomer and the red area shows the part inaccessible due to excluded volume interactions. Note the length of the chains and the amount of excluded volume interactions.

The effect of l_1 on excluded volume can be easily seen in the time taken to generate the self avoiding chains. As l_1 decreases, the probability of rejection becomes higher because of the increased monomer density around the growing end leading to large number of overlapping structures. It has been already reported that the probability of generating a self avoiding chain decreases exponentially with the chain length m as $P \sim \exp(-m/m^*)$ [117], where m^* is a constant, which depends on the model used and $1/m^*$ is termed as attrition constant [117]. We have not carried out any detailed study in this direction, but as an example: for self avoiding chains, the time taken to generate 10^5 chains of $m = 500$, $\omega = 0.2$ took about 15 minutes, while with $\omega = 1.0$ for the same chain length it took around 5 days for the generation due to tremendous amount of rejection.

To estimate the relation between this new length scale and the persistence length, we consider the real polymer chain (made of N monomers) as made of blobs called *thermal blobs*, inside which the chain is considered as ideal. Each blob is having a characteristic size ξ_T and is freely jointed to the next one in a self avoiding manner. See figure 4.29 for a schematic representation. For length scales smaller than ξ_T, the chain behaves as an ideal chain as soon as the persistence length b is reached. Considering the monomer to have a characteristic size a, a blob contains N_T monomers and the size of the chain is termed $\langle R_\mathrm{F} \rangle$, we have the following relationships

$$\langle R_\mathrm{F} \rangle \propto \left(\frac{N}{N_\mathrm{T}} \right)^{3/5} \cdot \xi_\mathrm{T} \tag{4.47}$$
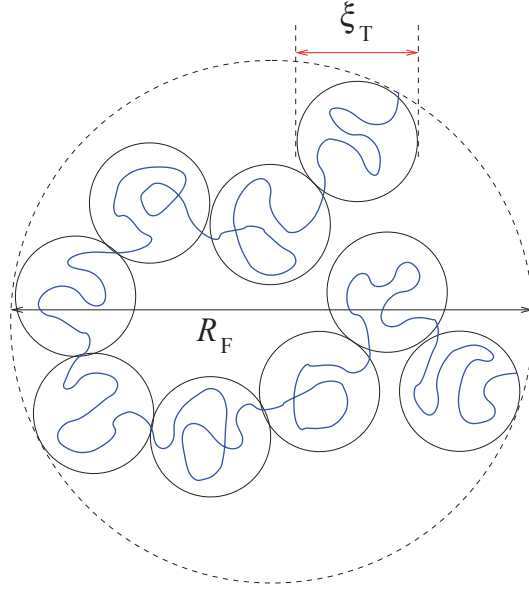
Figure 4.29: Schematic representation of the thermal blob concept with ξ_T the characteristic size of the blob and R_F the characteristic size of the swollen chain.

and

$$\xi_T \propto (a \cdot b \cdot N_T)^{1/2} \tag{4.48}$$

By taking a simplified expression of the chain free energy and minimizing it [118, 107, 119], Flory found that the characteristic size of the chain scale as

$$\langle R_F \rangle \propto N^{3/5} \cdot b^{1/5} \cdot a^{4/5} \tag{4.49}$$

Defining l_T as the thermal contour length, we obtain

$$l_T = a \cdot N_T \propto \frac{b^3}{a^2} \tag{4.50}$$

Comparing with our model we have $b \simeq l_1$ and $a \simeq l_b$, giving

$$l_T \propto \frac{l_1^3}{l_b^2} \tag{4.51}$$

From the thermodynamic point of view, thermal blob is a concept where each blob corresponds to a chain length at which the monomer-monomer interaction energy is of the order of the thermal energy $k_B \cdot T$. On smaller length scales, interactions within the chain is small and hence chains follow unperturbed statistics. For chains longer than l_T, the monomer-monomer interaction energy is larger than $k_B \cdot T$ and polymer conformation becomes controlled by interactions.

This concept of thermal blobs gives a more comprehensive detail on different length scales. For $L \ll l_1$, the chain is considered as rigid rod like; for $l_1 \ll L \ll l_T$,
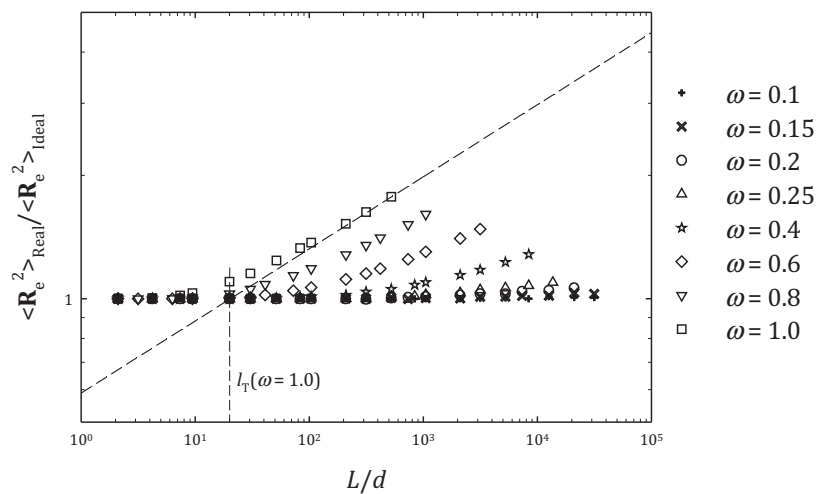
Figure 4.30: The ratio of squared end to end distance of real chain to that of an ideal chain as a function of L/d for various local flexibilities as indicated in the figure. The dashed line has a slope $2\nu - 1$.
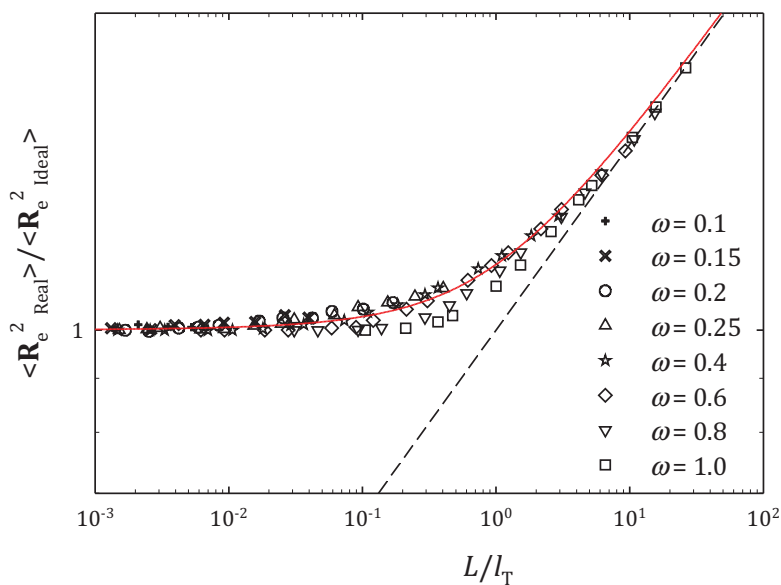

Figure 4.31: Same data as in figure 4.30 but as a function of the rescaled parameter L/l_T. The dashed guiding line has a slope of 0.176 and the red curve is from equation 4.53 with $a = 0.25$.

it behaves as an ideal chain and when $L \gg l_{\mathrm{T}}$, it becomes a swollen chain. This crossover could only be distinguished when l_1 is large enough.

For $L \gg l_{\mathrm{T}}$, using the thermal blob concept, and identifying b with l_1, we can write

$$\langle \mathbf{R}_{\mathrm{e}}^2 \rangle \sim \left(\frac{L}{l_{\mathrm{T}}} \right)^{2\nu} \cdot l_{\mathrm{T}} \cdot l_1 \tag{4.52}$$

Figure 4.30 shows the ratio of the mean square end to end distance of a real chain to that of an ideal chain plotted as a function of L. We see that we are not able to reach the long chain limit for many ω. But, a deviation from the ideal behavior is visible for every ω under study. Due to insufficient data, we cannot use a direct shifting method on the asymptotic behavior to obtain the shift factor l_{T} (see figure 4.30). Hence we use another method as follows: We arbitrarily define $l_{\mathrm{T}}(\omega = 1.0)$ as the intersection of the swollen behavior and the ideal behavior for $\omega = 1.0$. Then the next lower ω curves is shifted in L such that it superimposes on to $\omega = 1.0$ curve for the largest values. This process is continued in the decreasing order of ω such that curves superimpose on previously shifted ones for largest L values and the shift factor is noted. These relative shift factors when multiplied by the defined $l_{\mathrm{T}}(\omega = 1.0)$ gives the l_{T} for the corresponding ω. This shifting process is based on the assumption that a valid universal behavior exists in the WLC limit. This assumption gives the ratio of the end to end distances to be a universal function of L/l_{T} giving a value of 1 for $L/l_{\mathrm{T}} \ll 1$ and giving the Flory's scaling behavior when $L/l_{\mathrm{T}} \gg 1$. The final shifted plot clearly shows that it is possible to create a master curve (figure 4.31). However, for larger ω, curves does not superimpose exactly. A rough analytical description of this kind of crossover could be achieved using the following phenomenological equation

$$\frac{\langle \mathbf{R}_{\mathrm{e\text{-}real}}^2 \rangle}{\langle \mathbf{R}_{\mathrm{e\text{-}ideal}}^2 \rangle} = [1 + a \cdot (L/l_{\mathrm{T}})^{0.5} + (L/l_{\mathrm{T}})]^{2\nu - 1} \tag{4.53}$$

where the parameter a controls the smoothness of the crossover. If we plot the shift parameter l_{T} as a function of l_1 (figure 4.32), we see that we are able to recover the relation 4.51, confirming the presence of a crossover and in accord with the predictions.

We recall that in the case of bottle brush polymers, the intermediate ideal behavior is not visible. This is because the effective l_1/l_{b} could not be varied and hence the model never reaches a condition close to WLC. Thus, we will see a direct crossover from ideal regime to swollen regime [115].
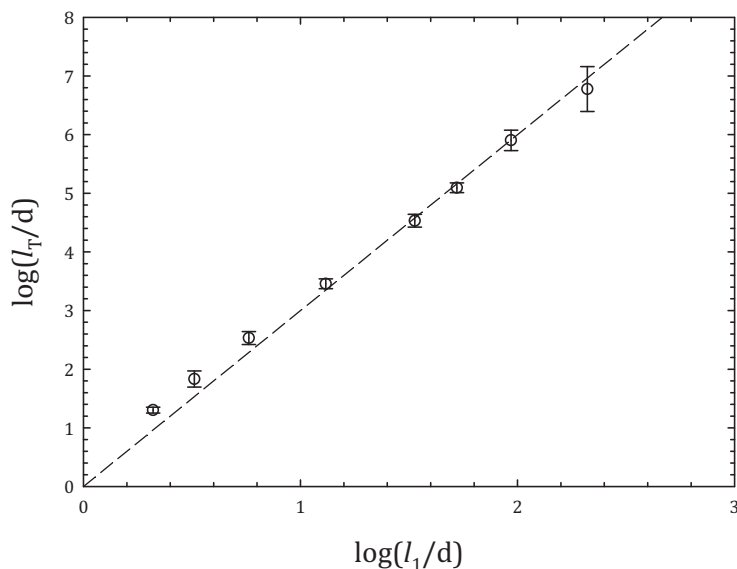
Figure 4.32:   Logarithm of the shift factor l_T/d plotted against logarithm of l_1/d. The dashed line has a slope of 3.

4.4   Dynamic properties of a single polymer chain

In this section, we present theoretical behaviors in the beginning. After, the data treatment method will be explained, followed by the limitations we have faced and finally, results from our study.

4.4.1   Theory

Rouse model is the first molecular model developed to study the dynamics of an ideal polymer chain in dilute regime. The model assumes m beads connected using springs of root mean square length l_b with each bead having a friction coefficient ζ. It is assumed that there is neither hydrodynamic interactions nor excluded volume interactions. From Einstein's relation, we know that the translational diffusion coefficient is inversely proportional to the friction coefficient. For an ideal polymer chain, the total friction felt is the sum of the friction felt by individual monomers. This gives

$$D_m^T = \frac{k_B \cdot T}{m \cdot \zeta} = \frac{D_1^T}{m} \tag{4.54}$$

A polymer chain diffuses a distance comparable to its size during a characteristic time called Rouse time τ_R given by

$$\tau_R \propto \frac{\mathbf{R}_e^2}{D_m^T} \tag{4.55}$$

At times smaller than the Rouse time, chain shows viscoelastic vibration modes and at longer time and the motion becomes simply diffusive. Using Flory's scaling

law for ideal chain, this relation becomes

$$\tau_R \propto t_0 \cdot m^2 \tag{4.56}$$

where, t_0 is the time taken by a free monomer to diffuse a distance of its square diameter (d^2). For polymer chains with excluded volume interactions (like our model), it is approximated that the relaxation behavior is homeomorphic to that of the Rouse model [120]. This relation holds as far as the time scale considered is larger than the relaxation time of a single bond. From equation 4.55 we get

$$\tau_R \propto t_0 \cdot m^{1+2\nu} \tag{4.57}$$

The rotational motion of a polymer chain is characterized using the time correlation of the end to end vector. For a rigid beaded rod, only a single relaxation mode exists and the rotational diffusion coefficient is given as [82]

$$D_m^R = \frac{4 \cdot k_B \cdot T}{\pi \cdot \eta \cdot L^3} \tag{4.58}$$

This implies that rotational relaxation time is proportional to m^3 (since in this case $L = m \cdot l\langle b \rangle$). This relaxation is similar to the orientational decorrelation of spin vectors, as explained in section 3.4 and could be expressed as an exponential decay with a single relation time. As the chain becomes flexible, more vibration modes appear and the relaxation becomes complex. Panja and Barkema [121] have proposed an analytical expression for the mode amplitude correlation function for long fully flexible real chains in a good solvent, leading to

$$C(t) = \frac{1}{\sum_p \frac{1}{p^{1+2\nu}}} \cdot \sum_p \frac{1}{p^{1+2\nu}} \cdot \exp\left(\frac{-t \cdot p^{1+2\nu}}{\tau_{max}}\right) \tag{4.59}$$

where, $p = 1, 3, 5, \cdots$, with

$$\tau_{max} \propto m^{(1+2\nu)} \tag{4.60}$$

and for ideal cases when $\nu = 0.5$, this equation reduces to the classical Rouse equation. This function is the sum of many terms but the coefficient of terms decreases rapidly with p. For $t \gg \tau_{max}$, this complex function $C(t)$ could be approximately seen to be decreasing exponentially with a single longest relaxation time τ_{max} called rotational relaxation time. We can define a rotational diffusion coefficient $D_m^R \propto 1/\tau_{max}$. The validity of this assumption could be seen in figure 4.33, where we compare the theoretical equation above with a single exponential. Terms up to $p = 13$ were used in the sum for making the plot, after which they appear to be negligible. To differentiate the closeness of the data points, the ratio between the two curves is plotted. This curve shows that soon after τ_{max}, the ratio $C(t)/\exp(-t/\tau_{max})$ becomes a constant. This means that

$$\boxed{C(t) \propto \exp(-t/\tau_{max}) \qquad , t \gg \tau_{max}} \tag{4.61}$$

It can be noted that the rotational relaxation time is having the same scaling as that of the time required for the chain to move its own size ($\tau_{max} \sim \tau_R$).
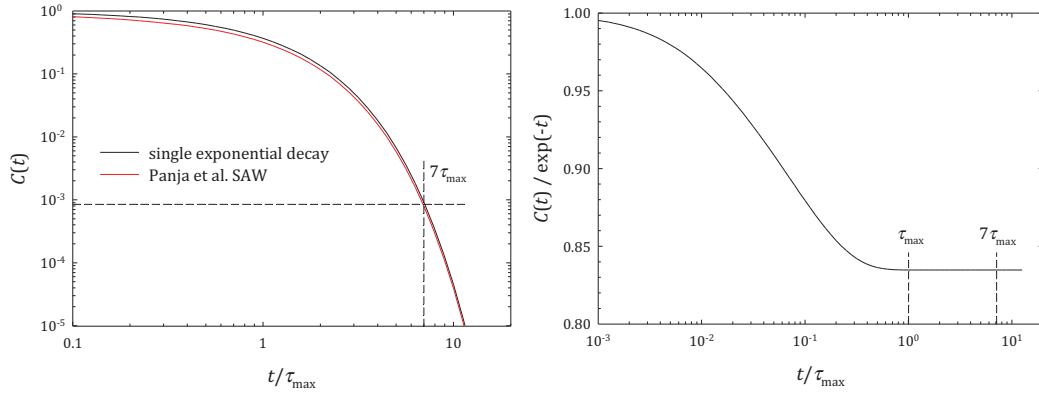
Figure 4.33: (left) End to end relaxation function from the theoretical equation given by Panja et al. [121] (red) and a single exponential (black) and (right) the ratio between the two curves. Note the behavior of the ratio at $t/\tau_{\max} > 1$.
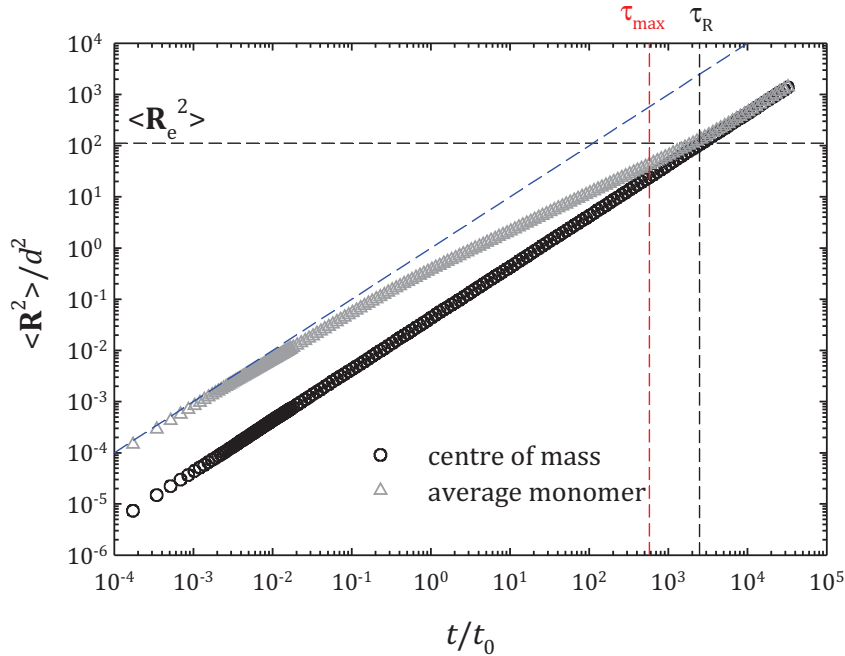

Figure 4.34: The behavior of MSD of the center of mass of a chain and that of an average monomer for a chain of $m = 20$, $\omega = 1.0$ and $s_{\mathrm{T}} \approx 0.0132$. The blue dashed line has a slope 1 and gives the MSD of a free monomer. The value $\tau_{\max}$ is the longest rotational relaxation time obtained by fitting the decorrelation of the end-to-end vector using REPES algorithm [122] (see text).

4.4.2 Data processing

To study the dynamical behavior of a single real polymer chain, simulations were carried out for various m, ω and s_T. During simulation, the reduced MSD of an average monomer in the chain and that of the center of mass of a chain are monitored as a function of the reduced time t/t_0. The behavior of the MSD is shown in figure 4.34. The MSD of center of mass follows a linear behavior from very short time, while an average monomer moves freely until the constraints are felt (the cone angle ω and ε_1) and later merges with the behavior of the center of mass. Note that the merging occurs when MSD is equivalent to the squared size of the chain, giving τ_R. Knowing MSD, the translational diffusion coefficient of a chain of size m, $D_m^\mathrm{T}/D_1^\mathrm{T}$ could be easily calculated by dividing MSD by t/t_0. Refer image 4.35 for the variation of apparent diffusion coefficient with time. The average value of $D_m^\mathrm{T}/D_1^\mathrm{T}$ over time is taken as the translational diffusion coefficient of the specific system under consideration. Also, note the position of τ_R obtained from figure 4.34. In this figure, we do not recover the short time behavior of an average monomer. This is due to the usage of large s_T. The short time behavior will be clearly seen as $s_\mathrm{T} \to 0$, where this simulation method becomes ideal. The effect of s_T will be discussed in the next section.

From the time relaxation of the normalized end-to-end vector $C(t)$, the distribution of the relaxation time was extracted by fitting the curve using the REPES algorithm [122]. In this method, $C(t)$ is considered to be a sum of several relaxations and could be represented as

$$C(t) = \int A(\tau) \cdot \exp(-t/\tau) d\tau \tag{4.62}$$

In this algorithm, a regularized inverse Laplace transform of $C(t)$ is carried out, which is mathematically ill-conditioned [123] and very sensitive to noise data [124]. The relaxation time distribution is obtained as a discrete set of points on a logarithmic time scale. An example is shown in figure 4.36. The different peaks correspond to different relaxation times for different modes of relaxation. From the distribution, the longest relaxation time is taken to be τ_max/t_0.

To obtain reasonable values for the longest relaxation as a single exponential, we need to let the system evolve for very long time. Around 7 times τ_max/t_0 leads to $C(t)$ of the order of 10^{-3}. This appears to be a good precision for the REPES processing to obtain τ_max/t_0 within acceptable error range.

4.4.3 Finite size effects and limitations

For a Brownian system, the step size should be very small compared to the constraints of the system under study, to obtain good dynamics. We cannot use a very large step size as this will result in an increased number of motion rejections. However, using a very small value of step size will cause the simulation to be slowed down (see equation 3.21). So, some compromise has to be made with the s_T to
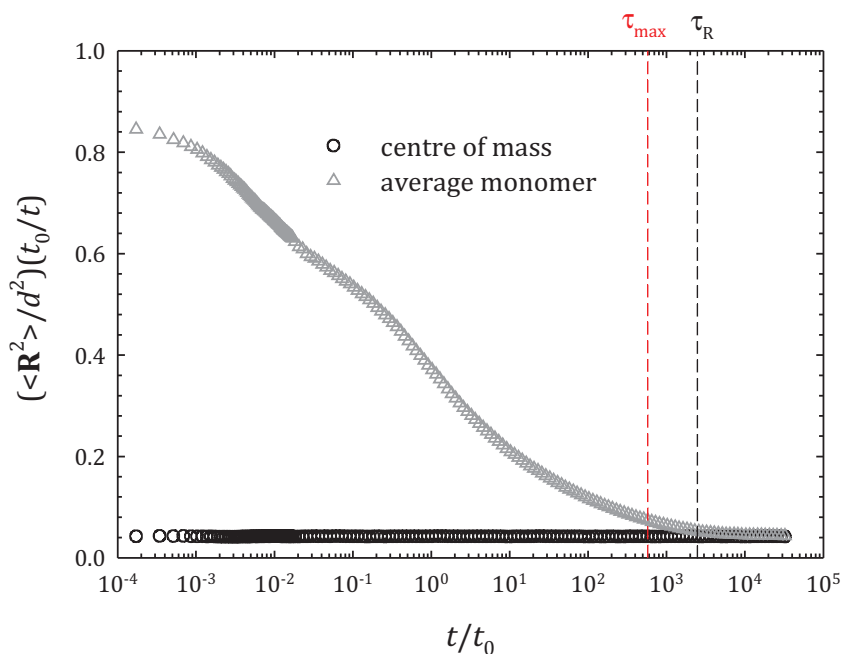
Figure 4.35: The behavior of the apparent diffusion coefficient of the center of mass of a chain and that of a monomer for a chain of $m = 20$, $\omega = 1.0$ and $s_T \approx 0.0132$. τ_R is taken from figure 4.34. The value τ_{max} is the longest rotational relaxation time obtained by fitting the time correlation of end-to-end vector using REPES algorithm [122] (see text).
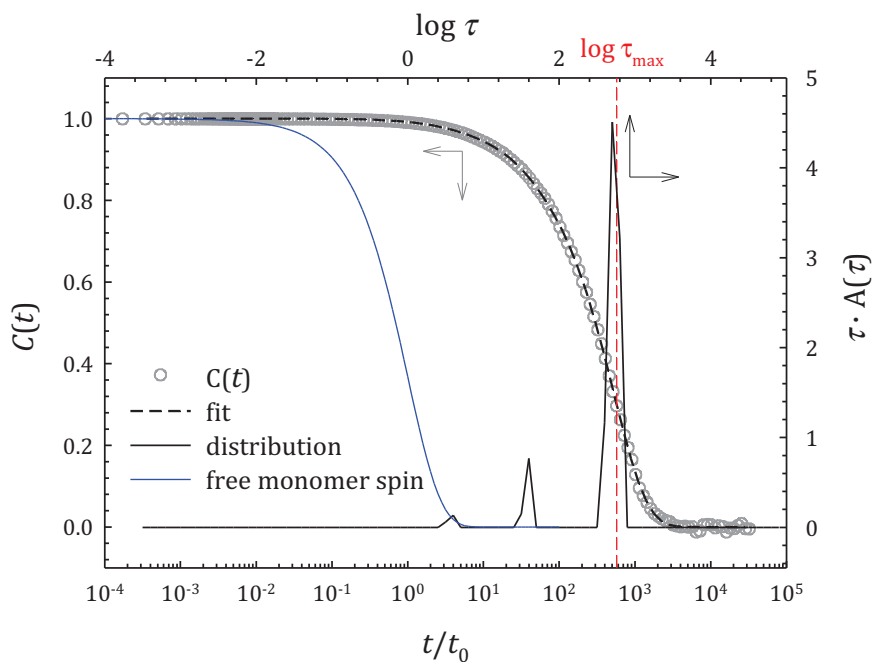

Figure 4.36:   Example of a end to end vector relaxation function $C(t)$ superimposed with the corresponding relaxation time distribution $A(\tau)$ obtained by REPES algorithm. For this example, $m = 20$, $\omega = 1.0$ and $s_R \approx 0.0186$.

get good results in a reasonable amount of time. Figure 4.37 shows an example of the calculated translational and rotational diffusion coefficients as a function of the step size. We find that with the increase in s_T, we underestimate the values of both diffusion coefficients. We see from the figure (in log scale) that $s_\text{T} \to 0$ condition exists and gives a finite value for diffusion coefficients. So, we linearly extrapolate the diffusion coefficients to $s_\text{T} \to 0$. This method only works for the polymer chains, where m is always fixed. In the case of aggregating systems, this method becomes impossible due to the large amount of time required for running one simulation. We know from previous works in the group that for irreversibly aggregating spheres, the step size should be at least 3 times smaller than the average surface to surface distance to the first neighbor $d \cdot (\Delta - 1)$ of interacting particles [125]. $d \cdot \Delta$ is the average distance to the first neighbor in a random distribution of hard spheres at a given volume fraction, which is the starting point in the aggregation studies. In our case, we have the constraints ϕ, ε_1 and ω. We select a step size such that it gives a maximum error within 10% of the asymptotic values of diffusion coefficients. We find that this choice requires

$$\boxed{s_\text{T}/d < \varepsilon_1/5, \; s_\text{R}/d < \omega/10 \text{ and } s_\text{T}/d < (\Delta - 1)/3} \tag{4.63}$$

and ensures a Brownian behavior within the interaction volume and in between collisions.

For the polymer chains, a set of simulations were carried out for different values of s_T and the extrapolated quantities at $s_\text{T} \to 0$ are taken as the calculated properties of the system. Combining the various limitations - step size, the range of relaxation time to be covered in the simulation and the size of the chain - we were able to study only up to $m = 20$ for the rotational dynamics.
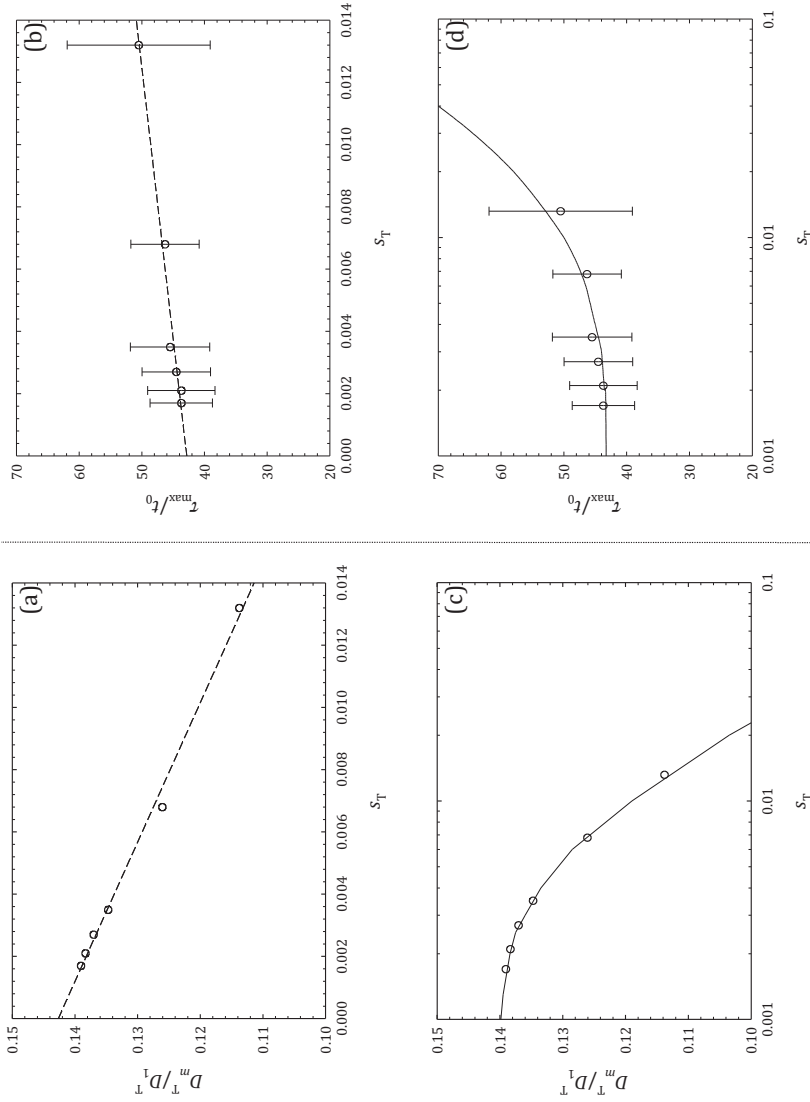
Figure 4.37: (Left)Evolution of translational diffusion coefficient of a polymer chain with $m = 7$, $\omega = 0.2$ as a function of Brownian step size in (a) linear and (c) in logarithmic scales. (Right) Evolution of the longest relaxation time of a polymer chain with $m = 5$, $\omega = 0.2$ as a function of the Brownian step size (b) linear and (d) in logarithmic scales. We consider the asymptotic values of the measurements as $s_T \to 0$ to be the measurements of the system. The dotted lines are linear extrapolations and the solid curves are the guides to the eye.

4.4.4 Results

First we study the behavior of average chain dimension with time. In figure 4.38, we plot $\langle \mathbf{R}_e^2 \rangle$ as a function of t/t_0. From the figure, we see that there is no apparent change in values, meaning that in average, the chains are at equilibrium from the beginning. As we see in 4.35, we do not have to wait for large time to get $D_m^{\mathrm{T}}/D_1^{\mathrm{T}}$, we can calculate diffusion coefficient for chains up to $m = 80$.
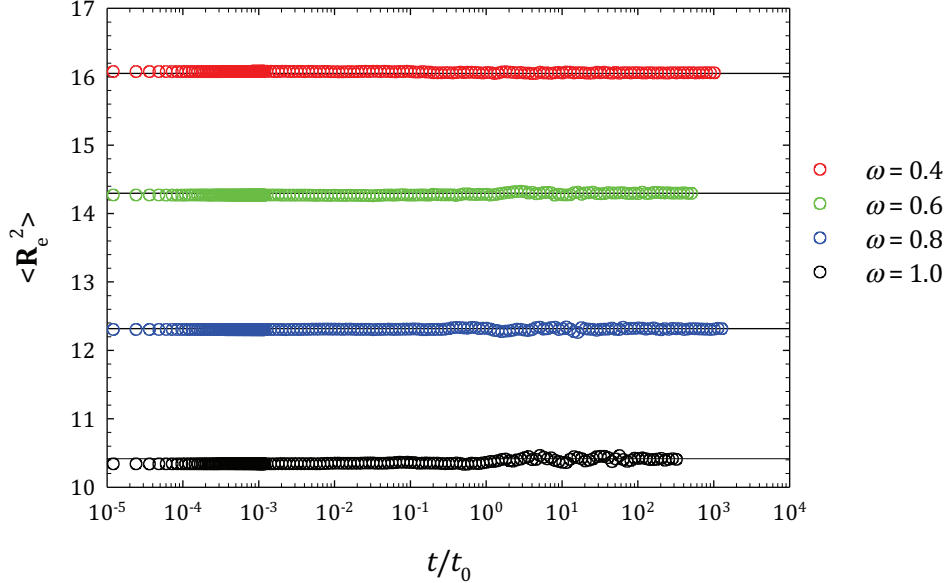

Figure 4.38: The evolution of $\langle \mathbf{R}_e^2 \rangle$ as a function of time for $m = 5$ and various ω as indicated in the figure. The black straight lines indicate corresponding values obtained from static property measurements at $t/t_0 = 0$.

We study the effect of ω and chain length on the diffusion coefficient of G in figure 4.39. We find that for any given m, the value of $D_m^{\mathrm{T}}/D_1^{\mathrm{T}}$ is independent of ω. This means that

the motion of G is insensitive to the local flexibility of the chain.

This is expected, since equation 4.54 does not show any dependency on local flexibility. This ω independent value of $D_m^{\mathrm{T}}/D_1^{\mathrm{T}}$ is taken and plotted as a function of m in figure 4.40. We recover the theoretical prediction from 4.54 implying correct translational dynamics of the model when no hydrodynamic interactions are considered.

Figure 4.41 shows the effects of ω on $\tau_{\max}$. We have seen previously in figure 4.37 that the obtained $\tau_{\max}$ are having a large error margin, but on log scale these error bars become small compared to the symbol size and hence is not shown in the plots. We see that for a given chain length, the rotational relaxation time highly depends on the local flexibility. For a given mass, as the $\omega \to 0$, $\tau_{\max}$ increases very rapidly. For higher ω, the relaxation time lowers, indicating that the chain relaxes
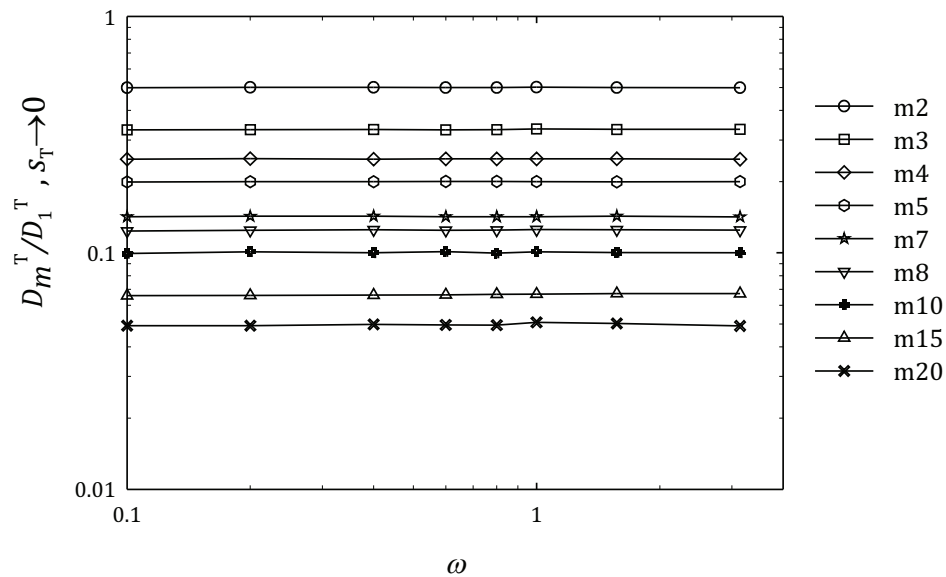
Figure 4.39: Asymptotic values for D_m^{T} as $s_{\mathrm{T}} \to 0$ plotted against ω for various m as indicated in the figure.
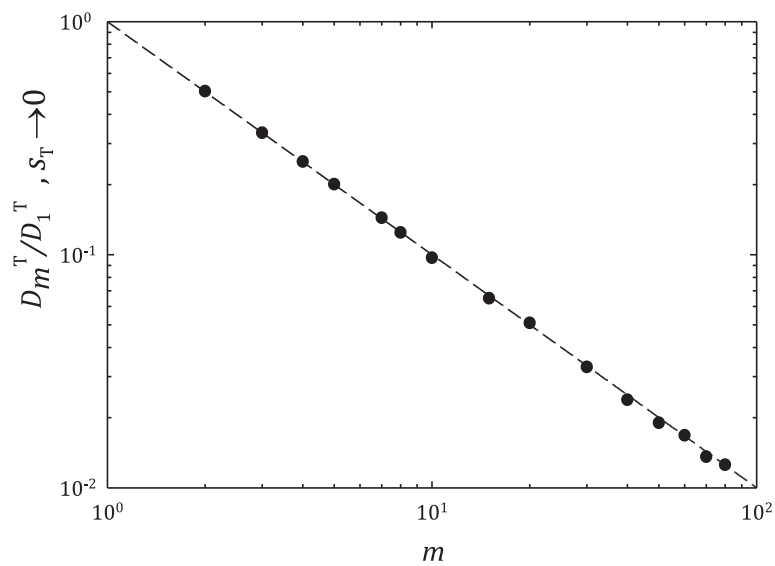

Figure 4.40: The asymptotic behavior of $D_m^{\mathrm{T}}/D_1^{\mathrm{T}}$ plotted against m. Dashed line is the function $1/m$.
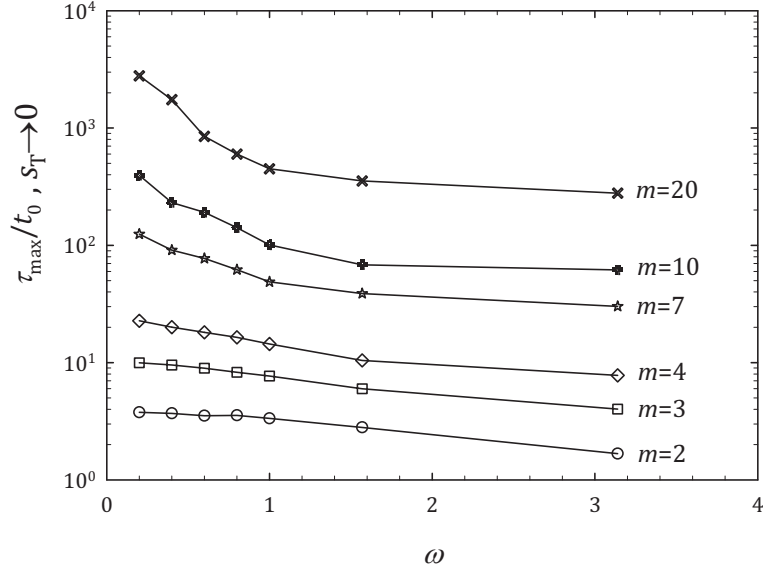
Figure 4.41: Asymptotic values of $\tau_{\max}$ plotted as a function of ω for various chain lengths as indicated in the figure.

faster due to its increased flexibility.

Comparing 4.58 with Einstein's relation as explained in section 3.4, $D_1^{\mathrm{R}} = \frac{k_{\mathrm{B}} \cdot T}{\pi \cdot \eta \cdot d^3}$, we get $D_m^{\mathrm{R}}/D_1^{\mathrm{R}} \propto 1/m^3$ for a rigid beaded rod. This implies a constant value for $(\tau_{\max}/t_0)/m^3$. For flexible chains, since $\tau_{\max}/t_0$ scales as $m^{2\nu+1}$ (see section 4.4.1), we get

$$(\tau_{\max}/t_0)/m^3 \propto m^{2\nu-2} \tag{4.64}$$

Thus, if we plot $(\tau_{\max}/t_0)/m^3$ as a function of L, we should get a plateau till the length reaches the persistence length, after which it follows the scaling behavior. This implies that these curves could be rescaled using $X = L/l_1$, which determines the rod-like limit. These rescaled curves are plotted in figure 4.42. We see that the curve for locally rigid chain shows the initial plateau like behavior. Also, the deviation from rod like behavior is seen for more locally flexible curves. As the chain grows longer, according to the thermal blob concept, there are two possible behaviors:

1. Chains with very high local flexibility directly tends to follow the swollen chain behavior, giving a slope $2\nu - 2$, with $\nu = 0.588$.

2. Chains with very low flexibility tends to follow the ideal chain behavior initially, giving a slope of -1. After the thermal blob contour length is reached, it deviates to the swollen behavior as in the previous case.

In our results, we cannot distinguish the two behaviors since the chains are too short, but we see that all the results are within both limits.
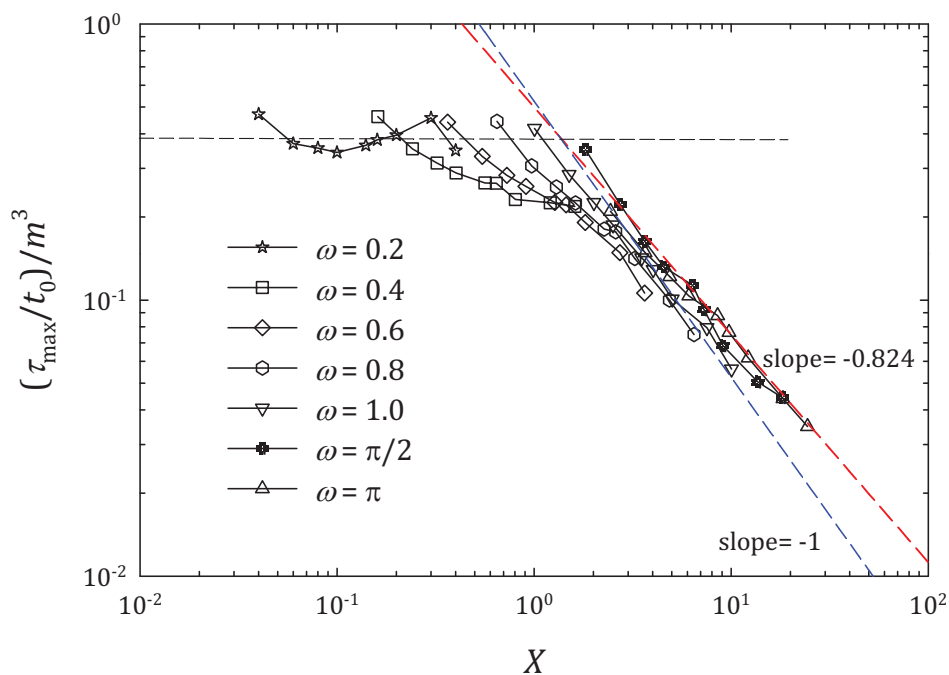
Figure 4.42: Variation of $(\tau_{\max}/t_0)/m^3$ as a function of X for various local flexibility as indicated in the figure. Dashed lines show the expected theoretical slopes in the real (red) and ideal (blue) cases.

4.5   General conclusions

In this chapter, we used patchy particle system combined with a modified version of the Brownian cluster Dynamics algorithm to study static and dynamic properties of a single polymer chain. Using this method, we were able to recover theoretical predictions within statistical errors and we see that this model gives a more realistic description of polymer chains. The results of static property study could be summarized in the figure 4.43. For both real and ideal semi flexible chains, there exists a persistence length l_1 below which they show a rigid-rod behavior with $\langle \mathbf{R}_e^2 \rangle \propto m^2$. For length greater than l_1 the behavior changes and for ideal chain, we have $\langle \mathbf{R}_e^2 \rangle \propto m$. This crossing over from rod like behavior to flexible behavior occurs at Kuhn length l_K. A real chain with length scale below l_T acts like an ideal chain. As soon as the length is increased beyond l_T, excluded volume effects show up and the chain starts to behave like a real chain with $\langle \mathbf{R}_e^2 \rangle \propto m^{2\nu}$. Dynamical properties of single polymer chains were also investigated in detail. We were able to recover expected results in the case of translational and rotational dynamics confirming the validity of our model and method. At $t \gg \tau_{\max}$ the rotational relaxation follows an exponential decay with a single relaxation time. At short time scales, the lower fast modes of vibration come in to interest, which defines the initial decay behavior. $C(t)$ is a bound function, which varies from a single exponential decay for
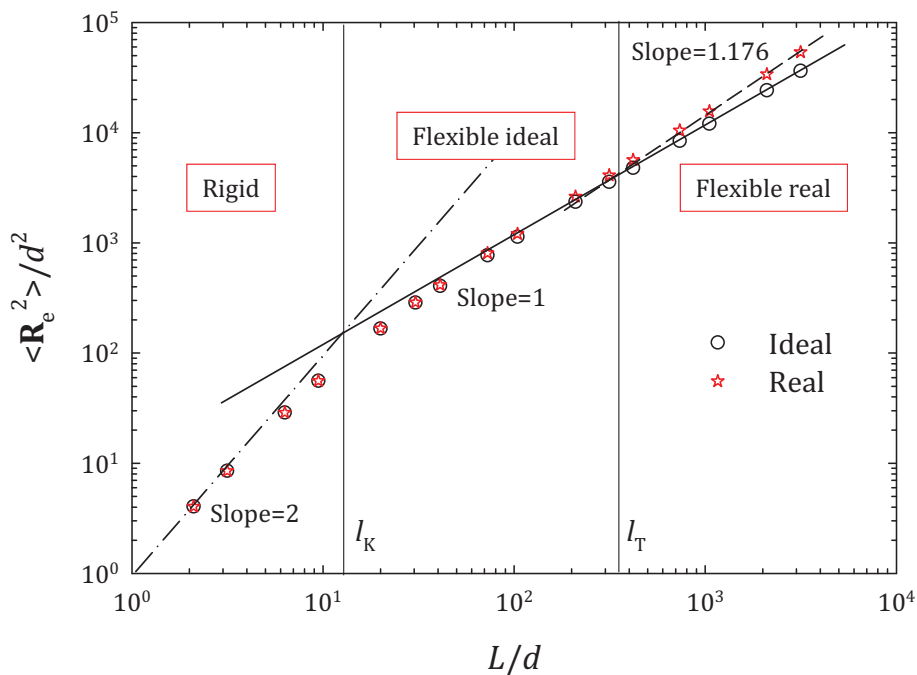
Figure 4.43: Different length scales present in a semi flexible polymer ($\omega = 0.6$) chain for real and ideal models. The different guiding lines have the theoretical slopes for the different length regimes.
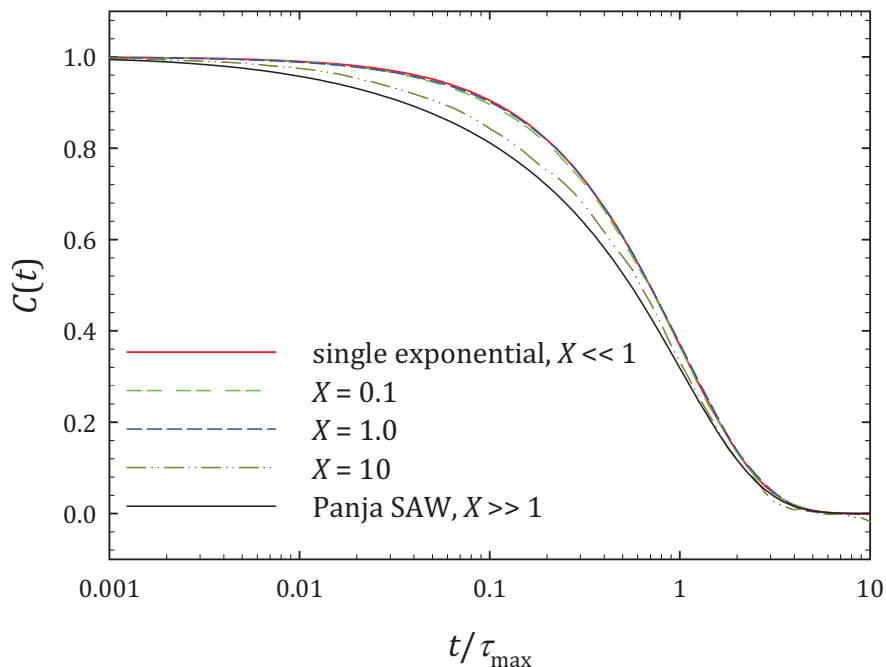

Figure 4.44: Rescaled end to end relaxation function as a function of $t/\tau_{\max}$ for various X values as indicated in the figure plotted together with the theoretical equation given by Panja et al. [121] and a single exponential decay with a single relaxation time $\tau_{\max}$.

rigid rods to the behavior suggested by Panja et al. for fully flexible chains. Figure 4.44 shows the rescaled curves for chains with different flexibility and we see that all of them are perfectly within the bounds. In the initial part, they are different as expected, but converge to the exponential decay for large time. From the study of effect of step size, we were able to extract optimum input values for s_T to be used further (for polymerization), so that correct dynamics is recovered within 10% error.

Kinetics of patchy aggregation

5.1 Intoduction: Smoluchowski aggregation

In solution, colloidal particles undergo Brownian motion and can form irreversible bonds on collision. In the limit of very dilute solutions, von Smoluchowski [38] calculated the rate of binary collisions that lead to the formation of dimers in terms of the flux of particles about an immobile particle/point (see figure 5.1). The immobile point is set to be at the origin and the particle density around it is isotropic. The dilute regime ensures independence between collisions, absence of ternary collisions and guarantees Brownian behavior between collisions. In the original derivation, particles move freely in the medium until they reach a certain capture radius $R_{col,i}$ around the immobile particle/point. At the capture radius, we consider that a dimer is formed and is immediately removed from the system. The idea is to find the number of particles that reach the capture radius in a given time. The isotropic nature of this model reduces it to a one dimensional problem which depends only on the distance of the moving particle from the origin r and time t. The other essential parameters and results from von Smoluchowski are as follows:

At time $t = 0$, particles are uniformly distributed in space and the number density is denoted as C_0. $C_1(r,t)$ is the number density of particles at a distance r from the origin at time t. D_1^{T} is the translational diffusion coefficient of a free particle in the medium. Using spherical coordinates and isotropic nature, Fick's equation of diffusion (Fick's second law) can be written as

$$\frac{\partial(r \cdot C_1(r,t))}{\partial t} = D_1^{\mathrm{T}} \cdot \frac{\partial^2(r \cdot C_1(r,t))}{\partial r^2} \tag{5.1}$$

It satisfies the following boundary conditions

$$C_1(r,t) = C_0 \text{ when } t = 0,\, r > R_{col,1} \tag{5.2}$$

$$C_1(r,t) = 0 \text{ when } t > 0,\, r = R_{col,1} \tag{5.3}$$

The solution under these boundary conditions is given as

$$C_1(r,t) = C_0 \cdot \left[1 - \frac{R_{col,1}}{r} + \frac{2 \cdot R_{col,1}}{r \cdot \sqrt{\pi}} \cdot \int_0^{\frac{1}{2} \cdot \frac{r - R_{col,1}}{\sqrt{D_1^{\mathrm{T}} \cdot t}}} \exp(-x^2) \cdot \mathrm{d}x \right] \tag{5.4}$$
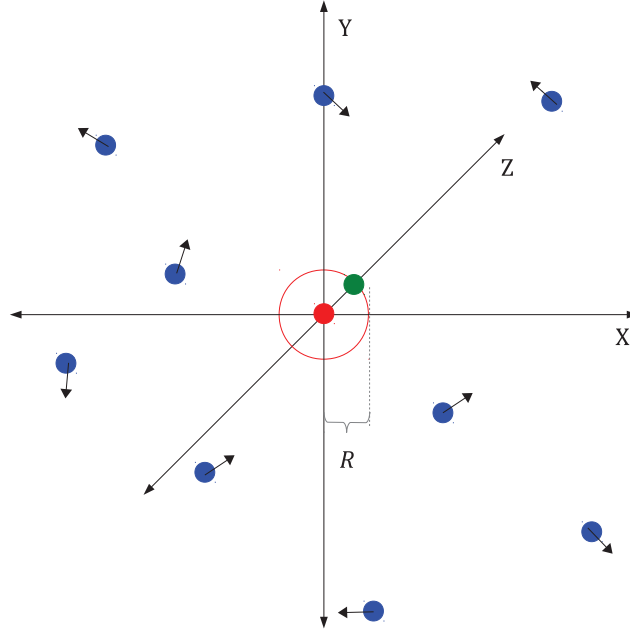
Figure 5.1: Schematic of Smoluchowski's model. The central red particle is immobile and the green particle just reached the capture radius $R_{col,1}$, denoted by the red circle to form a dimer. Blue particles are mobile and show Brownian motion.

Using Fick's first law of diffusion, we can calculate the rate at which particles arrive at the surface of the sphere with radius R as

$$4 \cdot \pi \cdot D_1^{\mathrm{T}} \cdot \left(r^2 \cdot \frac{\partial C_1(r,t)}{\partial r} \right)_{r=R_{col,1}} = 4 \cdot \pi \cdot D_1^{\mathrm{T}} \cdot R_{col,1} \cdot C_0 \cdot \left[1 + \frac{R_{col,1}}{\sqrt{\pi \cdot D_1^{\mathrm{T}} \cdot t}} \right] \quad (5.5)$$

In reality, particles in a colloidal system are in a finite volume and we define C_0 to be the initial concentration of the system with ϕ the total volume fraction of particles. $C_1(t)$ is the number density of the unreacted particles in the volume at time t. Moreover, all colloidal particles are equivalent and hence any particle can react with any other one forming a dimer. The relative diffusion coefficient between two particles is simply the sum of the individual diffusion coefficients. Under these conditions, integrating equation 5.5 over time gives the total number of reacted particles at any time t and we have

$$\frac{1}{C_1(t)} - \frac{1}{C_0} = 8 \cdot \pi \cdot D_1^{\mathrm{T}} \cdot R_{col,1} \cdot t \cdot \left(1 + \frac{2 \cdot R_{col,1}}{\sqrt{2 \cdot \pi \cdot D_1^{\mathrm{T}} \cdot t}} \right) \quad (5.6)$$

This mutual collision and bonding of two particles could be also considered from a kinetic point view with rate equation given by

$$\frac{\mathrm{d}C_1(t)}{\mathrm{d}t} = -K_{1,1} \cdot C_1^2(t) \quad (5.7)$$

where $K_{1,1}$ is the rate constant for the monomer-monomer reaction as introduced before in section 2.1.2. Integrating and applying the boundary condition that $C_1(t) = C_0$ at $t = 0$ gives

$$\frac{1}{C_1(t)} - \frac{1}{C_0} = \int_0^t K_{1,1} \cdot \mathrm{d}t \qquad (5.8)$$

Comparing equations 5.6 and 5.8, we get

$$\boxed{K_{1,1} = 8 \cdot \pi \cdot D_1^{\mathrm{T}} \cdot R_{col,1} \cdot \left(1 + \frac{R_{col,1}}{\sqrt{2 \cdot \pi \cdot D_1^{\mathrm{T}} \cdot t}}\right)} \qquad (5.9)$$

$K_{1,1}$ becomes independent of time as soon as $t \gg R_{col,1}^2/D_1^{\mathrm{T}}$.

Bimolecular reaction leading to the formation of dimers in dilute conditions corresponds to a DLCA process until a trimer is formed. For our patchy BCD model denoted by PBCD, this corresponds to a step polymerization with $\omega = \pi$ where each patch covers the entire surface and any collision results in double bond formation. Since no trimer is possible, simulations could be run for longer times unlike the DLCA case where larger clusters appear.

In our model, we form irreversible bonds at the square well interaction range, giving $R_{col,1} = d \cdot (1 + \varepsilon)$ where d is the particle diameter and ε the relative well width of the square well potential. Using our definition of time $t_0 = d^2/(6 \cdot D_1^{\mathrm{T}})$ we obtain

$$\frac{C_0}{C_1(t)} - 1 = 8 \cdot \phi \cdot (1 + \varepsilon) \cdot (t/t_0) \cdot \left(1 + (1 + \varepsilon) \cdot \sqrt{\frac{12}{\pi}} \cdot \frac{1}{\sqrt{(t/t_0)}}\right) \qquad (5.10)$$

which gives two limiting behaviors

$$\frac{C_0 - C_1(t)}{8 \cdot (1 + \varepsilon) \cdot \phi \cdot C_1(t)} = \begin{cases} \frac{t}{t_0} & \text{for } \frac{t}{t_0} \gg \frac{12(1+\varepsilon)^2}{\pi} \\ \sqrt{\frac{12}{\pi}} \cdot (1 + \varepsilon) \cdot \sqrt{\frac{t_0}{t}} & \text{for } \frac{t}{t_0} \ll \frac{12(1+\varepsilon)^2}{\pi} \end{cases} \qquad (5.11)$$

Figure 5.2 shows the comparison of our simulation results with the theoretical Smoluchowski equation (equation 5.10). We see that they are in very good agreement. As expected, curves for DLCA ends after a short time due to the formation of trimers, whereas the patchy model continues to larger times and shows the expected behavior all along the simulation.

5.2 Cluster-cluster aggregation

In section 2.1.2, we have already discussed Smoluchowski approach for the irreversible cluster-cluster aggregation. Using the constant kernel, which is a very
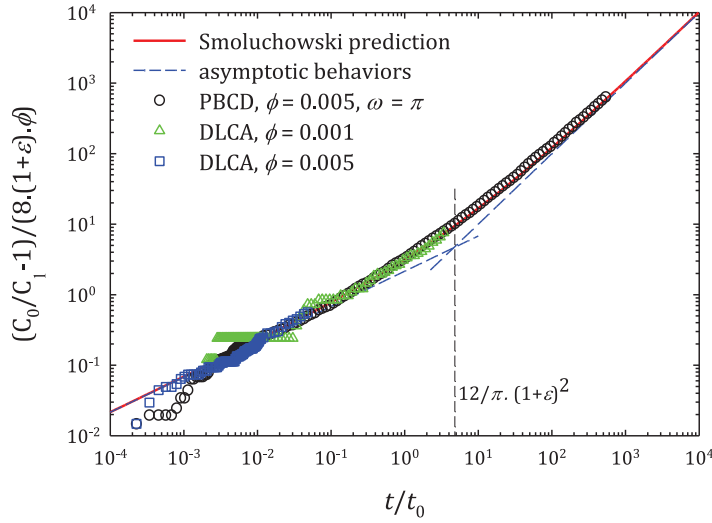
Figure 5.2: Comparison of Smoluchowski's theoretical prediction with results from DLCA and PBCD (with $\omega = \pi$) simulations as indicated in the figure.

strong hypothesis, we have the following expression for the weight average aggregation number

$$m_w = 1 + K_{1,1} \cdot C_0 \cdot t \qquad (5.12)$$

Substituting the value of $K_{1,1}$ from equation 5.9, we get

$$m_w - 1 = 8 \cdot \phi \cdot (1 + \varepsilon) \cdot (t/t_0) \cdot \left(1 + (1 + \varepsilon) \cdot \sqrt{\frac{12}{\pi}} \cdot \frac{1}{\sqrt{(t/t_0)}}\right) \qquad (5.13)$$

giving

$$m_w - 1 = 8 \cdot \phi \cdot (1 + \varepsilon) \cdot (t/t_0) \qquad , (t/t_0) \gg 12/\pi \cdot (1 + \varepsilon)^2 \qquad (5.14)$$

which is the generally used form of this relation in aggregation studies [101].

We monitor the evolution of m_w using the different BCD simulation models and using PBCD under dilute conditions. For the BCD method, there exist three different models, depending on the way clusters move (refer section 3.1 and [23] for details):

1. **BCD1** - displacement of a center of mass of the cluster is achieved by small random displacements of particles constituting the cluster - *slippery Rouse clusters* with diffusion coefficient of the center of mass inversely proportional to the aggregation number of the cluster

2. **BCD2** - clusters are rigid and their center of mass moves with a diffusion coefficient inversely proportional to a characteristic size of the cluster. There is no local motion of the individual monomers inside the cluster - *rigid Zimm clusters*
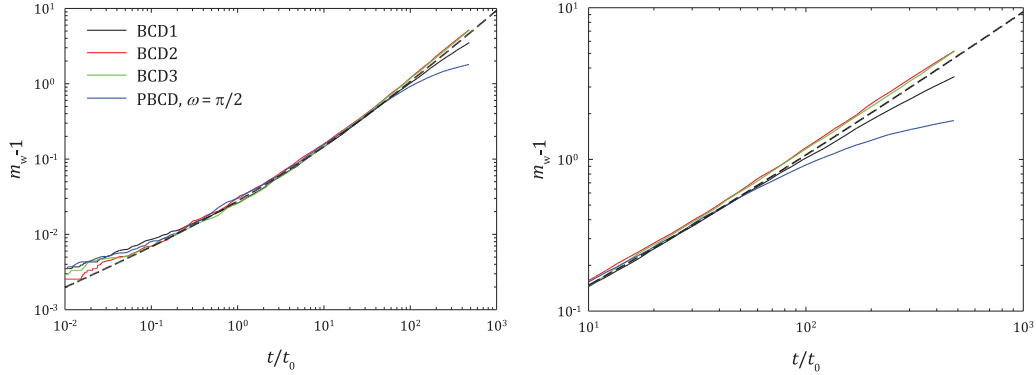
Figure 5.3: Comparison of Smoluchowski's theoretical prediction (thick black dashed curve) with results from various simulation methods as indicated in the figure (left).The same data zoomed to show the deviation at large times (right) $\phi = 0.005$ in all cases.

3. **BCD3** - BCD1 followed by BCD2 - *slippery Zimm clusters*. Note that the internal structure in this case is different from that of BCD2.

PBCD algorithm is designed to show *slippery Rouse dynamics*. To observe clusters larger than dimers, we need to use an $\omega \leq \pi/2$. In figure 5.3, we compare these different models with Smoluchowski's prediction. We see that expression 5.13 gives a very good description of all systems for short times. BCD2 and BCD3 follows the theoretical prediction all along, while BCD1 and PBCD shows deviations at larger time (see figure 5.3 (right)). Initially when there are only monomers, all these models are equivalent and hence behave similarly. As collisions involving larger clusters become important, diffusion slows down for BCD1 and PBCD (Rouse dynamics). But for PBCD, there is more than one reason for the deviation. Valency restriction prevents bond formation on already reacted patches, leading to unreactive collisions. Moreover, reactive ends of a chain can form loops. This is due to dilute conditions which favor intra-chain reactions. For the case $\omega = \pi/2$, mainly cyclic trimers are formed. All these reasons slow down PBCD kinetics.

5.3 Influence of valency restriction and surface coverage by the patch

In PBCD, the reactivity is restricted to monovalent opposite patches. The relative surface coverage of patches is termed as χ and is related to the patch cone angle $\omega \leq \pi/2$ as

$$\chi = 1 - \cos\omega \tag{5.15}$$

Reducing χ decreases the loop formation, but also increases the amount of unsuccessful collisions. The effect of χ is studied in figure 5.4. As expected, we see the rate of the reaction lowering with decreasing χ. Also, we see that the cyclization

decreases with χ and a linear scaling is obtained at large times for lower ω cases. For any two uncorrelated colliding monomers, the probability to have their reactive surface aligned is χ^2. So, as a first approximation we try to normalize the rate constant using χ^2, which gives

$$m_w - 1 = 8 \cdot \phi \cdot \chi^2 \cdot (1 + \varepsilon) \cdot (t/t_0) \cdot \left(1 + (1 + \varepsilon) \cdot \sqrt{\frac{12}{\pi}} \cdot \frac{1}{\sqrt{(t/t_0)}}\right) \qquad (5.16)$$

In figure 5.5, we see that χ does not seem to have such a strong influence (power 2) on the rate equation and this correction does not provide a good description of kinetics.
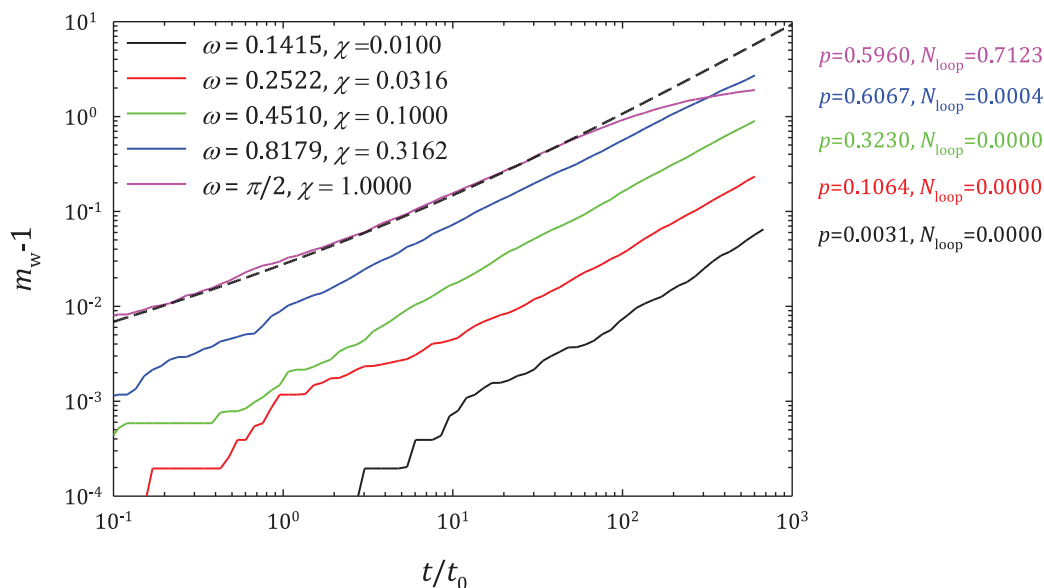

Figure 5.4: Comparison of Smoluchowski's theoretical prediction (thick black dashed curve) with results from PBCD with various χ as indicated in the figure. $\phi = 0.001$ in all cases. The extent of the reaction (p) and the fraction of monomers involved in loop (N_{loop}) at the final point on the curves is also given.

Dimerization reaction through patches

Cluster-cluster aggregation process and polymerization are complex reactions and the simple expression 5.12 assumes a strong hypothesis on kernels $K_{i,j}$. So , we restrict our study to the effect of χ on the simple case of dimerization. For this, the PBCD program has been modified to prevent further patchy aggregation of dimers. A series of simulations were run for various χ values under very dilute conditions ($\phi = 0.005$ in general). Values of ω are chosen equally spaced on a logarithmic scale of χ^2 and range from $\chi^2 = 1$ down to $\chi^2 = 10^{-4}$.
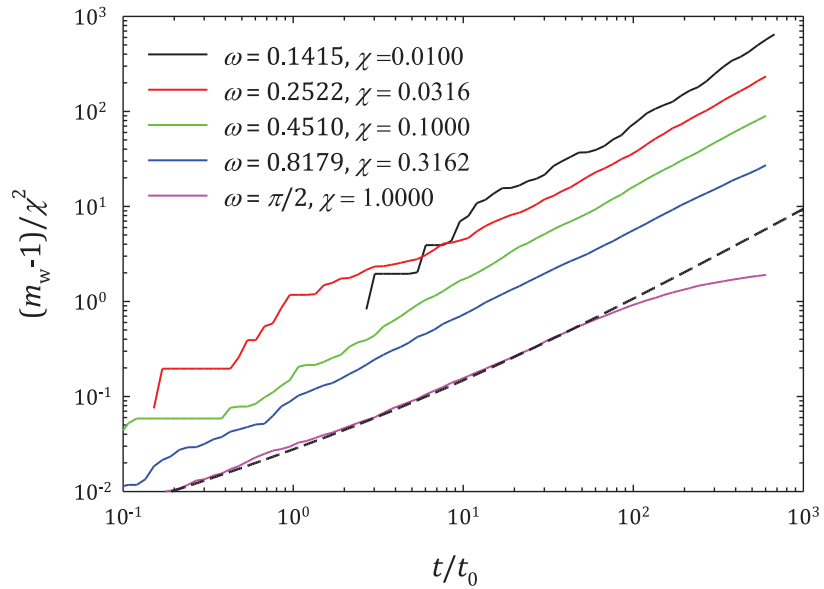
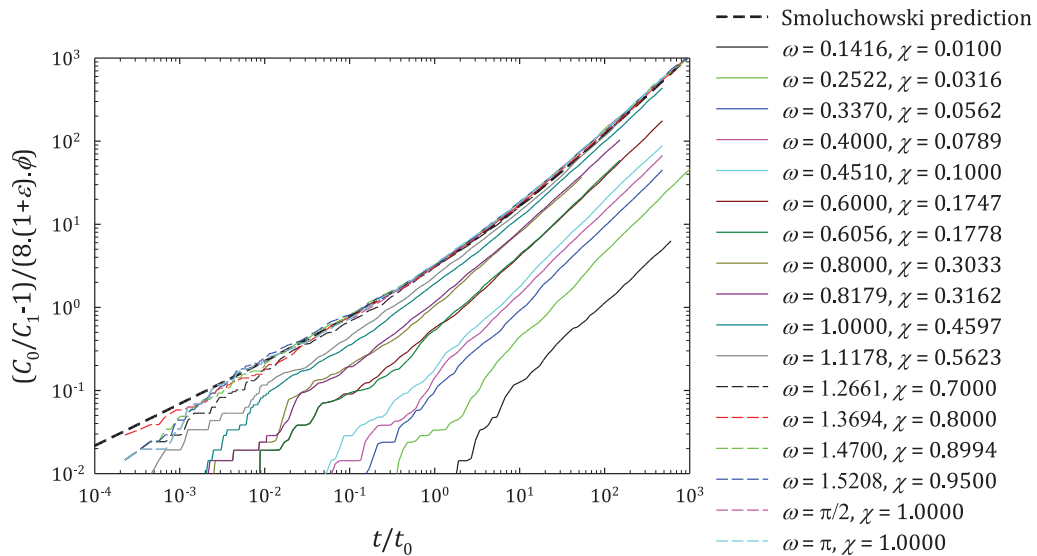Figure 5.5: Same data as in figure 5.4, but $m_w - 1$ is rescaled using χ^2.

Figure 5.6: Comparison of Smoluchowski's theoretical prediction (thick dashed black curve, from equation 5.10) with results from PBCD-dimerization with various χ as indicated in the figure.
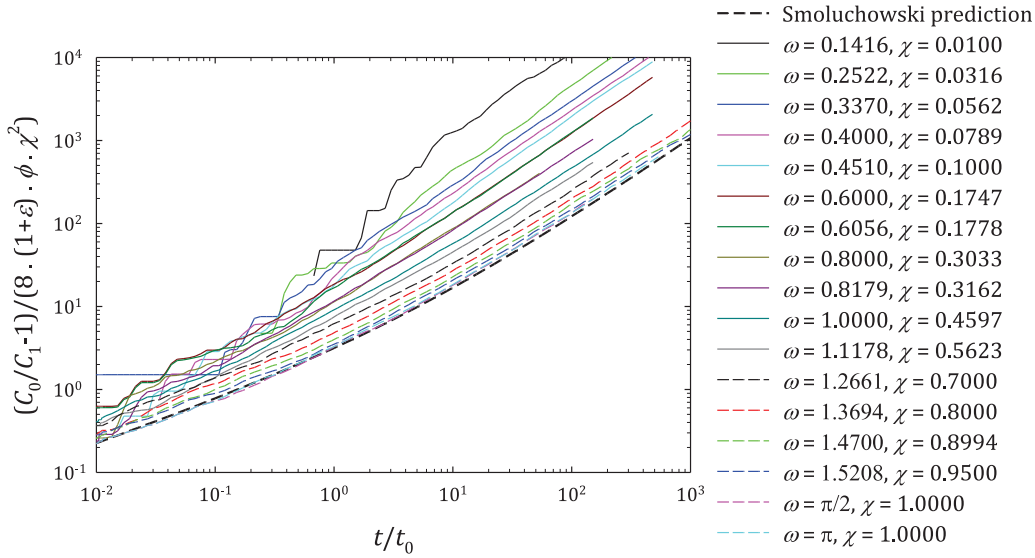
Figure 5.7: Same data as in figure 5.6, but rescaled using χ^2.

Figure 5.6 shows kinetics of dimerization for various χ. We see that at large time, a Smoluchowski like linear behavior is recovered. As in cluster-cluster aggregation, we tried to rescale equation 5.10 using χ^2, leading to

$$\frac{C_0}{C_1(t)} - 1 = 8 \cdot \phi \cdot (1+\varepsilon) \cdot (t/t_0) \cdot \left(1 + (1+\varepsilon) \cdot \sqrt{\frac{12}{\pi}} \cdot \frac{1}{\sqrt{(t/t_0)}}\right) \cdot \chi^2 \qquad (5.17)$$

From figure 5.7, we see that this rescaling is not valid and the real rate is higher than $\chi^2 \cdot K_{1,1}$ when $\chi \to 0$. But at very small time, all curves seem to merge on the Smoluchowski one. We will discuss about this later. Since χ^2 correction is too strong, we tried to rescale these curves using a different exponent for χ. In the limit $\chi \to 0$ and at large time, using $\chi^{1.23\pm0.02}$ (see figure 5.8) gives a good superimposition to form a limiting curve (different from Smoluchowski one). Under this condition, we define $k(\chi, t)$ as

$$\frac{C_0}{C_1(t)} - 1 = K_{1,1} \cdot C_0 \cdot \chi^{1.23} \cdot k(\chi, t) \cdot t \qquad (5.18)$$

which turns to be in our framework

$$\frac{C_0}{C_1(t)} - 1 = 8 \cdot \phi \cdot \chi^{1.23} \cdot k(\chi, t) \cdot (1+\varepsilon) \cdot (t/t_0) \cdot \left(1 + (1+\varepsilon) \cdot \sqrt{\frac{12}{\pi}} \cdot \frac{1}{\sqrt{(t/t_0)}}\right) \quad (5.19)$$

Evolution of $k(\chi, t)$ is shown in figure 5.9. First, we see that $k(\chi, t)$ reaches a constant plateau at large times different from the theoretical one ($k(1, \infty) = 1$). Secondly, this $k(\chi, \infty)$ becomes independent on χ as $\chi \to 0$. This limiting behavior is seen for $\chi < 0.2$. From figure 5.9, $k(\chi, \infty)$ for a given χ was noted and plotted as
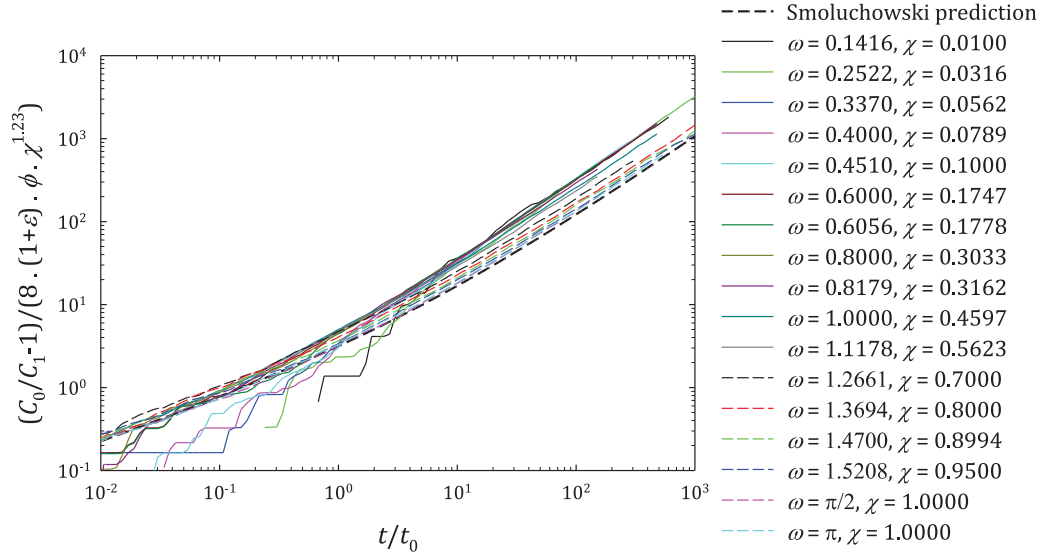
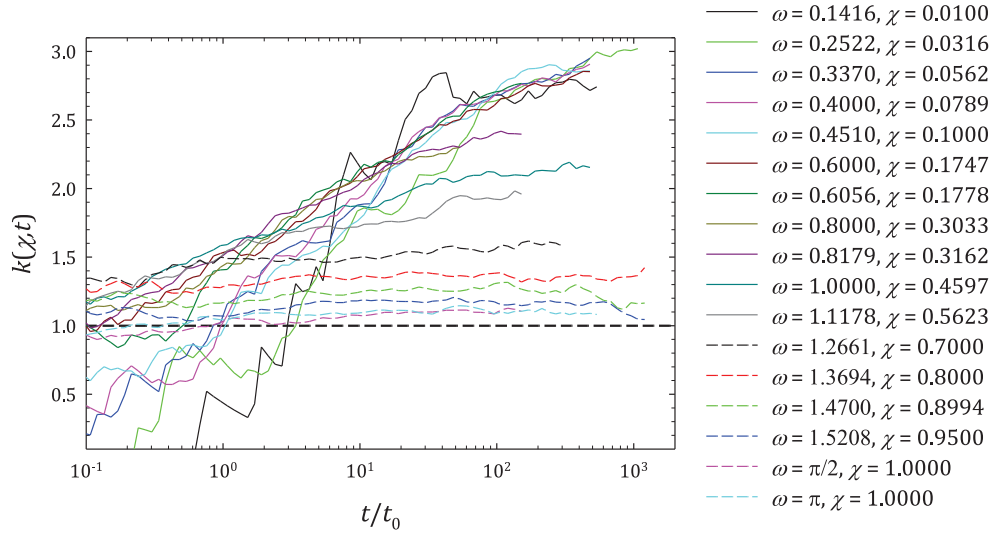Figure 5.8: Same data as in figure 5.6, but rescaled using $\chi^{1.23}$.

Figure 5.9: Evolution of $k(\chi, t)$ as a function of t/t_0 for various χ as indicated in the figure. The thick black dashed horizontal line corresponds to Smoluchowski behavior. $k(\chi, \infty)$ calculated from this data is plotted in figure 5.10. $\phi = 0.005$ in all cases.

a function of χ in figure 5.10. It is clearly seen that $k(\chi, \infty)$ becomes independent of χ in the limit $\chi \to 0$ and reaches a value close to 3. Also, we see that for $\chi = 1$, we get $k(1, \infty) \simeq 1.1$, which is different from the expected value of 1. Reason for this may be that $\phi = 0.005$ we used being probably not small enough. Theoretical behavior is only recovered in the limit of infinite dilution. See figure 8 in [101] where the same is observed. Theoretical behavior with good prefactor is recovered only for ϕ smaller than 5×10^{-4}.
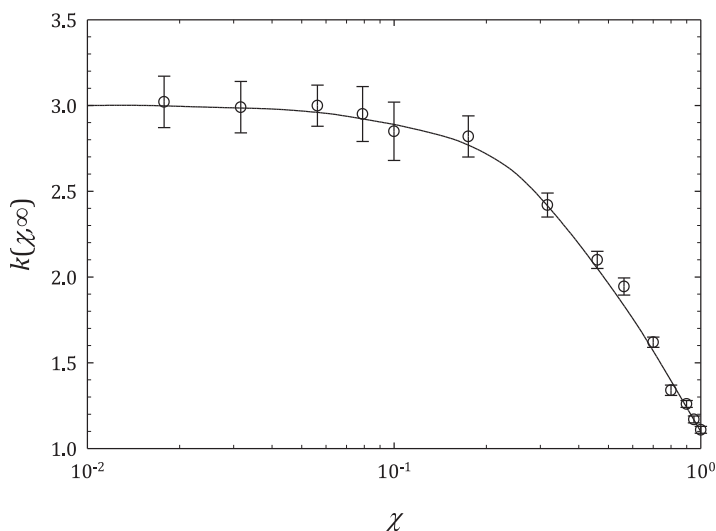

Figure 5.10: $k(\chi, \infty)$ at large time plotted as a function of χ. The solid curve is a guide to the eye.

This difference in reaction rate is attributed to inefficient collisions due to the decrease in reactive surface. In the original derivation by Smoluchowski, two uncorrelated colliding particles form a dimer with probability 1 at the interaction radius. In patchy case, when patches are not aligned, colliding particles form unbound correlated couples with a probability $(1 - \chi^2)$. These couples will contribute later to the dimer formation by a secondary process mainly involving rotational diffusion. Moreover, if a weak isotropic interaction keeps monomers close together for a longer time, the effect of this secondary process will be of greater importance. So, we propose a detailed study of dimerization process from a dynamic point of view and see what happens when two particles start close together ($r_0 = R_{col,1} = d \cdot (1 + \varepsilon)$).

5.4 Correlated couples

Let us imagine a dilute system of patchy particles with initial number density C_0. Let C_1, C_c and C_2 denote the number density of unreacted uncorrelated monomers, unreacted correlated monomers and dimers respectively. In patchy case, dimers could be formed in two ways: from a direct collision between two uncorrelated monomers with a probability of success χ^2 and from reorientation of the remaining
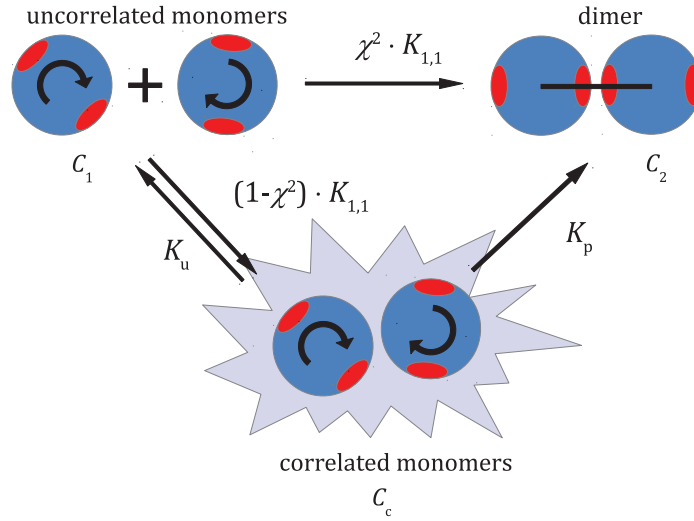
Figure 5.11: Schematic representation of the two pathways for dimer formation in the patchy case. Two uncorrelated patchy monomers have a probability χ^2 to form a dimer, when they come in interaction range. $K_{1,1}$ is the rate constant given by Smoluchowski for a bimolecular reaction, K_u is the rate constant that two correlated particles get uncorrelated again and K_p is the rate constant for reorientation and bonding of a correlated couple.

$(1 - \chi^2)$ correlated monomers before they become uncorrelated again. This could be pictorially represented as in figure 5.11. We can consider correlated couples as another species and we have the relation

$$C_0 = C_1 + 2 \cdot C_2 + 2 \cdot C_c \tag{5.20}$$

From C_c correlated couples, a fraction gets uncorrelated again and another fraction forms patchy bond (see figure 5.11). So, rate equations for these reactions could be written as follows.

$$\frac{dC_1}{dt} = - K_{1,1} \cdot C_1^2 + 2 \cdot K_u \cdot C_c^{x_u} \tag{5.21}$$

$$\frac{dC_2}{dt} = \frac{K_{1,1}}{2} \cdot \chi^2 \cdot C_1^2 + K_p \cdot C_c^{x_p} \tag{5.22}$$

$$\frac{dC_c}{dt} = \frac{K_{1,1}}{2} \cdot (1 - \chi^2) \cdot C_1^2 - K_p \cdot C_c^{x_p} - K_u \cdot C_c^{x_u} \tag{5.23}$$

where, K_u and x_u are the rate constant and the order of the uncorrelation reaction respectively, and K_p and x_p are the rate constant and order of the reaction for the patch formation from correlated couples respectively. Using these set of equations, we will explain the dimerization process by studying each individual reaction in the following.

In order to precisely understand the effect of correlation when two patchy monomers come in the interaction range, we simulated couples of monomers with

randomly orientated patches, separated by a given distance $r_0 = d(1+\varepsilon)$ at starting time $t = 0$, after which they begin their random walk. We answer the following questions:

1. For non patchy couples, what is the average time spent in interaction range when no isotropic interaction is present?

2. What is the effect of an isotropic square well attractive interaction on the previous average time?

3. For patchy couples, what is the time taken to form the bond when there is a rotational motion and the translational motion is restricted into the well ($B_{att} = \infty$)? What is the influence of χ on this average time?

4. From the three simplified case above, can we understand the situation where both rotational and translational motion take place in a finite depth well? Can we estimate K_u and K_p and orders of the two reactions?

Various C programs has been written to study these individual effects turning on and off the patchy interactions, the isotropic square well potential and excluded volume effects.

5.4.1 Non patchy monomers - the ideal case - an analytical approach

Consider monomer 1 starts at O and stays immobile while monomer 2 starts at A, at a distance $r_0 = d\cdot(1+\varepsilon)$ from monomer 1 (see explanatory figure 5.12) and moves with a translational diffusion coefficient $D = 2 \cdot D_1^\mathrm{T} = d^2/(3 \cdot t_0)$. This is to take into account the effect of the relative diffusion coefficient when both particles are moving. $\mathbf{R}(t) = \mathbf{r}_0 + \mathbf{r}(t)$ is the position of particle 2 at time t, where $\mathbf{r}(t)$ denotes its relative displacement from the initial position at time t. We are interested in the probability to find the second monomer within a distance $d \cdot (1 + \varepsilon)$ from the first one at a given time t. This also corresponds to the fraction of monomers in the interaction range, n_w, at time t.

Assuming no excluded volume interactions, the density probability of finding monomer 2 at position $\mathbf{R}(t)$ is given by

$$f(\mathbf{R}(t)) = (4 \cdot \pi \cdot D \cdot t)^{-3/2} \cdot \exp\left(\frac{-\mathbf{r}^2(t)}{4 \cdot D \cdot t}\right) \tag{5.24}$$

and only depends on $r^2(t)$. The probability that particle 2 lies in interaction range could be calculated by integrating the above expression over the volume of a sphere centered at O and with a radius $(d \cdot (1 + \varepsilon))$

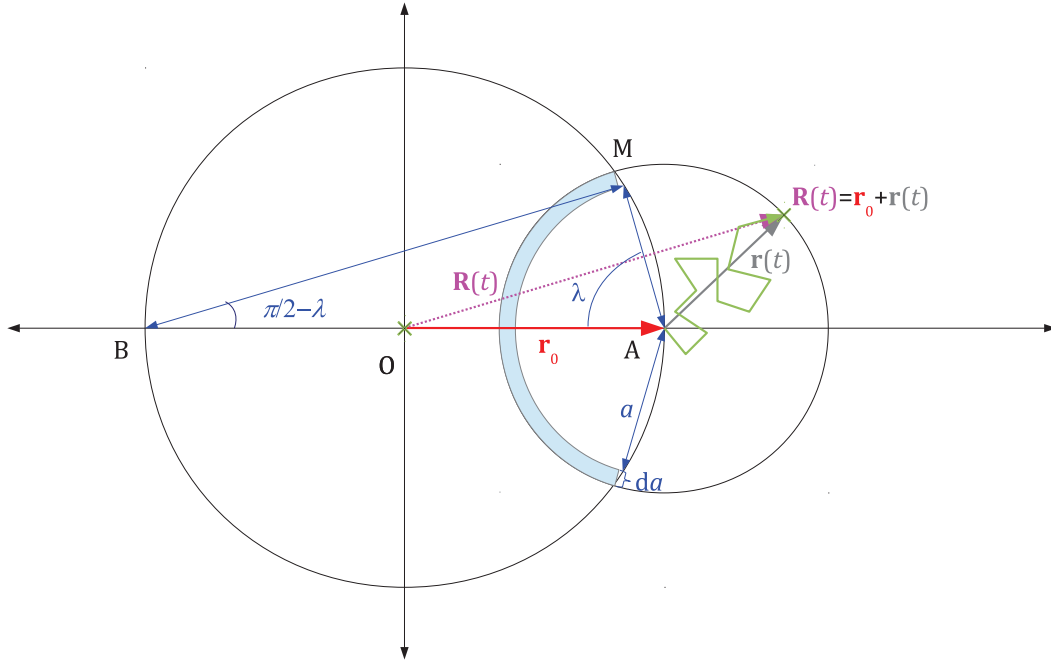$$P(\mathbf{R}(t) \leq d \cdot (1 + \varepsilon)) = \iiint_\mathrm{V} f(\mathbf{R}(t)) \cdot \mathrm{d}v \tag{5.25}$$

Figure 5.12: Schematic of the problem.

Let us consider the intersection of the sphere centered on O with radius r_0 and the one centered on A with radius $a \leq 2r_0$ (see figure 5.12 for a two dimensional representation). Let M be any of the intersection points. We are interested in the spherical conic surface with an angle λ given by $\cos \lambda = \text{AM}/\text{AB} = a/(2r_0)$ in the interior of the interaction volume. Introducing a small radius increment da as in the figure, we can define a piece of spherical conic shell with a volume dv given as (see also appendix A)

$$\mathrm{d}v = 2 \cdot \pi \cdot a^2 \cdot (1 - \cos \lambda) \cdot \mathrm{d}a \tag{5.26}$$

Now, we can integrate over the volume of interest using these spherical shells centered on A with radius ranging from 0 to $2 \cdot r_0$ (from A to B). Note that this is based on the fact that the density probability of particle 2 is equally distributed in these shell elements. This implies

$$P(\mathbf{R}(t) \leq r_0) = \int_0^{2 \cdot r_0} 2 \cdot \pi \cdot a^2 \cdot \left(1 - \frac{a}{2 \cdot r_0}\right) \cdot (4 \cdot \pi \cdot D \cdot t)^{-3/2} \cdot \exp\left(\frac{-a^2}{4 \cdot D \cdot t}\right) \cdot \mathrm{d}a \tag{5.27}$$

On rearrangement

$$P(\mathbf{R}(t) \leq r_0) = \frac{1}{\sqrt{\pi}} \cdot \left[\gamma\left(\frac{3}{2}, \frac{r_0^2}{D \cdot t}\right) - \sqrt{\frac{D \cdot t}{r_0^2}} \cdot \gamma\left(2, \frac{r_0^2}{D \cdot t}\right)\right] \tag{5.28}$$

where $\gamma(a, x)$ is the incomplete gamma function defined by

$$\gamma(a, x) = \int_0^x t^{a-1} \cdot \exp(-t) \cdot \mathrm{d}t \qquad (5.29)$$

with the following limiting behaviors

$$\gamma(a, x) = \Gamma(a) \quad , \, x \to \infty \qquad (5.30)$$

$$\gamma(a, x) = x^a/a \quad , \, x \to 0 \qquad (5.31)$$

This probability gives the fraction of couples in interaction range at a given time t. Using our system of units, we get

$$n_{\mathrm{w}} = \frac{1}{\sqrt{\pi}} \cdot \left[\gamma\left(\frac{3}{2}, \frac{A}{t/t_0}\right) - \sqrt{\frac{t/t_0}{A}} \cdot \gamma\left(2, \frac{A}{t/t_0}\right) \right] \qquad (5.32)$$

where $A = 3 \cdot (1 + \varepsilon)^2$.

For $t/t_0 \ll A$, incomplete gamma functions in equation 5.32 turn to be gamma functions and using the relation $\Gamma(1/2) = \sqrt{\pi}$, we get

$$n_{\mathrm{w}} \approx \frac{1}{2} - \sqrt{\frac{t/t_0}{\pi \cdot A}} \quad , \, t/t_0 \ll A \qquad (5.33)$$

and for $t/t_0 \gg A$, using equation 5.31, we get

$$n_{\mathrm{w}} \approx \frac{A^{3/2}}{6 \cdot \sqrt{\pi}} \cdot (t/t_0)^{-3/2} \quad , \, t/t_0 \gg A \qquad (5.34)$$

In the beginning of the study, we positioned the second particle at the edge of the well, $d \cdot (1 + \varepsilon)$. From equation 5.33, we get for very small time, $n_{\mathrm{w}}(t \to 0) = 1/2$. This means that only half of the couples are within the interaction range, or in other words, half of the couples leave the well instantaneously as time tends to zero.

Figure 5.13 shows equation 5.32 with the above two limiting behaviors for comparison. We see that the integral over time for n_{w} remains finite. It has been shown that the average time spent in the well is a finite quantity and is an intrinsic property of Brownian motion which is transient in the volume $\mathbb{R}^3$ (see page 77 of [126]). This integral gives the average time that a couple stays in the interaction range, before it gets uncorrelated. We call this time the average correlation time t_{c}^l, where l denotes the excluded volume conditions: $l = 0$ for the ideal case and $l = 1$ denotes the real case. Changing variable $y = A/(t/t_0)$ and integrating by parts, equation 5.32 gives

$$t_{\mathrm{c}}^{l=0}/t_0 = \int_0^\infty n_{\mathrm{w}} \cdot \mathrm{d}(t/t_0) = (1 + \varepsilon)^2 \qquad (5.35)$$
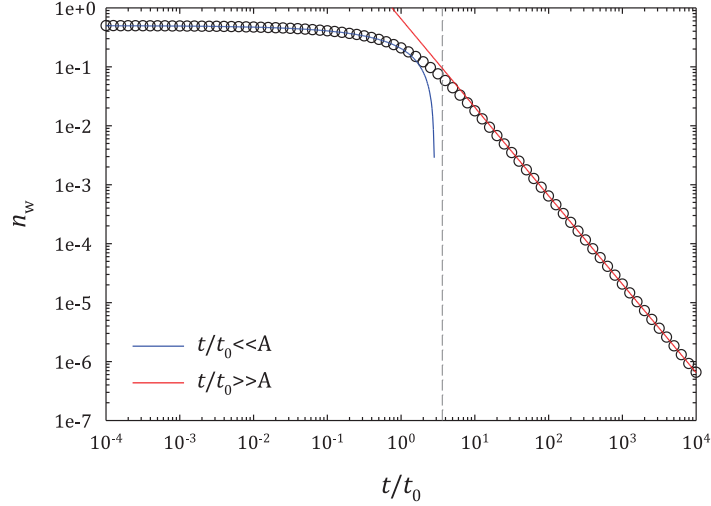
Figure 5.13: Equation 5.32 plotted against time for $\varepsilon = 0.1$ (circles). Also, the short time behavior (equation 5.33, in blue) and large time behavior (equation 5.34, in red) are shown. The vertical dashed line is drawn at $t/t_0 = A$.

The derivative of n_w with respect to time gives the net flux of couples leaving the interaction range at a given time. From equation 5.32, we get

$$\frac{-\mathrm{d}n_\text{w}}{\mathrm{d}(t/t_0)} = \frac{1}{2} \cdot \frac{1}{\sqrt{\pi \cdot A \cdot (t/t_0)}} \cdot \gamma\left(2, \frac{A}{t/t_0}\right) \tag{5.36}$$

For $t/t_0 \ll A$, we get

$$\frac{-\mathrm{d}n_\text{w}}{\mathrm{d}(t/t_0)} = \frac{1}{2} \cdot \frac{1}{\sqrt{\pi \cdot A}} \cdot (t/t_0)^{-1/2} \quad , t/t_0 \ll A \tag{5.37}$$

and for $t/t_0 \gg A$, we obtain

$$\frac{-\mathrm{d}n_\text{w}}{\mathrm{d}(t/t_0)} = \frac{1}{4} \cdot \frac{A^{3/2}}{\sqrt{\pi}} \cdot (t/t_0)^{-5/2} \quad , t/t_0 \gg A \tag{5.38}$$

Figure 5.14 shows the analytical expression 5.36 with the two limiting power law behaviors at small and large times.

Comparing 5.38 with equation 5.34, we see that at large time $t/t_0 \gg A$, the flux could be written as a function of n_w

$$\boxed{\frac{-\mathrm{d}n_\text{w}}{\mathrm{d}(t/t_0)} = B \cdot n_\text{w}^{5/3} \quad , B = \sqrt[3]{\frac{243 \cdot \pi}{2 \cdot A^3}} \quad , t/t_0 \gg A} \tag{5.39}$$

This means that uncorrelation of an ideal correlated couple follows a kinetics of the order 5/3 (see figure 5.15). B also gives us an idea about K_u (see figure 5.11).
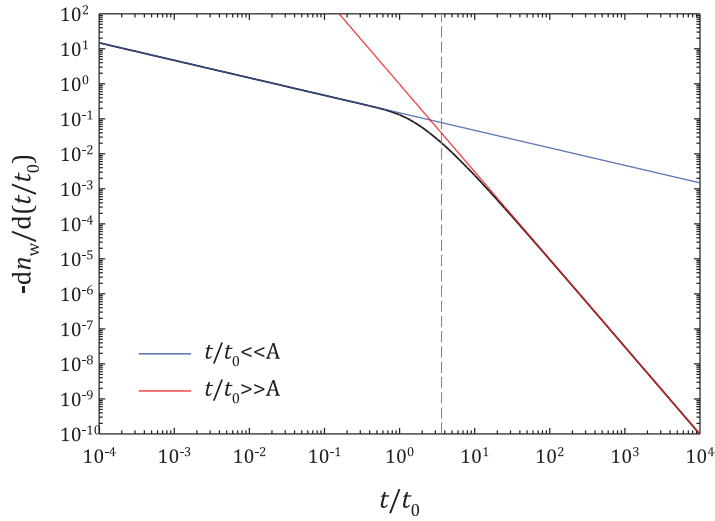
Figure 5.14: Equation 5.36 plotted against time for $\varepsilon = 0.1$. Also, short time and large time behaviors are shown as indicated in the figure. The vertical dashed line is drawn at $t/t_0 = A$.
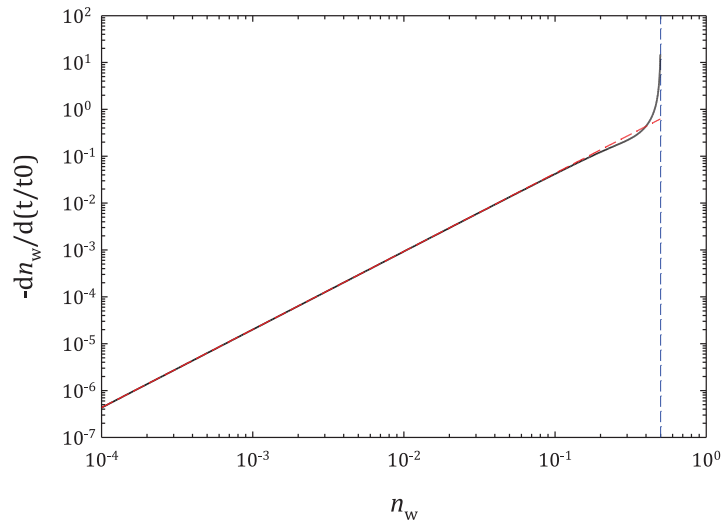

Figure 5.15: The flux of couples leaving the well plotted against n_w for $\varepsilon = 0.1$ (black curve). The red dashed line is the expression 5.39. The blue dashed line corresponds to the maximum value $n_w((t/t_0) = 0) = 0.5$.

5.4.2 Non patchy monomers - the case with excluded volume effects - a simulation study

For the excluded volume case, we don't have any analytical expressions to work with. So, simulations were carried out with same details as described in the previous case, but taking into account excluded volume interactions. Motion steps leading to overlapping configurations were rejected. For the simulation, at least 10^5 couples were considered to compute n_w. Also, different values of B_{att} were tested by refusing a couple to leave the well with probability P (see 2.5 which connects B_{att} and P). The Brownian step size (s_T) is also chosen as an input parameter and n_w was monitored as a function of time in the output, along with other quantities of interest like the average number of exits from the well, the average time spent in the well between two exits, the maximum distance traveled between an exit and subsequent entrance, the mean square displacement etc.

5.4.2.1 Influence of s_T

We know that using s_T as small as possible gives unbiased results. But, as said before, this is highly CPU time consuming. Figure 5.16 shows results obtained using various s_T at $B_{att} = 0$. We see that as s_T increases, the correct behavior is recovered only at larger times, when it superimposes with the one with a smaller s_T. This means that using small s_T for small times and large s_T for larger times, the unbiased behavior could be obtained for very large times, given enough superimposition with a lower s_T one. Using this method, we can reconstruct the complete curve within a reasonable CPU time.
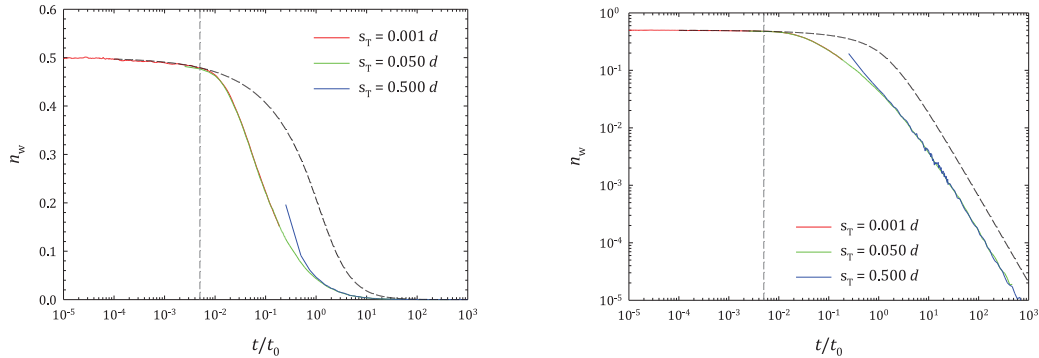
Figure 5.16: (Left) Influence of s_T on n_w for the real case (with excluded volume), $\varepsilon = 0.1$ and $B_{att} = 0$. The ideal case is also plotted for comparison (black dashed curve). (Right) The same data in the plot on the left, but in a log-log plot. The gray vertical dashed line in the figure denotes the average time needed for a couple to collide for the first time, starting at a distance $d \cdot (1 + \varepsilon)$.

As we are mainly interested in the average time spent in the well, we plot $n_{\mathrm{w}} \cdot (t/t_0)$ on a logarithmic scale of time - area below the curve being t_{c}^l/t_0 (see figure 5.17). This gives us an idea of the time to be reached to compute more accurate value for the correlation time. The reconstructed curve is then interpolated in a logarithmic time scale to get equally spaced points and is numerically integrated to obtain t_{c}^l/t_0. In figure 5.18, we plot area under the curve $n_{\mathrm{w}} \cdot (t/t_0)$ as a function of t/t_0. As expected, the value converges to a constant plateau at large times. We take this plateau value as the average correlation time (t_{c}^l/t_0) or the average time spent in the potential well. For the real case, the obtained t_{c}^1/t_0 is lesser than the ideal case (see figures 5.16 and 5.18 for a comparison). For $B_{att} = 0$ and $\varepsilon = 0.1$, figure 5.18 gives $t_{\mathrm{c}}^1/t_0 \approx 0.30$ for the real case, while for the ideal case we get $t_{\mathrm{c}}^0/t_0 = 1.21$. This is simply because of the reduction of the interaction volume for the real case due to excluded volume interactions, which favor particles to leave the well sooner. We can also notice by comparison with the ideal case, that the real one gives a similar power-law behavior for n_{w} at large time with the same exponent $-3/2$ (see figure 5.19 (left)). Also, plotting the evolution of $-\mathrm{d}n_{\mathrm{w}}/\mathrm{d}(t/t_0)$ as a function of n_{w} or t/t_0, we obtain a similar kinetic behavior at large times with the same exponent $5/3$ but a higher rate constant compared to the ideal one (figure 5.19 (right)). This means that excluded volume effects play no role on the kinetic class of uncorrelation. We also note that ε affects the rate constant of the reaction, yet the exponent of the power law behavior at large time remains the same. At short times, both ideal and real cases have same behaviors until the average time to the first hardcore collision is reached ($\varepsilon^2/2$). This time is shown as gray dashed line in figures 5.16 and colored arrows in 5.19.
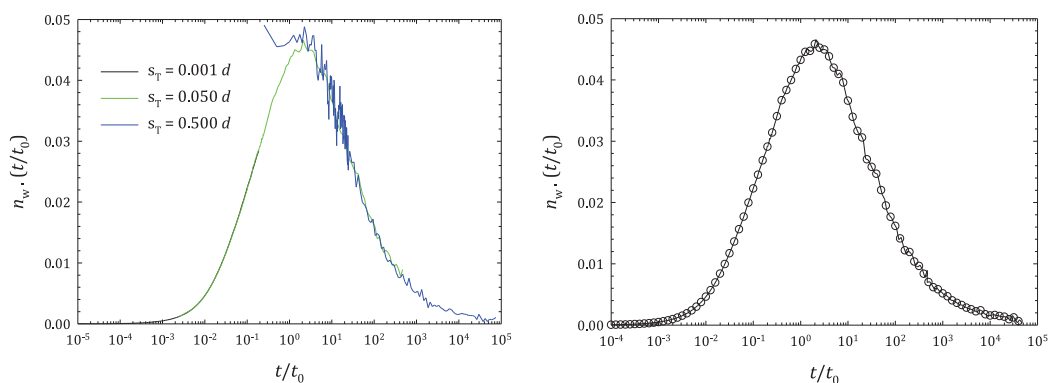

Figure 5.17: (Left) Influence of s_{T} on $n_{\mathrm{w}} \cdot (t/t_0)$ for the real case with excluded volume, $\varepsilon = 0.1$. (Right) The reconstructed curve (black curve) is made using good regimes of data from the plot on the left side. Circles represent interpolated values.
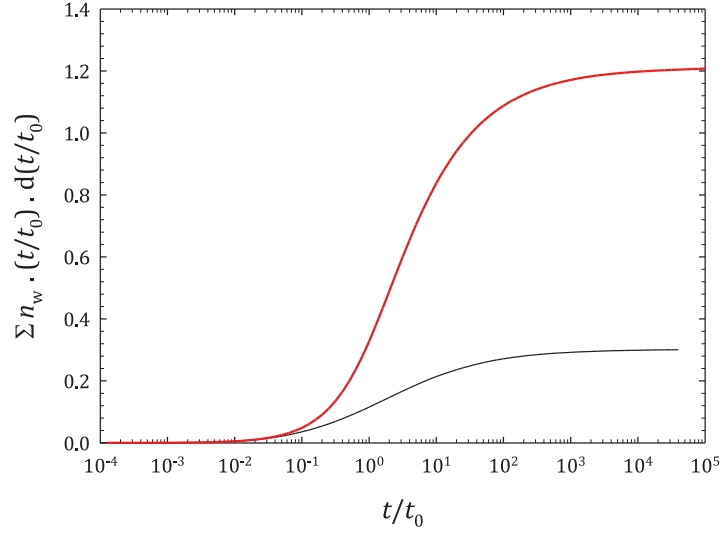
Figure 5.18: Area under the curve for reconstructed data in figure 5.17 plotted as a function of t/t_0 for the real case with excluded volume, $\varepsilon = 0.1$ (black curve). The plateau value at the long time is taken as the average correlation time. The ideal case is given in red color for comparison.
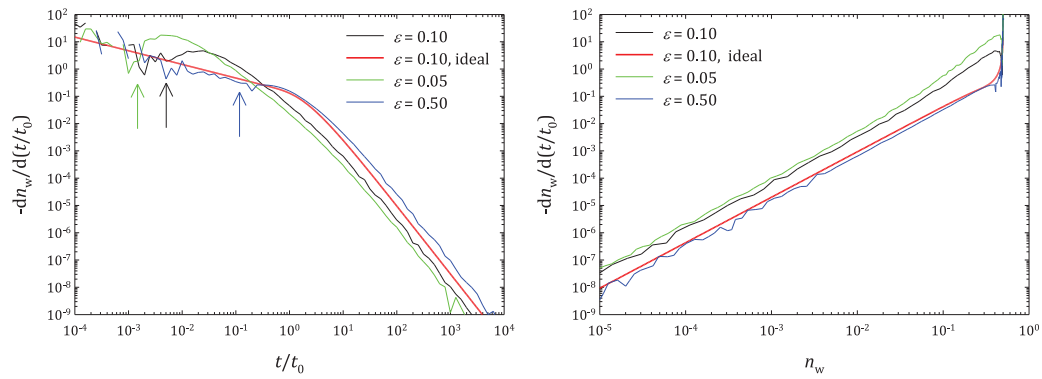
Figure 5.19: Evolution of $-\mathrm{d}n_\mathrm{w}/\mathrm{d}(t/t_0)$ as a function of time (left) and of n_w (right) for $B_{att} = 0$ and various ε as indicated in figure. The ideal case for $\varepsilon = 0.1$ (red curve) is also given for comparison. The vertical arrows correspond to the average time at which excluded volume is felt for the first time ($\varepsilon^2/2$).

5.4.2.2 Effect of B_{att}

Using the above method to construct the curves, we study in detail, the effects of B_{att} on t_c^l/t_0 for $\varepsilon = 0.1$. As in BCD, the effect of B_{att} is modeled by using a probability term P. This means that when particles are entitled to leave the well, a fraction P remains in the well. We recall the relation between B_{att} and P

$$B_{att} = \frac{4 \cdot P}{(1 - P)} \cdot \left[(1 + \varepsilon)^3 - 1 \right] \tag{5.40}$$

Figure 5.20 shows the effect of B_{att} on n_w. As in the ideal case with $B_{att} = 0$, all curves start with almost a flat plateau like region at very small time. For $B_{att} = 0$, both ideal and real case behave similarly at very small time, but real cases starts to show deviation later. However, we see that all curves have a similar power law at large time, proportional to $(t/t_0)^{-3/2}$. This means neither excluded volume nor B_{att} change the kinetic class of the process. So, the order of the reaction (uncorrelation from correlated state) remains the same and only the absolute value of K_u is influenced.
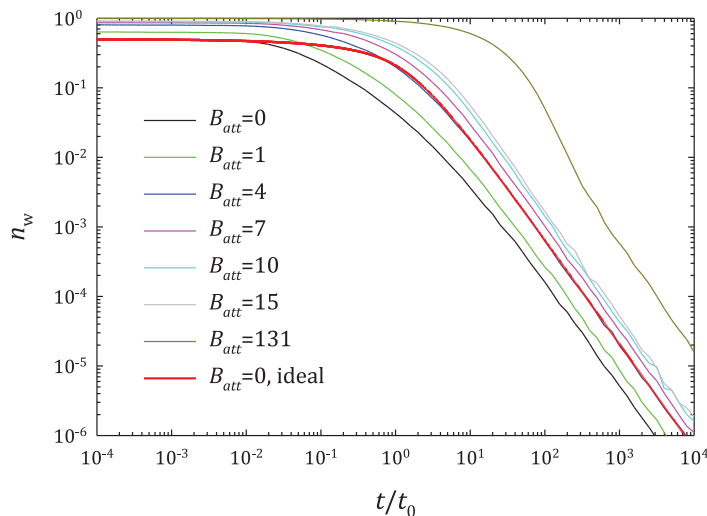
Figure 5.20: Evolution of n_w as a function of t/t_0 for $\varepsilon = 0.1$ and various B_{att} as indicated in the figure. The ideal behavior ($B_{att} = 0$) from equation 5.32 is also given for a comparison.

The initial plateau behavior at small time depends on B_{att} (see figure 5.21) and could be explained as follows. In our simulation, couples start at inner edge of the interaction range (in fact, at a distance $(d \cdot (1 + \varepsilon) - 10^{-6})$). This is to have a well defined initial condition that does not depend on the floating point precision of the computer when the squared distances are calculated with a precision of 10^{-12}. Let $N_{in}(n)$ denote the number of couples within the interaction range at motion step n and similarly $N_{out}(n)$ the number of the couples outside. The total number of

couples is $N_0 = N_{\text{in}}(n) + N_{\text{out}}(n)$ at any n. In the limit of small s_{T} (bigger than $d \cdot 10^{-6}$, but smaller than the radius of curvature of the surface) and small n, we can consider that particles are very close to the border. Then, in a motion step n, the following things could happen

1. Half of particles outside the border are entitled to come in

2. Half of particles inside the border are entitled to leave the well

3. Of the above particles entitled to leave, the probability that they overcome the barrier is given by $(1-P)$. So, depending on P, some particles remain in the well.

We could write the flux of particles entering the boundary as $N_{\text{out}}(n)/2$ and the flux of particles leaving the boundary as $(1-P) \cdot N_{\text{in}}(n)/2$. A quasi stationary state is obtained when both flux are equal, leading to

$$\frac{1}{2} \cdot N_{\text{out}}(n) = \frac{1}{2} \cdot (1-P) \cdot N_{\text{in}}(n) \tag{5.41}$$

which gives

$$\frac{N_{\text{in}}(n)}{N_0} = \frac{1}{2-P} = n_{\text{w}}(t \to 0) \tag{5.42}$$

This means that the initial behavior of n_{w} is a function of P or in other words B_{att}. Even when we start with all couples at the edge, some of them instantaneously leave the well and we never get all the monomers to be in the range, except for $P = 1$. Figure 5.21 shows values calculated for different P along with the $n_{\mathbf{w}}$ curves. We see that the above equation gives a perfect description of the initial limit.

To compute the average time spent in the well, we plot the data of figure 5.21 using our previous method to get figure 5.22. From this plot, we integrate area under the curve and find average correlation time. The obtained t_{c}^l/t_0 is plotted as a function of B_{att} in figure 5.23 for different ε and real/ideal case. We see that the average correlation time increases linearly with B_{att}, and it depends on excluded volume effects and the value of ε. We write these dependencies as $t_{\text{c}}^l(\varepsilon, P)$. (Since B_{att} is a function of both P and ε, we explicitly separate the two variables). Linear dependence of the correlation time could be mathematically represented as

$$\frac{t_{\text{c}}^l}{t_0} = a^l(\varepsilon) + b^l(\varepsilon) \cdot B_{att} \tag{5.43}$$

where $a^l(\varepsilon)$ and $b^l(\varepsilon)$ are only function of ε and l (l=0 ideal, l=1 real). We try to find the correct expression for them in the following.

Interestingly, we observe that for any ε, the average correlation time obtained for the ideal case with $B_{att} = 0$ is very close to that of the real case with $B_{att} = 4$, even though the exact shape of curves are different (see for example figures 5.21 and
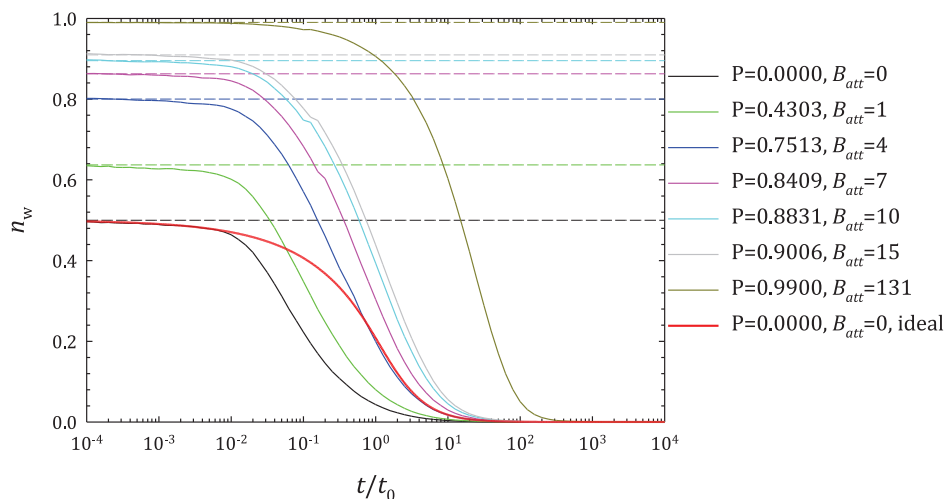
Figure 5.21: Same data as in figure 5.20 but plotted on a lin-log scale. The dashed lines correspond to the respective values of $n_{\rm w}$ at $t/t_0 \to 0$ from the equation 5.42. Note the behavior of $B_{att} = 4$ for the real and $B_{att} = 0$ for the ideal case.

5.22 where $\varepsilon = 0.1$). This means that for $B_{att} = 4$ the average time spent in the well for real case is the same as if both monomers were transparent to each other in the absence of any interactions, leading to an apparent increase of the interaction volume. The condition $B_{att} = 4$ corresponds to the case $B_2 = 0$ (second virial parameter is zero). It is equivalent to theta solvent condition for polymers. Our observation is the dynamical transcription of the theta condition where real chains behave as ideal ones from a static point of view. From 5.35, with $B_{att} = 0$ for an ideal case, we have

$$\boxed{\frac{t_{\rm c}^1(\varepsilon, B_{att} = 4)}{t_0} = \frac{t_{\rm c}^0(\varepsilon, B_{att} = 0)}{t_0} = (1 + \varepsilon)^2} \tag{5.44}$$

To verify this relation, we plot $(t_{\rm c}^1(\varepsilon, B_{att} = 4)/t_0)/(1 + \varepsilon)^2$ as a function of ε in figure 5.24. We see that it holds nicely.

In order to understand the linear behavior and dependency on P, l and ε, we study in detail discrete events like the number of exits from the interaction range, the number of steps spent in the well between two exits etc. For all of these discrete events, we have to study effects from ε, $s_{\rm T}$, P and l.

We study the number of exits from the well that a couple makes in average ($N_{\rm exit}$) as a function of time for various $s_{\rm T}$ in figure 5.25. First, we notice that $N_{\rm exit}$ is highly dependent on the Brownian step length. Secondly, we see that for a given $s_{\rm T}$, the value of $N_{\rm exit}$ converges to a plateau at very large time. This behavior is expected, as we have seen that at infinite time, no couples remain in interaction range. Before leaving the range for ever, they make in average a finite number of
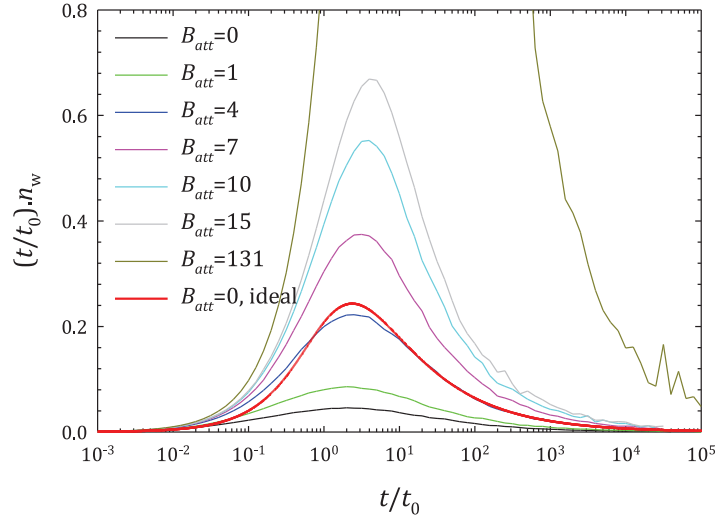
Figure 5.22: Effect of B_{att} on $t/t_0 \cdot n_\mathrm{w}$ for various B_{att} as indicated in the figure, $\varepsilon = 0.1$.
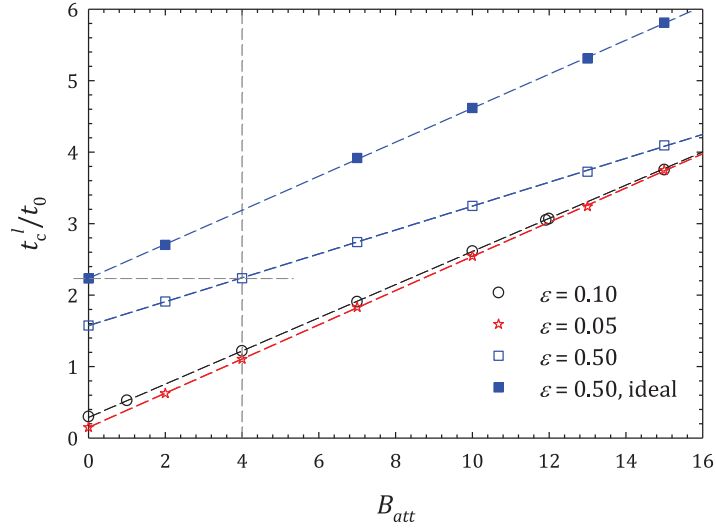
Figure 5.23: Variation of t_c^l/t_0 as a function of B_{att} for various ε as indicated in the figure. Dashed lines are linear fits which regression coefficients $R^2 \geq 0.999$. The open symbols represent the real case and the closed symbols represent the ideal case. Gray dashed lines mark the value $B_{att} = 4$ and corresponding correlation times for $\varepsilon = 0.5$ ideal and real.

Figure 5.24: $(t_{\mathrm{c}}^1(\varepsilon, B_{att} = 4)/t_0)/(1 + \varepsilon)^2$ plotted as a function of ε.

exits and the average time between two exits can also be defined. Knowing this, we plot the plateau value of N_{exit} at large times as a function of d/s_{T} for various values of ε, P and l in figure 5.26. We see a perfect linear behavior when s_{T} is sufficiently small. We also find N_{exit} to be only a function of ε since all data points for different combinations 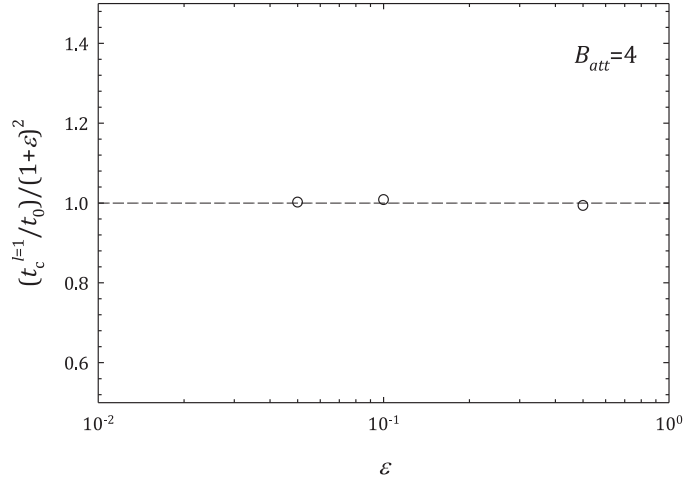of P and l superimpose for a given ε. Whatever P is, the average number of exits at long time remains the same for a given ε. This means that the probability $(1 - P)$ to exit from the well and do the next step does not influence geometrical properties of the walk close to the border. Independency on excluded volume effects also point out that N_{exit} is an intrinsic property of the system, which does not depend on the geometrical restrictions, which are far from the border. The deviation at larger step size is due to finite size effects (as step size approaches the size of well, excluded volume interactions distort the geometrical path of the walk close to the border as well). N_{exit} can be expressed as

$$N_{\mathrm{exit}} = k_1(\varepsilon) \cdot d/s_{\mathrm{T}} \tag{5.45}$$

where the function k_1 depends only on ε. We find $k_1(\varepsilon)$ to be remarkably close to $(1 + \varepsilon)$. To verify, we plot $N_{\mathrm{exit}} \cdot s_{\mathrm{T}}/((1 + \varepsilon) \cdot d)$ in figure 5.27. We see that for small values of s_{T}, compared to ε, we have

$$k_1(\varepsilon) \simeq (1 + \varepsilon) \tag{5.46}$$

irrespective of excluded volume effects and P. We do not have any theroretical considerations to explain this simple result.

The other quantity of interest is the average time spent in the well between two consecutive exits ($N_{\mathrm{resid}}/N_{\mathrm{trial}}$). Here N_{resid} is the average number of steps spent in the well and N_{trial} is the average number of trials realized for exit. From the
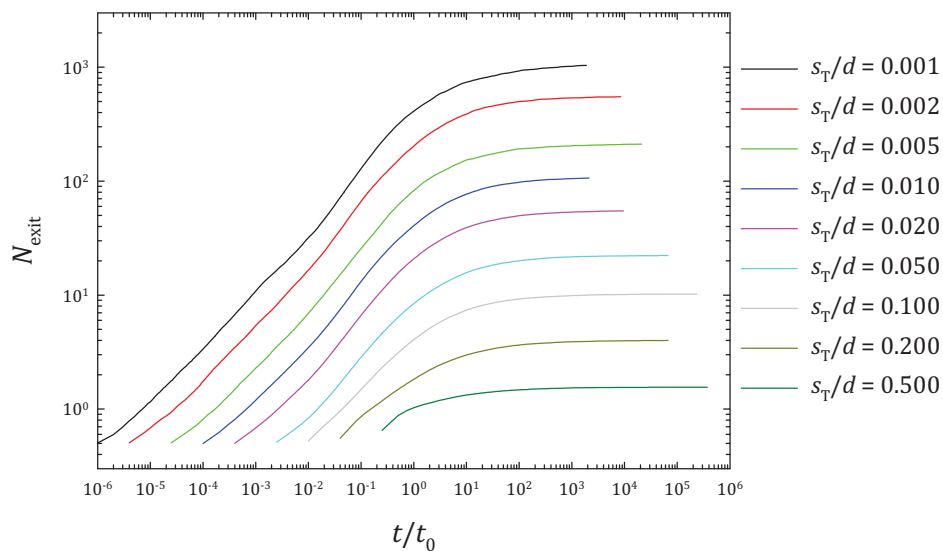
Figure 5.25: N_{exit} plotted as a function of time for various s_{T}/d as shown in figure. $\varepsilon = 0.10$, $l = 1$ (with excluded volume) and $P = 0.0000$.
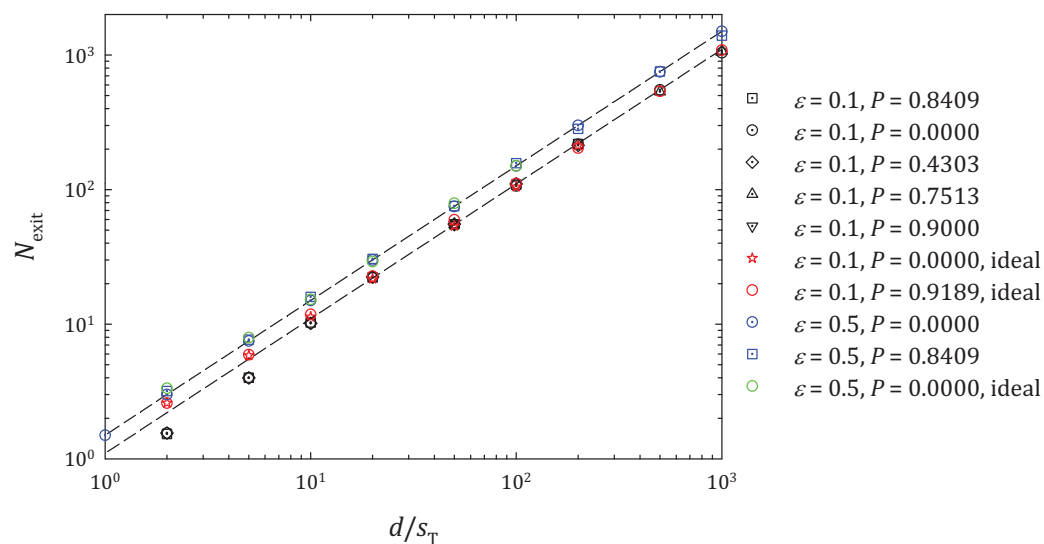

Figure 5.26: N_{exit} plotted as a function of d/s_{T} for various ε, P and l. Dashed lines are guides to the eye with slope 1.
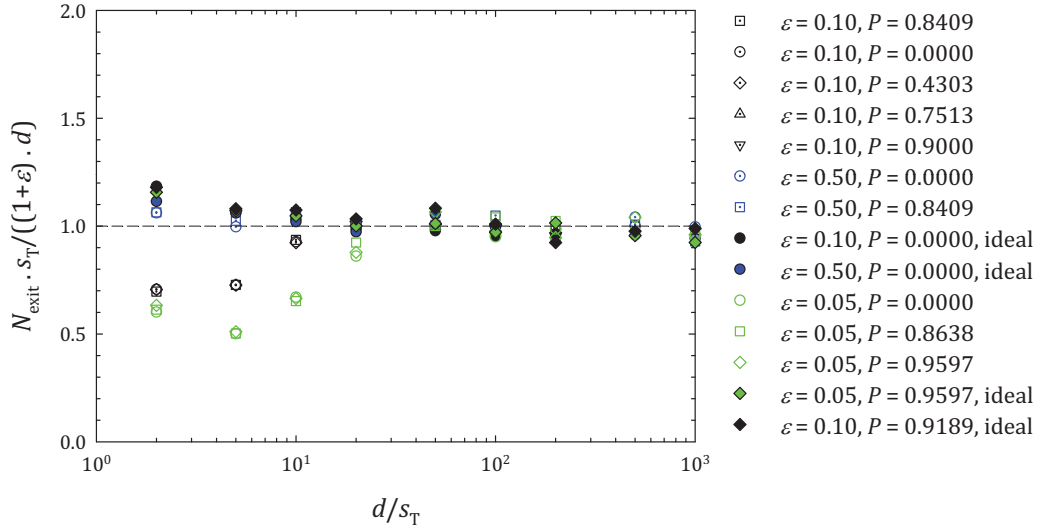
Figure 5.27: $N_{\text{exit}} \cdot s_{\text{T}}/(d \cdot (1 + \varepsilon))$ plotted as a function of d/s_{T} for various ε, P and excluded volume conditions. The horizontal dashed line indicates the expected behavior.

definition of physical time in our system (see equation 3.17), we get

$$\frac{t_c^l}{t_0} = N_{\text{resid}} \cdot (s_{\text{T}}/d)^2 \tag{5.47}$$

N_{resid} and N_{exit} remain finite and we also have

$$N_{\text{exit}} = (1 - P) \cdot N_{\text{trial}} \tag{5.48}$$

This means that the ratio $N_{\text{resid}}/N_{\text{trial}}$, the average number of steps spent in the well between an entrance and an exit, stays finite at large times.

As before, we study the effect of s_{T} on $N_{\text{resid}}/N_{\text{trial}}$ in figure 5.28. We see that $N_{\text{resid}}/N_{\text{trial}}$ plotted as a function of t/t_0 converges faster than N_{exit} and is also very dependent on s_{T}. In figure 5.29, we plot the plateau values obtained as a function of d/s_{T}. We observe a linear dependence, and for a given ε, we find no influence of P. But in this case we see that excluded volume effects play a role. To describe the behavior, we use the following

$$\frac{N_{\text{resid}}}{N_{\text{trial}}} = k_2^l(\varepsilon) \cdot \frac{d}{s_{\text{T}}} \tag{5.49}$$

where $k_2^l(\varepsilon)$ is independent on P.

Using the relations 5.45, 5.48 and 5.49 in equation 5.47 gives

$$\boxed{\frac{t_c^l(\varepsilon, P)}{t_0} = \frac{k_1(\varepsilon) \cdot k_2^l(\varepsilon)}{(1 - P)}} \tag{5.50}$$
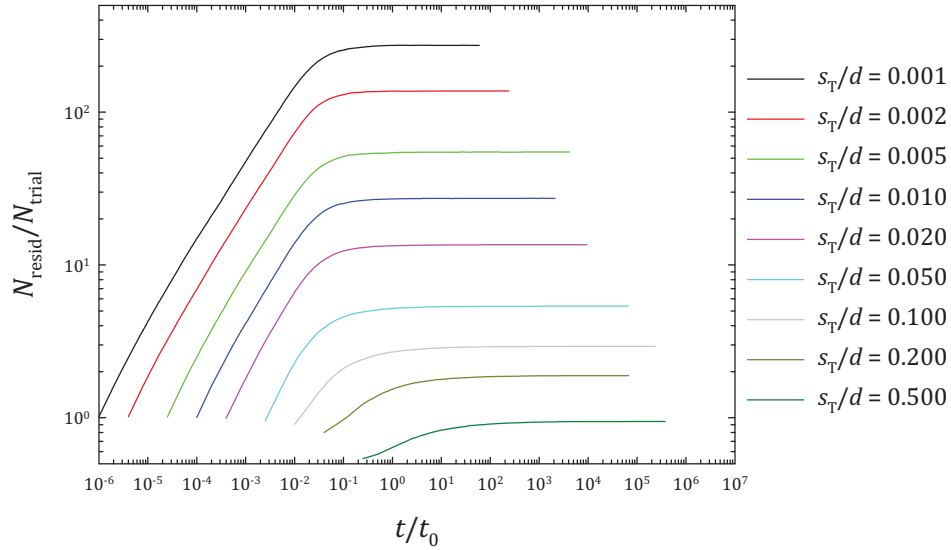
Figure 5.28: $N_{\mathrm{resid}}/N_{\mathrm{trial}}$ plotted as a function of time for various s_{T}. $\varepsilon = 0.10$, $l = 1$ and $P = 0.0000$.
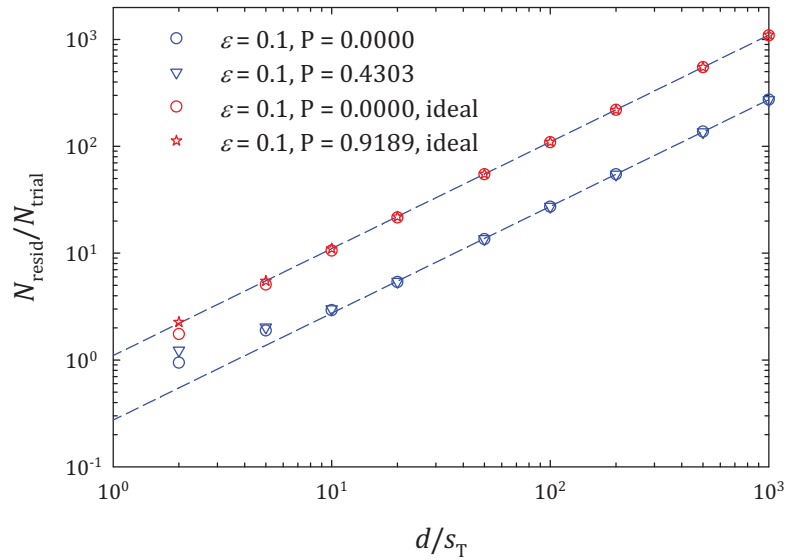
Figure 5.29: Plateau value of $N_{\mathrm{resid}}/N_{\mathrm{trial}}$ plotted as a function of d/s_{T} for $\varepsilon = 0.10$ and various combinations of l and P as shown in the figure. The dashed lines are from equation 5.49 using expression for $k_2^l(\varepsilon)$ from equation 5.52 or 5.54 assuming $k_1(\varepsilon) = (1 + \varepsilon)$.

We note that the s_T/d dependency is canceled. Comparing with 5.43 and 5.40 gives

$$a^l(\varepsilon) = k_1(\varepsilon) \cdot k_2^l(\varepsilon)$$
$$b^l(\varepsilon) = \frac{a^l(\varepsilon)}{4 \cdot [(1+\varepsilon)^3 - 1]}$$

(5.51)

Using the relation 5.44 in equation 5.50 and using $P = (1+\varepsilon)^{-3}$ at $B_{att} = 4$, we get

$$a^1(\varepsilon) = k_1(\varepsilon) \cdot k_2^1(\varepsilon) = \frac{(1+\varepsilon)^3 - 1}{(1+\varepsilon)}$$

(5.52)

which gives

$$b^1(\varepsilon) = \frac{1}{4 \cdot (1+\varepsilon)}$$

(5.53)

In a similar manner, for $P = 0$ and ideal condition, equations 5.50 and 5.35 gives

$$a^0(\varepsilon) = k_1(\varepsilon) \cdot k_2^0(\varepsilon) = (1+\varepsilon)^2$$

(5.54)

which gives

$$b^0(\varepsilon) = \frac{(1+\varepsilon)^2}{4[(1+\varepsilon)^3 - 1]}$$

(5.55)

We note that these equations assume no knowledge about $k_1(\varepsilon)$.

Substituting the values of $a^1(\varepsilon)$,... etc. in equation 5.43, we get

$$\frac{t_c^1(\varepsilon, P)}{t_0} = \frac{[(1+\varepsilon)^3 - 1]}{(1+\varepsilon)} \cdot \frac{1}{(1-P)}$$

(5.56)

and

$$\frac{t_c^0(\varepsilon, P)}{t_0} = \frac{(1+\varepsilon)^2}{1-P}$$

(5.57)

In terms of B_{att}, these expressions become

$$\boxed{\frac{t_c^1(\varepsilon, B_{att})}{t_0} = \frac{B_{att} + 4 \cdot [(1+\varepsilon)^3 - 1]}{4 \cdot (1+\varepsilon)}}$$

(5.58)

and

$$\boxed{\frac{t_c^0(\varepsilon, B_{att})}{t_0} = (1+\varepsilon)^2 \cdot \left(1 + \frac{B_{att}}{4 \cdot [(1+\varepsilon)^3 - 1]}\right)}$$

(5.59)

Using these expressions, we are able to explain the linear behavior of different t_c^l curves as a function of B_{att} (see figure 5.30). Experimental data is perfectly adjusted with expressions 5.58 and 5.59 , proving the consistency of our approach. Note that for $\varepsilon = 0$, we get the limiting behavior for the real case

$$\frac{t_c^1(0, B_{att})}{t_0} = \frac{B_{att}}{4}$$

(5.60)
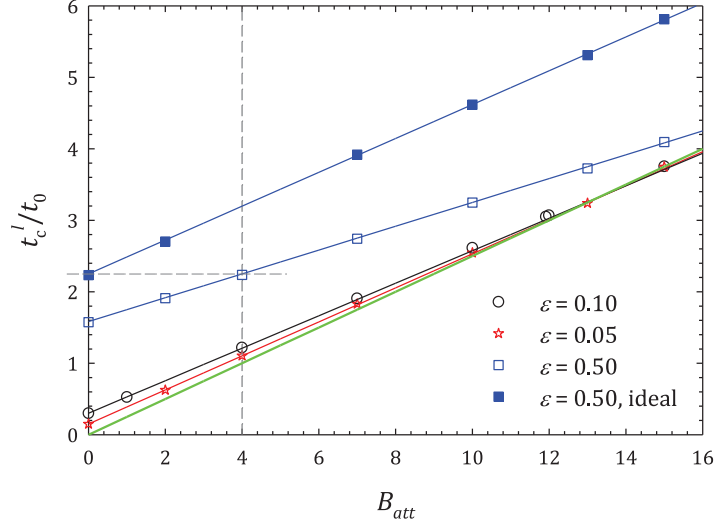
Figure 5.30: The same data in figure 5.23. Open symbols stand for the real case and filled symbols indicate ideal case. Solid lines come from the expressions 5.58 and 5.59 with corresponding values for ε and the solid green line is the limiting condition $\varepsilon = 0$ for the real case. The dashed lines correspond to $B_{att} = 4$ for the real and ideal case of $\varepsilon = 0.5$.
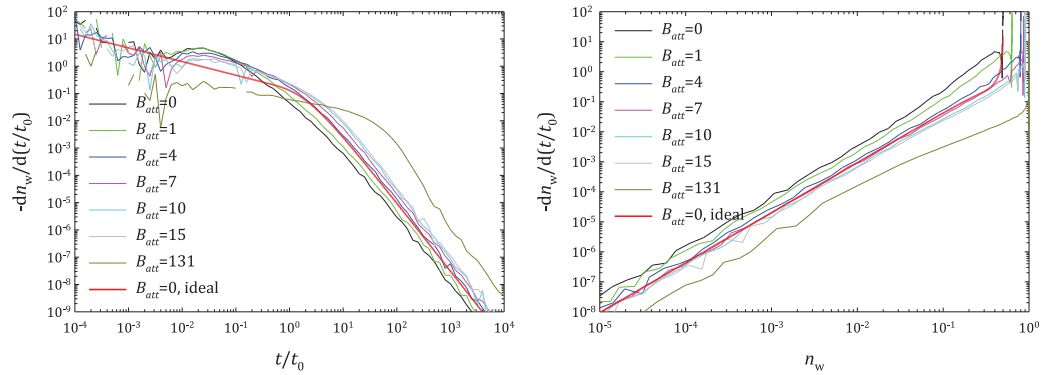
Figure 5.31: $-\mathrm{d}n_{\mathrm{w}}/\mathrm{d}(t/t_0)$ plotted as a function of time (left) and n_{w} (right) for $\varepsilon = 0.1$ and for different B_{att} as indicated in the figure.

This means, even in the limit of a contact potential (Baxter model [127]), a non zero correlation time can be defined for a given $B_{att} > 0$. It is insensitive to the exact shape of the potential (see the Noro and Frenkel law of corresponding states [27]). This is shown in figure 5.30.

Coming back to uncorrelation kinetics, we have seen that for $B_{att} = 0$, both ideal and real cases follow at large time, the relation

$$-\frac{\mathrm{d}n_\mathrm{w}}{\mathrm{d}(t/t_0)} \propto n_\mathrm{w}^{5/3} \tag{5.61}$$

From figure 5.31, we see that this behavior is affected by P, but the kinetic order remains the same. For convenience of an analytical treatment, we assume that this power law behavior is valid at any time and gives the same average correlation time to define a rate constant k_u^l,

$$-\frac{\mathrm{d}n_\mathrm{w}}{\mathrm{d}(t/t_0)} = k_\mathrm{u}^l \cdot n_\mathrm{w}^{5/3} \tag{5.62}$$

Integrating equation 5.62 for initial conditions $(n_\mathrm{w}(0) = 1/(2 - P))$ we obtain

$$n_\mathrm{w} = \left[\frac{2}{3} \cdot k_\mathrm{u}^l \cdot (t/t_0) + (2 - P)^{2/3}\right]^{-3/2} \tag{5.63}$$

which gives for the correlation time t_c^l/t_0

$$\frac{t_\mathrm{c}^l}{t_0} = \int_0^\infty n_\mathrm{w} \cdot \mathrm{d}(t/t_0) = \int_0^\infty \left[\frac{2}{3} \cdot k_\mathrm{u}^l \cdot (t/t_0) + (2 - P)^{2/3}\right]^{-3/2} \cdot \mathrm{d}(t/t_0) \tag{5.64}$$

Substituting $u = 2/3 \cdot k_\mathrm{u}^l \cdot (t/t_0) + (2 - P)^{2/3}$ and $\mathrm{d}u = 2/3 \cdot k_\mathrm{u}^l \cdot \mathrm{d}(t/t_0)$, we get

$$\frac{t_\mathrm{c}^l}{t_0} = \frac{3}{k_\mathrm{u}^l} \cdot (2 - P)^{-1/3} \tag{5.65}$$

Identifying with equation 5.50, we get

$$k_\mathrm{u}^l = \frac{3 \cdot (1 - P) \cdot (2 - P)^{-1/3}}{k_1(\varepsilon) \cdot k_2^l(\varepsilon)} \tag{5.66}$$

To check the consistency of the obtained expression, we compare in figure 5.32 equations 5.63 and 5.32 for the ideal case at $P = 0$ and $\varepsilon = 0.1$. We see that curves behave not very differently and give by definition the same value for the average correlation time.
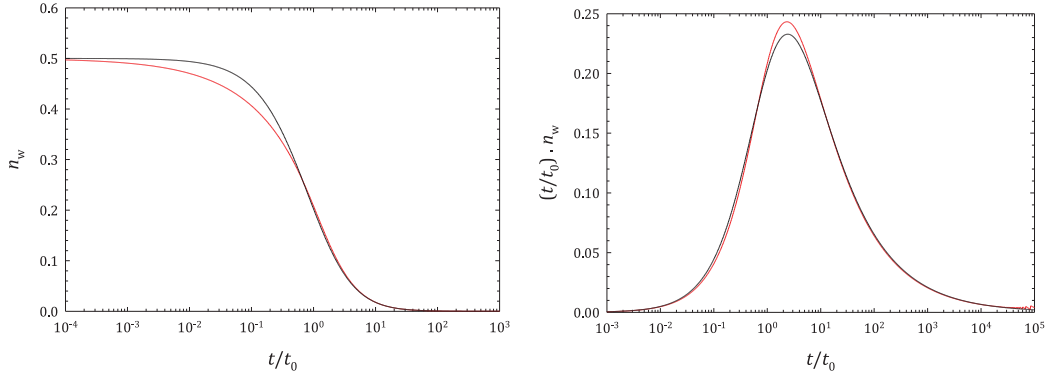
Figure 5.32: Evolution of n_{w} as a function of time (left) and evolution of $(t/t_0) \cdot n_{\mathrm{w}}$ as a function of time (right) obtained from equation 5.63 for the ideal case with $P = 0$ and $\varepsilon = 0.1$ (in black) and equation 5.32 (in red).

What is a correlated couple?

For a couple starting at a distance $d \cdot (1+\varepsilon)$, the uncorrelation process can be viewed as a kinetic reaction with order $5/3$ and normalized rate constant k_{u}^l dependent on ε, P and l. But we have seen that couples in the well are entitled to many exits and returns before they leave the well for ever. Nevertheless, we can define a finite average time spent in the well and give an expression for the evolution of the fraction of couples in the well.

In figure 5.33 (left), we plot the mean square displacement of monomers $\langle r^2(t) \rangle / d^2$ as a function of time for $P = 0$, $\varepsilon = 0.1$ and for various s_{T}. We see some very minor defects in the beginning and later, it recovers the expected linear behavior ($\langle r^2(t) \rangle / d^2) = 2 \cdot (t/t_0)$ in this case). This means that after some time, monomers act as free monomers and this supports our previous finding that at long times, all the monomers tend to uncorrelate and move apart. Now, if we plot the apparent diffusion coefficient $(\langle r^2(t) \rangle / d^2)/(t/t_0)$ as a function of time (figure 5.33 (right)), we clearly see a distortion at small time. This happens close to the average time when two monomers starting at a distance $d \cdot (1 + \varepsilon)$ feel the hard core repulsion of the other. The average time required for the first contact is $\varepsilon^2/2$. After, it recovers the linear behavior giving the expected diffusion coefficient $2 \cdot D_1^{\mathrm{T}}$. Now, the question arises, whether it is possible to describe a characteristic length, above which we can consider a couple to be uncorrelated.

To study this, we record the distribution of the farthest distance traveled by a monomer between an exit and subsequent entrance, termed as $r_{\max}$. We also monitor the maximum of $r_{\max}$, denoted by $r_{\max\_\max}$. This is updated each time a monomer returns to the well after traveling a distance longer than the previous $r_{\max\_\max}$. In figure 5.34 we plot, $r_{\max\_\max}^2$ as a function of time. We clearly see that $r_{\max\_\max}$ diverges and has a behavior similar to that of the mean square

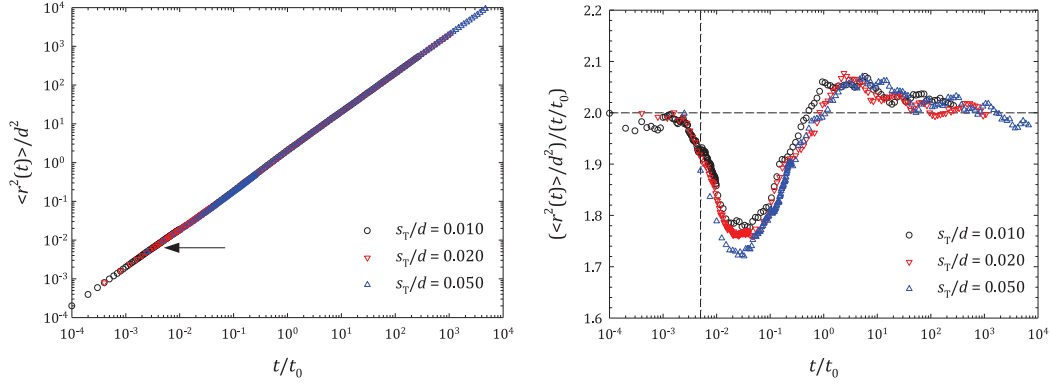Figure 5.33: MSD of the monomer (left) and relative diffusion coefficient of the couple (right) as a function of time for various Brownian step lengths. The arrow points to the defect (see text). The vertical dashed line corresponds to the average time required for the first contact.
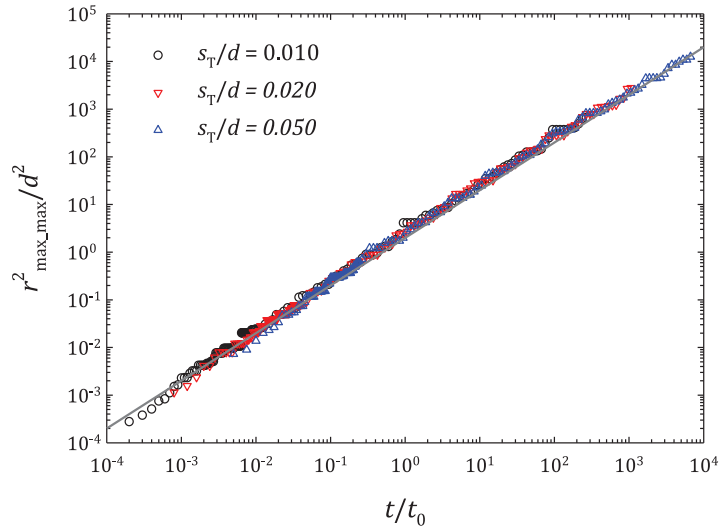
Figure 5.34: $r^2_{\mathrm{max\_max}}/d$ plotted as a function of time for various Brownian step lengths. The gray line is $2t/t_0$.
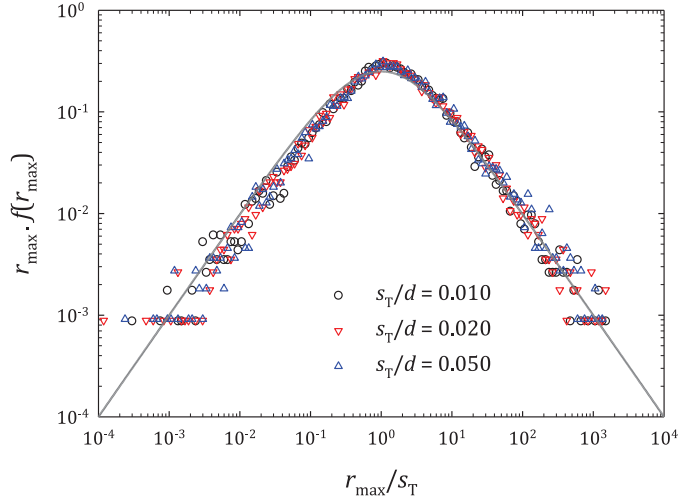
Figure 5.35: Distribution of the maximum distance traveled by a couple between an entrance and an exit for various Brownian step lengths as in figure. The gray line indicates the function 5.67.

displacement (this is certainly an intrinsic property of a Brownian motion in $\mathbb{R}^3$) and hence no characteristic distance could be defined beyond which a couple will never return into the well. We know, $r_{\max}$ will be dependent on the step size s_T and in figure 5.35 we plot the distribution of $r_{\max}$ on a log scale of $r_{\max}$, normalized by s_T. All distributions superimpose for various s_T and can be correctly fitted with

$$r_{\max} \cdot f(r_{\max}) = \frac{r_{\max}}{s_T} \left(1 + \frac{r_{\max}}{s_T}\right)^{-2} \tag{5.67}$$

This means that the probability density that a particle has traveled a maximum distance $r_{\max}$ before returning to the well is

$$f(r_{\max}) = \frac{1}{s_T} \left(1 + \frac{r_{\max}}{s_T}\right)^{-2} \tag{5.68}$$

The diverging first moment indicates that no characteristic maximum distance traveled can be defined for a couple that comes back to the well.

From above observations, we see that it is not possible to define any specific correlation range, after which particles cannot come back. Hence we have no other alternatives other than arbitrarily identifying correlated couples to be the ones lying in the well. This gives for our kinetic model (figure 5.36), $n_w \equiv C_c/C_0$. But this is a very strong simplification, considering multiple exits and returns they make. Moreover, this hypothesis implies that a fraction of couples which start in range endures an "instant" uncorrelation to respect $n_w(t \to 0) = 1/(2 - P)$.

Under these assumptions, we can relate k_u^l to K_u as follows. Equation 5.62,
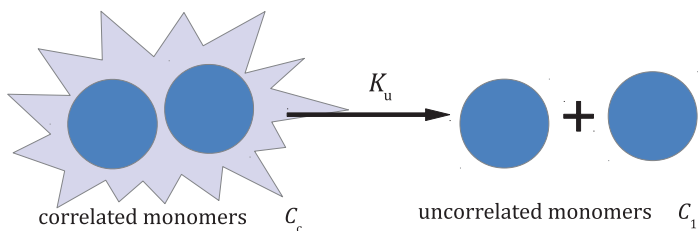
Figure 5.36: Schematic of uncorrelation reaction.

gives

$$-\frac{\mathrm{d}(2 \cdot C_\mathrm{c}/C_0)}{\mathrm{d}(t/t_0)} = k_\mathrm{u}^l \cdot \left(\frac{2 \cdot C_\mathrm{c}}{C_0}\right)^{5/3} \tag{5.69}$$

On rearrangement gives

$$-\frac{\mathrm{d}C_\mathrm{c}}{\mathrm{d}t} = \frac{2^{2/3} \cdot k_\mathrm{u}^l}{t_0 \cdot C_0^{2/3}} \cdot C_\mathrm{c}^{5/3} \tag{5.70}$$

Comparing with kinetic equations introduced before (figure 5.11), we can identify K_u as

$$K_\mathrm{u} = \frac{2^{2/3} \cdot k_\mathrm{u}^l}{t_0 \cdot C_0^{2/3}} \tag{5.71}$$

Due to the instantaneous uncorrelation described above, kinetic equations 5.21 and 5.22 need to be modified accordingly. This will be discussed in section 5.5.

5.4.3 Patchy couple - patch locking time for $B_{att} = \infty$

At infinite B_{att}, we study the time taken to form the patchy link for the real case (see figure 5.37). We start from the same initial condition as in the previous case but with randomly oriented patches and we also allow rotational motion of the particles along with the translational motion. As $B_{att} = \infty$, all couples react since they do not leave the well. In the course of the simulation, we monitor the number of bonded couples and the time of bonding. Thus, we can have the distribution of patchy bonding time t_p/t_0. See figure 5.38 for an example. When χ becomes small, it takes in average more time to complete the reaction, shifting the distribution towards larger times. In figure 5.39, we plot the average patch locking time as a function of χ^2. As expected, $\langle t_\mathrm{p}\rangle/t_0$ increases with decreasing χ, but we were not able to find any expression which fits the curve. It seems to approach a power law where $\langle t_\mathrm{p}\rangle$ is inversely proportional to χ and we have no particular evidence to claim it. In literature there are results for rotating colloids with a single patch [128], which follow a similar trend but differing in the absolute value of the rate constant. A study regarding the effect of number, position and coverage of patches on the average patch time will be an interesting study, but out of scope for the present work.
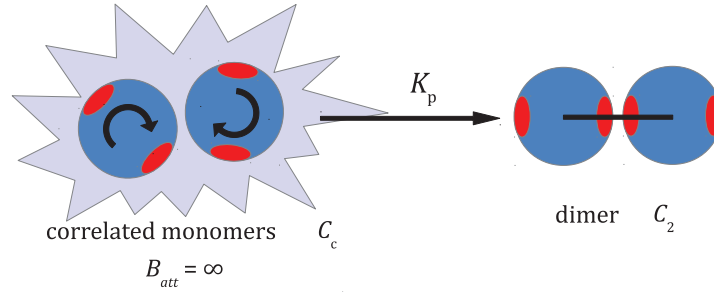
Figure 5.37: Schematic of reaction for section 5.4.3.
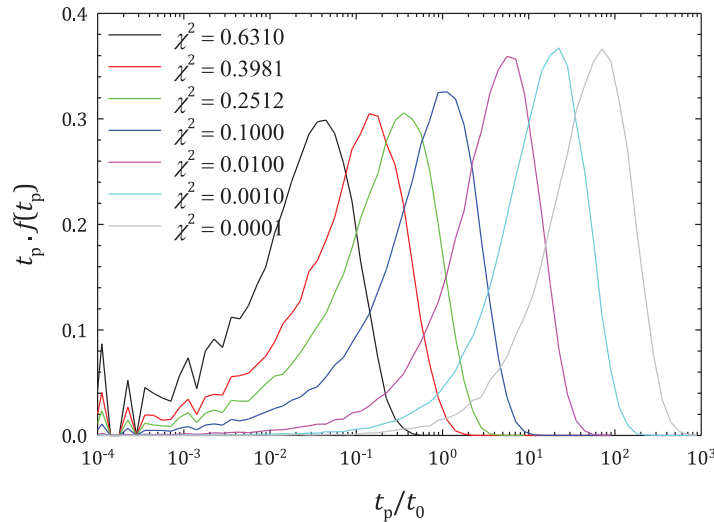
Figure 5.38: Distribution of t_p/t_0 for various χ as indicated in the figure for $B_{att} = \infty$. The area below each curve is 1.

We tried to rescale the distribution curves using $\langle t_\mathrm{p} \rangle / t_0$ as in figure 5.40. We see that it is χ dependent and as $\chi \to 0$, it seems to reach a limiting behavior, of the form $y = x \cdot \exp(-x)$.

We also monitor the fraction of patchy bonds formed as a function of time ($N_\mathrm{p}(t)$), as plotted in figure 5.41. We see that with increasing χ, the initial fraction of bonds, denoted by $N_\mathrm{p}(0)$ increases. We already know that the probability that two monomers have their patch aligned is equal to χ^2 and we recover this behavior. However, we are not interested in this and look for the time evolution of unbound fraction of couples. So, we use $(N_\mathrm{p}(t) - N_\mathrm{p}(0))/(N_0 - N_\mathrm{p}(0))$ instead of $N_\mathrm{p}(t)$ and rescale this plot in time using $\langle t_\mathrm{p} \rangle$ as in figure 5.42, so that the function varies from 0 to 1. We see that this plot also depends on χ and as $\chi \to 0$, we have a limiting
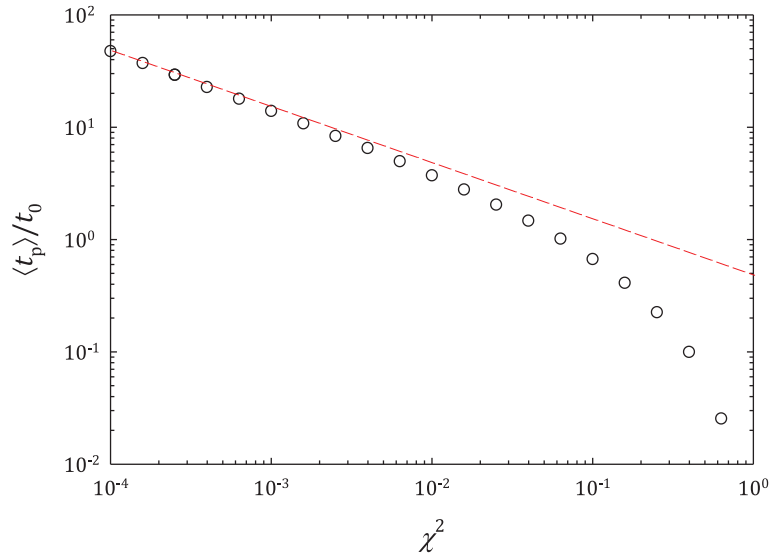
Figure 5.39: $\langle t_{\mathrm{p}} \rangle / t_0$ plotted as a function of χ^2. The dashed line has a slope $1/2$.
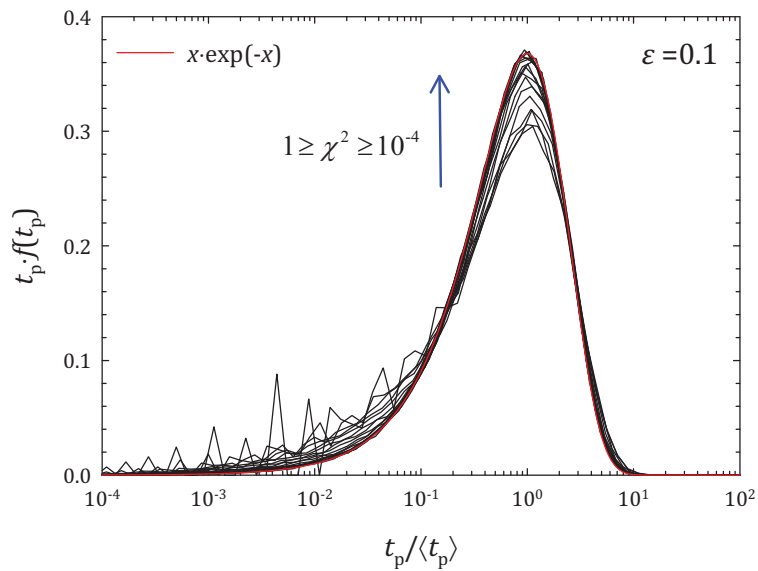
Figure 5.40: Distribution of patchy bonding time rescaled using $\langle t_{\mathrm{p}} \rangle / t_0$. The red curve is the equation of the form $x \cdot \exp(-x)$.
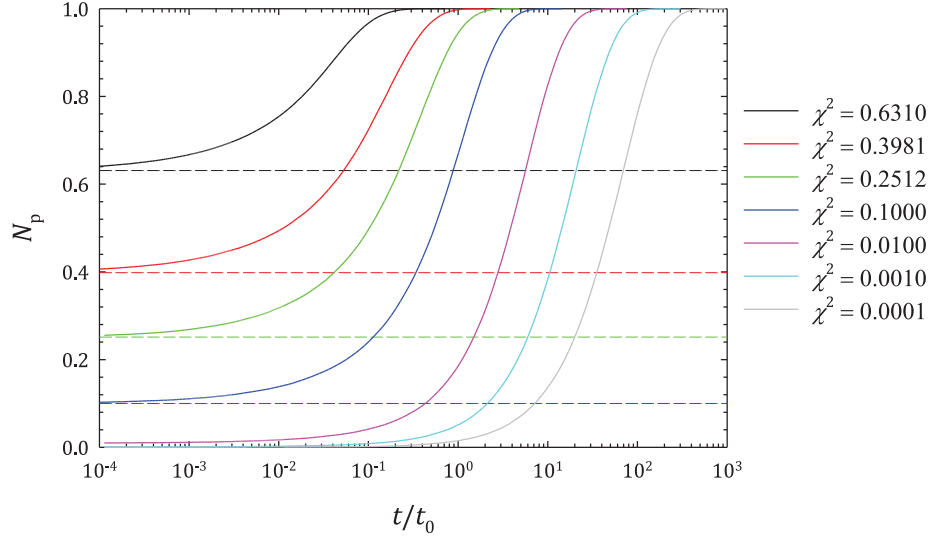
Figure 5.41: Fraction of patchy bonds formed as a function of time for various χ as indicated in the figure. The dashed lines represent the corresponding χ^2.

behavior, which could be explained using an exponential growth

$$n_{\mathrm{p}} = \frac{N_{\mathrm{p}}(t) - N_{\mathrm{p}}(0)}{N_0 - N_{\mathrm{p}}(0)} = 1 - \exp\left(-\frac{t}{\langle t_{\mathrm{p}}\rangle}\right) \tag{5.72}$$

Differentiating with respect to time, we get

$$\frac{\mathrm{d}n_{\mathrm{p}}}{\mathrm{d}(t/t_0)} = \frac{t_0}{\langle t_{\mathrm{p}}\rangle} \cdot \left(\exp -\frac{t}{\langle t_{\mathrm{p}}\rangle}\right) \tag{5.73}$$

On comparison with previous equation, we get

$$\frac{\mathrm{d}n_{\mathrm{p}}}{\mathrm{d}(t/t_0)} = \frac{t_0}{\langle t_{\mathrm{p}}\rangle} \cdot (1 - n_{\mathrm{p}}) \tag{5.74}$$

Here, we can unambiguously write the fraction of unreacted couples in the well as correlated couples. As $P = 1$ none of them can leave the well at any time. This gives $C_{\mathrm{c}} + C_2 = C_0/2$. At $t = 0$, no dimers are formed and we have $C_{\mathrm{c}}(0) = C_0/2$. Using the definition of n_{p}, we have

$$n_{\mathrm{p}} = \frac{2 \cdot C_2}{C_0} = 1 - \frac{2 \cdot C_{\mathrm{c}}}{C_0} \tag{5.75}$$

Comparing with equation 5.72, we get

$$\frac{2 \cdot C_{\mathrm{c}}}{C_0} = \exp\left(-\frac{t}{\langle t_{\mathrm{p}}\rangle}\right) \tag{5.76}$$

Differentiating with respect to time, we get

$$\frac{dC_c}{dt} = \frac{1}{\langle t_p \rangle} \cdot C_c \quad , \chi \to 0, B_{att} = \infty \tag{5.77}$$

This means that patchy bond formation reaction of a correlated couple is a first order reaction with rate constant $K_p = 1/\langle t_p \rangle$ as $\chi \to 0$.
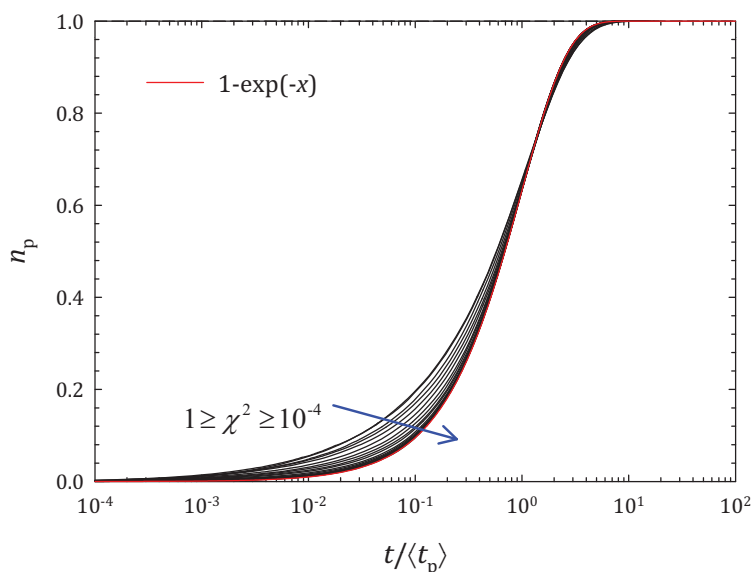
Figure 5.42: Fraction of patchy bonds formed, but modified for links formed at zero time for various χ^2 ranging from 1 to 10^{-4}. The red curve is coming from equation 5.72.

5.4.4 Patchy couple - patch locking kinetics for $B_{att} < \infty$

In this section, we deal with a finite B_{att} (see figure 5.43). This time, couples can escape the well. Some of the escaped particles may return and form patchy bonds later or continue this process of exit and return and some eventually escape definitely and never form a bond. This means that the reaction never reaches total completion.

This can be clearly seen in figure 5.44, where we plot the effect of B_{att} and χ on n_p. These figures could be compared with figure 5.42 for $B_{att} = \infty$. We see that for a given $B_{att} < \infty$ (consider $B_{att} = 0$ in figure 5.44), the plateau value for n_p never reaches 1 but a lower value which depends on χ. We also see that with increasing B_{att}, the plateau gets higher for a given χ. These behaviors are expected but we are interested in predicting the plateau values from our previous study.

Comparing the case with $B_{att} = \infty$, we have seen that for $\chi \to 0$, the reaction is first order and n_p is described by an exponential growth to a plateau value of 1 with a single relaxation time $\langle t_p \rangle$. As B_{att} becomes finite, we know there also exist an average time spent in the well t_c. To a first approximation, we assume that patchy
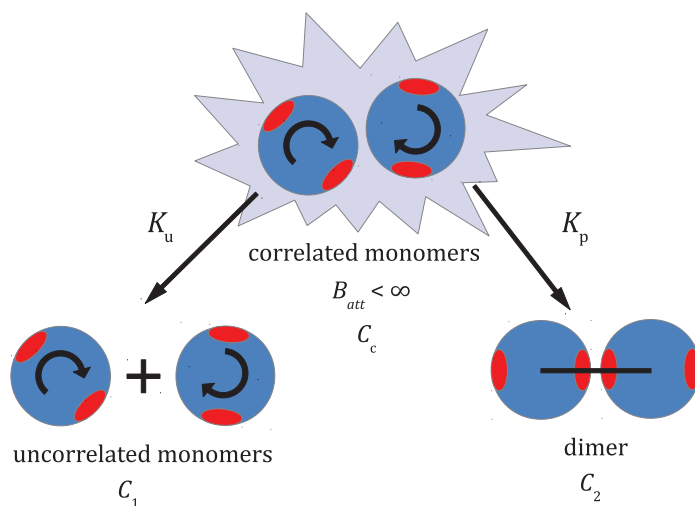
Figure 5.43: Schematic of reaction for section 5.4.4.
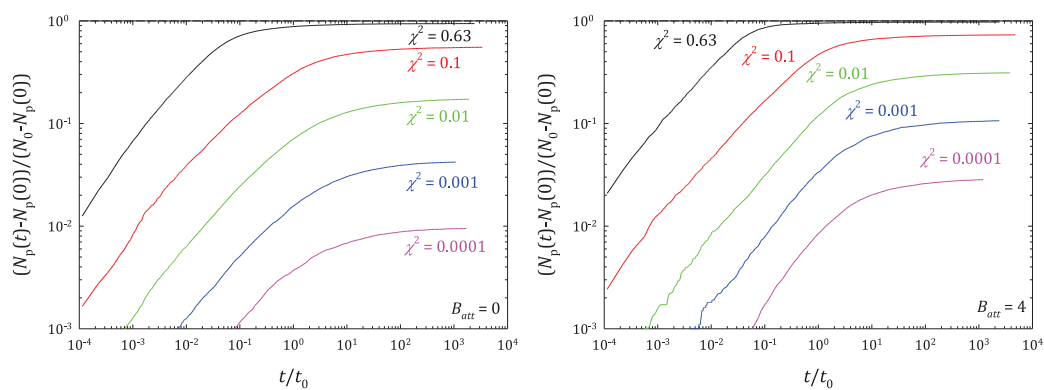
Figure 5.44: Evolution of n_p as a function of time at $B_{att} = 0$ (left) and $B_{att} = 4$ (right) for various χ as indicated in figure and with $\varepsilon = 0.1$.
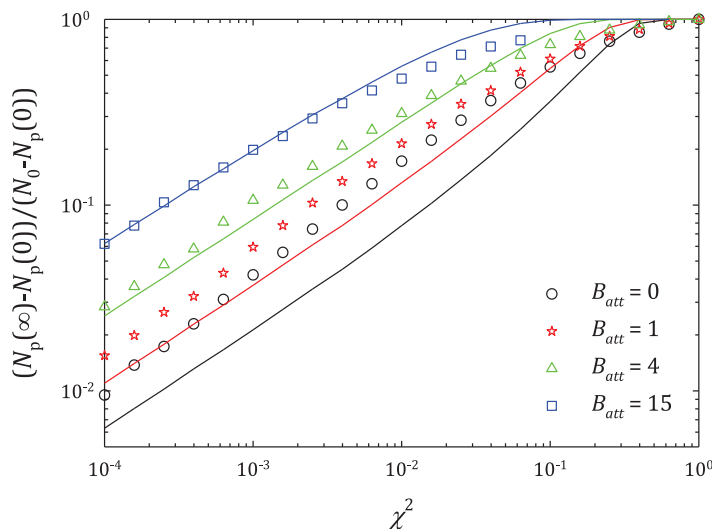
Figure 5.45: Evolution of $n_{\mathrm{p}}(\infty)$ as a function of χ^2 for various B_{att} as indicated in the figure. Solid curves come from the equation 5.78 using values of t_{c} and $\langle t_{\mathrm{p}} \rangle$ for corresponding χ and B_{att} obtained from figures 5.30 and 5.39.

bond formation at a finite B_{att} is also a first order reaction that depends only on the time spent in the well. So we can write the extent of the reaction at large time, $n_{\mathrm{p}}(\infty)$ to be

$$n_{\mathrm{p}}(\infty) = 1 - \exp\left(-\frac{t_{\mathrm{c}}}{\langle t_{\mathrm{p}} \rangle}\right) \quad , \chi \to 0 \tag{5.78}$$

To check the validity of this expression, we plot in figure 5.45 plateau values of n_{p} as a function χ^2 for various B_{att} and values calculated using equation 5.78. For lower B_{att} and lower χ, higher conversion is obtained. This could be explained as follows: we know that the reaction takes place inside the well in a process mainly involving rotational motion. When couples leave the well, they still perform rotational motion and continue relaxing their orientations. When they come back, they require in average lesser time to find the complementary patch leading to faster kinetics and higher conversion. As B_{att} becomes higher, couples seldom leave the well and hence a close value with the expected behavior is recovered. However, we see that for large χ, this expression does not give any good results as reaction has no more first order kinetics.

In figure 5.46, we plot the variation of $n_{\mathrm{p}}(\infty)$ as a function of $(t_{\mathrm{c}}/\langle t_{\mathrm{p}} \rangle)$ for various B_{att} compared to the predicted expression 5.78. We see that this expression is valid only when B_{att} is large and for very low values of $(t_{\mathrm{c}}/\langle t_{\mathrm{p}} \rangle)$ (meaning, for very small patches, since t_{c} does not depend on patch size). When couples stay closer for longer time due to whatever reason (steric, high concentration, secondary interaction etc.) the reaction should follow the expected first order behavior.
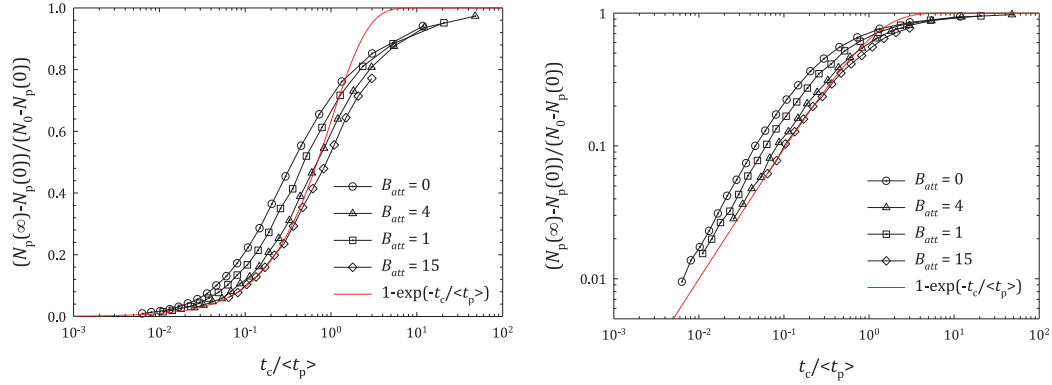
Figure 5.46: Evolution of $n_\mathrm{p}(\infty)$ as a function of $(t_\mathrm{c}/\langle t_\mathrm{p}\rangle)$ in lin-log (left) and log-log (right) scales. The red curve shows $1 - \exp(-t_\mathrm{c}/\langle t_\mathrm{p}\rangle)$.

Kinetic approach

Considering the reaction scheme in figure 5.43 and using the same notations as before, we can write

$$C_1 + 2 \cdot C_2 + 2 \cdot C_\mathrm{c} = C_0 \tag{5.79}$$

The rate equations are

$$\frac{\mathrm{d}C_2}{\mathrm{d}t} = K_\mathrm{p} \cdot C_\mathrm{c} \tag{5.80}$$

$$\frac{\mathrm{d}C_1}{\mathrm{d}t} = 2 \cdot K_\mathrm{u} \cdot C_\mathrm{c}^{5/3} \tag{5.81}$$

$$\frac{\mathrm{d}C_\mathrm{c}}{\mathrm{d}t} = -K_\mathrm{p} \cdot C_\mathrm{c} - K_\mathrm{u} \cdot C_\mathrm{c}^{5/3} \tag{5.82}$$

Also, we have the initial condition: as $t = 0$, $2 \cdot C_\mathrm{c}/C_0 = 1/(2 - P)$ and hence $C_1/C_0 = (1 - P)/(2 - P)$. Changing to our reduced variables, and recalling $K_\mathrm{p} = k_\mathrm{p}/t_0 = 1/\langle t_\mathrm{p}\rangle$ and $K_\mathrm{u} = 2^{2/3} \cdot C_0^{-2/3} \cdot t_0^{-1} \cdot k_\mathrm{u}^l$, we can write

$$\frac{\mathrm{d}(C_2/C_0)}{\mathrm{d}(t/t_0)} = k_\mathrm{p} \cdot \frac{C_\mathrm{c}}{C_0} \tag{5.83}$$

$$\frac{\mathrm{d}(C_1/C_0)}{\mathrm{d}(t/t_0)} = k_\mathrm{u}^1 \cdot \left(\frac{2 \cdot C_\mathrm{c}}{C_0}\right)^{5/3} \tag{5.84}$$

$$\frac{\mathrm{d}(2 \cdot C_\mathrm{c}/C_0)}{\mathrm{d}(t/t_0)} = -k_\mathrm{p} \cdot \frac{2 \cdot C_\mathrm{c}}{C_0} - k_\mathrm{u}^1 \cdot \left(\frac{2 \cdot C_\mathrm{c}}{C_0}\right)^{5/3} \tag{5.85}$$

Integrating the equation 5.85 gives the amount of unreacted couples in the well

at any time t,

$$\frac{2 \cdot C_{\mathrm{c}}}{C_0} = \left[\frac{\dfrac{k_{\mathrm{p}}}{k_{\mathrm{u}}^1}}{\exp\left(\dfrac{2}{3} \cdot k_{\mathrm{p}} \cdot \dfrac{t}{t_0}\right)\left(1 + \dfrac{k_{\mathrm{p}}}{k_{\mathrm{u}}} \cdot (2-P)^{2/3}\right) - 1} \right]^{3/2} \tag{5.86}$$

When $1 \ll (t/t_0)$, the exponential term dominates and the expected power law behavior is not recovered (see 5.63). When $2/3 k_{\mathrm{p}} \cdot (t/t_0) \ll 1$ we can write the exponential function as a series up to the second term, giving

$$\frac{2 \cdot C_{\mathrm{c}}}{C_0} \sim \left[\frac{\dfrac{k_{\mathrm{p}}}{k_{\mathrm{u}}^1}}{\left(1 + \dfrac{2}{3} \cdot k_{\mathrm{p}} \cdot \dfrac{t}{t_0}\right)\left(1 + \dfrac{k_{\mathrm{p}}}{k_{\mathrm{u}}^1} \cdot (2-P)^{2/3}\right) - 1} \right]^{3/2} \tag{5.87}$$

This equation shows a power law behavior under the condition $k_{\mathrm{p}}/k_u \cdot (2P)^{2/3} \ll 2/3 k_{\mathrm{p}} \cdot (t/t_0)$, giving

$$\frac{2 \cdot C_{\mathrm{c}}}{C_0} \simeq \left[\frac{2}{3} \cdot k_{\mathrm{u}}^1 \cdot \frac{t}{t_0} \right]^{3/2} \tag{5.88}$$

So, the power law behavior is only seen in between $3/2 \cdot (2-P)^{2/3} \cdot /k_{\mathrm{u}}^1 \ll t/t_0$ and $t/t_0 \ll 3/2/k_{\mathrm{p}}$. When no patch is present, $k_{\mathrm{p}} = 0$, and equation 5.86 reduces to the expected equation 5.63.

To visualize this, we plot in figure 5.47 equations 5.86 and 5.63 for various k_{p} (various χ) and for a given P. We see that the power law behavior is only recovered in a specified range explained by the conditions to obtain equation 5.88. Results from simulation are presented in figure 5.48. We clearly see the power law behavior is preserved all along the time (for large time), whatever P and χ are, even for large χ (large k_{p}). As χ becomes smaller, the non patchy behavior 5.63 is approached. The exponential cut off in the kinetic model significantly underestimates the number of couples in the well and thus the average time spent in the well.

From equation 5.83, we see the fraction of patches formed is simply proportional to the integral of equation 5.86

$$\frac{2 \cdot C_2}{C_0} = \int\limits_0^{t/t_0} k_{\mathrm{p}} \cdot \left[\frac{\dfrac{k_{\mathrm{p}}}{k_{\mathrm{u}}}}{\exp\left(\dfrac{2}{3} \cdot k_{\mathrm{p}} \cdot x\right) \cdot \left(1 + \dfrac{k_{\mathrm{p}}}{k_{\mathrm{u}}} \cdot (2-P)^{2/3}\right) - 1} \right]^{3/2} \mathrm{d}x \tag{5.89}$$

with initial conditions: at $t/t_0 = 0$, $2 \cdot C_2/C_0 = 0$. Rearranging it takes the form

$$\frac{2 \cdot C_2}{C_0} = \frac{k_{\mathrm{p}}^{5/2}}{k_{\mathrm{u}}^{3/2}} \cdot \int\limits_0^{t/t_0} (B \cdot \exp(A \cdot x) - 1)^{-3/2} \cdot \mathrm{d}x \tag{5.90}$$
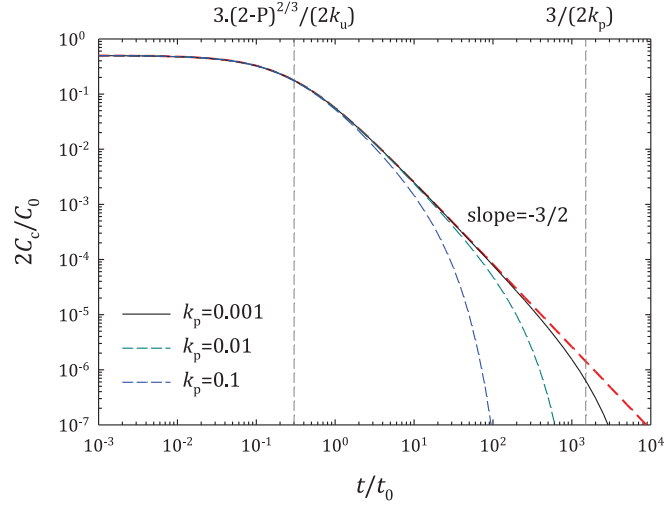
Figure 5.47: Comparison of evolution of $2 \cdot C_\mathrm{c}/C_0$ for a non patchy system (equation 5.63) and the predicted behavior for patchy system (equation 5.86) for $P = 0$, $\varepsilon = 0.1$ real case and various k_p (10^{-1}, 10^{-2} and 10^{-3}). The bounding values to observe the power law behavior are shown by the black solid curve with $k_\mathrm{p} = 0.001$.
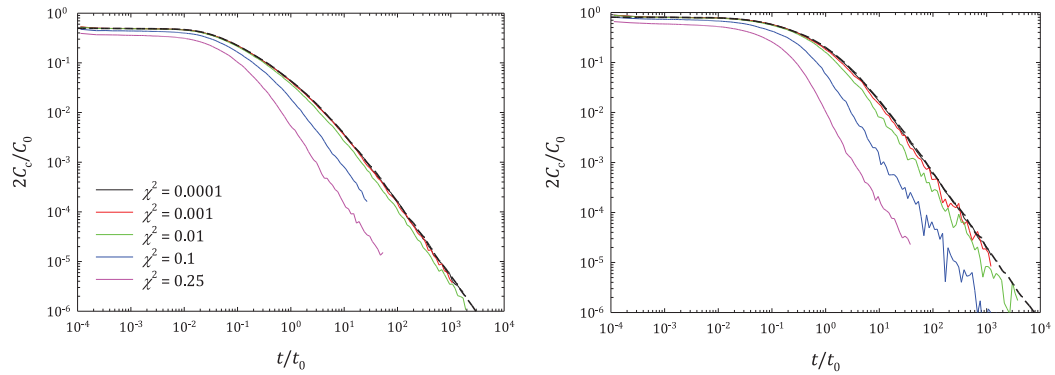
Figure 5.48: Evolution of $2C_\mathrm{c}/C_0$ for $\varepsilon = 0.1$ and $P = 0$ (left) and $P = 0.7513$ (right) for various χ. The black dashed curve is the behavior for non patchy systems under same conditions.
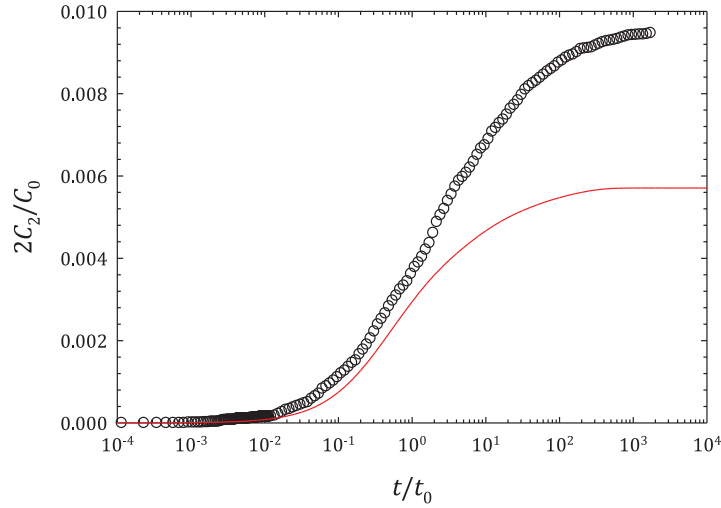
Figure 5.49: Evolution of $2 \cdot C_2/C_0$ as a function of time for $\varepsilon = 0.1$ $\chi^2 = 0.0001$ and $P = 0$ ($k_u = 7.9130$ and $k_p = 0.0210$). The red curve shows the prediction from the kinetic approaches equation 5.91.

where $x = t/t_0$, $A = 2/3k_p$ and $B = k_p/k_u \cdot (2 - P)^{2/3} + 1$ and the solution is given by

$$\frac{2 \cdot C_2}{C_0} = 3 \cdot \left(\frac{k_p}{k_u}\right)^{3/2} \cdot \left[\frac{1}{\sqrt{(B-1)}} + \arctan(\sqrt{B-1}) - \frac{1}{\sqrt{B \cdot \exp(A \cdot \frac{t}{t_0}) - 1}} \right.$$
$$\left. - \arctan\left(\sqrt{B \cdot \exp\left(A \cdot \frac{t}{t_0}\right)}\right) \right]$$

(5.91)

The amount of dimers formed at the plateau is

$$\frac{2 \cdot C_2}{C_0}(\infty) = 3 \cdot \left(\frac{k_p}{k_u}\right)^{3/2} \cdot \left[\frac{1}{\sqrt{B-1}} + \arctan\left(\frac{1}{\sqrt{B-1}}\right) - \frac{\pi}{2} \right]$$

(5.92)

In figure 5.49, we compare the evolution of $2 \cdot C_2/C_0$ as a function of time for a small $\chi = 0.01$ and $P = 0$, along with the prediction from equation 5.91. Even in the most favorable case where χ is very small, the kinetic approach always underestimates the amount of couples in the well at large time and hence gives a lower amount for the number of patches formed.

To conclude, our kinetic model does not take into account the fact that the fraction of couples that is instantaneously decorrelated ($1/(2 - P)$) can return in to the well later and may get bonded. This leads to a wrong large time behavior

for the amount of correlated couples. However, this approach gives correct results in both extreme cases when $P = 1$, with small χ or when $\chi = 0$ for all P.

5.5 Complete dimerization reaction

In the case of the complete dimerization reaction, we start with a very dilute solution of particles and allow the dimer formation under no ternary collision. We proposed the mechanism for dimerization in figure 5.11 and wrote corresponding rate equations. But in the light of our previous results, we see that equations 5.21 and 5.22 are not correctly weighted. When two monomers come at the edge of the interaction radius, a fraction of them gets instantaneously uncorrelated (goes out of the well) and only a fraction $1/(2-P)$ of them remains correlated (stays in the well). This means that in case of an uncorrelated collision, a fraction of χ^2 couples directly forms dimers, a fraction $(1-\chi^2)/(2-P)$ becomes correlated couples and a fraction $(\chi^2 \cdot (1-P)+1)/(2-P)$ remains as uncorrelated monomers. Also, we have found that for very low patch size, patchy bond formation is a first order reaction and the uncorrelation reaction has an order $5/3$. So, we have to correct equations 5.21 to 5.23 by these factors and replace $x_\mathrm{p} = 1$ and $x_\mathrm{u} = 5/3$. The new set of kinetic equations becomes

$$\frac{\mathrm{d}C_1}{\mathrm{d}t} = -\frac{(\chi^2 \cdot (1-P)+1)}{(2-P)} \cdot K_{1,1} \cdot C_1^2 + 2 \cdot K_\mathrm{u} \cdot C_\mathrm{c}^{5/3} \tag{5.93}$$

$$\frac{\mathrm{d}C_2}{\mathrm{d}t} = \frac{\chi^2}{2} \cdot K_{1,1} \cdot C_1^2 + K_\mathrm{p} \cdot C_\mathrm{c} \tag{5.94}$$

$$\frac{\mathrm{d}C_\mathrm{c}}{\mathrm{d}t} = \frac{(1-\chi^2)}{2 \cdot (2-P)} \cdot K_{1,1} \cdot C_1^2 - K_\mathrm{p} \cdot C_\mathrm{c} - K_\mathrm{u} \cdot C_c^{5/3} \tag{5.95}$$

Changing to our dimensionless units and using the value of $K_{1,1}$ from equation 5.9, we get

$$\frac{\mathrm{d}(C_1/C_0)}{\mathrm{d}(t/t_0)} = -\frac{(\chi^2 \cdot (1-P)+1)}{(2-P)} \cdot 8 \cdot \phi \cdot (1+\varepsilon) \cdot \left[1 + \frac{(1+\varepsilon)}{\sqrt{\frac{\pi}{3} \cdot t/t_0}}\right] \cdot \left(\frac{C_1}{C_0}\right)^2$$
$$+ k_\mathrm{u}^1 \cdot \left(\frac{2 \cdot C_\mathrm{c}}{C_0}\right) \tag{5.96}$$

$$\frac{\mathrm{d}(C_2/C_0)}{\mathrm{d}(t/t_0)} = \chi^2 \cdot 4 \cdot \phi \cdot (1+\varepsilon) \cdot \left[1 + \frac{(1+\varepsilon)}{\sqrt{\frac{\pi}{3} \cdot t/t_0}}\right] \cdot \left(\frac{C_1}{C_0}\right)^2 + \frac{t_0}{\langle t_\mathrm{p} \rangle} \cdot \frac{C_\mathrm{c}}{C_0} \tag{5.97}$$

$$\frac{\mathrm{d}(C_\mathrm{c}/C_0)}{\mathrm{d}(t/t_0)} = \frac{(1-\chi^2)}{(2-P)} \cdot 4 \cdot \phi \cdot (1+\varepsilon) \cdot \left[1 + \frac{(1+\varepsilon)}{\sqrt{\frac{\pi}{3} \cdot t/t_0}}\right] \cdot \left(\frac{C_1}{C_0}\right)^2$$
$$- \frac{k_\mathrm{u}^1}{2} \cdot \left(\frac{2 \cdot C_\mathrm{c}}{C_0}\right)^{5/3} - \frac{t_0}{\langle t_\mathrm{p}\rangle} \cdot \frac{C_\mathrm{c}}{C_0} \qquad (5.98)$$

We see that these set of equations are complex and not easily solvable. So, we use the fourth order Runge-Kutta method to get the solution numerically. In the dimerization simulations, we do not monitor the amount of monomers that belong to unreacted couples in range (correlated couples). We keep track only of the fraction of monomers C_1 and fraction of dimers C_2. This makes C_2 the only well defined measurable quantity, as C_1 contains both uncorrelated and correlated monomers.

The Smoluchowski equation 5.10 could be rearranged in terms of C_2 as

$$\frac{2 \cdot C_2/C_0}{1 - 2 \cdot C_2/C_0} = 8 \cdot \phi \cdot (1+\varepsilon) \cdot (t/t_0) \cdot \left(1 + (1+\varepsilon) \cdot \sqrt{\frac{12}{\pi}} \cdot \frac{1}{\sqrt{(t/t_0)}}\right) \qquad (5.99)$$

We have seen that this equation does not describe the obtained results when $\chi < 1$ (see figure 5.6). The χ^2 correction works only at very short times when the production of dimers from correlated couples is negligible (see figure 5.7). The $k(\chi, \infty) \cdot \chi^{1.23}$ one gives correct results for large time. Now, we have a numerical solution to the proposed kinetics and despite of its defects, we compare it with our results.

In figure 5.50, we compare the evolution of $(2 \cdot C_2/C_0)/(1 - 2 \cdot C_2/C_0)/(8\phi \cdot (1 + \varepsilon) \cdot (t/t_0))$ as a function of time for $P = 0$ and $\chi^2 = 0.1$. In the same plot, the χ^2 correction is added at short times together with our kinetic model (solution given by Runge-Kutta method) and the $k(\chi, \infty) \cdot \chi^{1.23}$ correction at large times. At small time, the χ^2 corrected Smoluchowski behavior and the kinetic curve superimpose with our results. This is expected since inefficient collisions hardly get time to produce dimers using the alternative pathway. Also, our kinetic model is designed to obey the χ^2 behavior in the beginning (see equation 5.94). At large time, as already seen, results are correctly described by the $k(\chi, \infty) \cdot \chi^{1.23}$ correction. For this given χ, the kinetic model seems to give a good qualitative behavior at both extreme limits. It must be noted that our simulation results are very sensitive at very small times, as we have only a small number of dimers formed (for example two or three dimers are formed out of the initial 10^4 monomers at time of the order of 10^{-4}).

We see in figure 5.51 for $P = 0$, as χ is decreasing, the kinetic model leads to faster reactions than those observed from our simulations. The difference is clearly seen, if we plot the evolution of the appearance of dimers $2 \cdot C_2/C_0$ (figure 5.52). We see that the kinetic model is faster, while the corrected Smoluchowski curve follows the experimental curves. Given the many non realistic assumptions of the kinetic approach, we do not propose any interpretation for that.
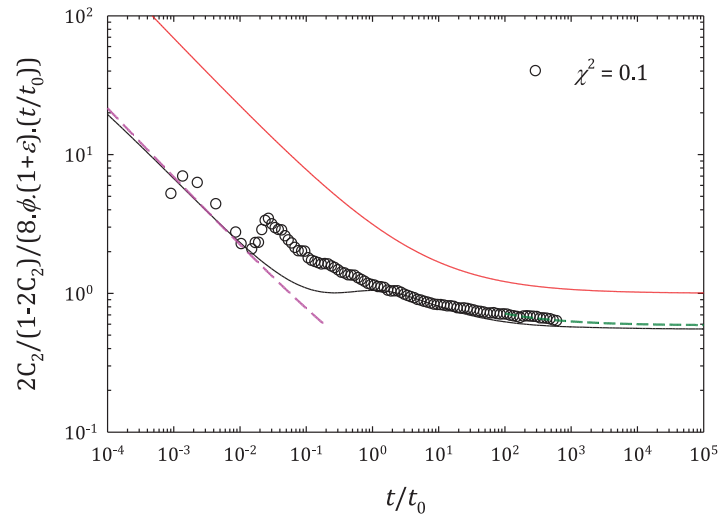
Figure 5.50: Evolution of $2 \cdot C_2/(1-2 \cdot C_2)/(8 \cdot \phi \cdot (1+\varepsilon) \cdot (t/t_0))$ as a function of time for $\varepsilon = 0.1$ and $P = 0$ for $\chi^2 = 0.1$. The red curve is the classical Smoluchowski behavior for full coverage. Dashed curves are corrected Smoluchowski curves: corrected with χ^2 (pink) and $k(\chi, \infty) \cdot \chi^{1.23}$ (green). The black curve is from our kinetic model (using $k_u = 7.913$ and $k_p = 1.493$. $\phi = 0.005$ and $L = 100$).
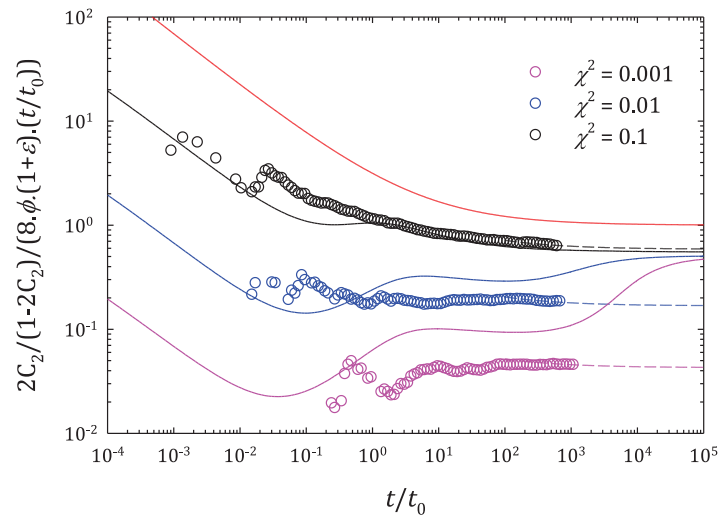
Figure 5.51: Evolution of $2 \cdot C_2/(1 - 2 \cdot C_2)/(8 \cdot \phi \cdot (1 + \varepsilon) \cdot (t/t_0))$ as a function of time for $\varepsilon = 0.1$ and $P = 0$ for various χ^2 as indicated in the figure. The solid lines are from our kinetic model and dashed curves are $k(\chi, \infty) \cdot \chi^{1.23}$ corrected Smoluchowksi behavior. $\phi = 0.005$, $L = 100$.
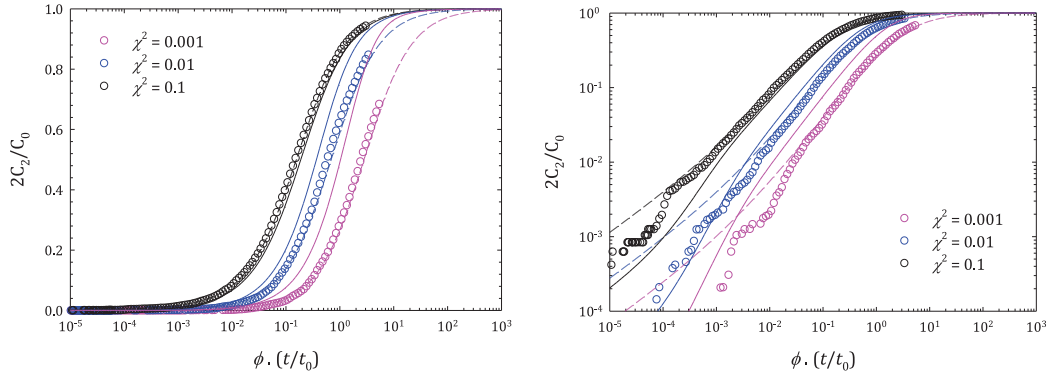
Figure 5.52: Evolution of $2 \cdot C_2/C_0$ as a function of $\phi \cdot t/t_0$ shown on left for the same set as in figure 5.51. The solid curves are from our kinetic model. The dashed curves are $k(\chi, \infty) \cdot \chi^{1.23}$ corrected Smoluchowksi behavior. On right is the same data but on a log-log scale.
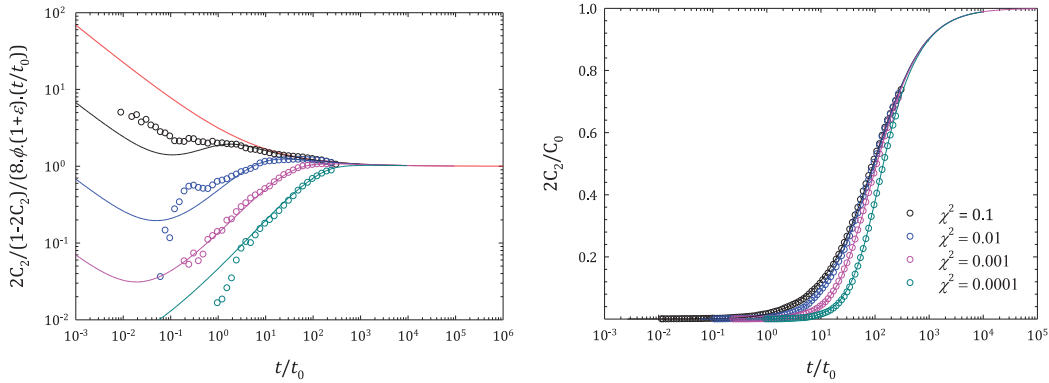
Figure 5.53: Similar plots as in figure 5.51 but for $P = 1$ and for $\varepsilon = 0.1$, $\phi = 0.001$, $L = 220$ (left). Evolution of $2 \cdot C_2/C_0$ as a function of t/t_0 for the same data (right). Solid curves corresponds to the kinetic model.

In figure 5.53, we study the case for $P = 1$. We see that for small χ, kinetics could be correctly described by our kinetic model. In this case, the complex behavior in case of inefficient collision is highly simplified by the confinement of the couple in the well leading to $k_u = 0$.

5.6 Conclusion

We studied the irreverisble aggregation of anisotropic particles and found that these reactions have a complex kinetic behavior. To simplify the approach and understand the basic reaction, we focused on patchy dimerization reactions based on the proposed kinetic model. Experimentally, we find that dimerization reactions give a linear Smoluchowski type behavior at very large time, which can be described by a modified kinetic rate equation

$$\frac{2 \cdot C_2}{C_0 - 2 \cdot C_2} = C_0 \cdot K_{1,1} \cdot k(\chi) \cdot \chi^{1.23} \cdot t \tag{5.100}$$

We find $k(\chi)$ to be a constant in the limit of small χ and large time. It is also a function of B_{att}. But we do not have enough data at the moment to present a complete study.
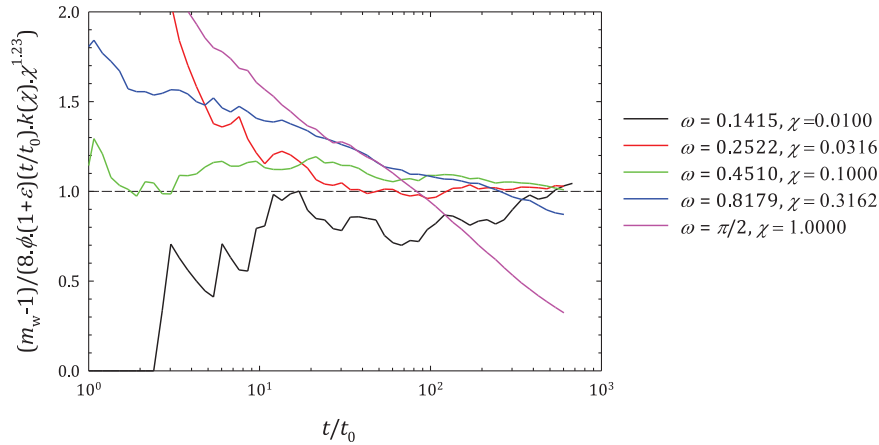
Figure 5.54: $(m_w - 1)/(8 \cdot \phi \cdot (1 + \varepsilon) \cdot (t/t_0) \cdot k(\chi) \cdot \chi^{1.23})$ plotted as a function of t/t_0 for complete polymerization reaction with $\phi = 0.001$, $B_{att} = 0$ and for various χ as indicated in the figure. The black dashed line is Smoluchowksi prediction.

In figure 5.54, we plot the $k(\chi) \cdot \chi^{1.23}$ modified rate equations for polymerization reactions under dilute conditions, where the $k(\chi)$ is obtained from dimerization reactions (see figure 5.10). Comparing with figure 5.4, we see that this correction also seems to work for polymerization reactions, when no loops are formed. Even a slight amount of loop for the larger χ shows a noticeable deviation from the predicted behavior (the case of $\chi = 0.3162$, where $N_{loop} = 0.0004$ at the final point shown in the figure).

The dynamical behavior and the average time that a couple stays in a given interaction volume were studied in detail as a function of B_{att}. We were able to give a dynamical explanation for the ideal like behavior of real polymer chains in theta solvent, using the concept of average correlation time. Unfortunately, results from our proposed kinetic model were unsatisfactory because the model incorporated many unrealistic assumptions: According to our results, the definition of a correlated couple is ambiguous and we arbitrarily set couples coming into the interaction range to be correlated. This implies that a fraction of couples coming near the edge of the interaction range will uncorrelate instantaneously. Moreover, the rotational relaxation of the patches outside the well is not accounted for in our model.

CHAPTER 6

Conclusion and Perspectives

The present thesis mainly focused on the development of Brownian Cluster Dynamics to account for directional interactions. In the new Patchy Brownian Cluster Dynamics, we used a modified Kern-Frenkel [9] model with two oppositely placed monovalent patches. A square well potential was applied to the patchy region, through which irreversible aggregation takes place. The coverage of the patch can be varied. We also have an additional isotropic square well interaction to model the solvent quality. For easiness, the well widths of both interactions were chosen to be 10% of the diameter of the particle.

To verify this new model, the algorithm was tested on single polymer chains, the simplest object that can be built using our model. To study the static properties, a large number of polymer chains were built with varying degrees of patch sizes and chain lengths. We found by studying the ideal chains that our model could be correctly described by the Freely Rotating Chain model. For the self avoiding chains, there exist two kinds of chain length crossover: from rod-like to semi-flexible chain like, and from ideal like to self avoiding behavior. The first one occurs at a chain length termed persistence length and is also applicable for ideal chains. Both of these crossovers are highly dependent on the local flexibility of the chain. For the self avoiding chain, a detailed study was carried out concerning various definitions of the persistence length given in the literature. Some persistence lengths diverged with the chain length and some others were independent on chain length. We found that even after the persistence length is passed, some real chains with very high persistence lengths were showing ideal like behavior. This observation is also visible in the case of the bond correlation function, for which a detailed analysis was carried out.

For the persistence length definition $l_3 = \langle \mathbf{R}_e^2 \rangle / (2l_b \cdot (m-1)^{2\nu})$, we saw that in the case of more locally rigid chains, there is an intermediate ideal regime before reaching the excluded volume dominated behavior which cannot be scaled using the generally used persistence lengths. The same is seen in the case of the local persistence length $l_p(k) = \langle \mathbf{r}_k \cdot \mathbf{R}_e \rangle / l_b$. In the case of bottle brush polymers, we always get the same value for $l_p(k)$. In the literature [115], it is also reported that even for very high persistence lengths, it is not possible to reach the worm like chain limit. Bottle brush chains have a fully flexible backbone and the chain flexibility is tuned using the number and length of side chains. The essential condition for the WLC behavior is that the aspect ratio ie. the ratio of the persistence length to

the thickness of the chain should be very high. Analyzing the data for bottle brush polymers from the literature, we found that with an increase of the persistence length, the chain thickness also increases in such a way that the aspect ratio does not vary. Hence the essential condition for WLC condition is never achieved. Also, we do not see any ideal like behavior for bottle brush chains.

When the persistence length is tuned by another way, without thickening the chain, as in our model, we see the ideal like regime for more locally rigid chains. When the aspect ratio is very high ($l_\mathrm{p} \gg$ thickness of the chain) the chain can grow longer without feeling the excluded volume interactions, and an ideal like behavior can be developed. The transition to the excluded volume dominated behavior occurs at the thermal blob length. From our analysis, we were able to give a phenomenological expression for this crossover.

For studying dynamics, even though we were limited by the chain length, we recover most of the expected behaviors for the translational and rotational motions.

To resume, with the study of polymer chains, we were able to recover most of the predicted behaviors for the static and dynamic properties, which prove the validity of our algorithm: individual translational and rotational motions give correct collective dynamics. We recall that hydrodynamic interactions are ignored in our approach.

To understand the kinetics of aggregation reaction through patches, we studied the basic dimerization reaction under dilute conditions. We observe that the Smoluchowski approach fails even at very dilute conditions due to the correlated motion of the monomers. We proposed a mechanism for the dimerization and studied each part of the mechanism independently. From our results, we see that, starting from the edge of an interaction range, a monomer can travel up to whatever distance it wants and still come back, meaning that there is no characteristic length beyond which it escapes for ever. Also we note that for a non patchy system, the fraction of monomers in the range decreases with time and an average time spent in the well can be rigorously defined. Its dependency on B_{att} has been perfectly explained. With an arbitrarily defined interaction radius for defining correlated couples, we tried to solve the proposed kinetic equations. Unfortunately, in the mechanism, we did not take in to account the fact that monomers can come back many times after leaving the interaction range. Hence we always underestimated the amount of dimers formed.

The analysis of the patchy aggregation indicated that all the kinetic curves can be shifted to the Smoluchowski behavior for large time using a parameter $k(\chi) \cdot \chi^{1.23}$ under very dilute conditions, in order to account for surface coverage. As $\chi \to 0$, $k(\chi)$ becomes constant and only depends on B_{att}. However, we were not able to give an explanation for the exponent.

Perspectives

In addition to the topics we have covered in this work, the new model that we have developed opens up many new directions. We can explore the phase behavior of the system in comparison with the isotropic phase diagram, characterize the diverse structures and morphologies that can be built by tuning different parameters involved in the model, study the competition between linear chains and cycles, mimic protein polymerizations, etc.

Exploration of the phase behavior

Firstly, we can consider the influence of irreversible patches on the classical phase diagram (figure 6.1) for reversible isotropic interaction. We compare different system morphologies for the patchy and non patchy cases at the same time (See figure 6.1 for snapshots of the system at $t/t_0 \sim 1073$) at regions marked by red circles on the phase diagram. We see that the aggregate structures for the patchy case are entirely different from the isotropic one. For example, we observe well packed phase of bundles of rods at $B_{att} = 4$ for $\phi = 0.10$ and $\omega = 0.2$, which contained crystalline domains. At the same time, the phase diagram indicates homogeneous gas phase, also shown in the same figure. Also, we note that a higher ω ($B_{att} = 4$ for $\phi = 0.10$ and $\omega = 0.8174$) gives more open structures rather than bundles and the amount of crystalline phase is less compared to the $\omega = 0.2$ case. For $\phi = 0.1$ at $B_{att} = 12$, we are at the coexistence region in the phase diagram, where some spherical droplet like structures containing crystalline domains are in equilibrium with the gas phase. For the patchy case with $\omega = 0.2$, we have a dense network like structure, made of highly anisotropic bundles of chains. We do not see many free particles here and we also have more crystalline domains. We will present more images from our model to compare with the isotropic phase diagram in the coming part.

Characterization of the aggregate morphology

As a function of the patch size, B_{att} and concentration, we can obtain various aggregate morphologies. Some examples are given in the following figures. Figure 6.2 shows the extreme case of $\phi = 0.01$, and $\omega = 0.2$ at four different B_{att} as indicated in figure. Figure 6.3 shows the case of $\phi = 0.1$ and $\omega = 0.2$ and similarly, figure 6.4 shows the case for $\phi = 0.1$ and $\omega = 0.8179$ at the same B_{att} as before for a comparison. All these snapshots were taken at a time $t/t_0 \sim 1073$. We see very diverse and anisotropic structures. For the dilute case with small patch (figure 6.2), depending on B_{att}, the structures vary from single chains to bundles of chains, and at very high $B_{att} = 100$, we have many clusters of small chains. In figure 6.3, we see some interpenetrating rod like structures leading to a network of bundles of chains. For the more flexible case (figure 6.4), we have highly entangled chains, which at higher B_{att} give more open network structures. We see that these structures are very complex and anisotropic. Hence, we cannot use conventional methods like the

B_{att}=12

B_{att}=4

$\omega = 0.2$ $\omega = 0.8179$
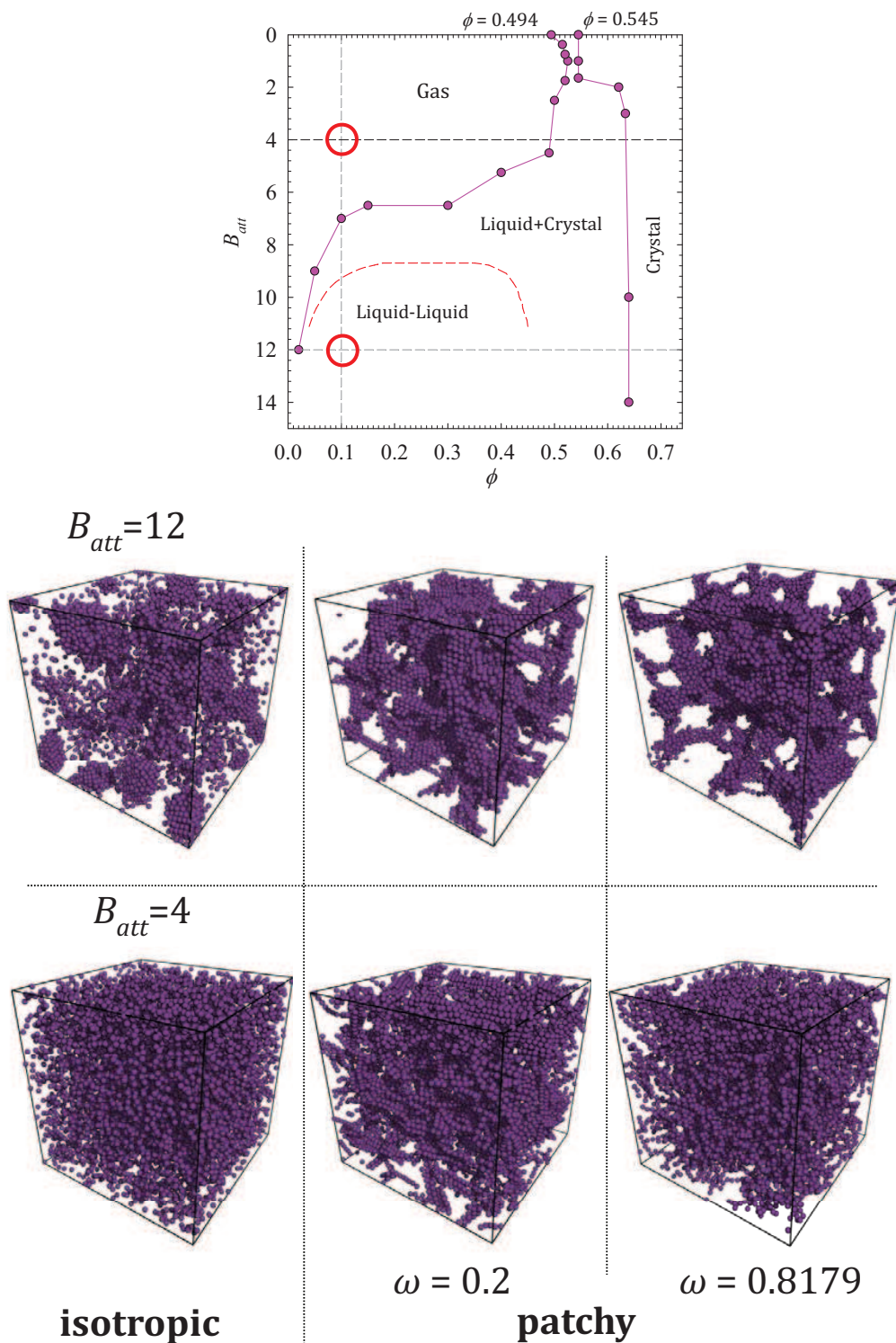
isotropic   **patchy**

Figure 6.1: Comparison of the aggregate morphologies obtained from isotropic and patchy interactions for $\phi = 0.1$ with box size $L_{\text{box}} = 37$. On top is the phase diagram for reversible isotropic interaction with $\varepsilon_0 = 0.10$. On bottom, the first row shows snapshots for $B_{att} = 12$ and the bottom row shows the same system at $B_{att} = 4$. For patchy interactions, cases with $\chi^2 = 0.0004$ ($\omega = 0.2$) and $\chi^2 = 0.1$ ($\omega = 0.8179$) are shown. $t/t_0 \sim 1073$ for all cases.

Figure 6.2: Snapshots of simulation at $t/t_0 = 1073$ for $\phi = 0.01$ and $\omega = 0.2$ for various values of B_{att} as shown in figure to compare with the phase diagram for isotropic interaction. The fractional conversion p and the number average aggregation number, m_n, are also shown. $L_{\text{box}} = 81$, $N_0 = 10149$. Different colors indicate different chains.

calculation of the pair correlation function, $g(r)$, which gives the spherical average of particle distribution for these aggregates. Other methods should be developed, like the use of inertial tensor to characterize anisotropy [129].
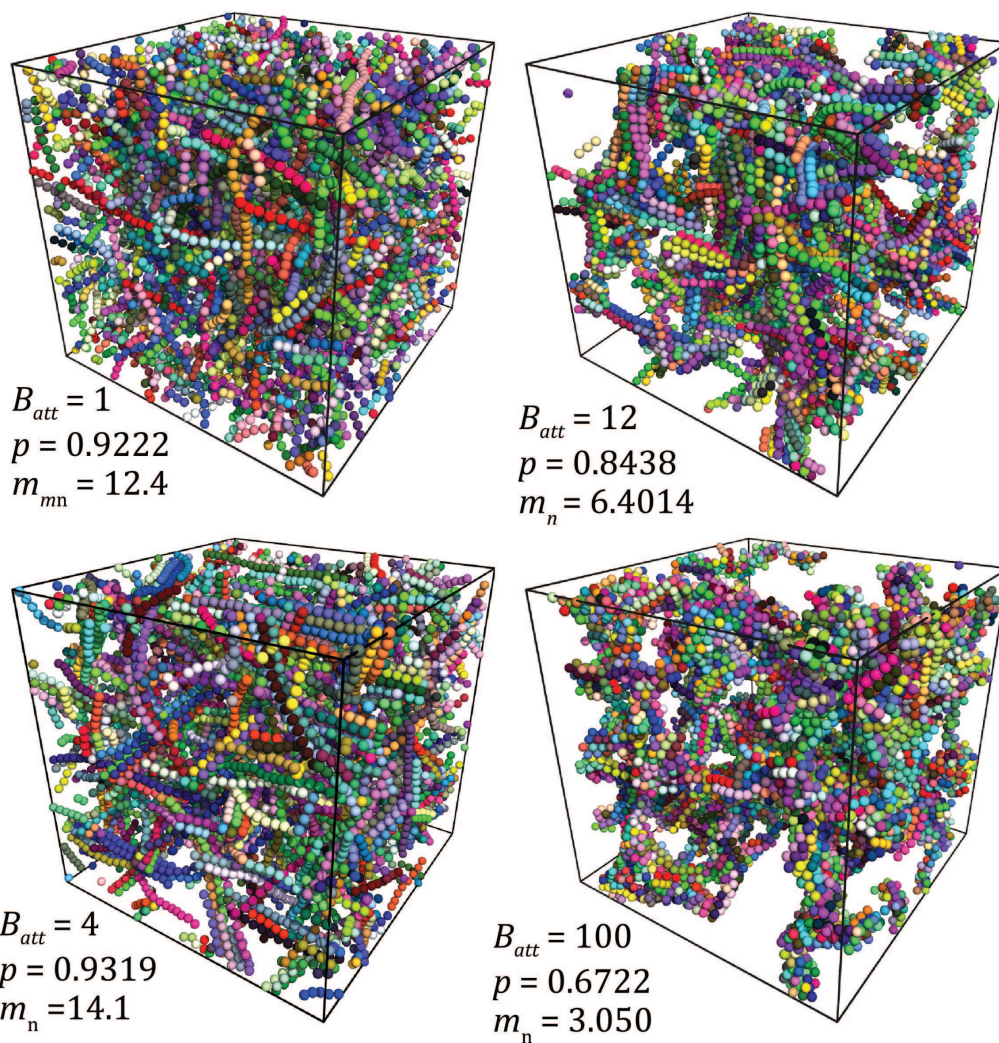
Figure 6.3: Snapshots of simulation at $t/t_0 = 1073$ for $\phi = 0.10$ and $\omega = 0.2$ for various values of B_{att} as shown in figure to compare with the phase diagram for isotropic interaction. The fractional conversion p and the number average aggregation number, m_n, are also shown. $L_{\text{box}} = 37$, $N_0 = 9674$. Different colors indicate different chains.

An interesting observation from figures 6.3 and 6.4 is that for relatively highly flexible case ($\omega = 0.8179$ or $\chi^2 = 0.1$) under a moderate isotropic interaction ($B_{att} = 12$), we find a thin network of long stretched chains, similar to structures obtained at low flexibility, but with much higher m_n. The presence of the neighboring chains (the excluded volume effect) restricts the configurations and forces stretched structures. In comparison, at very low concentration and higher flexi-

$B_{att} = 0$
$p = 0.9965$
$m_n \sim 182$

$B_{att} = 0$
$N_{\text{loop}} = 0.0337$

$B_{att} = 4$
$p = 0.9971$
$m_n \sim 220$
$N_{\text{loop}} = 0.0364$

$B_{att} = 12$
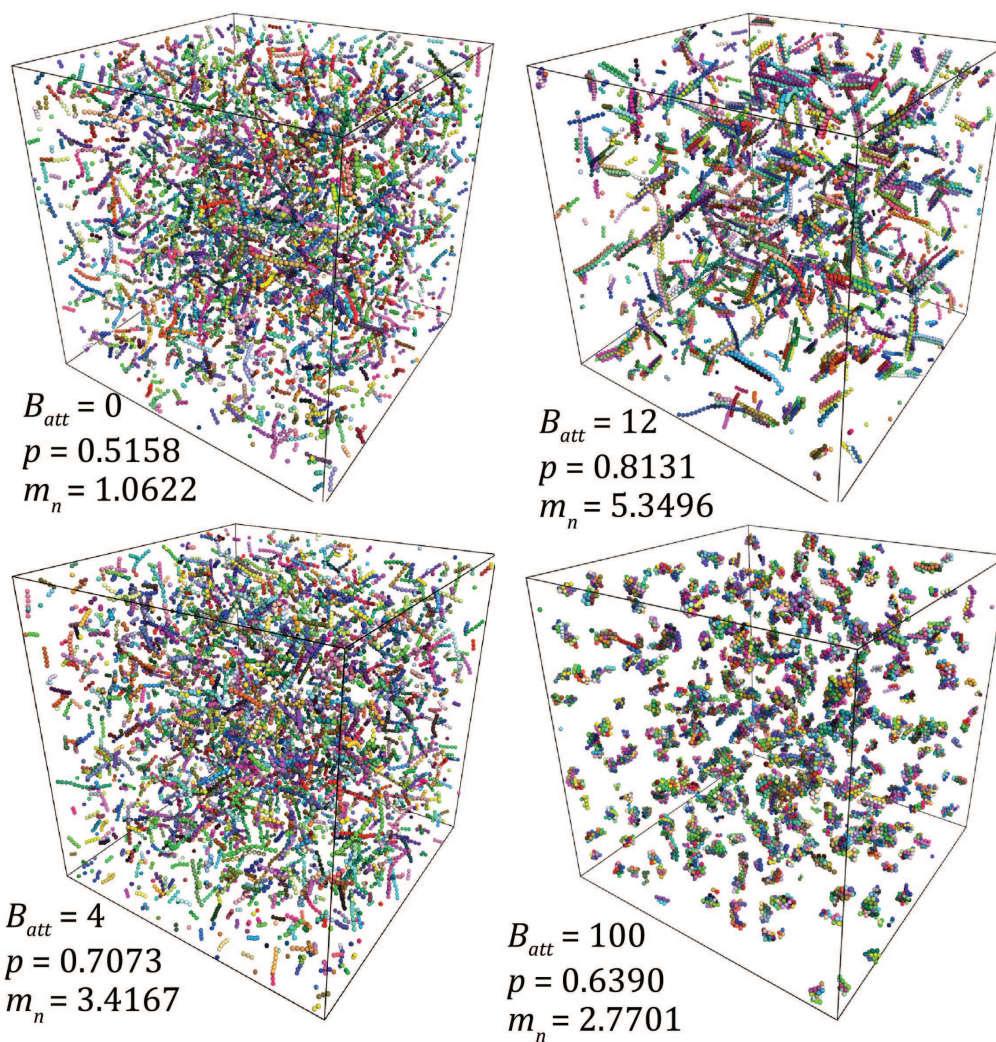$p = 0.9923$
$m_n \sim 100$
$N_{\text{loop}} = 0.0369$
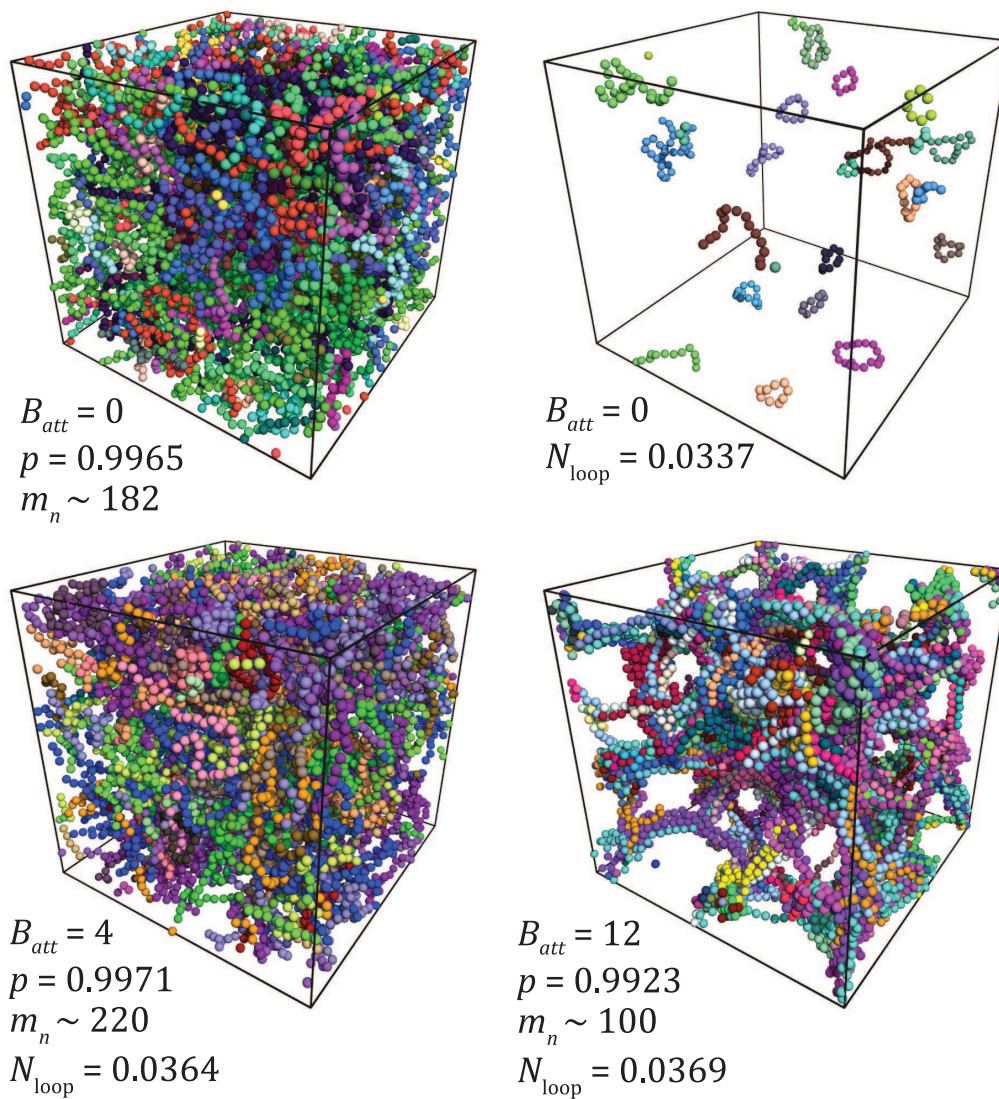
Figure 6.4: Snapshots of simulation at $t/t_0 = 1073$ for $\phi = 0.10$ and $\omega = 0.8179$ for various values of B_{att} as shown in figure to compare with the phase diagram for isotropic interaction. The top right image shows only the loops present in the top left image. The fractional conversion p, the fraction monomers involved in loop N_{loop} and the number average aggregation number, m_n, are also shown. $L_{\text{box}} = 37$, $N_0 = 9674$. Different colors indicate different chains.

bility, we should obtain collapsed globule like conformation at higher B_{att}. At a lower $B_{att} = 4$, we see that lower ω case has more aligned structure than the high ω counterpart. The lower flexibility forces the chains to align themselves while the flexible case has more freedom to exchange contacts and grow longer (clearly seen in m_n) and has a more disordered structure.
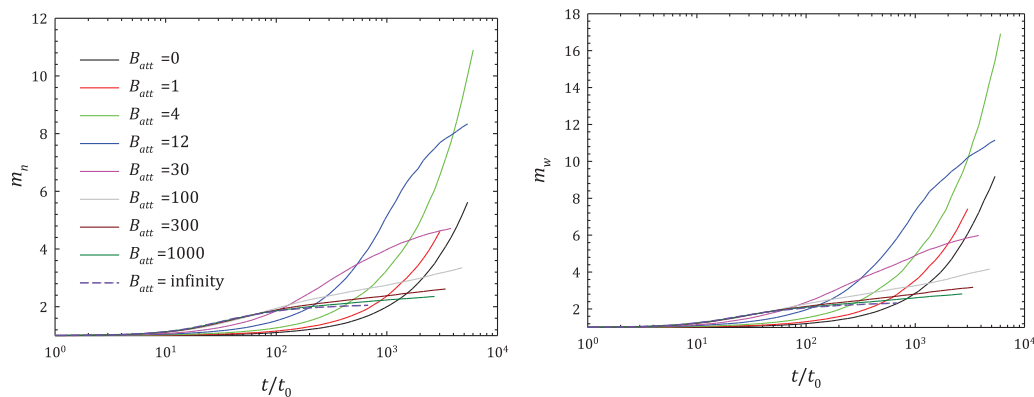
Figure 6.5: Time evolution of number average aggregation number, m_n, (left) and weight average aggregation number, m_w, (right) for $\phi = 0.01$, $\omega = 0.2$ and various B_{att} as indicated in the figure.

We get some idea for the chain lengths from the time evolution of m_n for the patchy clusters. Figure 6.5 shows the time evolution of the aggregation number for $\phi = 0.01$ and $\omega = 0.2$ and for various B_{att}. We see that for lower B_{att}, the evolution was slow, but for higher B_{att}, initially it became faster and then slowed down, while the low B_{att} case continues to increase steadily. Comparing this with corresponding images in 6.2, we can see how the solvent plays a role in the aggregation by changing the mechanism for aggregation. As B_{att} increases, it favors the formation of patches by keeping monomers in range for longer times giving an increased opportunity to react. When B_{att} became even higher, it starts to compete with patchy aggregation due to the high life time of reversible bonds. See figure 6.6 for snapshots of the time evolution of the droplet structures for the extreme case of very high B_{att} and very low ω. Here all chains in a droplet have the same color. Initially, the huge B_{att} causes particles to form droplet like structures. Within these droplets, small chains are rapidly formed. After all free monomers are consumed within a droplet, it takes longer time for it to diffuse and merge with another one and continue the polymerization reaction. Hence, the chain growth is slowed down for higher B_{att}, leading to smaller aggregation numbers. In terms of reaction rate, this means that after an initial increase for the polymerization inside a droplet, it should decrease since there all the monomers are consumed within the droplet. In fact this is what we observe in figure 6.7, where we plot $(m_w - 1)/(8 \cdot \phi \cdot \chi^{1.23} \cdot (t/t_0))$ (or $k(\chi, t)$) as a function of time. We see that $k(\chi)$ is highly dependent on B_{att}. More studies could be carried out in this direction, compared with the results we obtained for

$t/t_0 \sim 30$

$t/t_0 \sim 1073$

$t/t_0 \sim 107$

$t/t_0 \sim 3024$

$t/t_0 \sim 302$

$t/t_0 \sim 6770$
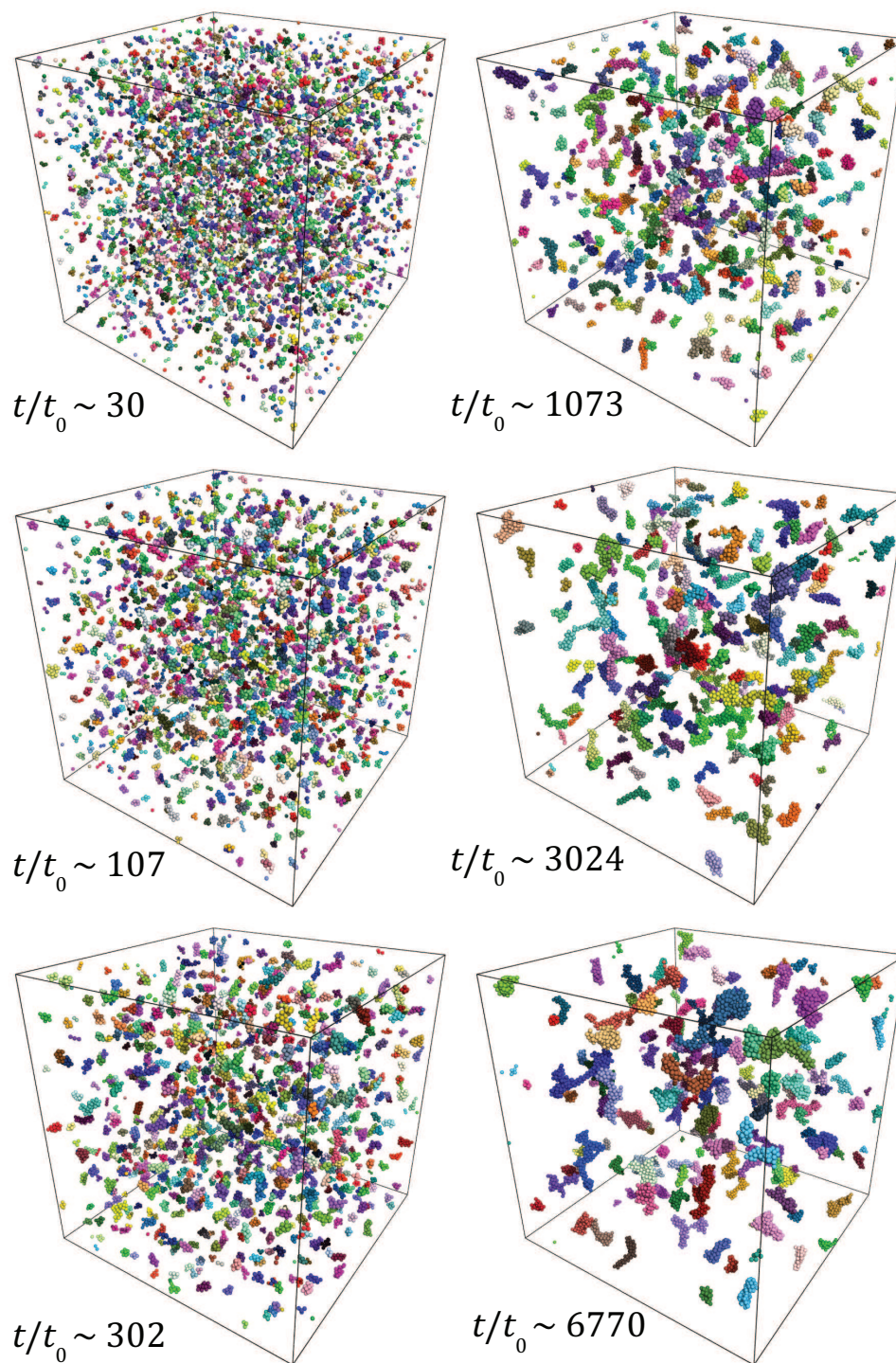
$B_{att} = 300$, $\phi = 0.01$, $\omega = 0.2$

Figure 6.6: Time evolution of the aggregate structures for $\phi = 0.01$ and $B_{att} = 300$ with $\chi^2 = 0.0004$ ($\omega = 0.2$). Box size $L_{\mathrm{box}} = 81$ and $N_0 = 10149$. Colors indicate different clusters formed through isotropic interaction.

the relationship of the rate constant with χ and the influence of B_{att}. Another interesting phenomena that can be seen in this case is the presence of dumbbell like structures. We see that due to the high rigidity, the droplets are anisotropic. When two droplets merge, a few chains in the merging droplets get interconnected to each other through the free patches at the tip of the chains. Due to the anisotropy, these formations look like dumbbells.
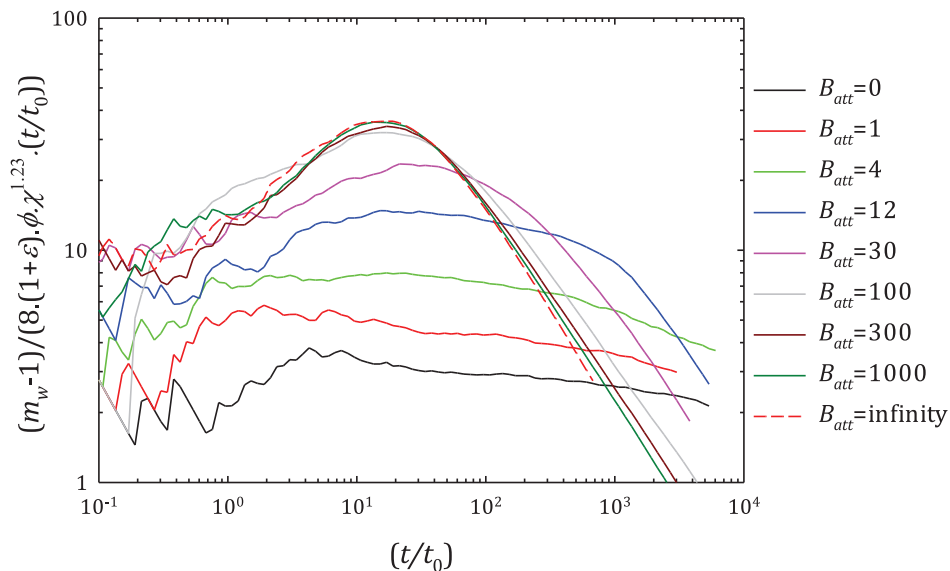
Figure 6.7: $(m_w - 1)/(8\phi \cdot \chi^{1.23} \cdot (t/t_0))$ plotted against (t/t_0) for $\phi = 0.01$ and $\chi^2 = 0.0004$ ($\omega = 0.2$) for various B_{att} as indicated in the figure. Box size $L_{\text{box}} = 81$ and $N_0 = 10149$.

Ring-chain competition and diffusion effects

We have seen that under dilute conditions and when the polymer chain is very rigid, the polymerization reaction will slow down. The same is the case when the system becomes highly entangled. For more locally flexible chains, the chain ends could diffuse faster and polymerize further. But for the dilute cases, this often leads to self exploration and formation of loops. This alters the chain length distribution. An example is shown in figure 6.8, where we compare the evolution of fractional conversion in dilute case of $\phi = 0.01$ and two different patch sizes. We see that the conversion is very slow for the more rigid one, which does not form significant amount of loops. At the same time, the more flexible one shows faster conversion with about 27% monomers involved in loops. The snapshots of the respective systems at the last point shown in the graph also exhibit the different nature of chains.
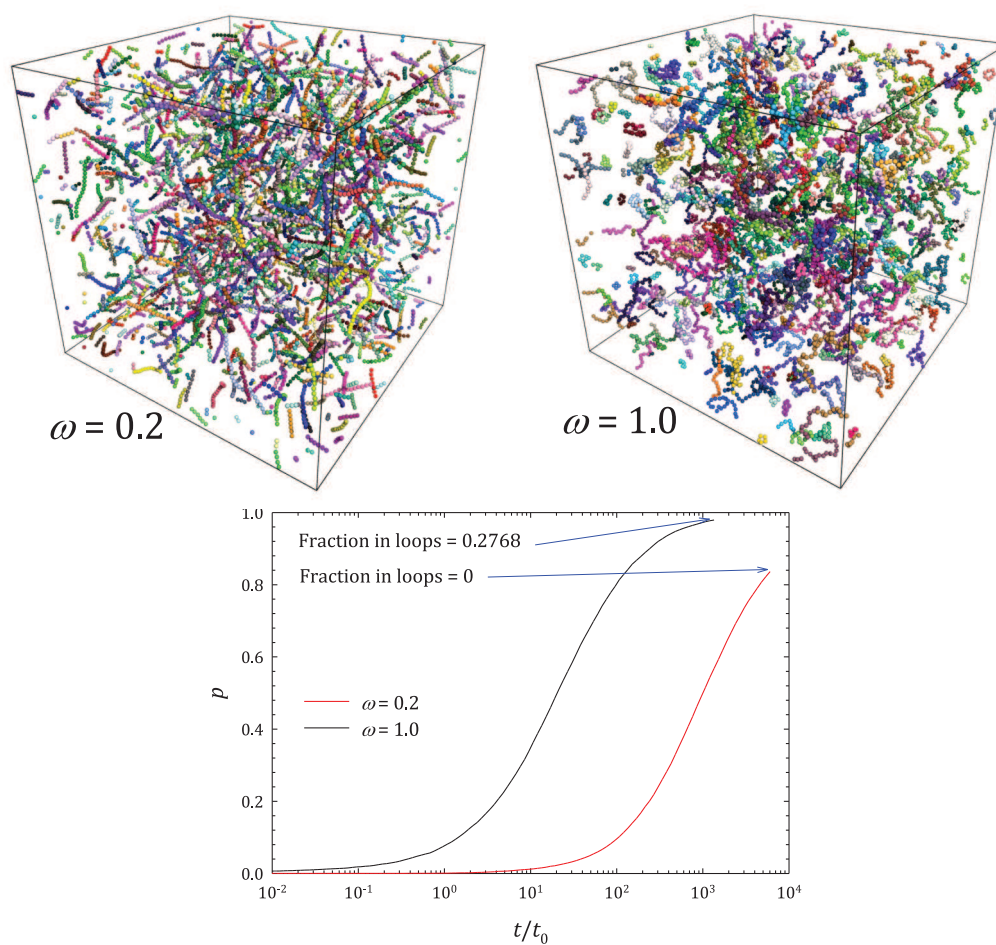
Figure 6.8: Time evolution of fractional conversion for $\phi = 0.01$ and $B_{att} = 0$ for two different ω as indicated in the figure (below). The fraction of monomers involved in loop at the final point is also shown. Above are the snapshots of the system at the last point shown in the graph. $L_{\text{box}} = 81$ and $N_0 = 10149$ and colors indicate different chains.

Modeling protein aggregation

Our model can be extended to mimic protein aggregation and polymerization. We can represent proteins using small chains of fixed length and rigidity with additional free irreversible patches (with appropriate size ω) in appropriate places with respect to the protein structure (see figure 6.9 (left)). Some good targets could be the wheat gluten proteins [130, 131, 132] or the proteins of the spider silk [133, 134]. See figure 6.9 for an example of our proposition. In the case of glutenins, the additional patches will act as free cysteine groups that can form irreversible disulfide bonds, while reversible isotropic potentials model weak interaction in the central repetitive domain of these proteins [135]. Unfortunately, we do not have yet sufficiently matching data in the literature to compare with our model. Moreover the ternary structure of candidate proteins together with the exact three dimensional position of the free cystein units are still not precisely known. Suitable experimental conditions have also to be found in order to be consistent with a step polymerization process. Otherwise, the simulation has to be modified to take into account the real reaction pathway (enzyme, catalyst, etc.).

Figure 6.9: Our proposition for protein model (left). Computer-generated molecular model of the 42K low molecular weight glutenin subunit (image adapted from [136]) underlaid on our trial model (right).

Distribution of bond length and patch vector

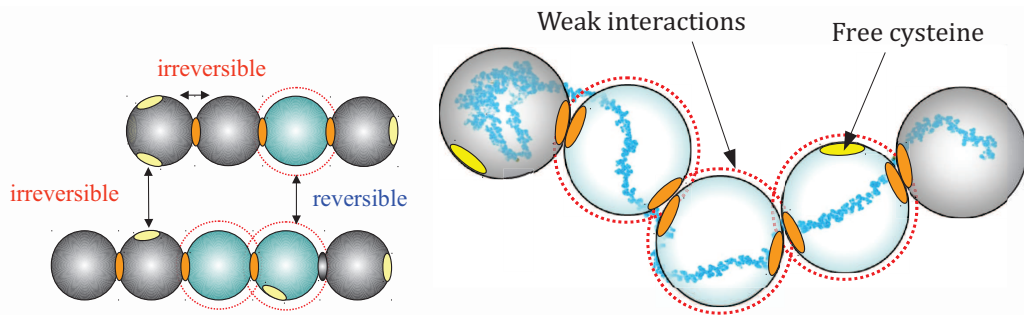In the algorithm to build chains, we have to distribute each monomer such that it lies with uniform probability within the interaction volume of the previous monomer. This means that the bond vector should point to a direction which lies within the cone angle ω defined by the spin of the previous monomer. The same is true for the selection of the spin vector for the next connected monomer such that the bond vector connecting the previous monomer is within its patch cone. Once we have the direction of the bond vector, we need to choose a magnitude to set the bond length such that the center of mass of the monomer lies within the range d and $d \cdot (1 + \varepsilon)$, where d is the diameter of the monomer (see figure A.1). Selecting a random direction in the cone and fixing a position of the center of mass in that direction in the well width are two independent processes and could be carried out independently.

A.1 Selecting a random bond length

We assume that the position of the connected monomer is uniformly distributed within the bond volume. Based on this assumption, we can calculate the distribution function for bond lengths. We have the boundaries to distribute the bond length as d and $d(1 + \varepsilon)$ constrained by the patch cone ω.

The bond volume, or the volume of the spherical cone with the vertex of the cone at the center of the sphere is given by $V = \frac{2 \cdot \pi}{3} \cdot (1 - \cos \omega) \cdot r^3$, where r the radius of the sphere. In this case, for defining the conic spherical shell, r varies from d to $d \cdot (1 + \varepsilon)$, giving the total interaction volume

$$V_{\mathrm{b}} = \frac{2 \cdot \pi}{3} \cdot (1 - \cos \omega) \cdot [(1 + \varepsilon)^3 - 1] \cdot d^3 \tag{A.1}$$

Under uniform distribution of the center of mass of the connected monomer in this volume, we have the equilibrium condition that the average bond length (l_{b}) divides the bond volume in two spherical conic shells with equal volume. This condition gives

$$[d^3 \cdot (1 + \varepsilon)^3 - l_{\mathrm{b}}^3] = (l_{\mathrm{b}}^3 - d^3) \tag{A.2}$$

and solving for l_b gives

$$l_\mathrm{b} = d \cdot \left(\frac{(1 + \varepsilon)^3 + 1}{2} \right)^{\frac{1}{3}} \tag{A.3}$$

Substituting the value $\varepsilon = 0.1$, we get $l_\mathrm{b}/d \approx 1.052$.
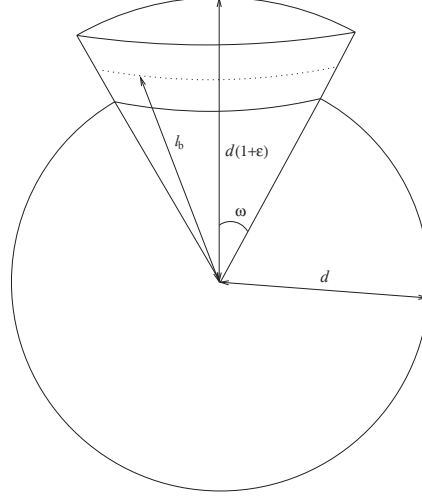
Figure A.1: Figure showing the construction of the conic shell in which the position should be chosen and the equilibrium bond length, dividing the interaction volume into two equal halves.

A.1.1   Determining the density probability function for the bond length distribution

Consider a spherical conic shell formed on a sphere of radius (in this case, the bond length) r with the vertex of the cone at the center of the sphere. The surface area on the sphere covered by the cone is given by

$$S = 2 \cdot \pi \cdot (1 - \cos \omega) \cdot r^2 \tag{A.4}$$

Any point on this surface is equally probable. Here we are interested in the distribution of the bond lengths or in other words, the probability of selecting a given surface around the sphere within the range d and $d(1 + \varepsilon)$. Let R_0 be the probability density for the surfaces/bond lengths. Let $\mathrm{d}v$ be a small interaction volume determined by the small radius increment $\mathrm{d}r$ and the surface of the cone, where $\mathrm{d}v = 2\pi(1 - \cos \omega) \cdot r^2 \cdot \mathrm{d}r$. We know that

$$\int_d^{d(1+\varepsilon)} R_0 \cdot \mathrm{d}v = 1 \tag{A.5}$$

Integration gives

$$R_0 = \frac{3}{2 \cdot \pi \cdot (1 - \cos \omega) \cdot [(1 + \varepsilon)^3 - 1] \cdot d^3} \tag{A.6}$$

The probability of choosing a given surface determined by radius r is given by R_0. Then the expectation value of r could be calculated as

$$E(r) = \int_d^{d(1+\varepsilon)} r \cdot R_0 \cdot \mathrm{d}v = \frac{3}{4} \cdot \frac{(1+\varepsilon)^4 - 1}{(1+\varepsilon)^3 - 1} \cdot d \tag{A.7}$$

On substituting $\varepsilon = 0.1$, we get $E(r) \approx 1.052$.

A.1.2   Determining the function giving the random bond length

In the C language, we use the uniform pseudo random number generator `drand48()`. The function `drand48()` returns a uniformly distributed double-precision number that is greater than or equal to 0.0 and less than 1.0. Now identifying `drand48()` to the partition function of the bond length distribution in the upper boundary condition, we have

$$\texttt{drand48()} = \int_d^x R_0 \cdot \mathrm{d}v \tag{A.8}$$

where, $d \leq x \leq d \cdot (1 + \varepsilon)$. Integration gives

$$x = d \cdot [\texttt{drand48()} \cdot [(1+\varepsilon)^3 - 1] + 1]^{\frac{3}{2}} \tag{A.9}$$

This gives us a random bond length according to our need.

A.2   Selecting random direction within a cone about Z axis

We use normalized vectors throughout this section . For easiness, we consider a virtual sphere with unit radius centered at origin, such that all the normalized vectors could be represented by a point on the surface of the sphere. According to the spherical polar coordinate convention a vector makes an angle ϕ with the positive direction of the Z axis and its projection on the XY plane makes an angle θ with the X axis. First we try to obtain a unit vector **k** within the cone ω about the Z axis, where $0 \leq \omega \leq \pi$. See figure A.2 for a schematic of the cone. For a randomly selected direction to lie in the cone, it needs to satisfy the conditions

$$\theta \in (0, 2\pi]$$
$$\cos \phi \in (\cos \omega, 1) \tag{A.10}$$

This means that we need to have a uniform distribution of random directions within these ranges. As in the section above, using `drand48()`, we can define two functions which return uniformly distributed random values within these ranges

$$r_1 = 2 \cdot \pi \cdot \texttt{drand48()}$$
$$\cos(r_2) = (1 - \cos \omega) \cdot \texttt{drand48()} + \cos \omega \tag{A.11}$$

Now, using these distributions in spherical polar coordinates, we have the random unit vector in the cone

$$\mathbf{p} = \begin{bmatrix} \sin r_2 \cdot \cos r_1 \\ \sin r_2 \cdot \sin r_1 \\ \cos r_2 \end{bmatrix} \tag{A.12}$$

where, $r_2 = \arccos((1 - \cos\omega) \cdot \texttt{drand48()} + \cos\omega)$
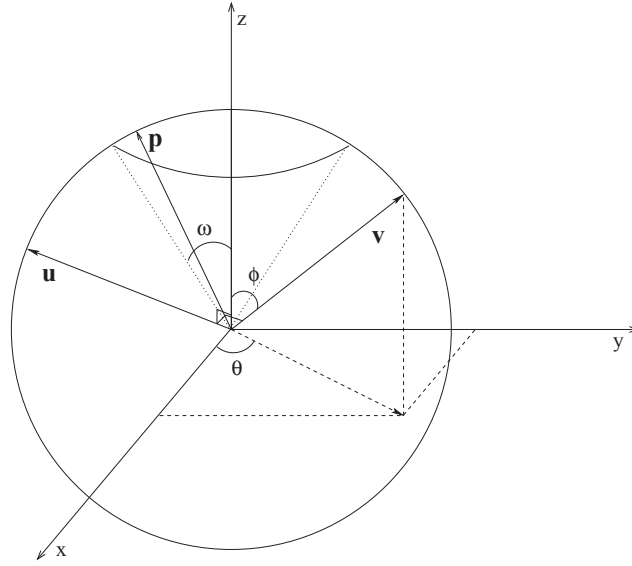
Figure A.2: Figure showing the cone ω in which the direction should be chosen and the axis of rotation $\mathbf{u} \perp \mathbf{v}$ and Z axis.

The surface area of the cone formed on the surface of the virtual sphere about the Z axis with the edge making an angle ω with it and the vertex placed at the origin is given by $S_{\text{cone}} = 2 \cdot \pi \cdot r^2 \cdot (1 - \cos\omega)$, where r is the radius of the sphere. A uniform distribution of the tip of the selected vector in this area gives an average ϕ such that it equally divides the area of the spherical surface in to two. Under this condition, we have the relation between ω and ϕ as

$$(1 - \langle\cos\phi\rangle) = \frac{1}{2} \cdot (1 - \cos\omega) \tag{A.13}$$

or in other words

$$\langle\cos\phi\rangle = \frac{1 + \cos\omega}{2} \tag{A.14}$$

A.2.1   Rotation about an axis to align the spin

In our case, we need to select a normalized direction vector $\mathbf{p}$ within the cone about the spin vector $\mathbf{v}$ (or the bond vector). $\mathbf{v}$ is rarely the Z direction. So, we transform the coordinates using the Rodrigues rotation formula such that Z axis lies on the spin vector.

See figure A.2. We have $\mathbf{v} = \begin{bmatrix} \sin\phi \cdot \cos\theta \\ \sin\phi \cdot \sin\theta \\ \cos\phi \end{bmatrix}$ and the unit vector along Z direction

$\mathbf{z} = \begin{bmatrix} 0 \\ 0 \\ 1 \end{bmatrix}$ and we need to find the rotation operator to transform $\mathbf{z}$ to $\mathbf{v}$ and apply
it to the chosen random direction $\mathbf{p}$.

A vector perpendicular to both these vectors ($\mathbf{z}$ and $\mathbf{v}$) could be found by taking
the crossproduct ($\mathbf{u} = \mathbf{z} \times \mathbf{v}$), giving a normalized $\mathbf{u} = \begin{bmatrix} -\sin\theta \\ \cos\theta \\ 0 \end{bmatrix}$. Now, we need
to rotate $\mathbf{z}$ about this vector by an angle ϕ to transform $\mathbf{z}$ to $\mathbf{v}$. The Rodrigues
rotation matrix for transforming a vector by an angle ϕ about a perpendicular
vector $\mathbf{u} = u_x \cdot \mathbf{i} + u_y \cdot \mathbf{j} + u_z \cdot \mathbf{k}$ is given by

$$\mathbf{R} = \begin{bmatrix} \cos\phi & 0 & 0 \\ 0 & \cos\phi & 0 \\ 0 & 0 & \cos\phi \end{bmatrix} + \sin\phi \cdot \begin{bmatrix} 0 & -u_z & -u_y \\ u_z & 0 & -u_x \\ -u_y & u_x & 0 \end{bmatrix}$$
$$+ (1 - \cos\phi) \cdot \begin{bmatrix} u_x^2 & u_x \cdot u_y & u_x \cdot u_z \\ u_x \cdot u_y & u_y^2 & u_y \cdot u_z \\ u_x \cdot u_z & u_y \cdot u_z & u_z^2 \end{bmatrix} \tag{A.15}$$

Substituting the values of u_x, u_y and u_z from the calculated perpendicular vec-
tor, gives the rotation matrix.

$$\mathbf{R} = \begin{bmatrix} \cos\phi + (1 - \cos\phi) \cdot \sin^2\theta & -(1 - \cos\theta) \cdot \sin\theta \cdot \cos\theta & \sin\phi \cdot \cos\theta \\ -(1 - \cos\theta) \cdot \sin\theta \cdot \cos\theta & \cos\phi + (1 - \cos\phi) \cdot \cos^2\theta & \sin\theta \cdot \sin\phi \\ -\sin\phi \cdot \cos\theta & -\sin\phi \cdot \sin\theta & \cos\phi \end{bmatrix} \tag{A.16}$$

Applying this operator $\mathbf{R}$ to the selected direction $\mathbf{p}$ transforms it in to the
correct direction relative to the spin.

A.3   Alternate method to calculate the expectation values

In this calculate the expectation values using a single distribution. We know that the
bond vector is uniformly distributed within the conic shell. Using same notations
from previous sections, we can write

$$B_0 \cdot \int_d^{d \cdot (1+\varepsilon)} r^2 \cdot dr \cdot \int_0^{2 \cdot \pi} d\theta \cdot \int_0^\omega \sin\phi \cdot d\phi = 1 \tag{A.17}$$

where B_0 is the probability density for the bond vector distribution. The solution
gives

$$B_0 = \frac{3}{2 \cdot \pi \cdot (1 - \cos\omega) \cdot [(1 + \varepsilon)^3 - 1] \cdot d^3} \tag{A.18}$$

Now, we can easily calculate the expectation value of bond length

$$\langle l_{\rm b}^2 \rangle = B_0 \cdot \int_d^{d \cdot (1+\varepsilon)} r^4 \cdot {\rm d}r \cdot \int_0^{2 \cdot \pi} {\rm d}\theta \cdot \int_0^{\omega} \sin \phi \cdot {\rm d}\phi \tag{A.19}$$

which gives

$$\langle l_{\rm b}^2 \rangle = \frac{3}{5} \cdot \frac{(1+\varepsilon)^5 - 1}{(1+\varepsilon)^3 - 1} \cdot d^2 \tag{A.20}$$

Substituting $\varepsilon = 0.1$, the above equation gives $\langle l_{\rm b}^2 \rangle = 1.10666$.

Similarly, we can calculate $\langle \cos \gamma \rangle$

$$\langle \cos \gamma \rangle = B_0 \cdot \int_d^{d \cdot (1+\varepsilon)} r^2 \cdot {\rm d}r \cdot \int_0^{2 \cdot \pi} {\rm d}\theta \cdot \int_0^{\omega} \cos \phi \cdot \sin \phi \cdot {\rm d}\phi \tag{A.21}$$

which gives the same relation we obtained before

$$\langle \cos \gamma \rangle = \frac{1 + \cos \omega}{2} \tag{A.22}$$

Bibliography

[1] Christos N. Likos. Effective interactions in soft condensed matter physics. *Physics Reports*, 348(4-5):267–439, 2001.

[2] Zhenli Zhang and Sharon C. Glotzer. Self-assembly of patchy particles. *Nano Letters*, 4(8):1407–1413, 2004.

[3] Amar B. Pawar and Ilona Kretzschmar. Fabrication, assembly, and application of patchy particles. *Macromolecular Rapid Communications*, 31(2):150–168, 2010.

[4] Sharon C. Glotzer and Michael J. Solomon. Anisotropy of building blocks and their assembly into complex structures. *Nat Mater*, 6(7):557–562, 2007.

[5] Francesco Sciortino. Primitive models of patchy colloidal particles. a review. *Collection of czechoslovak chemical communications*, 75(3):349–358, 2010.

[6] C. De Michele. Simulating hard rigid bodies. *J. Comput. Phys.*, 229(9):3276–3294, 2010.

[7] Cristiano De Michele, Simone Gabrielli, Piero Tartaglia, and Francesco Sciortino. Dynamics in the presence of attractive patchy interactions. *The Journal of Physical Chemistry B*, 110(15):8064–8079, 2006.

[8] F. Sciortino. Gel-forming patchy colloids and network glass formers: thermodynamic and dynamic analogies. *Eur. Phys. J. B*, 64(3-4):505–509, 2008.

[9] Norbert Kern and Daan Frenkel. Fluid–fluid coexistence in colloidal systems with short-ranged strongly directional attraction. *The Journal of Chemical Physics*, 118(21):9882–9889, 2003.

[10] D. M. Tsangaris and J. J. de Pablo. Bond-bias simulation of phase equilibria for strongly associating fluids. *The Journal of Chemical Physics*, 101(2):1477–1489, 1994.

[11] Francesco Sciortino, Emanuela Bianchi, Jack F. Douglas, and Piero Tartaglia. Self-assembly of patchy particles into polymer chains: A parameter-free comparison between wertheim theory and monte carlo simulation. *The Journal of Chemical Physics*, 126:194903, 2007.

[12] Riccardo Fantoni, Domenico Gazzillo, Achille Giacometti, Mark A. Miller, and Giorgio Pastore. Patchy sticky hard spheres: Analytical study and monte carlo simulations. *The Journal of Chemical Physics*, 127(23):234507–16, 2007.

[13] John Russo, Piero Tartaglia, and Francesco Sciortino. Reversible gels of patchy particles: Role of the valence. *The Journal of Chemical Physics*, 131:014504–014512, 2009.

[14] Alex W. Wilber, Jonathan P. K. Doye, Ard A. Louis, Eva G. Noya, Mark A. Miller, and Pauline Wong. Reversible self-assembly of patchy particles into monodisperse icosahedral clusters. *The Journal of Chemical Physics*, 127(8):085106, 2007.

[15] Achille Giacometti, Fred Lado, Julio Largo, Giorgio Pastore, and Francesco Sciortino. Effects of patch size and number within a simple model of patchy colloids. *The Journal of Chemical Physics*, 132(17):174110, 2010.

[16] Silvia Corezzi, Cristiano De Michele, Emanuela Zaccarelli, Daniele Fioretto, and Francesco Sciortino. A molecular dynamics study of chemical gelation in a patchy particle model. *Soft Matter*, 4(6):1173–1177, 2008.

[17] Wouter K den Otter, Marten R Renes, and W J Briels. Self-assembly of three-legged patchy particles into polyhedral cages. *Journal of Physics: Condensed Matter*, 22(10):104103, 2010.

[18] Robert Vácha and Daan Frenkel. Relation between molecular shape and the morphology of self-assembling aggregates: A simulation study. *Biophysical Journal*, 101(6):1432–1439, 2011.

[19] Flavio Romano, Eduardo Sanz, and Francesco Sciortino. Phase diagram of a tetrahedral patchy particle model for different interaction ranges. *The Journal of Chemical Physics*, 132(18):184501, 2010.

[20] Willem K. Kegel and Henk N. W. Lekkerkerker. Colloidal gels: Clay goes patchy. *Nat Mater*, 10(1):5–6, 2011.

[21] Barbara Ruzicka, Emanuela Zaccarelli, Laura Zulian, Roberta Angelini, Michael Sztucki, Abdellatif Moussaïd, Theyencheri Narayanan, and Francesco Sciortino. Observation of empty liquids and equilibrium gels in a colloidal clay. *Nat Mater*, 10(1):56–60, 2011.

[22] Vladimir N. Uversky and Anthony L. Fink. Conformational constraints for amyloid fibrillation: the importance of being unfolded. *Biochimica et Biophysica Acta (BBA) - Proteins and Proteomics*, 1698(2):131 – 153, 2004.

[23] S. Babu, J. C. Gimel, T. Nicolai, and C. De Michele. The influence of bond rigidity and cluster diffusion on the self-diffusion of hard spheres with square well interaction. *Journal of Chemical Physics*, 128(20):204504, 2008.

[24] Valerie J. Anderson and Henk N. W. Lekkerkerker. Insights into phase transition kinetics from colloid science. *Nature*, 416(6883):811–815, 2002.

[25] Tamas Vicsek. *Fractal growth phenomena*. World scientific, Singapore, 1989.

[26] Paul Meakin. Aggregation kinetics. *Physica Scripta*, 46(4):295, 1992.

[27] Massimo G. Noro and Daan Frenkel. Extended corresponding-states behavior for particles with variable range attractions. *The Journal of Chemical Physics*, 113(8):2941–2944, 2000.

[28] Sujin Babu, Jean-Christophe Gimel, and Taco Nicolai. Phase separation and percolation of reversibly aggregating spheres with a square-well attraction potential. *Journal of Chemical Physics*, 125(19):184512–1–10, 2006.

[29] Taro Kihara. Virial coefficients and models of molecules in gases. *Reviews of Modern Physics*, 25(4):831–843, 1953.

[30] Sujin Babu, Jean-Christophe Gimel, and Taco Nicolai. Crystallization and dynamical arrest of attractive hard-spheres. *Journal of Chemical Physics*, 130:064504–1–10, 2009.

[31] S. Babu, J. Gimel, and T. Nicolai. Diffusion limited cluster aggregation with irreversible slippery bonds. *The European Physical Journal E: Soft Matter and Biological Physics*, 27(3):297–308, 2008.

[32] P. N. Pusey. The effect of polydispersity on the crystalization of hard spherical colloids. *J. Physique*, 48:709–712, 1987.

[33] W. Schaertl and H. Sillescu. Brownian dynamics of polydisperse colloidal hard spheres: Equilibrium structures and random close packings. *Journal of Statistical Physics*, 77(5):1007–1025, 1994.

[34] P. N. Pusey, E. Zaccarelli, C. Valeriani, E. Sanz, Wilson C. K. Poon, and Michael E. Cates. Hard spheres: crystallization and glass formation. *Philosophical Transactions of the Royal Society A: Mathematical, Physical and Engineering Sciences*, 367(1909):4993–5011, 2009.

[35] E. Zaccarelli, I. Saika-Voivod, S. V. Buldyrev, A. J. Moreno, P. Tartaglia, and F. Sciortino. Gel to glass transition in simulation of a valence-limited colloidal system. *The Journal of Chemical Physics*, 124(12):124908, 2006.

[36] Emanuela Zaccarelli and Wilson C. K. Poon. Colloidal glasses and gels: The interplay of bonding and caging. *Proceedings of the National Academy of Sciences*, 106(36):15203–15208, 2009.

[37] M. von Smoluchowski. Drei vorträge über diffusion, brownsche molekularebewegung und koagulation von kolloidteilchen. *Physikalische Zeitschrift*, 17:557–571, 1916.

[38] M. von Smoluchowski. Versuch einer mathematischen theorie der koagulations kinetic kolloider lösugen. *Zeitschrift fur physikalische Chemie*, 92:129, 1917.

[39] Arne Westgren and Josef Reitstötter. On the coagulation of colloids. *The Journal of Physical Chemistry*, 26(6):537–548, 1921.

[40] S. Chandrasekhar. Stochastic problems in physics and astronomy. *Reviews of Modern Physics*, 15(1):1–89, 1943.

[41] G. Odriozola, Arturo Moncho-Jorda, A. Schmitt, J. Callejas-Fernandez, R. Martinez-Garcia, and Roque Hidalgo-Alvarez. A probabilistic aggregation kernel for computer-simulated transition from dlca to rlca. *Europhysics Letters*, 53:797–803, 2001.

[42] Sujin Babu, Jean-Christophe Gimel, and Taco Nicolai. Diffusion limited cluster aggregation with irreversible slippery bonds. *European Physical Journal E*, 27:297–308, 2008.

[43] Clair R. Seager and Thomas G. Mason. Slippery diffusion-limited aggregation. *Physical Review E*, 75(1):011406, 2007.

[44] Jean-Marie Lehn. Supramolecular chemistry—scope and perspectives molecules, supermolecules, and molecular devices (nobel lecture). *Angewandte Chemie International Edition in English*, 27(1):89–112, 1988.

[45] Jianhua Rong, Zhongwei Niu, L. Andrew Lee, and Qian Wang. Self-assembly of viral particles. *Current Opinion in Colloid and Interface Science*, 16(6):441–450, 2011.

[46] Laura Rossi, Stefano Sacanna, William T. M. Irvine, Paul M. Chaikin, David J. Pine, and Albert P. Philipse. Cubic crystals from cubic colloids. *Soft Matter*, 7(9), 2011.

[47] Daan Frenkel and David J. Wales. Colloidal self-assembly: Designed to yield. *Nat Mater*, 10(6):410–411, 2011.

[48] Sahand Hormoz and Michael P. Brenner. Design principles for self-assembly with short-range interactions. *Proceedings of the National Academy of Sciences*, 108(13):5193–5198, 2011.

[49] Nicolas Dorsaz, Laura Filion, Frank Smallenburg, and Daan Frenkel. Spiers memorial lecture: Effect of interaction specificity on the phase behaviour of patchy particles. *Faraday Discuss.*, 159:9–21, 2012.

[50] Flavio Romano, Piero Tartaglia, and Francesco Sciortino. Gas–liquid phase coexistence in a tetrahedral patchy particle model. *Journal of Physics: Condensed Matter*, 19(32):322101, 2007.

[51] Emanuela Bianchi, Julio Largo, Piero Tartaglia, Emanuela Zaccarelli, and Francesco Sciortino. Phase diagram of patchy colloids: Towards empty liquids. *Physical Review Letters*, 97:168301, 2006.

[52] Emanuela Bianchi. *Equilibrium Behavior of Patchy Particles: Thermo-reversible Gelation, Phase Separation and Self-Assembly*. PhD thesis, 2008.

[53] J. M. Tavares, P. I. C. Teixeira, and M. M. Telo da Gama. Criticality of colloids with distinct interaction patches: The limits of linear chains, hyperbranched polymers, and dimers. *Physical Review E*, 80(2):021506, 2009.

[54] George Jackson, Walter G. Chapman, and Keith E. Gubbins. Phase equilibria of associating fluids. *Molecular Physics*, 65(1):1–31, 1988.

[55] Flavio Romano, Eduardo Sanz, and Francesco Sciortino. Role of the range in the fluid−crystal coexistence for a patchy particle model. *The Journal of Physical Chemistry B*, 113(46):15133–15136, 2009.

[56] B. A. H. Huisman, P. G. Bolhuis, and A. Fasolino. Phase transition to bundles of flexible supramolecular polymers. *Physical Review Letters*, 100(18):188301, 2008.

[57] Bastian Antonius Hermanus Huisman. *Dynamical and structural self-organization: A study of friction, liquid-crystal nulceus growth and supramolecular polymers through simple models*. PhD thesis, 2008.

[58] Gabriel Villar, Alex W. Wilber, Alex J. Williamson, Parvinder Thiara, Jonathan P. K. Doye, Ard A. Louis, Mara N. Jochum, Anna C. F. Lewis, and Emmanuel D. Levy. Self-assembly and evolution of homomeric protein complexes. *Physical Review Letters*, 102(11):118106, 2009.

[59] M. S. Wertheim. Fluids with highly directional attractive forces. i. statistical thermodynamics. *Journal of Statistical Physics*, 35(1):19–34, 1984.

[60] M. S. Wertheim. Fluids with highly directional attractive forces. ii. thermodynamic perturbation theory and integral equations. *Journal of Statistical Physics*, 35(1):35–47, 1984.

[61] M. S. Wertheim. Fluids with highly directional attractive forces. iv. equilibrium polymerization. *Journal of Statistical Physics*, 42(3):477–492, 1986.

[62] J. M. Tavares, P. I. C. Teixeira, M. M. Telo da Gama, and F. Sciortino. Equilibrium self-assembly of colloids with distinct interaction sites: Thermodynamics, percolation, and cluster distribution functions. *The Journal of Chemical Physics*, 132(23):234502, 2010.

[63] Giuseppe Foffi and Francesco Sciortino. On the possibility of extending the noro−frenkel generalized law of correspondent states to nonisotropic patchy interactions. *The Journal of Physical Chemistry B*, 111(33):9702–9705, 2007.

[64] Emanuela Bianchi, Ronald Blaak, and Christos N. Likos. Patchy colloids: state of the art and perspectives. *Physical Chemistry Chemical Physics*, 13(14):6397–6410, 2011.

[65] Hongjun Liu, Sanat K. Kumar, and Francesco Sciortino. Vapor-liquid coexistence of patchy models: Relevance to protein phase behavior. *The Journal of Chemical Physics*, 127(8):084902, 2007.

[66] Wallace H. Carothers. Studies on polymerization and ring formation. i. an introduction to the general theory of condensation polymers. *Journal of the American Chemical Society*, 51(8):2548–2559, 1929.

[67] Wallace H. Carothers. Polymerization. *Chemical Reviews*, 8(3):353–426, 1931.

[68] Paul J. Flory. *Principles of Polymer Chemistry*. Cornell University Press, Ithaca, Naw York, 1953.

[69] Hans R. Kricheldorf and Gert Schwarz. Cyclic polymers by kinetically controlled step-growth polymerization. *Macromolecular Rapid Communications*, 24(5-6):359–381, 2003.

[70] Anil Kumar, Santosh K. Gupta, N. Somu, and M. V. Satyanarayana Rao. Simulation of cyclics and degradation product formation in polyethylene terephthalate reactors. *Polymer*, 24(4):449–456, 1983.

[71] Karel Dušek, Ján Šomvársky, Mirka Smrčková, William J. Simonsick Jr, and Lech Wilczek. Role of cyclization in the degree-of-polymerization distribution of hyperbranched polymers modelling and experiments. *Polymer Bulletin*, 42(4):489–496, 1999.

[72] Robert Stepto, Jonathan Cail, and David Taylor. Formation, structure and properties of polymer networks: theory and modelling. *Macromolecular Symposia*, 183(1):165–172, 2002.

[73] Robert M. Ziff. Kinetics of polymerization. *Journal of Statistical Physics*, 23(2):241–263, 1980.

[74] Masao Doi. Diffusion-controlled reaction of polymers. *Chemical Physics*, 9(3):455–466, 1975.

[75] U. S. Agarwal and D. V. Khakhar. Simulation of diffusion-limited step-growth polymerization in 2d: Effect of shear flow and chain rigidity. *The Journal of Chemical Physics*, 99(4):3067–3074, 1993.

[76] J. Srinivasalu Gupta, Ameya Agge, and D. V. Khakhar. Polymerization kinetics of rodlike molecules under quiescent conditions. *AIChE Journal*, 47(1):177–186, 2001.

[77] J. Srinivasalu Gupta and D. V. Khakhar. Brownian dynamics simulation of diffusion-limited polymerization of rodlike molecules: Isotropic translational diffusion. *The Journal of Chemical Physics*, 107(8):3289–3294, 1997.

[78] J. Srinivasalu Gupta and D. V. Khakhar. Brownian dynamics simulation of diffusion-limited polymerization of rodlike molecules: Anisotropic translation diffusion. *The Journal of Chemical Physics*, 108(13):5626–5634, 1998.

[79] Dimitris S. Achilias. A review of modeling of diffusion controlled polymerization reactions. *Macromolecular Theory and Simulations*, 16(4):319–347, 2007.

[80] Job D. Guzmán, Richard Pollard, and Jay D. Schieber. Modeling of diffusion effects on step-growth polymerizations. *Macromolecules*, 38(1):188–195, 2004.

[81] Billie J. Kline, Smita S. Lele, Eric J. Beckman, and Alan J. Russell. Role of diffusion in biocatalytic polytransesterification. *AIChE Journal*, 47(2):489–499, 2001.

[82] M. Doi and S. F. Edwards. *The Theory of Polymer Dynamics*. Oxford Science Publications, 1994.

[83] R. F. T. Stepto and D. R. Waywell. A study of intramolecular reaction during linear polyurethane formation. *Die Makromolekulare Chemie*, 152(1):263–275, 1972.

[84] Robert F. T. Stepto, Jonathan I. Cail, and David J. R. Taylor. Formation, structure and properties of polymer networks: theory and modelling. *Materials Research Innovations*, 7(1):4–9, 2003.

[85] M. Gordon and W. B. Temple. Ring-chain competition kinetics in linear polymers. *Die Makromolekulare Chemie*, 152(1):277–289, 1972.

[86] Gianfranco Ercolani, Luigi Mandolini, and Paolo Mencarelli. Kinetic treatment of irreversible cyclooligomerization of bifunctional chains and its relevance to the synthesis of many-membered rings. *Macromolecules*, 21(5):1241–1246, 1988.

[87] Alexei Podtelezhnikov and Alexander Vologodskii. Simulations of polymer cyclization by brownian dynamics. *Macromolecules*, 30(21):6668–6673, 1997.

[88] K. P. Santo and K. L. Sebastian. Dynamics of loop formation in a semiflexible polymer. *Physical Review E*, 80(6):061801, 2009.

[89] George Odian. *Principles of Polymerization*. John Wiley and Sons, New Jersey, 2004.

[90] Richard P. Sear. Phase behavior of a simple model of globular proteins. *The Journal of Chemical Physics*, 111(10):4800–4806, 1999.

[91] Xiaofei Li, J. D. Gunton, and A. Chakrabarti. A simple model of directional interactions for proteins. *The Journal of Chemical Physics*, 131(11):115101, 2009.

[92] Hongjun Liu, Sanat K. Kumar, Francesco Sciortino, and Glenn T. Evans. Vapor-liquid coexistence of fluids with attractive patches: An application of wertheim's theory of association. *The Journal of Chemical Physics*, 130(4):044902, 2009.

[93] Daan Frenkel and Berend Smit. *Understanding Molecular Simulation From algorithms to Applications*, volume 1 of *Computational Science From Theory to Applications*. Academic Press, 1996.

[94] M P Allen and D. J. Tildesley. *Computer Simulation of Liquids*. Oxford Science Publications, Oxford, 1987.

[95] Jean-Pierre Hansen and Ian R. McDonald. *Theory of Simple Liquids*. Academic Press, London, 2 edition, 1986.

[96] Jim C. Chen and Albert S. Kim. Brownian dynamics, molecular dynamics, and monte carlo modeling of colloidal systems. *Advances in Colloid and Interface Science*, 112(1-3):159–173, 2004.

[97] Paul Meakin. Formation of fractal clusters and networks by irreversible diffusion-limited aggregation. *Phys. Rev. Lett.*, 51:1119–1122, Sep 1983.

[98] M. Kolb, R. Botet, and R. Jullien. Scaling of kinetically growing clusters. *Phys. Rev. Lett.*, 51:1123–1126, Sep 1983.

[99] Jean Christophe Gimel, Dominique Durand, and Taco Nicolai. Transition between flocculation and percolation of a diffusion-limited cluster-cluster aggregation process using three-dimensional monte carlo simulation. *Physical Review B*, 51(17):11348–11357, 1995.

[100] Jean Christophe Gimel, Taco Nicolai, and Dominique Durand. 3d monte carlo simulations of diffusion limited cluster aggregation up to the sol-gel transition: structure and kinetics. *Journal of Sol-Gel Science and Technology*, 15(2):129–136, 1999.

[101] Manuel Rottereau, Jean Christophe Gimel, Taco Nicolai, and Dominique Durand. Monte-carlo simulation of particle aggregation and gelation: I growth, structure and size distribution of the clusters. *European Physical Journal E*, 15:133–140, 2004.

[102] Manuel Rottereau. *Agrégation, percolation et séparation de phase d'une assemblée de sphères dures adhésives. Approche par simulation hors réseau.* PhD thesis, 2005.

[103] Sujin Babu. *Propriétés statiques et dynamiques de sphères dures attractives. Etude par simulation numérique.* PhD thesis, 2008.

[104] I. Carmesin and Kurt Kremer. The bond fluctuation method: a new effective algorithm for the dynamics of polymers in all spatial dimensions. *Macromolecules*, 21(9):2819–2823, 1988.

[105] Rolf Mulhaupt. Hermann staudinger and the origin of macromolecular chemistry. *Angewandte Chemie International Edition*, 43(9):1054–1063, 2004.

[106] Paul J. Flory. *Statistical Mechanics of Chain Molecules*. Interscience Publishers, 1969.

[107] Michael Rubinstein and Ralph H. Colby. *Polymer Physics*. Oxford University Press, 2006.

[108] Hiromi Yamakawa. *Modern theory of polymer solutions*. Harper and Row, New York, 1971.

[109] P G de Gennes. *Scaling Concepts in Polymer Physics*. Cornell University Press, 1979.

[110] L. Schäfer and K. Elsner. Calculation of the persistence length of a flexible polymer chain with short-range self-repulsion. *The European Physical Journal E: Soft Matter and Biological Physics*, 13(3):225–237, 2004.

[111] Hsiao-Ping Hsu, Wolfgang Paul, and Kurt Binder. Standard definitions of persistence length do not describe the local "intrinsic" stiffness of real polymer chains. *Macromolecules*, 43(6):3094–3102, 2010.

[112] Hsiao-Ping Hsu, Kurt Binder, and Wolfgang Paul. How to define variation of physical properties normal to an undulating one-dimensional object. *Physical Review Letters*, 103(19):198301, 2009.

[113] Lothar Sch¨afer, Andrea Ostendorf, and Johannes Hager. Scaling of the correlations among segment directions of a self-repelling polymer chain. *Journal of Physics A: Mathematical and General*, 32(45):7875, 1999.

[114] J. P. Wittmer, H. Meyer, J. Baschnagel, A. Johner, S. Obukhov, L. Mattioni, M. Müller, and A. N. Semenov. Long range bond-bond correlations in dense polymer solutions. *Physical Review Letters*, 93(14):147801, 2004.

[115] Hsiao-Ping Hsu, Wolfgang Paul, and Kurt Binder. Polymer chain stiffness vs. excluded volume: A monte carlo study of the crossover towards the worm-like chain model. *EPL*, 92(2):28003, 2010.

[116] Hsiao-Ping Hsu, Wolfgang Paul, Silke Rathgeber, and Kurt Binder. Characteristic length scales and radial monomer density profiles of molecular bottlebrushes: Simulation and experiment. *Macromolecules*, 43(3):1592–1601, 2010.

[117] Alan D. Sokal. *Monte Carlo and Molecular Dynamics Simulations in Polymer Science*, chapter Monte Carlo Methods for Self Avoiding Walk. Oxford University Press, 1995.

[118] Folarin Latinwo and Charles M. Schroeder. Model systems for single molecule polymer dynamics. *Soft Matter*, 7(18), 2011.

[119] D. W. Schaefer, J. F. Joanny, and P. Pincus. Dynamics of semiflexible polymers in solution. *Macromolecules*, 13(5):1280–1289, 1980.

[120] Andrzej Kolinski, Mariusz Milik, and Jeffrey Skolnick. Static and dynamic properties of a new lattice model of polypeptide chains. *The Journal of Chemical Physics*, 94(5):3978–3985, 1991.

[121] Debabrata Panja and Gerard T. Barkema. Rouse modes of self-avoiding flexible polymers. *The Journal of Chemical Physics*, 131(15):154903, 2009.

[122] Jaromír Jakeš. Regularized positive exponential sum (repes) program : A way of inverting laplace transform data obtained by dynamic light scattering. *Collection of czechoslovak chemical communications*, 60(11):1781–1797, 1995.

[123] Peters Rainer. Noise on photon correlation functions and its effect on data reduction algorithms. In Wyn Brown, editor, *Dynamic Light Scattering. The Method and Some Applications*, pages 149–176. Oxford University Press, Oxford, 1993.

[124] Petr Stepanek. Data analysis in dynamic light scattering. In Wyn Brown, editor, *Dynamic Light Scattering. The Method and Some Applications*, pages 177–241. Oxford University Press, Oxford, 1993.

[125] M. Rottereau, J. Gimel, T. Nicolai, and D. Durand. Influence of the brownian step size in off-lattice monte carlo simulations of irreversible particle aggregation. *The European Physical Journal E: Soft Matter and Biological Physics*, 18(1):15–19, 2005.

[126] Peter Mörters and Yuval Peres. *Brownian Motion*. Cambridge University Press, 2010.

[127] R. J. Baxter. Percus–yevick equation for hard spheres with surface adhesion. *The Journal of Chemical Physics*, 49(6):2770–2774, 1968.

[128] Nam-Kyung Lee, Albert Johner, Fabrice Thalmann, Laetitia Cohen-Tannoudji, Emanuel Bertrand, Jean Baudry, Jerome Bibette, and Carlos M. Marques. Ligand−receptor interactions in chains of colloids: When reactions are limited by rotational diffusion. *Langmuir*, 24(4):1296–1307, 2008.

[129] W. R. Heinson, C. M. Sorensen, and A. Chakrabarti. A three parameter description of the structure of diffusion limited cluster fractal aggregates. *Journal of Colloid and Interface Science*, 375(1):65–69, 2012.

[130] Andrea Orsi, Francesca Sparvoli, and Aldo Ceriotti. Role of individual disulfide bonds in the structural maturation of a low molecular weight glutenin subunit. *The Journal of Biological Chemistry*, 276(4):32322–32329, 2001.

[131] Peter Köhler, Bettina Keck-Gassenmeier, Herbert Wieser, and Donald D. Kasarda. Molecular modeling of the n-terminal regions of high molecular weight glutenin subunits 7 and 5 in relation to intramolecular disulfide bond formation. *Cereal Chemistry*, 74(2):154–158, 1997.

[132] Donald D. Kasarda, Gregory King, and Thomas F. Kumosinski. Comparison of spiral structures in wheat high molecular weight glutenin subunits and elastin by molecular modeling. In *Molecular Modeling*, ACS Symposium Series, pages 209–220. American Chemical Society, Washington, DC, 1994.

[133] Hongyan Song and John Parkinson. Modelling the self-assembly of elastomeric proteins provides insights into the evolution of their domain architectures. *PLoS Comput Biol*, 8(3):e1002406, 03 2012.

[134] Markus Heim, Christian B. Ackerschott, and Thomas Scheibel. Characterization of recombinantly produced spider flagelliform silk domains. *Journal of Structural Biology*, 170(2):420 – 425, 2010.

[135] P R Shewry, N G. Halford, Peter S. Belton, and A. S. Tatham. The structure and properties of gluten: an elastic protein from wheat grain. *Phil. Trans. R. Soc. Lond. B*, 357:133–142, 2002.

[136] Stefania Masci, Renato D'Ovidio, Domenico Lafiandra, and Donald D. Kasarda. Characterization of a low-molecular-weight glutenin subunit gene from bread wheat and the corresponding protein that represents a major subunit of the glutenin polymer. *Plant Physiology*, 118:1147–1158, 1998.